

---

Dissertation zur Erlangung des Doktorgrades  
der Fakultät für Chemie und Pharmazie  
der Ludwig-Maximilians-Universität München

**Design, synthesis and application of rigid  
rod-like foldamers using 6-aminoquinoline-2-  
carboxylate building blocks**

Kathrin Aftahy

aus

München, Deutschland

2023

---

Erklärung

Diese Dissertation wurde im Sinne von § 7 der Promotionsordnung vom 28. November 2011 von Herrn Prof Ivan Huc betreut.

Eidesstattliche Versicherung

Diese Dissertation wurde eigenständig und ohne unerlaubte Hilfe erarbeitet.

München, den 30.11.2023

Kathrin Aftahy

---

(Kathrin Aftahy)

Dissertation eingereicht am: 06.12.2023

1. Gutachter: Prof. Dr. Ivan Huc

2. Gutachter: Prof. Dr. Franz Bracher

Mündliche Prüfung am 01.02.2024

---

*Diese Arbeit widme ich meiner Familie –  
insbesondere meiner Mutter.*

## Acknowledgements

This work was done during the time between January 2018 until October 2022 at the Ludwig-Maximilian-University in Munich, at the Department of Pharmacy and Chemistry under the supervision of Prof. Ivan Huc, whom I thank the most for giving me the chance to grow in his workgroup and for helping me at any time with his helpful advice. Secondly, I thank the Examination committee and in particular, Prof. Dr. Bracher for acting as the second assessor.

I thank Dr. Victor Maurizot for helping me anytime with synthetic problems. I am thankful for having worked with Dr. Joan Atcher during my first two years in this group with whom I always appreciated spending hours in front of the hood. I thank Dr. Celine Douat and Dr. Yann Ferrand for giving me advice for crystallization, ESI-MS and HPLC measurements and Dr. Lars Allmendinger and Claudia Glas for measuring NMR spectra.

Of course, I thank all my coworkers I worked with in this group during my PhD, i.e. my lab neighbours Dr. Binhao Teng, Niklas Böcher, Lingfei Wang, Dr. Mathieu Denis and Dr. Sai Reddy Post, Dr. Mahshid Alizadeh, furthermore Dr. Ryan Howard, Dr. Valentina Corvaglia, Dr. Sudhakar Ghaikwad, Dr. Siyuan Wang, Dr. Sunbum Kwon, Dr. Susnata Pramanik, Dr. Pradeep Mandal, Dr. Vasily Mozorov, Florian, Sanchez, Jiaojiao Wang, Melis Chabbar, Deepak Deepak, Shuhe Wang, Dr. Sebastian Dengler, Dr. Daniel Bindl, Dr. Friederike Menke, Ivan Alonso, Mariia Palchyk, Dr. Arundhati Roy, and Dr. Daniel Gill. Also I thank my master student Sebastian Reiner for collecting data for characterization of the monomers.

Of Course, I thank Prof. Vadim Frolov and Pedro Arrasate from the Biofisika Institute in Bilbao for the good time I had during our collaboration.

In the end, I need to thank my family and friends for their support and motivating advice.

## Table of Contents

Acknowledgements	
Abbreviations	7
Abstract	9
1. General Introduction	11
1. Foldamers	12
2. Aromatic foldamers in membranes	17
3. Conformational behavior of foldamers	19
4. Conclusion	23
5. References	26
2. Motivation and Research objectives	29
3. Molecular sensing and manipulation of protein oligomerization in membrane nanotubes with bolaamphiphilic foldamers	31
1. Publication	32
2. Supplementary Information	58
4. Strained shape persistent macrocycles	144
1. Introduction	145
2. Concept and Experimental Design	146
3. Results and Discussion	147
a. Compound synthesis	149
b. Solvent dependent conformational behavior	150
c. Host Guest formation	154
4. Conclusion and Perspectives	156
5. References	157
6. Experimental part	158
1. General remarks	158
2. Monomer synthesis	160
3. Solid phase assisted synthesis of oligomers	168
4. NMR and HPLC data	174
5. Peptide-foldamer macrocycle hybrid	201
1. Introduction	202
2. Concept and Experimental Design	203

3. Results and Discussion -----	206
a. Compound synthesis -----	206
b. Solution state studies of the macrocycles -	207
c. Computational studies -----	208
4. Conclusion and Perspectives -----	210
5. References -----	212
6. Experimental part -----	213
1. General remarks -----	213
2. Computational data -----	214
3. Monomer and oligomer synthesis -----	216
4. NMR and HPLC data -----	223
6. Summary and Outlook -----	233

## List of Abbreviations

1,2-DCE:	1,2-dichloroethane
1,1,2,2-TCE-d <sub>2</sub> :	1,1,2,2-tetrachloroethane-d <sub>2</sub>
$\lambda$ :	wavelength (nm)
$\delta$ :	NMR chemical shift (ppm)
$\nu$ :	Wavenumber (cm <sup>-1</sup> )
AA:	amino acid
Å	Angstrom
Boc:	Ditertbutylcarbamategroup
Boc <sub>2</sub> O:	Di-tert-butyl dicarbonate
cryo-EM:	Cryo electron microscopy
CPK:	Corey, Pauling, Koltune space filling
Da:	Dalton
DCM:	Dichloromethane
DIAD:	Diisopropyl azodicarboxylate
DIPEA or DIEA:	N,N-diisopropylethylamine
DMB:	Dimethoxybenzylgroup
DMF:	N,N-dimethylformamide
EDC:	N-(3-dimethylaminopropyl)-N'-ethylcarbodiimide
ESI:	Electrospray ionization
EtOH:	ethanol
FLIM:	fluorescent lifetime imaging microscopy
Fmoc:	Fluorenylmethyloxycarbonyl protecting group
Ghosez' reagent	1-Chloro-N,N,-2-trimethyl-1-propenylamine
GPC:	gel permeation chromatography
HRMS:	High-resolution mass spectrometry
HPLC:	High performance liquid chromatography
HFP:	Hexafluorophosphate
HBF <sub>3</sub> :	Trifluoroborane
HBr:	Hydro bromic acid
HCl:	Hydrochloride acid
HSQC:	Heteronuclear single quantum coherence
HMBC:	Heteronuclear multiple bond correlation

NOESY:	Nuclear Overhauser Effect Spectroscopy
ROESY:	Rotating frame Overhauser Enhancement Spectroscopy
<i>i</i> Bu:	isobutoxygroup
KOH:	potassium hydroxide
LNT:	lipid nanotube
LC:	liquid chromatography
NaOH:	sodium hydroxide
MD:	Molecular Dynamics
Me:	methyl
MeOH:	methanol
MIC:	minimal inhibitory concentration ( $\mu$ M)
MMFFs:	<i>Merck Molecular</i> Force Field static
MW:	molecular weight
MS:	mass spectrometry
NMR:	nuclear magnetic resonance
NP:	normal phase
PFP:	Pentafluorophenole
Ph <sub>3</sub> P:	triphenylphosphine
PyBOP:	benzotriazol-1-yl-oxytripyrrolidino-phosphonium hexafluorophosphate
RBF:	round bottom flask
RHEB:	Ras homolog enriched in brain
RP:	reversed phase
SPS:	solid phase synthesis
SPFS:	solid phase foldamer synthesis
TCAN:	trichloroacetonitrile
THF:	tetrahydrofuran
TFA:	trifluoroacetic acid
TLC:	thin layer chromatography

## Abstract

$\beta$ -barrel proteins represent a wide family of  $\alpha$ -helical and  $\beta$ -sheet conformed molecules with distinct conformation and overall pore-like structures. Their biological functions are manifold. When targeting their mimetics, one way is to design and synthesize linear foldamer oligomer fragments that can be purified, assembled and macrocyclized. These fragments, however, – corresponding to the  $\beta$ -sheet molecule in a  $\beta$ -barrel proteins – comprise a wide aromatic surface. Accordingly, these molecules are prone to unspecific aggregation and thus, purification *post* synthesis may be challenging.

Herein, we show different ways synthesizing these rod-like molecules based on 6-aminoquinoline 2-carboxylic acid units (hereafter referred to as Q<sup>p</sup>; see chapter 1 for details on this monomer). Firstly, we show that rod-like molecules based on Q<sup>p</sup> can be incorporated in lipid bilayer membranes. Furthermore, they propose a new tool to control geometry, bending rigidity and molecular composition of membranes by using ultra-short nanotubes (usNT). Moreover, they can be traced by single-molecule measurements *via* distinct current response and show binding affinity towards membrane proteins e.g., Annexin V and ENTH (see chapter 3 for more details). Secondly, we show that linearity disruptor groups i.e. DMB groups can change the conformation on linear foldamer oligomers. They enabled kinking of the foldamer backbone and changing the overall geometry through *cis/trans* isomerism. In this way, we show successful intramolecular macrocyclization of foldamer oligomers. Specifically, the shortest possible macrocyclic foldamer sequence is synthesized accordingly. Moreover, we show the ability of host-guest complexes with larger macrocycles (see chapter 5 for more details). Finally, we demonstrate that linear foldamers can be used for the design of macrocyclic foldamer-peptide hybrids which were obtained by hybridization with oligopeptides. In this context, we demonstrate that the foldamer's conformation affect the conformation of its neighboring oligopeptide and overturn the whole conformation of these hybrids (see chapter 5 for more details).

In conclusion, these results establish a scientific output on rigid and rod-like foldamers. Specifically, these results suggest that macrocyclic architectures consisting of 6-aminoquinoline 2-carboxylic acid units either – homomeric sequences or in

hybrid models – show significant potential in the application in membrane models, molecular recognition or peptidomimetic designs.

## 1. General Introduction

*“It is the pervading law of all things organic and inorganic, of all things physical and metaphysical, of all things human, and all things super-human, of all true manifestations of the head, of the heart, of the soul, that the life is recognizable in its expression, that form ever follows function.”<sup>(1)</sup>*

“*Form follows function*”- this dictum is fundamental for many modern architects nowadays and was coined in the late 19<sup>th</sup> century by Louis Henry Sullivan, who revolutionarily re-thought the concept of architectural design, and overcame technical and engineering limits by using new easy-to-handle materials. This dictum can be applied to natural processes, where specific protein conformations lead to distinct functionality. For example, a simple change in conformation of an agonist to a G-protein-coupled receptor (GPCR) upon binding leads to an activation of its bound G-protein complex. This is established by replacing GDP on the G<sub>α</sub> subunit with GTP. The latter leads to the dissociation of the complex into two subunits, i.e., the G<sub>α</sub> and the β - γ dimer – both no longer bound to the GPCR – and diffusing on the inner membrane. Accordingly, they are able to interact with further proteins. Adopting Sullivan’s way of thinking to the field of research, it should be consequently possible to overcome current problems and bottlenecks by working with new materials and compounds. Regarding the field of chemistry, foldamer research opened up a whole new field of possible applications. Over the last few decades, the field of foldamer chemistry expanded enormously and created many branches regarding their synthesis and application.<sup>(2)</sup> *Foldamers* are artificial molecules inspired by biomolecules, that fold into a well-defined three-dimensional structure. Foldamers may be based on an oligomeric sequence comprising a peptide or artificial non-peptide backbone, that may vary in the composition of the building block. Each building block – carrying different sidechains – may change folding properties, solubility and the three-dimensional architecture. The driving forces, responsible for their final conformation are manifold but mainly caused by non-covalent interactions.

## 1.1 Foldamers

In 1987, Lehn and coworkers presented an oligo bipyridine ligand based on 2,2-bipyridine building blocks, that undergoes spontaneous dimerization, “[...] reminiscent of the double-helical structure of nucleic acids”.<sup>(3)</sup> Since then, a variety of artificial helical foldamers were described (**Figure 1A, left**), i.e.  $\alpha/\beta$ -peptide foldamers, peptoids, aromatic foldamers or nucleic acid foldamers.<sup>(4-6)</sup> For example, Pilsel et al. report that a dimeric subunit of a six-helix bundle is formed between a natural  $\alpha$ -helix and  $\alpha/\beta$ -peptide. These dimeric units were shown to trimerize into six-helix bundles, where the unnatural  $\alpha/\beta$ -peptides mimic their natural counterparts (**Figure 1A, right**).<sup>(7)</sup>

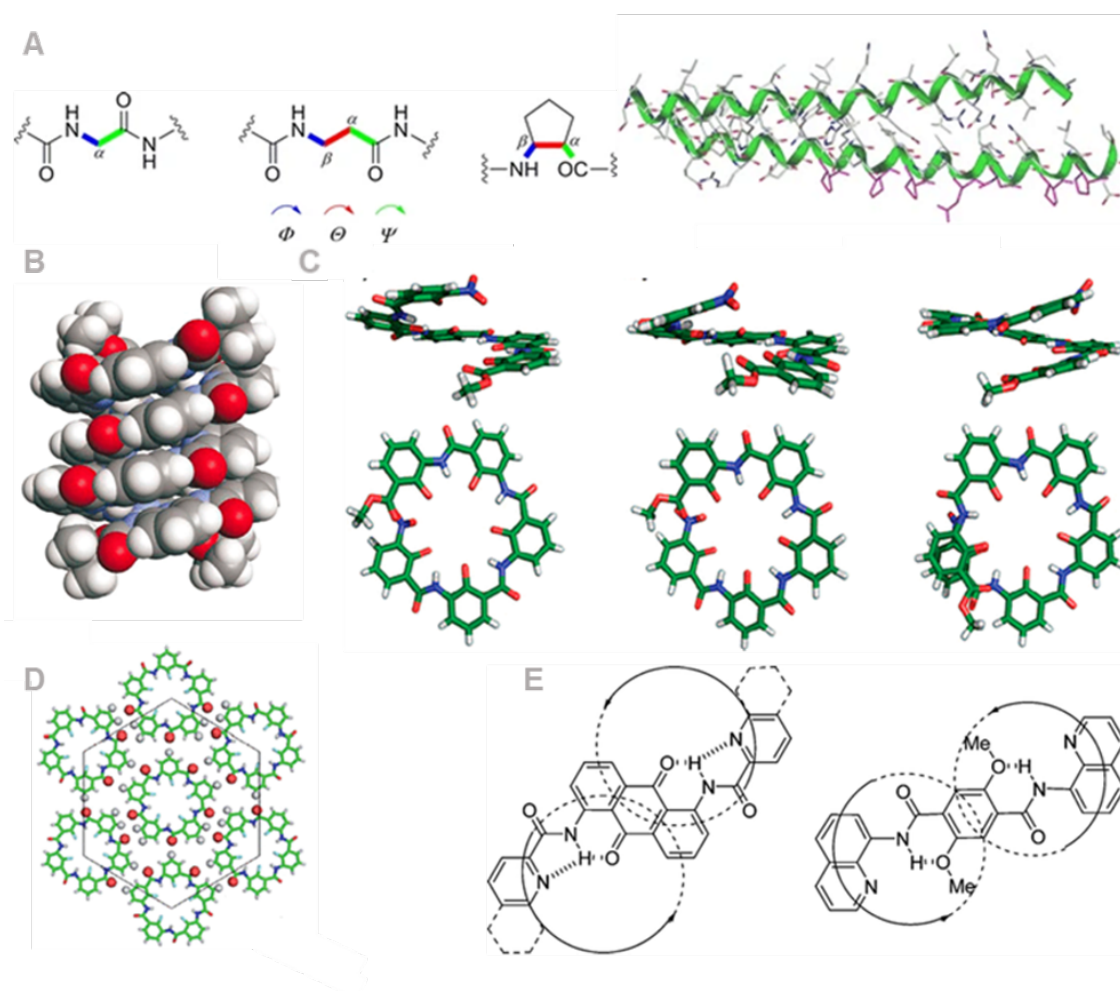


**Figure 1. Different foldamer families:** (A) Left:  $\alpha$ - and  $\beta$ -amino acids and cyclic  $\beta$ -amino acids.  $\alpha$ -amino acids (left), acyclic  $\beta$ -amino acids (middle) and cyclic  $\beta$ -amino acids (right). Different torsion angles  $\phi$ ,  $\psi$ , and  $\theta$  are defined. Right: X-ray structure of a dimeric subunit of a six-helix bundle. The helix bundle is formed between a natural  $\alpha$ -helix and  $\alpha/\beta$ -peptide, which is in cartoon representation.<sup>(7)</sup> (B) X-ray structure of a pyridine-based double helical aromatic foldamer.<sup>(8)</sup> (C) X-ray structures of phenylene based amino acid oligomers.<sup>(9)</sup> (D) X-ray structure and packing mode of macrocyclic foldamer oligomers.<sup>(10)</sup> (E) hydrogen bonding pattern for helical foldamers with different building blocks.

Foldamers are defined by their folding properties (**Figure 1B, 1C**), which lead to a distinct conformation that determines the overall shape and therefore their function.<sup>(2, 11)</sup> Solvophobic effects, as well as specific local conformational preferences (**Figure 1D, 1E**) need to be taken into account in the early stage of design and synthesis. There are numerous potential applications of foldamers that are still unexplored. This prompts many workgroups to create new experimental designs and strategies to explore their behavior and properties. Prof. Huc's research group focuses on abiotic aromatic oligoamide foldamers (**Figure 2A**) using a library of different building blocks, that show specific characteristics, abilities and behaviors. Each *monomer* used in oligomeric sequences is designed in such a way to give rise to different three-dimensional structures, which differ in terms of diameter size, folding properties and solubility.<sup>(2, 12)</sup>

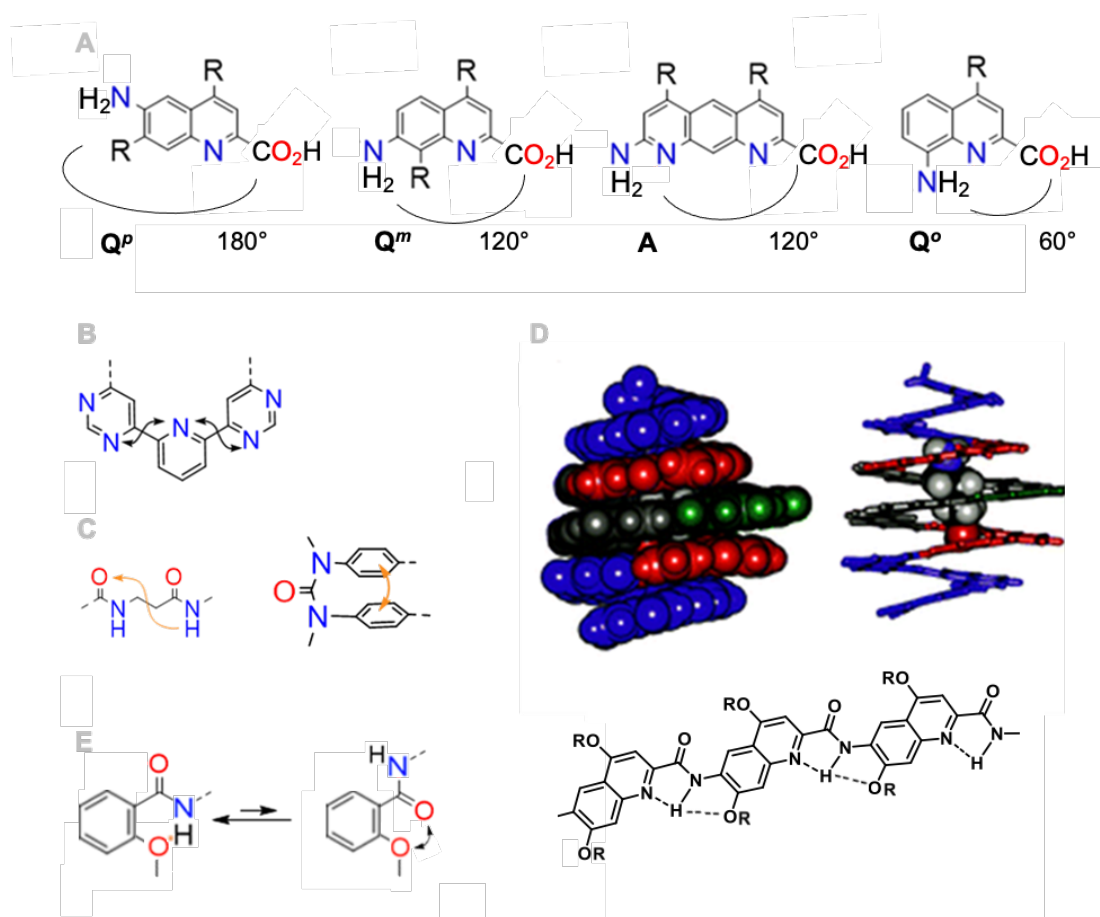


**Figure 2** Quinoline and anthracene-based monomers and local conformational preferences: (A)  $Q^p$  = 6-aminoquinoline 2-carboxylic acid;  $Q^m$  = 7-aminoquinoline 2-carboxylic acid;  $A$  = 7-amino-anthracene carboxylic acid and  $Q^o$  = 8-aminoquinoline 2-carboxylic acid. (B and C) Non covalent

interactions, i.e. attractive interactions such as hydrogen bonding and  $\pi$ - $\pi$  interactions shown in orange arrows. Repulsive interactions such as electron pair repulsion of the electron lone pairs on the N atoms shown with black arrows. **(D)** Crystal structure of helical capsule based on **A** and **Q** monomers. **(E) left:** Hydrogen bonding interaction in 2-methoxy benzamide between the methoxy oxygen and amide NH; **right:** chemical structure of  $Q^p$  trimer.

To obtain an overall helical shape (**Figure 2D**) and to create curvature, hydrogen bonding interactions on the inner rim of the backbone sequence are necessary (**Figure 2E**), e.g., hydrogen bonding between the amino group with a hydrogen bonding acceptor in a 5- membered ring, as well as hydrogen bonding interactions between the amino group on position 8 and the *endo* cyclic nitrogen on the quinoline ring system (**Figure 2E, right**). The amino position – either in position 6, 7 or 8 on the aminoquinoline-2-carboxylate building block determines the folding angle and influences the total number for units per turn needed. The 8-aminoquinoline 2-carboxylate requires 2.5 units per turn and has the amino and acid substituents point in the same directions as *ortho*-substituents, resembling an “*ortho*-like” substitution, gives rise to a folding angle of less than  $60^\circ$  (i.e., the angle between the N- and C-terminus on the aminoacid monomer). The 8-aminoquinoline 2-carboxylic acid unit gives rise to a high curved oligomer (**Figure 2A**, see “ $Q^o$ ”). When using the  $Q^o$  monomer, 2.5 units suffice to establish a full turn on the folded structure. The 7-aminoquinoline 2-carboxylate monomer, which resembles a “*meta*” substitution, has a folding angle of less than  $120^\circ$  which is less curved as compared to the 8-aminoquinoline 2-carboxylate trimer. Accordingly, this building block is capable of leading to a bigger cavity within the folded structure (**Figure 2A**, see “ $Q^m$ ”). With respect to the  $Q^m$  building block, approximately 4.5 units are needed to create a full turn on the folded structure. The largest angle of approximately  $180^\circ$  is provided by the 6-aminoquinoline 2-carboxylate monomer, which resembles a “*para*-like” substitution. The curvature in this case is very weak (see below and **Figure 3**). Using this building block leads to the widest cavity in a folded structure, as compared to the other monomers. A  $Q^p$  trimer shows an *almost* linear shape, but due to hydrogen bonding interaction between the amide NH and the quinoline nitrogen, the oligomer is slightly curved (**Figure 2A**, see “ $Q^p$ ” and **2E, right**). By combining these monomers different helical foldamers can be produced. For example, by combining *inter alia* the A and  $Q^o$  building block, the folding angle of the helical foldamer is enlarged, which impacts the helical cavity, i.e. creates a cavity that is larger as compared with a homomeric helical foldamer based on  $Q^o$  monomers (**Figure 2D**).

Beside attractive interactions, such as  $\pi$ - $\pi$  interactions or hydrogen bonding (**Figure 2C, 2E**), repulsive forces, i.e., electrostatic repulsion or steric hindrance are further interactions that may have an impact on the conformation of the folded structure. These interactions can create additional stability. For example, the endocyclic N atom comprises lone pairs that create repulsion between the neighboring electron pairs. Due to this repulsion the orientation of the N atoms in space is affected in the way that minimizes the repulsion. This leads inevitably to an orientation that shows a maximum distance between these electron pairs (**Figure 2B**).

Beside the classical helical foldamer, linear rod-like foldamers have rarely been described. *Ergo*, the overall shape and form is defined by the different composition of these monomers and their local conformational preferences i.e. repulsive or attractive non-covalent interactions.

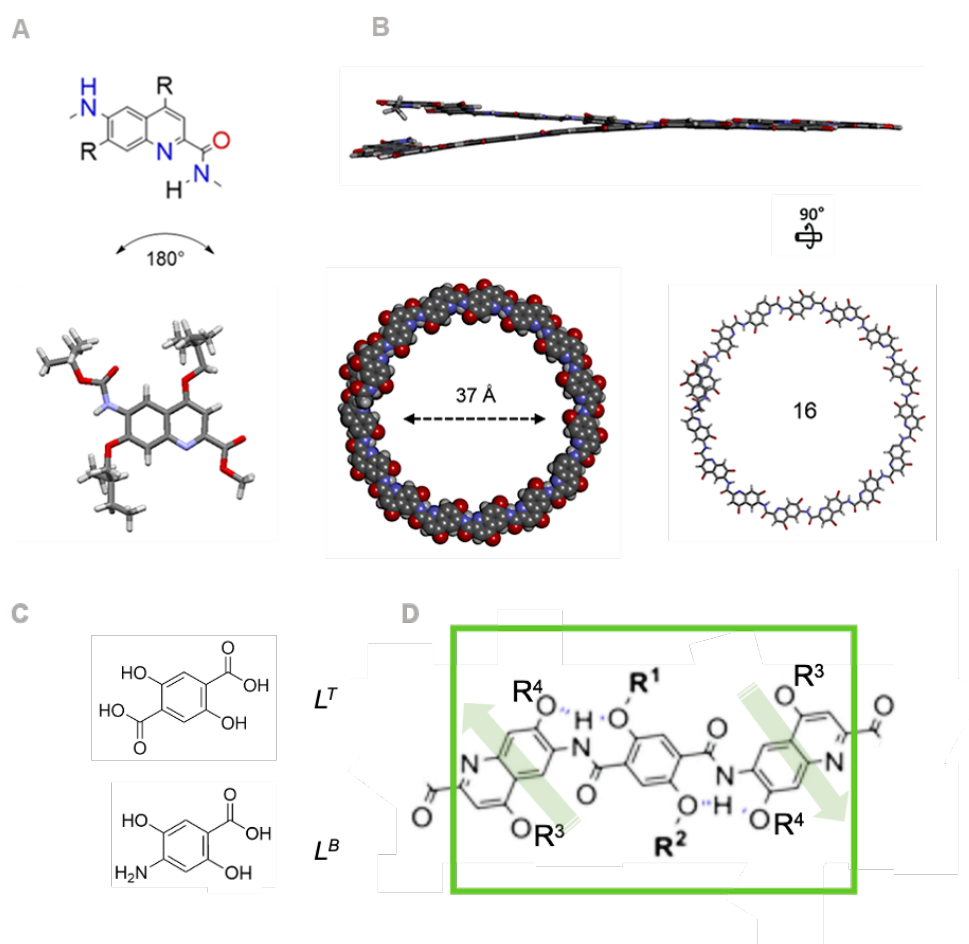


**Figure 3. Q<sup>P</sup> monomer used in this work.** (A) Chemical structure of Q<sup>P</sup>, and crystal structure of Q<sup>P</sup> building block. (B) Molecular model of homomeric Q<sup>P</sup> oligomer with 16 units (in CPK and Stick mode) with 37 Å diameter size. (C) Possible Linker units, L<sup>T</sup>: terephthalic acid building block, L<sup>B</sup>: *para* aminobenzoic acid building block. (D) Q<sup>P</sup> oligomer with L<sup>T</sup> unit in the center. The interconversion of the direction is shown in green arrows.

To aim for linear and planar foldamers, with rigid and rod-like characteristics, the use of the Q<sup>p</sup> building block is suitable. With respect to the explanations set forth, this monomer is able to lead to the least curved oligomer as compared to the other building blocks. The overall curvature angle of a linear rod like foldamer would need to be 180°, wherein some hydrogen bonding interactions on the backbone are needed to provide co-planarity and rigidity. However, a homomeric Q<sup>p</sup> (**Figure 3A**) oligomer is yet not linear. The hydrogen bonding interaction between the quinoline nitrogen and the adjacent amide, which creates stability on the backbone chain, is the reason for the resulting curvature on the inner chain. Molecular modelling proposes that the total number of units per turn is sixteen when using the Q<sup>p</sup> building block (**Figure 3B**).

The Q<sup>p</sup> monomer is capable of being curved (i.e., 16 units for a full turn), but at the same time, a Q<sup>p</sup> trimer is the “most linear” oligomer as compared with other trimeric oligomers based on either Q<sup>o</sup> or Q<sup>m</sup> building blocks. Accordingly, it would not be possible to create linear structures by merely using the Q<sup>p</sup> building block. Generally speaking, linearity can be reached with units that revert curvature. One way to “linearize” such oligomers is to introduce functional groups which disrupt the curvature of the Q<sup>p</sup> oligomer. For example, when targeting a Q<sup>p</sup> trimer, one would expect a slightly curved and non-linear oligomer. Indeed, the Q<sup>p</sup> trimer is slightly curved according to molecular modelling (see **Figure 2E, right**). By introducing a linker (“L”) in the center of the sequence (i.e., “Q<sup>p</sup>-L-Q<sup>p</sup>”) the sequence direction can be interconverted (see **Figure 3D**). The resulting trimer will be linear, as the curvature is directed in an “up-and-down” manner. In this context, suitable linkers that are curvature-disrupting are selected from the group of terephthalic acid (see **Figure 3C**, “L<sup>T</sup>”) or *p*-aminobenzoic acid units (see **Figure 3C**, “L<sup>B</sup>”). This concept will be further discussed in chapter 3.

Regarding the curved Q<sup>p</sup> 16<sup>mer</sup>, this structure shows a full turn and is helically shaped. Another approach to manipulate the conformational behavior of Q<sup>p</sup> oligomers is to “kink” the sequence of intermediate sequences. In order to kink the backbone, the secondary amide group on the foldamer backbone can be addressed. The secondary aryl amide bond can exist in two conformations, the *cis* and *trans* isomer. Due to steric hindrance the *trans* isomer is strongly favored. In contrary, the tertiary amide group favors the *cis* conformation. Accordingly, when interconverting the secondary aryl

amides on the foldamer backbone to a tertiary aryl amide, the amides favor cis configuration, which leads to an overall change in conformation (for more details see chapter 1.3, Figure 8).

## 1.2 Aromatic foldamers in membranes

Lipid bilayer membrane models are widely used in the field of biophysical studies and work as a common representation for cellular membranes. Depending on their composition they can be designed to resemble eukaryotic or prokaryotic outer cell membranes. Transmembrane transfer of ions and water molecules through the membrane is a fundamental and ubiquitous biological process. Therefore, artificial ion and water channels that resemble their biological counterpart are widely targeted and described. Artificial ion channels with high selectivity with precise control of the flow direction are rare. Aromatic helical foldamer channels built from pyridine and oxadiazole residues. These residues are synthesized *via* one-pot polymerization and have been described by Zeng and coworkers (**Figure 4A, C**). These foldamer channels have a length of 2.7 nm and a diameter size of 3 Å with high selectivity to Na<sup>+</sup> and K<sup>+</sup> ions. Single-channel current demonstrated transport activities and selectivity.<sup>(13)</sup>

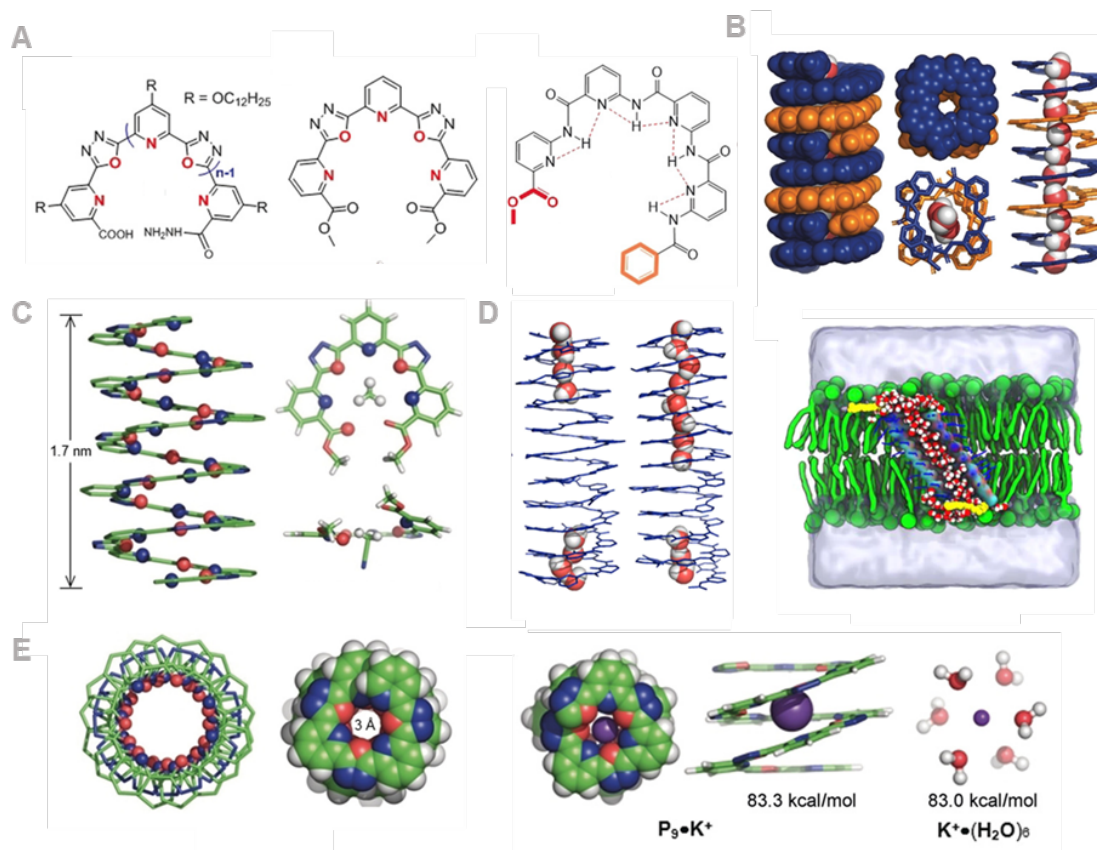


**Figure 4. Artificial channels (A):** Molecular design of helical pyridine, oxadizole and AWC foldamer channel<sup>(13) (14)</sup>. **(B)** Structure of the helically polypyridine folded pentamer nanopore of 2.8 Å in diameter for trapping hydrogen-bonded 1D water chain<sup>(15)</sup> **(C)** Crystal structure of **A** **(D)** MD-simulated water-containing foldamer channel structures at different simulation time points and cross-sections of water-filled Lipid Anchor-terminated channels (below)<sup>(14)</sup> **(E)** The computationally determined structures and the corresponding binding energies for foldamer (P9)+·K<sup>+</sup>, and K<sup>+</sup>·(H<sub>2</sub>O)<sub>6</sub> The CPK model of foldamer ion complex.<sup>(15)</sup>

Beside ion selective artificial foldamer channels, Zeng *et. al.* also described artificial aquaporin channels derived from polypyridine foldamers and hydrazine based helical foldamers (**Figure 4 B, E**).<sup>(27)</sup> These artificial water channels (AWCs) present water permeability and high salt rejection. Molecular design of these AWCs derive from earlier described one pot polymerization equipped with methyl, ethyl or isopropyl sidechains pointing towards the cavity of the channel (**Figure 4A, D**).<sup>(14, 16)</sup>

Fluorescent compounds incorporated into lipid bilayers create easy-to-quantify probes and open the possibility to measure their behavior in these compartments. Combined with mechanosensitive properties and segmental mobility, physical properties e.g. the bending rigidity can be visualized and quantified.<sup>(17-19)</sup> A Variety of lipid bilayer sheets and vesicles can be produced *in vitro*, using different fatty acids and lipids of interest.<sup>(20, 21)</sup> Matile and coworker proposed in 2009 a planarizable scaffold that senses curvature and bending in the lipid bilayer (**Figure 5A, left**).<sup>(22)</sup>

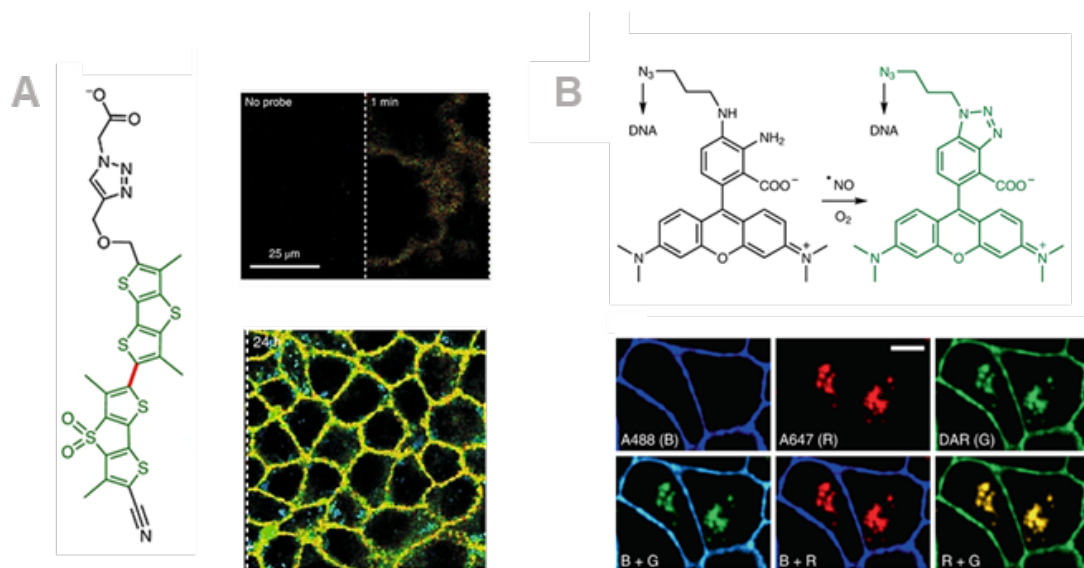


**Figure 5 Planar or rigid molecules in membranes (A)** Chemical structure of the FliptR and fluorescence imaging of the FliptR incorporated membrane. **(B)** Chemical structure of the rhodamine-based probe (DAR) and NO imaging at subcellular locations using fluorophore probes.

The FliptR (fluorescent lipid tension probe) is made of two dithienothiophene backbones, connected by one C-C bond. Each dithienothiophene ring carries one

methyl substituent at *ortho* position to the endocyclic sulfur. Due to electrostatic repulsion and steric hindrance of the sidechain, the only planarizable design consists of the “head-to-tail” conformation. Fluorescent lifetime had been measured using fluorescent lifetime imaging microscopy to quantify the membrane tension of cell membranes (**Figure 5A, right**). The proposed FliptR compound is influenced by different lipid membrane composition of the giant unilamellar vesicles (GUV's) and osmotic effects *in vivo*.

Krishnan *et al.* described a planar and linear DNA-based fluorescent probe by using a distinct DNA mimetic base pair sequence, and a NO sensing fluorophore.<sup>(23)</sup> The NO sensing fluorophore is based on a diaminorhodamine backbone, which forms a triazole when in presence of NO (**Figure 5B, top**). For targeting the subcellular compartment, two different moieties were chosen to be used for the DNA sequence - covalent bound cholesterol for the bilayer membrane as a target of choice and high affinity binding DNA-Aptamer 5-TRG2 to address the Golgi lumen inside the cell *via* endocytosis. The authors determined incorporation and binding of the probe to the lipid bilayer using fluorescent microscopy. The authors showed that by addressing the lipid bilayer with fluorescent probes, measurements such as localization of distinct target enzymes and quantification of enzyme activity can be simplified. To quantify incorporation and selectivity towards the bilayer membrane, reference dyes (Alexa 488 and 647) were used and the ratio of fluorescence intensity for green and red (G/R ratio) channel, and the ratio for green and blue (G/B ratio) channel, respectively was measured (**Figure 5B, bottom**).

### 1.3 Conformational control of foldamers

The classical foldamer shows *per definitionem* one well-defined conformation, i.e., folds in a controlled manner. The helix foldamer conformation can be affected by the chirality of the building blocks. For example, helices based on achiral monomers, show either left-handed (*M*) or right-handed (*P*) enantiomeric conformations in equal properties (**Figure 6B**). Homomeric helices bearing chiral monomers generate one handed helix, which are either P- or M-handed. Clayden *et al.* described the process in dynamic conformational mechanism, and explained the relation between fast and slow exchange of *P* and *M* helix in the NMR timescale. Basically, configurationally achiral helices interconvert rapidly between *P* and *M* conformations (see **Figure 6B, left**).

Due to this fact, the proton signal for one proton of both enantiomers give rise to one overlapping signal with the average chemical shift based on both signals. The situation is different if the P and M helices are chiral, e.g. due to a chiral group which is bound covalently or non-covalently to the helix. The proton signals will no longer overlap in this case. Rather two distinct proton signals with equal intensity will appear. The intensities of bot set of proton signals will differ according to the proportion of *P* and *M* of the helix (see **Figure 6B, right**). It is to be noted that this statement is only valid, if the chiral group does not directly influence the chemical shift of said proton.

Beside these backbone specific influences on the folding processes and the conformation, other known influences are for example sidechain and solvent dependencies. For example, Moore *et al.* described the importance of solvent-chain interactions on the folding-unfolding process of (R)-binaphthol-tethered bis-hexameric oligo(m-phenyleneethynylene) – an amphiphilic oligomer with a hydrophobic mainchain and polar triethyleneglycol side chains. They demonstrated the solvent dependency of its folding process (**Figure 6A**). For example, CH- $\pi$  interactions mediated by the solvent dependency were strong in chlorinated solvents, leading to complete unfolding.<sup>(24)</sup> On the contrary, polar solvents, such as DMSO, tetrahydrofuran or acetonitrile favored folding through solvophobic backbone-backbone interactions.

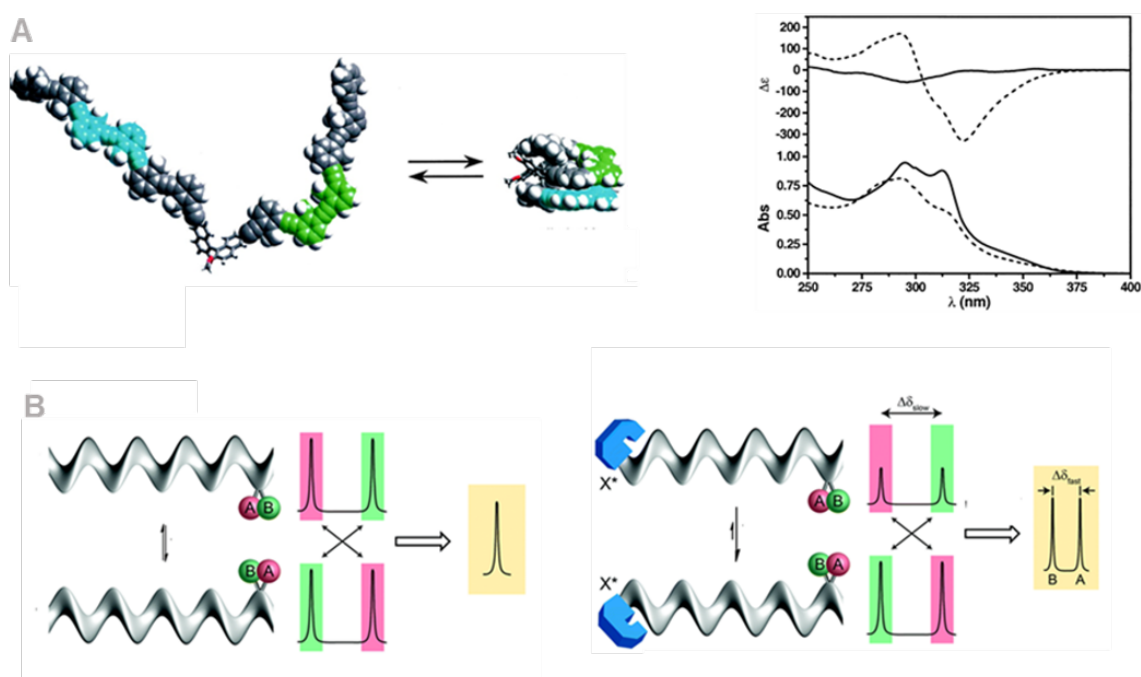


**Figure 6. Chirality of helical foldamers.** (A) Models of bis-hexameric phenylene ethynylene tethered through (R)-binaphthol (folded and unfolded) and solvent-dependent folding and UV spectrum of folded and unfolded foldamer.<sup>(24)</sup> (B) Principle of a *P* and *M* helix in fast and equally populated conformers (left) and (right) slow exchange regime, unequally populated, and corresponding NMR signals.<sup>(25, 26)</sup>

It has been demonstrated that few foldamers show conformational dynamics, i.e. polyisocyanates<sup>(25)</sup> that convert – under fast exchange regime – from *P* to *M* and, vice versa. Another approach to distinguish the conformational dynamics of a foldamer helix is to apply dynamic NMR, which can distinguish between fast and slow exchange processes. Dynamic processes include i.e., chemical or physical changes and can be distinguished via NMR spectroscopy. Huc et al. described solvent dependent folding of a (Q<sup>o</sup>)<sub>8</sub> helix, and surprisingly explored fast conversion of the helix in chloroform, and more stable folding properties by using apolar solvents, due to enhancement of hydrogen bonding interactions of the foldamer backbone. Protic solvents – on the contrary – weakens hydrogen bonding interactions, but strengthens hydrophobic effects, such as  $\pi$ - $\pi$  stacking of aromatic surfaces between quinoline ring systems.<sup>(26)</sup>

Kawai et al. proposed another way of conformational dynamical control of single molecule conformations by irradiation with ultraviolet light on diarylethene derivatives (**Figure 7A**).<sup>(27)</sup>

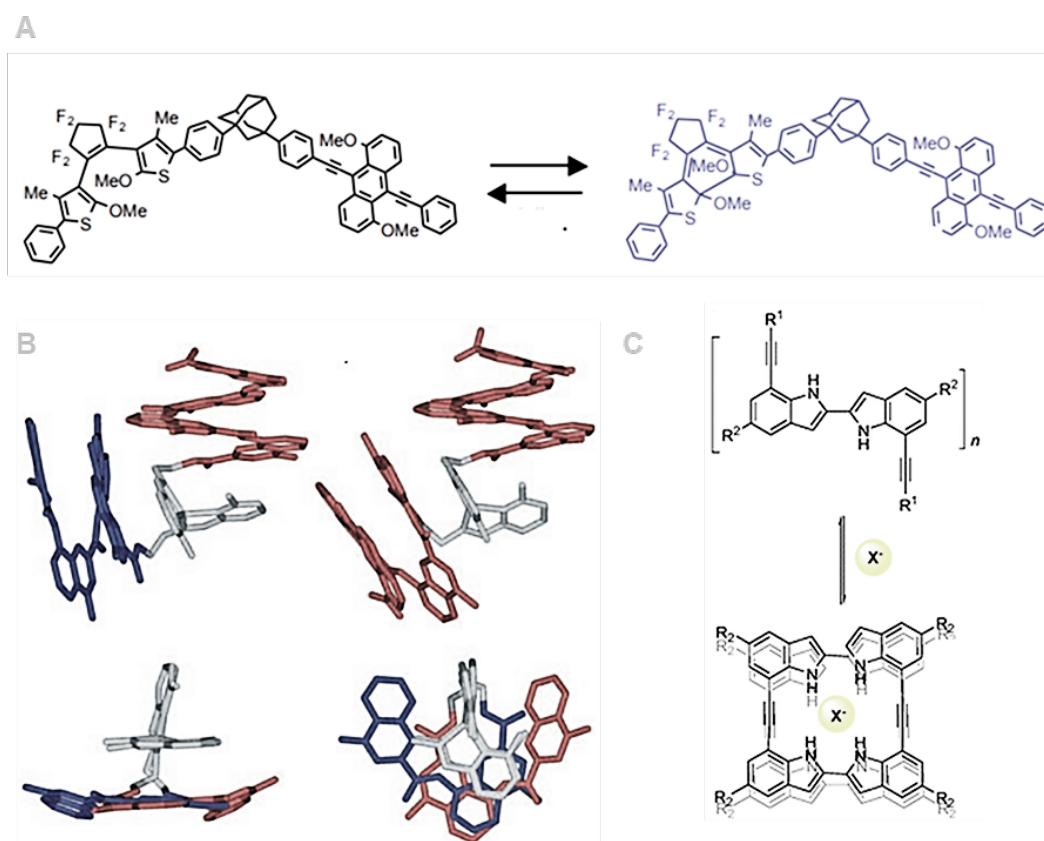


**Figure 7. Conformational switching of foldamers** (A) The chemical structure of open (left) and closed (right) of diarylethene photoswitch.<sup>(27)</sup> (B) Crystal structure of Cu<sup>I</sup> complex with first *M* and *P* helix in blue red<sup>(28)</sup> and (C) chloride mediated conformational switch of oligoindole foldamers.<sup>(29)</sup>

The principle of photoswitchable conformational control relies on a reversible photoresponsive molecular design, i.e. based on a photochromic moiety with maximal conformational response to light. Furthermore, this external control advantages from non-invasive modification and thus, bears pharmacological application potential. Distinct change of the conformation upon irradiation can be designed either on the backbone or on the sidechain, for example azobenzene derived aromatic foldamers that switch from E to Z-Isomer (**Figure 7A**).<sup>(30)</sup> Furthermore, folding of the helix backbone based on azobenzenes aromatic oligoamide foldamers with thermally reversible photoswitchable characteristics has been described by Huc and coworkers. Two 1,8-dianthracene moieties of an aromatic  $\beta$ -sheet foldamer dimerize upon irradiation via [4+4] cycloaddition leading to a covalently bond symmetrical dimer. Extending the latter, selective photocycloaddition within aromatic oligo amide sheets were described<sup>(31)</sup> where diazaanthracene moities were photocyclized within a helix-sheet-helix foldamer.

Another principle of dynamic assembly of helical foldamer segments relies upon coordination through ions or metals. Huc and coworkers showed reversible imine formation of oligoamide oligomer amines with 6-methyl-2-formylpyridine and coordination with CuI ions to generate chiral pseudotetrahedral complexes (**Figure 7B**).<sup>(28)</sup> Moreover, Ag<sup>+</sup> mediated switching of  $\beta$ -peptide foldamers were shown by Lee et al. with 4-pyridyl residues establishing Ag<sup>+</sup> coordinated frameworks.<sup>(32)</sup> Furthermore, Jeong et al. demonstrated folding upon ion coordination of unfolded oligoindoles bearing an ethynyl linker, in particular by using chloride anions, bound to NH protons revealing downfield shifted NMR signals on <sup>1</sup>H-NMR spectroscopy and NOE crosspeaks on 2-D <sup>1</sup>H -<sup>1</sup>H ROESY-NMR spectroscopy of the aromatic CH of stacked indoles (**Figure 7C**).<sup>(29)</sup>

Beside ion or metal induced conformational switching, protonation induced conformational transitions were described.<sup>(33)</sup> Huc et. al revealed conformational un- and refolding of helical oligomers derived from 2,6-pyridinedicarboxylic acids and 2,6-diaminopyridines upon partial protonation and complete protonation.

Diaminopyridine residues were protonated and hydrogen bonded to the adjacent amide N-Hs, forming a planar and unfold conformation. Upon harsher protonation, the 2,6-pyridine carboxylic acids were quarternized and revealed a folded conformation though a different hydrogen bonding pattern (N+H---O=C) on the backbone.<sup>(34)</sup>

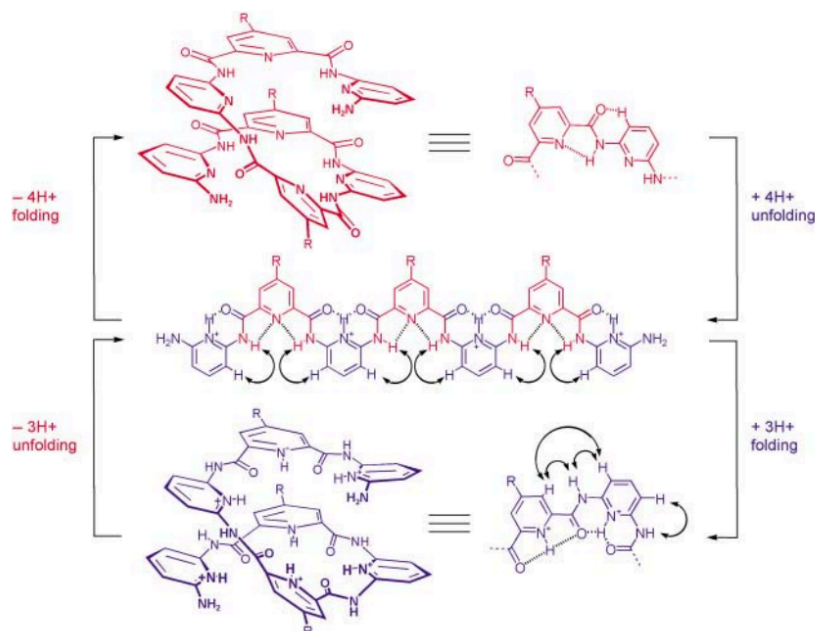


**Figure 8. Protonation induced conformational switching.**<sup>(34)</sup>

In contrary, aryl alkyl tertiary amides are known to prefer *cis*- conformation (**Figure 9A**), due to a close to equivalent energetic barrier between the two isomers<sup>(35)</sup> and can be even stabilized on aromatic aryl amides (**Figure 9B, C**). The *trans* amide comprises an angle of 120° whereas the *cis* amide angle consists of 60° (**Figure 9A**). Therefore, it can be considered that this interplay between *trans* and *cis* amide will affect the overall conformation. The usage of i.e., *N*-methylated arylamide monomers was described by Tanatani et. al, synthesizing a novel class of stable *cis* conformed helical foldamers (**Figure 9C**).<sup>(36)</sup> This concept has also been described by Huc and coworkers, which define aryl alkyl amide oligomers with preferred *cis* conformation, that give ground to inaccessible molecular designs (**Figure 9B**).<sup>(37)</sup> Consequently, for disrupting the linearity of a Q<sup>p</sup> oligomer, tertiary aryl amides can be considered, that lead to a *cis* conformed oligoamide (**Figure 9D**). This concept will be addressed in chapters 4 and 5.

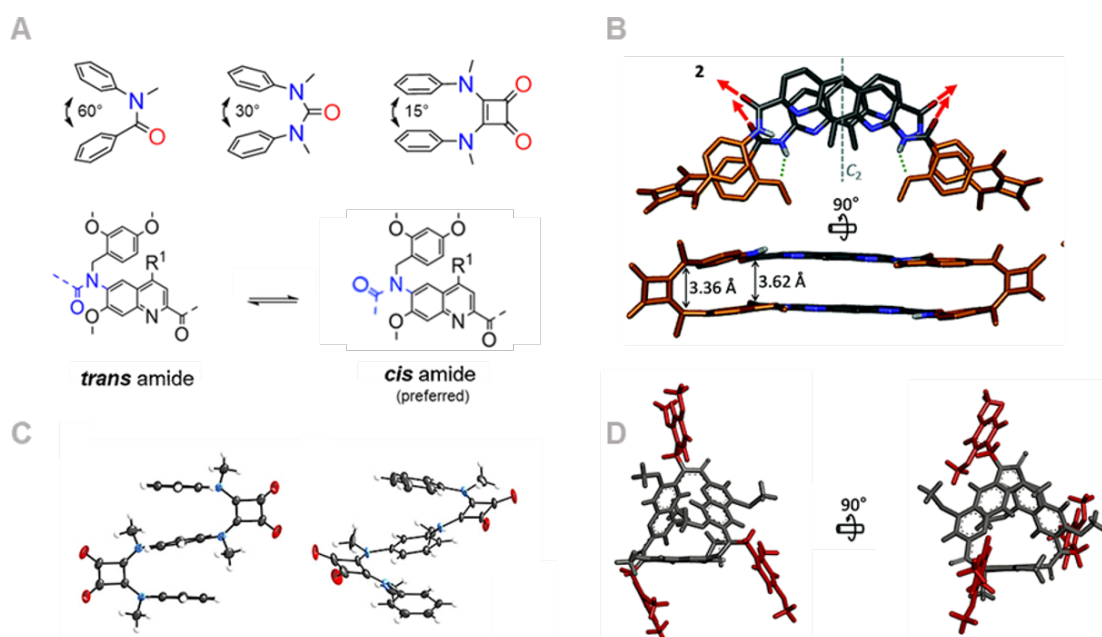


**Figure 9. Use of tertiary amide bonds in foldamer backbones** (A) different tertiary amide groups and their torsion angles. (B) crystal structure of  $\beta$  sheet foldamer with tertiary squaramide linker.<sup>(38)</sup> (C) crystal structure of tertiary squaramide linker.<sup>(36)</sup> (D) MD model of macrocyclic oligomer with *cis* aryl alkyl amides.

## 1.4 Conclusion

In conclusion, Q<sup>P</sup> foldamers can be used as a useful tool for curved as well as “linear” designs. By using interconverting linkers (e.g. L<sup>T</sup> or L<sup>B</sup>) in the Q<sup>P</sup> sequence, longer linear sequences are possible. These rod-like foldamers have the potential to be incorporated in a bilayer membrane. Moreover, the the Q<sup>P</sup> foldamer can be quantified by fluorescence microscopy. Like this, the rod-like foldamer can be used as a tool to allow for quantify membrane associated processes, such as membrane deformations. This concept will be addressed in more detail in chapter 3.

Moreover, a Q<sup>P</sup> foldamer bearing secondary amide functionalities has the potential to be DMB-functionalized. A DMB-functionalized Q<sup>P</sup> foldamer as discussed above is kinked due to the tertiary aryl amides. These kinked sequences allow for intramolecular macrocyclization, as their terminal N- and C-termini are in proximity to each other. Furthermore, the endocyclic nitrogen of the Q<sup>P</sup> building block allows for conformational switching via protonation. These concepts are discussed in more detail in chapters 4 and 5.

Furthermore, due to the large folding angle of the Q<sup>p</sup> monomer, a foldamer sequence based on a combination between the different monomers (e.g. Q<sup>o</sup> or Q<sup>m</sup>) with the Q<sup>p</sup> monomer allows for large cavities. These cavities may be used for potential future capsule designs with great cavity size. Due to the huge folding angle as well as the planar and large aromatic surface of a Q<sup>p</sup> foldamer, another future application of this sequence is their use in the synthesis of  $\beta$ -sheet- and  $\beta$ -barrel-mimics.

## 1.5 References

- (1) Sullivan, L. The tall office building artistically considered. *Lippincott's monthly magazine*, **1896**, 339, 403-409.
- (2) Hecht, S.; Huc, I. Foldamers: structure, properties and applications: *John Wiley & Sons*; **2007**.
- (3) Lehn, J-M.; Rigault, A.; Siegel, J.; Harrowfield, J.; Chevrier, B.; Moras, D. Spontaneous assembly of double-stranded helicates from oligobipyridine ligands and copper (I) cations: structure of an inorganic double helix. *PNAS*. **1987**, 84 (9), 2565-9.
- (4) Petitjean, A.; Cuccia, LA.; Schmutz, M.; Lehn, J-M. Naphthyridine-based helical foldamers and macrocycles: synthesis, cation binding, and supramolecular assemblies. *J. Org. Chem.* **2008**, 73 (7), 2481-95.
- (5) Jiang, H.; Léger, J-M.; Dolain, C.; Guionneau, P.; Huc I. Aromatic  $\delta$ -peptides: design, synthesis and structural studies of helical, quinoline-derived oligoamide foldamers. *Tetrahedron*. **2003**, 59 (42), 8365-74.
- (6) Zhang, D-W.; Zhao, X.; Hou, J-.; Li, Z-T. Aromatic amide foldamers: structures, properties, and functions. *Chemical Rev.* **2012**, 112 (10), 5271-316.
- (7) Pilsl, LK.; Reiser, O.  $\alpha/\beta$ -Peptide foldamers: state of the art. *Amino Acids*. **2011**, 41 (3), 709-18.
- (8) Berl, V.; Huc, I.; Khoury, RG.; Krische, MJ.; Lehn, J-M. Interconversion of single and double helices formed from synthetic molecular strands. *Nature*. **2000**, 407 (6805), 720-3.
- (9) Yan, Y.; Qin, B.; Shu, Y.; Chen, X.; Yip, YK.; Zhang, D. Helical organization in foldable aromatic oligoamides by a continuous hydrogen-bonding network. *Org. Lett.* **2009**, 11 (6), 1201-4.
- (10) Ren, C.; Zhou, F.; Qin, B.; Ye, R.; Shen, S.; Su, H. Crystallographic Realization of the Mathematically Predicted Densest All-Pentagon Packing Lattice by C<sub>5</sub>-Symmetric "Sticky" Fluoropentamers. *Angew. Chem.* **2011**, 123 (45), 10800-3.
- (11) Gellman, SH. Foldamers: a manifesto. *Acc. Chem. Res.* **1998**, 31 (4), 173-80.
- (12) Huc, I. Aromatic oligoamide foldamers. *Eur. J. Org. Chem.* **2004**, 2004 (1), 17-29.
- (13) Chen, F.; Shen, J.; Li, N.; Roy, A.; Ye, R.; Ren, C. Pyridine/Oxadiazole-Based Helical Foldamer Ion Channels with Exceptionally High K<sup>+</sup>/Na<sup>+</sup> Selectivity. *Angew. Chem.* **2020**, 59 (4), 1440-4.
- (14) Roy, A.; Shen, J.; Joshi, H.; Song, W.; Tu, Y.; Chowdhury, R. Foldamer-based ultrapermeable and highly selective artificial water channels that exclude protons. *Nat. Nanotechnol.* **2021**, 16 (8), 911-7.
- (15) Shen, J.; Fan, J.; Ye, R.; Li, N.; Mu, Y.; Zeng, H. Polypyridine-Based Helical Amide Foldamer Channels: Rapid Transport of Water and Protons with High Ion Rejection. *Angew. Chem.* **2020**, 59 (32), 13328-34.
- (16) Shen, J.; Ye, R.; Liu, Z.; Zeng, H. Hybrid Pyridine-Pyridone Foldamer Channels as M<sub>2</sub>-Like Artificial Proton Channels. *Angew. Chem.* **2022**.

- (17) Humeniuk, H.; Rosspeintner, A.; Licari, G.; Kilin, V.; Bonacina, L.; Vauthey, E.; White-Fluorescent Dual-Emission Mechanosensitive Membrane Probes that Function by Bending Rather than Twisting. *Angew. Chem.* **2018**, *57* (33), 10559-63.
- (18) Klymchenko, A. Solvatochromic and fluorogenic dyes as environment-sensitive probes: design and biological applications. *Acc. Chem. Res.* **2017**, *50* (2), 366-75.
- (19) Haidekker, M.; Theodorakis, E. Ratiometric mechanosensitive fluorescent dyes: design and applications. *J. Mater. Chem.* **2016**, *4* (14), 2707-18.
- (20) Mueller, P.; Chien, T.; Rudy, B. Formation and properties of cell-size lipid bilayer vesicles. *Biophys. J.* **1983**, *44* (3), 375-81.
- (21) Suzuki, H.; Tabata, K.; Kato-Yamada, Y.; Noji, H.; Takeuchi, S. Planar lipid bilayer reconstitution with a micro-fluidic system. *Lab Chip.* **2004**, *4* (5), 502-5.
- (22) Colom, A.; Derivery, E.; Soleimanpour, S.; Tomba, C.; Molin, M.; Sakai, N. A fluorescent membrane tension probe. *Nat. Chem.* **2018**, *10* (11), 1118.
- (23) Jani, M.; Zou, J.; Veetil, A.; Krishnan, Y. A DNA-based fluorescent probe maps NOS3 activity with subcellular spatial resolution. *Nat. Chem. Biol.* **2020**, 1-7.
- (24) Hill, DJ.; Moore, JS. Helicogenicity of solvents in the conformational equilibrium of oligo (m-phenylene ethynylene) s: Implications for foldamer research. *PNAS.* **2002**, *99* (8), 5053-7.
- (25) Le Bailly, B.; Clayden, J. Dynamic foldamer chemistry. *Chem. Comm.* **2016**, *52* (27), 4852-63.
- (26) Qi, T.; Maurizot, V.; Noguchi, H.; Charoenraks, T.; Kauffmann, B.; Takafuji, M. Solvent dependence of helix stability in aromatic oligoamide foldamers. *Chem. Comm.* **2012**, *48* (51), 6337-9.
- (27) Irie, M.; Fukaminato, T.; Sasaki, T.; Tamai, N.; Kawai, T. A digital fluorescent molecular photoswitch. *Nature.* **2002**, *420* (6917), 759-60.
- (28) Delsuc, N.; Hutin, M.; Campbell, V.; Kauffmann, B.; Nitschke, J.; Huc, I. Metal-directed dynamic formation of tertiary structure in foldamer assemblies: orienting helices at an angle. *Chem. Eur. J.* **2008**, *14* (24), 7140-3.
- (29) Juwarker, H.; Suk, J.; Jeong, K. Foldamers with helical cavities for binding complementary guests. *Chem. Soc. Rev.* **2009**, *38* (12), 3316-25.
- (30) Yu, Z.; Hecht, S. Remote control over folding by light. *Chem. Comm.* **2016**, *52* (40), 6639-53.
- (31) Gole, B., Kauffmann, B., Tron, A., Maurizot, V., McClenaghan, N., Huc, I. Selective and Cooperative Photocycloadditions within Multistranded Aromatic Sheets. *J. Am. Chem. Soc.* **2022**.
- (32) Knipe, PC.; Thompson, S.; Hamilton, A. Ion-mediated conformational switches. *Chem. Sci.* **2015**, *6* (3), 1630-9.
- (33) Barboiu, M.; Lehn, J. Dynamic chemical devices: Modulation of contraction/extension molecular motion by coupled-ion binding/pH change-induced structural switching. *PNAS.* **2002**, *99* (8), 5201-6.

- (34) Dolain, C.; Maurizot, V.; Huc, I. Protonation-Induced Transition between Two Distinct Helical Conformations of a Synthetic Oligomer via a Linear Intermediate. *Angew. Chem.* **2003**, *42* (24), 2738-40.
- (35) Itai, A.; Toriumi, Y.; Tomioka, N.; Kagechika, H.; Azumaya, I.; Shudo, K. Stereochemistry of N-methylbenzanilide and benzanilide. *Tetrahedron Lett.* **1989**, *30* (45), 6177-80.
- (36) Urushibara, K.; Masu, H.; Mori, H.; Azumaya, I.; Hirano, T.; Kagechika, H. Synthesis and conformational analysis of alternately N-alkylated aromatic amide oligomers. *J. Org. Chem.* **2018**, *83* (23), 14338-49.
- (37) Urushibara, K.; Ferrand, Y.; Liu, Z.; Katagiri, K.; Kawahata, M.; Morvan, E.; Tayatani, A.; Huc, I. Accessing Improbable Foldamer Shapes with Strained Macrocycles. *Chem. Eur. J.* **2021**, *27* (43), 11205.
- (38) Atcher, J.; Nagai, A.; Mayer, P.; Maurizot, V.; Tanatani, A.; Huc, I. Aromatic  $\beta$ -sheet foldamers based on tertiary squaramides. *Chem. Comm.* **2019**, *55* (70), 10392-5.

## 2. Motivation and research objectives

The main objective of my work was to design, synthesize, and analyze new compounds based on 6-aminoquinoline 2-carboxylic acid (hereafter referred to as Q<sup>P</sup>) building blocks to create various organic soluble oligomeric foldamer architectures involving linear rigid rod segments. These architectures were initially designed in a way to resemble to the  $\beta$ -sheets and  $\beta$ -barrels found in proteins. In order to simplify access to these large scaffolds, the synthesis was designed to be based on solid phase methodology. However, difficulties associated with non-specific aggregation emerged that complicated both synthesis and subsequent analysis of the sequences. Consequently, the objective was revised to target and exploit shorter oligomers still based on Q<sup>P</sup> building blocks, but which would be less prone to aggregation. For example, polar side chains for better solubility in presence of water were introduced to facilitate reverse phase HPLC analysis and purification.

My first work (see **chapter 3**) focused on the study and synthesis of amphiphilic rigid rod like aromatic oligomers deriving from Q<sup>P</sup> building blocks. These amphiphilic molecules were then studied towards their membrane affinity in collaboration with Prof. Vadim Frolov and Pedro Arrasate from the Biofisika institute in Bilbao, Spain. This curiosity driven work led to the discovery that our molecules may promote the binding and aggregation of some proteins at the surface of bilayer membranes and allow for their sensing and manipulation.

After establishing the straightforward synthesis of Q<sup>P</sup> oligomers on solid phase as well as in solution, macrocyclic designs based on this building block were targeted (see **chapter 4**). The rigid rods are obviously not prone to forming macrocycles and our aim was to investigate the consequences of the conformational frustration arising from joining the two ends of a rod. Macrocyclization was performed on sequences containing *cis* amide bonds obtained by introducing bulky substituents on the amide nitrogen atom, *i.e.* with aryl-alkyl tertiary amides. The substituents act as “linearity disruptors” and favor the overall conformation to be kinked. Advantageously, the kinked conformations of these sequences favor intramolecular reactions (macrocyclization) at the expense of intermolecular oligomerization due to the resulting proximity of the reacting functional groups. After removal of the linearity disruptors, the final macrocycles were studied towards their different conformational behavior.

In extension to the work presented in chapter 4, we set to assess whether the rigid rod conformation of an oligomer based on Q<sup>p</sup> could serve to stretch the conformation of another oligomer, in our case a peptide (see **chapter 5**). Thus, the kinking of a rigid rod by means of a tertiary amide and the subsequent removal of the kink to enforce a linear conformation were exploited in a second family of macrocycles. The macrocycles combined a segment of four Q<sup>p</sup> units and a peptide consisting of sarcosine and glycine residues. The kinked conformation mediated by one linearity disruptor allowed for macrocyclization to take place. The subsequent removal of the linearity disruptor generated the linear conformation of the tetrameric Q<sup>p</sup> segment leading to changes in the peptide conformation.

### **3. Molecular Sensing and Manipulation of Protein Oligomerization in Membrane Nanotubes with Bolaamphiphilic Foldamers (published)**

#### **Authors:**

Kathrin Aftahy,<sup>a,\*</sup> Pedro Arrasate,<sup>b,c,\*</sup> Pavel V. Bashkirov,<sup>d,e,\*</sup> Petr I. Kuzmin,<sup>f</sup> Victor Maurizot,<sup>g</sup> Ivan Huc,<sup>a,\*</sup> Vadim A. Frolov<sup>b,c,h,\*</sup>

<sup>a</sup> Department of Pharmacy, Ludwig-Maximilians-Universität, Munich (Germany)

<sup>b</sup> Biofisika Institute (CSIC, UPV/EHU), University of the Basque Country, Leioa (Spain)

<sup>c</sup> Department of Biochemistry and Molecular Biology, University of the Basque Country, Leioa (Spain)

<sup>d</sup> Research Institute for Systems Biology and Medicine, Moscow (Russia)

<sup>e</sup> Federal Research and Clinical Centre of Physical-Chemical Medicine, Moscow (Russia)

<sup>f</sup> A.N. Frumkin Institute of Physical Chemistry and Electrochemistry, Moscow (Russia).

<sup>g</sup> Univ. Bordeaux, CNRS, Bordeaux Institut National Polytechnique, CBMN (UMR 5248), Pessac (France)

<sup>h</sup> Ikerbasque, Basque Foundation for Science, Bilbao (Spain)

**Submitted:** *Journal of the American Chemical Society*, **2023**

#### **Contributions:**

The project and the designs of the rods was planned in collaboration with Prof. I. Huc and Dr. Victor Maurizot. The synthetic routes and conditions for the synthesis of the Q<sup>P</sup> monomer with isohexyl sidechains have been developed and established by Dr. Victor Maurizot and me. The oligomer synthesis and subsequent analysis was performed by me. Design of the biophysical studies were conducted by Prof. Vadim Frolov, Pavel Bashkirov and Petr Kuzmin. The biophysical experiments were performed by Pedro Arrasate.

## Abstract

Adaptive and reversible self-assembly of supramolecular protein structures is a fundamental characteristic of dynamic living matter. However, the quantitative detection and assessment of the emergence of mesoscale protein complexes from small and dynamic oligomeric precursor remain shightly challenging. Here, we present a novel approach utilizing a short membrane nanotube (sNT) pulled from a planar membrane reservoir as nanotemplates for molecular reconstruction, manipulation and sensing of protein oligomerization and self-assembly at the mesoscale. The sNT reports changes in membrane shape and rigidity caused by membrane-bound proteins as variations of the ionic conductivity of the sNT lumen. To confine oligomerization to the sNT, we have designed and synthesized rigid oligoamide foldamer tapes (ROFTs). Charged ROFTs incorporate into the planar and sNT membranes, mediate protein binding to the membranes and, driven by the luminal electric field, shuttle the bound proteins between the sNT and planar membranes. Using annexin-V (AnV) as a prototype, we show that the sNT detects AnV oligomers shuttled into the nanotube by ROFTs. Accumulation of AnV on the sNT induces its self-assembly into a curved lattice restricting the sNT geometry and inhibiting the material uptake from the reservoir during the sNT extension, leading to the sNT fission. By comparing the spontaneous and ROFT-mediated entry of AnV into the sNT, we reveal how intricate membrane curvature sensing by small AnV oligomers controls the lattice self-assembly. These results establish sNT-ROFT as a powerful tool for molecular reconstruction and functional analyses of protein oligomerization and self-assembly, with broad application to various membrane processes (**Figure 1**).

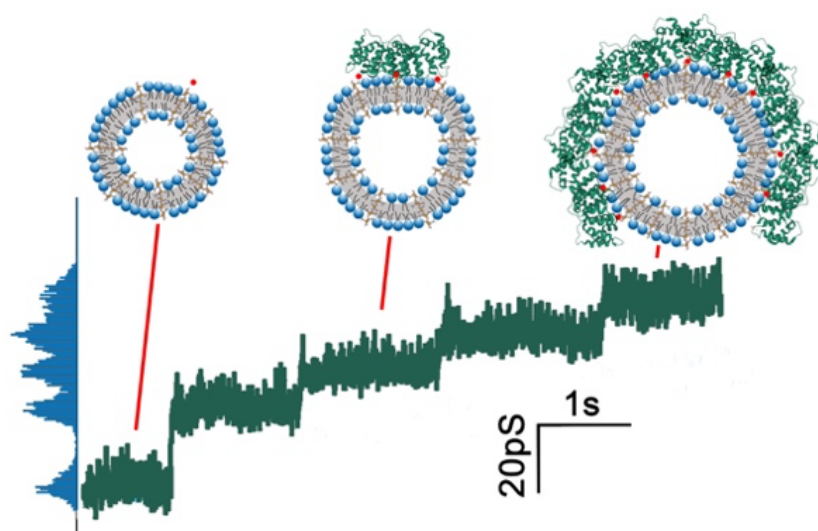


**Figure 1** Lipid membrane nanotubes equipped with ROFTs, showing AnV oligomerization and membrane interactions as an increase of conductance signal.

### **3.1 Introduction**

The formation of supramolecular protein complexes with a programmable architecture through noncovalent reversible self-assembly is crucial for the spatial and functional organization of intracellular space.<sup>1-4</sup> This process, based on weak interactions and adaptive self-assembly, enables the dynamic tuning of shape and material properties in protein complexes and nanostructures. The phenomenon has recently been replicated in synthetic biomaterials.<sup>4-6</sup> Typically, the initiation and outcomes of the self-assembly are kinetically regulated by small and dynamic oligomeric precursors.<sup>7,8</sup> Although our understanding of the mesoscale protein complexes and of the final products of the self-assembly has been advanced,<sup>9,10</sup> tracing their material properties and polymorphism back to the precursors remain experimentally challenging, hindering a comprehensive mechanistic analysis of the self-assembly process.

In the crowded intracellular environment, protein oligomerization often occurs with the involvement of membrane templates that provide various means to facilitate and regulate protein interactions.<sup>11</sup> Membranes can mediate protein oligomerization both in the cytosol and on their own surface.<sup>11-13</sup> The membrane shape is an established regulator of protein self-assembly.<sup>11,14</sup> Importantly, soft membrane templates are typically reshaped by emerging protein complexes. This reciprocal effect of proteins on the membrane template is implicated in cellular membrane morphogenesis.<sup>15</sup> Recent experiments demonstrated that membrane shape changes could reflect dynamic rearrangements of small protein subunits of a larger protein structure.<sup>16,17</sup> As even a single protein molecule can induce local the membrane deformations, changes in membrane shape can serve as a reporter of the self-assembly progress, spanning from the molecular scale to the mesoscale.

One technique that focuses on real-time tracking molecular-scale deformations is conductance measurements in short membrane nanotubes (sNTs) pulled from a planar membrane reservoir.<sup>18</sup> Through sNTs, it is possible to resolve individual and multiple binding events, as well as accompanying changes of membrane elasticity.<sup>18,19</sup> However, the high curvature of the sNT membrane restricts protein partitioning,<sup>19,20</sup> making it challenging for a random protein to accumulate and self-assemble on the sNT. Furthermore, even if protein crowding on the sNT membrane, a step generally required

to trigger self-assembly, could be achieved, it would remain difficult to discriminate the actions of individual protein oligomers as the protein ensemble would dominate the measurements. To exert control over protein partitioning and interactions on the sNT membrane, and thus to enable the discrimination and quantification of individual molecular complexes, we employed newly synthesized rodlike bolaamphiphile (BA) molecules. Charged BAs could be operated as primitive protein receptors mediating the membrane binding of peripheral proteins, such as annexin V (AnV), that specifically recognize charged lipid species.<sup>21,22</sup> Designed to traverse the sNT membrane, the BAs functioned as molecular shuttles propelled by an electric field applied to the lumen of the sNT, thereby controlling protein transfer between the sNT and the connected planar reservoir membrane. Using BA-mediated electrophoresis, we were able to detect the entry and exit of individual AnV oligomers and to assess their stoichiometry and shape. Furthermore, field-driven accumulation of AnV on the sNT triggered the polymerization of a curved protein lattice encaging the sNT.<sup>23</sup> This protein scaffold not only stabilized the membrane within it but also mediated the sNT fission upon extension.<sup>24,25</sup> Comparison of the spontaneous and voltage-driven entry of AnV in sNT revealed a novel mechanism of membrane curvature sensing that AnV uses to control its membrane partitioning and polymorphic self-assembly. Altogether, our results establish BA-containing sNTs as new tools to produce, manipulate, and investigate membrane-mediated protein assemblies.

### **3.2 Concept and experimental Design**

**Design of the shuttle BAs.** Different classes of rigid synthetic BAs have been demonstrated to incorporate into a lipid bilayer and span both of its leaflets.<sup>26</sup> To minimally interfere with protein detection by sNTs, small lipidsized BAs of predictable and stable shape were needed. To obtain such rigid bolalipid mimetics we opted for oligoamide foldamers (OFs).<sup>27-29</sup> OFs are synthetically accessible *via* simple iterative amide couplings and are easy to modulate through main chain and side chain modifications. OF amphiphiles capable of incorporation into lipid membranes have been described, but applications have until now been focused on ion and water transport mediated by transmembrane helices.<sup>30-35</sup> Apart from relatively large helices, OF may be designed to form thinner tapelike structures of defined length that may be converted into protein-interacting bolaamphiphiles *via* appropriate modification of the ends. We designed and synthesized minimal such compounds, symmetric charged rigid OF tapes (ROFTs). Compound 1 (Fig. 1A) was the parent compound of a series of

OF ribbons (see Supporting Information) designed according to well-established principles validated across a vast number of OF families.<sup>36</sup>

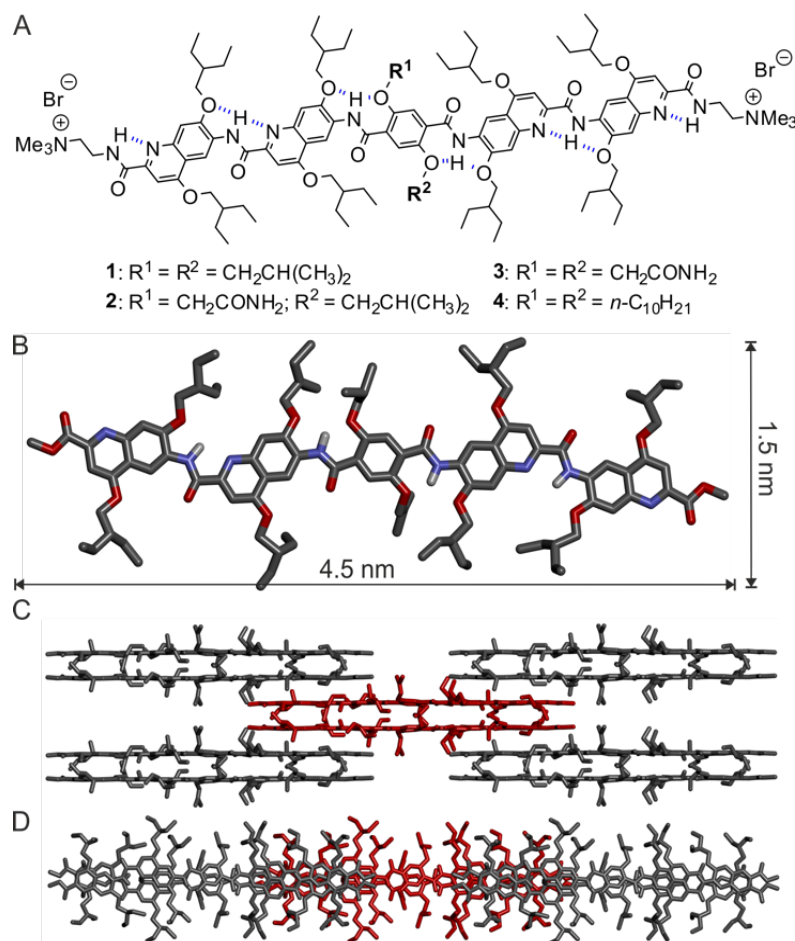


**Figure 2.** (A) Formula of amphipathic ROFTs **1-4**. Dashed blue lines indicate hydrogen bonds responsible for the flat shape of the structure. (B) Crystal structure of **5**, the bis-methyl-ester precursor of **1**. (C, D) views of molecular packing in the crystal.

In this design, amide protons are engaged in intramolecular hydrogen bonds, and thus unavailable for intermolecular interactions (Fig. 1B). Aryl and amide units are kept coplanar, generating a linear tape with a sizable surface area for aromatic stacking. Such linear tapes have been shown to have stable conformations in a wide range of polar and nonpolar media.<sup>36</sup> The branched alkyl side chains appended on the edges of the tape provide a lipophilic character. However, they may not completely prevent aggregation through stacking as shown by crystal packing (Fig. 1C, D). The ability of the tapes to aggregate was expected to be reduced in **4** which possesses two central decyl chains, and enhanced in **2** and **3** which instead have one or two polar primary amide appendages, respectively. The primary amides side chains are isosteric to the *i*Bu groups of **1** but, in contrast with the *i*Bu groups, they may engage in intermolecular hydrogen bonds within a membrane, as do asparagine residues in transmembrane

peptides.<sup>37</sup> All molecules are terminated with quaternary ammonium functions that give them a bolaamphiphilic nature<sup>26</sup> and thus potentially control their orientation within lipid bilayer membranes. While the 4.5 nm length of the ROFT molecule matches the lipid bilayer thickness, its 1.5nm width is only slightly bigger than that of a lipid (Fig. 1B). The small width in principle ensures that individual ROFTs perturb the sNTs much less than protein molecules. Compounds 1-4 are not soluble in water but met our expectations with respect to their insertion in membranes.

### **ROFTs incorporate into low-curved membrane reservoirs and mediate protein binding to the membranes.**

We began testing how ROFTs incorporate and interact with the lipid bilayer using low-curved membrane templates, Giant Unilamellar Vesicles (GUVs) and their supported analogues, Giant Supported Bilayers (GSBs) suitable for fluorescence microscopy observation and mechanical manipulations.<sup>38</sup> We found that ROFTs were readily incorporated into GUVs and GSBs, seen as a linear increase of the intrinsic fluorescence signal of ROFTs normalized to that of a lipid marker (Fig. 2A, S1). The incorporation efficiency was the best for **4**, while it decreased from **1** to **3**, in correlation with the expected increasing propensity of ROFTs to aggregate (Fig. S2). Another factor governing ROFT membrane incorporation was the lipid composition of the GSBs (Fig. 2A, Table S1). Cholesterol interfered with the GSB production in the presence of ROFTs (Table S1) as it induced the formation of crystalline-like ROFT-lipid films, possibly *via* cholesterol-ROFT stacking. In contrast, sphingomyelin (SM), a biological partner of cholesterol,<sup>39</sup> promoted the incorporation of high amounts of ROFTs (Table S1, Fig. 2A). The incorporation efficiency was further improved upon the addition of cone-shaped and polyunsaturated lipids abundant in cellular membranes (Table S1). Because of these properties, we selected **1** and **4** in a simple biomimetic PC/PE lipid background for further experiments.

The sensitivity of ROFT incorporation to the composition of the hydrophobic tails of the GSB lipids suggests that the ROFTs orient along the membrane normal and span the lipid bilayer as extended bola-amphiphiles, stipulated by the highly hydrophobic aromatic core of ROFTs.<sup>40</sup> Accordingly, the topographic AFM scanning of supported lipid bilayers made from ROFT-containing GSBs revealed no patterns indicative of ROFTs laying parallel to the membrane interface (Fig. S3). The normal orientation of ROFTs, suitable for amphiphilic self-assembly of a molecular film, was further confirmed by the formation of GSBs from detergent solutions of **4**. (Fig. S2C)

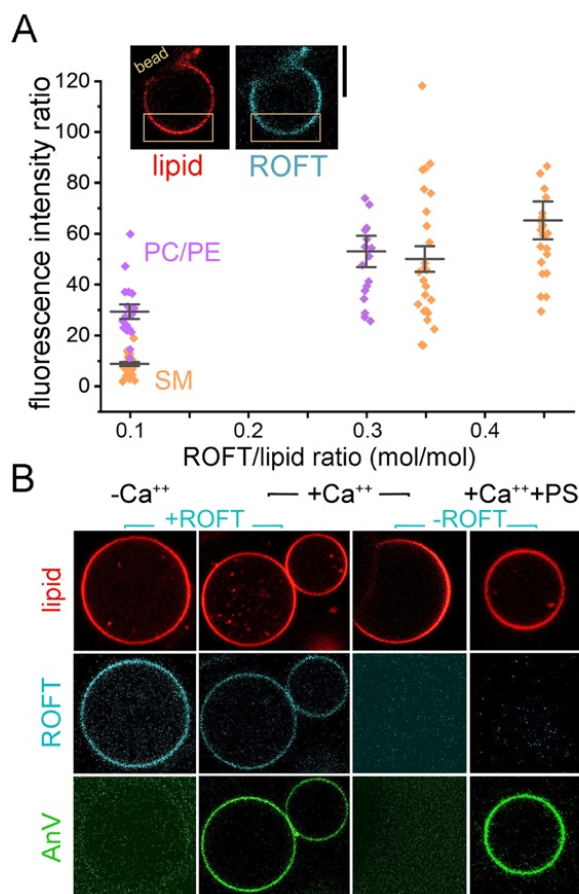


**Figure 3. Membrane incorporation and AnV binding by ROFTs.** (A) Incorporation of **1** into GSBs measured as the fluorescence intensity ratio FROFT/Flipid, with GSBs made of SM (sphingomyelin, apricot) and PC/PE (phosphocholine/phosphoethanolamine magenta) mixtures. The inset shows a ROFT-lipid GSB attached to a silica bead, the lipid probe (Rh-DOPE, red) and the intrinsic ROFT (blue) fluorescence are seen. The rectangles delimit the region of interest (ROI) used to calculate FROFT/Flipid, as the ratio of total fluorescence intensities measured upon the background subtraction. Scale bar 10 $\mu$ m. (B) Ca<sup>++</sup> mediates AnV binding to GSBs containing **1** or phosphoserine (PS). The fluorescence of AnnexinV-alexa488 (green), lipid (Rhodamine-PE, red) and **1** (blue) is seen. Scale bars 10 $\mu$ m.

Upon a random testing with fluorescently labeled membrane-remodeling proteins available in house, we found that **1** and **4** (in PC/PE background) mediate membrane binding of AnV (Fig. 2B), as well as other peripheral membrane proteins, namely the epsin *N*-terminal homology domain and Dynamin1 (Fig. S4), all known to depend upon negative membrane charge for membrane binding.<sup>19,41</sup> Thus, protein binding was evidenced with the first generation of ROFTs without requiring further functionalization of their solvent exposed polar groups. The binding indicates that ROFTs create negative surface potential, in agreement with the efficient incorporation of ROFTs into purely cationic membranes and also confirmed by measurements of the membrane boundary potential changes (Table S1, Fig. S5). While both Dyn1 and AnV can self-assemble into large cylindrical structures on the sNT membrane,<sup>23,41</sup> the low oligomeric precursors of AnV self-assembly on a planar membrane are well characterized.<sup>42,43</sup> We thus chose AnV for further testing.

## ROFTs emulate $\text{Ca}^{++}$ and curvature dependence of AnV membrane binding.

AnV (2 $\mu\text{M}$  in the bulk) binding to GSBs containing **1** or **4** showed  $\text{Ca}^{++}$  dependence characteristic of AnV interaction with its physiological target, PS (Fig. 2B, S4).<sup>22,43</sup> Chelating free  $\text{Ca}^{++}$  by EDTA caused AnV detachment from both ROFT- and PS containing GSBs (Fig. S4).<sup>44</sup> However, in both cases residual binding was detected (Fig. 2B, S4), indicating a weak  $\text{Ca}^{++}$ -independent binding mode. This is consistent with the overall complexity of membrane binding of annexins controlled by electrostatic and hydrophobic interactions.<sup>21,44</sup> We next checked how the AnV binding changes with the membrane curvature.

Micron-long NTs could be readily produced from both ROFT- and PS-containing GSBs (Fig. 3A). ROFTs were visibly expelled from the NTs (Fig. 3A). The ratio between the ROFT concentrations (area fraction) in the GSB ( $\varphi_0$ ) and NT ( $\varphi_{NT}$ ), the sorting coefficient  $q = \varphi_{NT}/\varphi_0$ , was measured as the ratio of the fluorescence intensities ( $F$ ) coming from the lipid probe (Rhodamine-PE) and the ROFTs in the NT membrane normalized to that measured in the GSB (Fig. 3A, S6).<sup>25</sup> For both **1** and **4**, preferential partitioning into low-curved GSB, equivalent to  $q < 1$ , was detected (Fig. 3B, S6). The ROFTs sorting away from NTs was associated with the ROFT rigidity. The sorting of a rigid membrane inclusion can be estimated as (see Supplementary Model 3.1):

$$(1) \quad q \approx 1 - \frac{ak_{flat}}{2k_B Tr} \left( \frac{1}{r} - 2J_s \right).$$

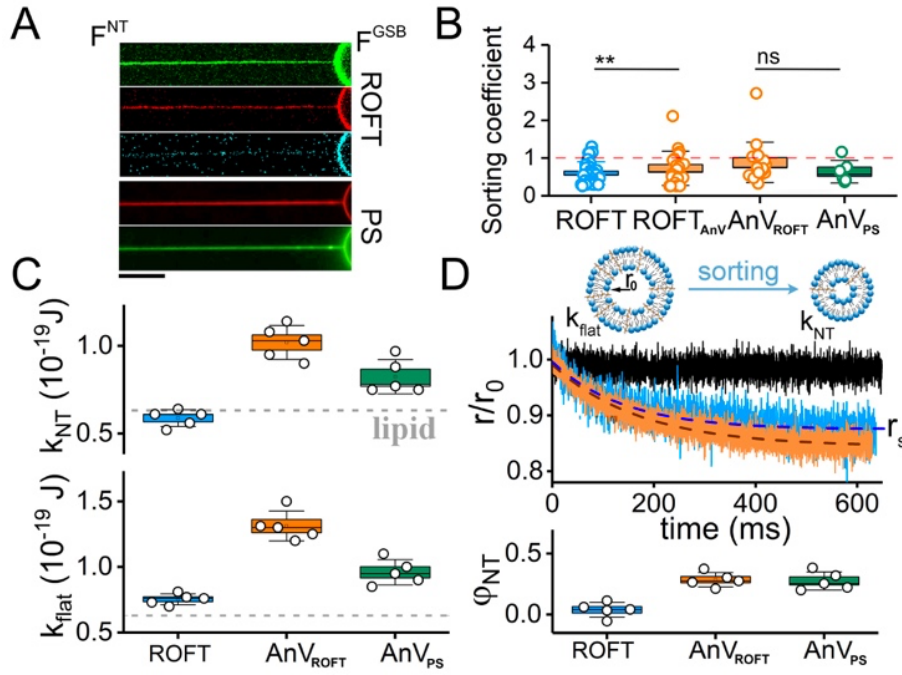


**Figure 4.** ROFT and AnV sorting detected by fluorescence microscopy and conductance measurements. (A) The fluorescence micrographs showing AnV binding to the outer leaflet of NT containing **4** (30

mol%) or PS (30 mol%). Scale bar 10mm. (B) The boxplot shows sorting coefficients  $q = \frac{F_{ROFT \text{ or } AnV}^{NT} F_{lipid}^{GSB}}{F_{ROFT \text{ or } AnV}^{GSB} F_{lipid}^{NT}}$ ;<sup>25,43</sup> the fluorescence of ROFTs ( $F_{ROFT}$ ) was used to calculate  $q_{ROFT}$  in the absence (ROFT) and presence (ROFT<sub>AnV</sub>) of AnV, the fluorescence of AnV-Alexa488 was used to calculate  $q_{AnV}$  in the ROFTs- (AnV<sub>ROFT</sub>) and PS- (AnV) containing membranes (see Fig. S6). (C) The boxplots show the effective bending rigidity of sNT (upper panel) and reservoir (lower panel) membranes (see Fig. S7 for details). The grey dash line shows the bending rigidity of the reference lipid membrane  $k_l$ .<sup>(18,19)</sup> (D) The upper panel shows kinetics of the sNT radius decrease caused by **4** (blue) and AnV and **4** (apricot) at low  $U=+50mV$ . The changes are normalized to the initial sNT radius, the control is pure lipid sNT (black). The lower panel shows  $\phi_{NT}$  calculated from the rigidity changes (see Supplementary Model 3.3. for details).

where  $a$  is the inclusion area on the membrane surface,  $k_{flat}$  is the bending rigidity of the reservoir membrane,  $r$  is the NT radius and  $J_s$  is the intrinsic curvature of a membrane fully covered by inclusions. Symmetric ROFT molecules oriented along the membrane normal and spanning both lipid monolayers are expected to create planar geometry with  $J_s = 0$ . Eq.1 then predicts a nonlinear ( $\sim r^{-2}$ ) dependence of the ROFT partitioning into the NT on the membrane curvature, in agreement with experimental observations (Fig. S6).

We next quantified  $q$  for the fluorescently labeled AnV. Following Eq.1, the expulsion of the rigid inclusions from the NT shall increase with  $a$ . Surprisingly, despite the large difference in  $a$  ( $\sim 30 \text{ nm}^2$  for AnV,<sup>44</sup> and 2-3  $\text{nm}^2$  for ROFTs, see Fig 1B) the AnV sorting was comparable with that of ROFTs on PS-containing membranes (Fig. 3B, green and blue, no significant difference at  $P=0.05$ ). Similar weak expulsion of AnV from NT was

observed on ROFT-containing membranes (Fig. 3B apricot and green). Following Eq.1, the diminished expulsion of AnV might be associated with a much reduced  $k_{flat}$  or, likelier, a greater preference for the NT curvature parametrized by positive  $J_s$ . Such a preference would be consistent with membrane insertion of AnV into the hydrophobic core of the lipid bilayer,<sup>21</sup> seen here as the weak  $Ca^{++}$ -independent AnV binding to both PS- and ROFT-containing membranes (Fig. 2B, S4). Furthermore, a strong interaction between ROFTs and AnV, seen in significant suppression of the ROFT exit from the NTs by AnV (Fig. 3B apricot and blue), implies that ROFTs might be directly engaged in the formation of the hydrophobic contacts between AnV and the membrane. We next tested whether this complex set of interactions can be unraveled by sNT conductance measurements.

### Detection of the bulk partitioning of ROFTs and AnV into sNTs.

The sNTs are shorter and thinner than the NTs pulled from GSB: the sNT length ranges from 80nm to a few microns and the luminal radius ranges from 2 to 10 nm (Fig. S7).<sup>18</sup> The ionic conductance through the sNT lumen measured in a voltage-clamp mode is the major experimental readout. The smallest sNTs resolve the conductance changes due to molecular scale membrane deformations. The longer micron-length tubes report the real time changes of the average sNT radius ( $r$ ) and the bending rigidity of the sNT membrane ( $k_{NT}$ ) upon protein entry into or exit from the tube.<sup>18</sup> We note that  $k_{NT}$  here is not a material parameter but an *effective* rigidity modulus dependent on the molecular exchange between the reservoir and sNT membranes.<sup>19,46</sup> As such, it defines the sNT curvature:

$$(2) r_s = \sqrt{\frac{k_{NT}}{2\sigma}}$$

where  $\sigma$  is the reservoir membrane tension.<sup>47</sup> In the stationary state,  $k_{NT}$  can be directly measured (Fig. S7).<sup>18</sup> We first utilized this bulk “elastic” detection mode to characterize the effect of AnV of on  $k_{NT}$ .

For rigid molecules such as ROFTs or AnV, that preserve their shape during membrane deformations,  $k_{NT}$  can be related to the bending rigidity of the planar reservoir  $k_{flat}$  as:

$$(3) k_{NT} \approx k_{flat} \left( 1 + \frac{3(q-1)\varphi_0}{2} \left( 1 - \frac{2}{3} r_s J_s \right) \right)$$

where  $r_s$  is the stationary sNT radius. The  $k_{NT}$  values approached that of the pure lipid sNT, indicating strong expulsion of **4** from sNT due to its high membrane curvature

(Fig. 3C, upper graph, Fig. S7). To reveal the curvature dependence of  $k_{NT}$ , we substituted Eq.1 into Eq.2 and, assuming  $J_s=0$ , obtained:  $k_{NT} \approx k_{flat} \left(1 - \frac{\varepsilon}{r_s^2}\right)$ . The quadratic dependence of  $k_{NT}$  on the curvature of sNT obtained experimentally with sNTs containing **4** confirmed the rigidity-driven mechanism of ROFT expulsion from sNT (Fig. S7).

Eq.2 shows that the softening of the sNT membrane due to egression of **4** from the sNT is coupled to the reduction of  $r$  as:

$$(4) \frac{\Delta k}{k_{NT}} \approx 2 \frac{\Delta r}{r_s}$$

A gradual decrease of  $r$  indeed followed sNT formation (Fig. 3D upper panel, blue, S8),<sup>19</sup> with the amplitude  $\Delta r = r_s - r_0$  estimating that of the bending rigidity  $\Delta k = k_{flat} - k_{NT}$ . The decrease was detected in the presence of **4** but not in the control single-lipid component tubes (Fig. 3D, upper panel, black, S7).<sup>19</sup> Using Eq. 4, we calculated  $k_{flat}$  from the measured  $k_{NT}$ ,  $\Delta r$  and  $r_s$  (Fig. S7,8). As expected, the addition of **4** drove  $k_{flat}$  significantly above ( $P < 0.01$ ) the bending rigidity of the reference lipid reservoir  $k_l$  (Fig. 3C, lower panel,). Importantly, the  $k_{flat}$  values were similar to that obtained from the  $k_{NT}$  dependence on the sNT curvature ( $0.75 \pm 0.04 \cdot 10^{-19} \text{J}$ , Fig.3C, analogous to  $0.72 \pm 0.02 \cdot 10^{-19} \text{J}$ , Fig. S7, at  $p = 0.05$ ) but significantly bigger than  $k_{NT}$  (at  $p = 0.01$ ).

The rigidity increase allowed estimating the efficiency of the incorporation of **4** into the reservoir membrane: using  $\varphi_0 = \frac{k_{flat} - k_l}{k_{flat}}$  (Supplementary Model, 3.1),<sup>19</sup> we found  $\varphi_0 = 0.16 \pm 0.05$ . Crucially, this value closely matched the mole fraction of **4** in the membrane-forming mixture, thus further confirming the seamless incorporation of **4** into the reservoir membranes (Fig. 1A). We finally used Eq.3 to obtain  $q$  and  $\varphi_{NT}$  from the difference between  $k_{flat}$  and  $k_{NT}$  (Supplementary Model 3.1 and 3.3, Eq. S5). Again, in agreement with the strong expulsion of **4** from highly curved sNT we found  $\varphi_{NT} \approx 0$  (not significantly different from 0 at  $p=0.1$ , Fig. 3D, lower panel).

With AnV ( $2 \mu\text{M}$  in the bulk) bound to either **4** (20mol%) or PS (20mol%) the sNT bending rigidity remained much higher than that of the lipid-only sNT (Fig. 3C, upper graph), in agreement with the efficient partitioning of AnV into NT reported by fluorescence microscopy (Fig. 3A). AnV also augmented the amplitude of the decrease of  $r$  measured after the sNT formation (Fig. 3D, upper panel, orange, S8) and, consequently, the increase of  $k_{flat}$  (Fig. 3C, lower panel), thus ruling out the AnV softness as the cause of its weak expulsion from the sNT. The dependence of  $k_{NT}$  on the

sNT curvature measured with AnV was more complex than with 4, with the fitting relying upon a moderately positive  $J_s$  (Fig. S7).

The  $k_{flat}$  increase was similar on the 4- and PS-containing membranes ( $\Delta k_{flat} \sim 4 \cdot 10^{-20} \text{J}$ ). The  $\varphi_0$  estimation yielded similar AnV coverage of the reservoir membrane for PS-containing ( $\varphi_0 = 0.38 \pm 0.05$ , SD n=5) and 4-containing  $\varphi_0 = 0.34 \pm 0.05$  (SD n=6) reservoirs (Supplementary Model 3.3). In turn, the sNT coverage was found similarly lower ( $\varphi_{NT} \sim 0.27$ , Fig. 3D, lower panel).

The weak expulsion of 4- and PS-bound AnV qualitatively agrees with fluorescence microscopy observations (Fig. 3C). Both data sets indicated that AnV could spontaneously partition into the curved membranes of the nanotubes due to a finite positive  $J_s$ . We next asked whether AnV oligomers could be moved from the planar reservoir to the sNT by ROFT-mediated electrophoresis to assess the full spectrum of their sizes and interactions.

### **ROFTs enable field-controlled partitioning of AnV into sNT.**

An electric field driving the ionic current through the sNT lumen also acts on charged molecular species in the inner leaflet of the sNT membrane (Fig. 4A).<sup>48</sup> In the presence of 4 the increase of the voltage bias  $U$  in the lumen to +150mV triggered a gradual growth of the sNT conductance, reversible upon the voltage decrease (Fig. 4B, blue). The kNT measurements at the plateau revealed that kNT increased above kflat (Fig. 4C, blue), in agreement with the voltage-driven accumulation of 4 in the sNT above its reservoir concentration. No sNT expansion was observed in the control experiments with sNTs containing PS and sNTs containing 4 upon the negative voltage application (Fig. S9).

AnV (2 $\mu\text{M}$  in the bulk) significantly enhanced the field-driven expansion of sNTs containing 4 (Fig. 4B, apricot). No voltage effect was seen with AnV bound to sNTs containing PS (Fig. 4B green), confirming that membrane-spanning 4 was needed to translate the electrophoretic force to the AnV bound to the outer sNT monolayer. In agreement with comigration of 4 and AnV, the kinetics of the sNT expansion in the presence of AnV ( $\tau/r_{NT} = 1.4 \pm 0.3 \text{s/nm}$ , Fig. 4B apricot) was about twice slower than in its absence ( $3.5 \pm 1.1 \text{s/nm}$ , Fig. 4B, blue). Curiously, AnV could also cause spontaneous expansion of PS-containing sNT, albeit at much slower time scale (Fig. 4D, green). No slow sNT expansion was observed in the control experiments without AnV (Fig. 4D,

black). Similarly, no expansion of sNTs containing **4** with bound AnV was detected when a negative U (-50mV) was applied to suppress the entry of **4**-AnV complexes into the sNT (Fig. 4D, orange, S9). We next assessed the AnV state on the expanded sNTs.

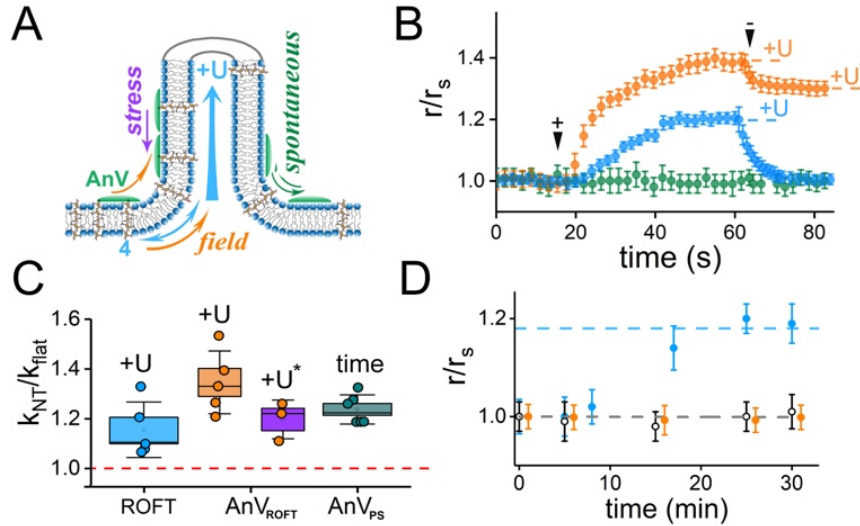


**Figure 5.** Field-driven partition of AnV into PS- and **4**-containing sNTs. (A) The cartoon shows different pathways of molecular exchange between the reservoir membrane and the sNT: field-driven exchange mediated by **4** (blue and apricot), spontaneous (green, relevant to PS-containing membranes) and stress-driven expulsion upon switching off the voltage bias (purple). (B) Changes of  $r$  caused by the U increase to +150mV (+arrow) followed by the decrease to +50mV (-arrow). The sNT contains **4** (blue), **4** and AnV (apricot) and PS and AnV (green). The time points are average values obtained from 3-5 independent experiments. (C) Boxplot shows the  $k_{NT}$  (normalized to  $k_{flat}$ ) measured upon the U increase (as indicated in panel B for ROFT and AnV<sub>ROFT</sub>) or upon spontaneous expansion of the PS-containing NT (blue dash line, panel D). (D) Changes of  $r$  measured with PS-containing sNT (black, control), PS-containing sNT with bound AnV (green) and **4**-containing sNT with bound AnV held at U=-50mV (apricot). The time points are average values obtained from 3-5 independent experiments.

### Detection of AnV polymerization on the sNT membrane.

Unlike with **4** alone, in the presence of AnV, the voltage-driven sNT expansion was only partially reversible (Fig. 4B, +U\*), implying that AnV accumulated on the sNT membrane remained there and maintained  $k_{NT}$  above  $k_{flat}$  (Fig. 4C, purple). Importantly, the  $k_{NT}$  became independent on the sNT curvature indicating that the curvature-dependent exchange of AnV between the sNT and reservoir membranes was abolished (Fig. S7), as AnV molecules on the sNT membrane self-assembled into an extended lattice.<sup>23</sup> Indeed, the sNT coverage by AnV estimated for the rigidity increase ( $\varphi_{NT}^* = 0.50 \pm 0.04$ , SD n=5, Supplementary Model 3.3) approached that of the  $p6$  lattice formed by AnV on a planar surface.<sup>42-44</sup>

The spontaneous expansion of PS-containing sNTs was also associated with a  $k_{NT}$  increase comparable with that observed upon the voltage reduction in sNTs (Fig. 4C, purple and green). The AnV coverage increased proportionally to  $k_{NT}$  (to  $\varphi_{NT}^* = 0.46 \pm$

0.04, SD n=6, Supplementary Model 3.3), implying spontaneous polymerization of AnV on the PS-containing sNT. Importantly, no spontaneous sNT expansion was detected without AnV (Fig. 4D, black) or when AnV bound to **4** was prevented from the sNT entry by negative U (Fig. 4D, apricot).

The formation of a stable AnV lattice on the sNT membrane was further probed via variations in the sNT length. We found that the dependence of the sNT conductance ( $G_{NT}$ ) on its length ( $L_{NT}$ ) changed with AnV polymerization on the sNT containing **4**. Prior to the polymerization (at low U), we recovered the hyperbolic  $G_{NT}(L_{NT})$  characteristic for a cylinder of constant  $r$ :<sup>18</sup>

$$(4) G_{NT} \approx r^2 / \rho_{NT} L_{NT}.$$

This dependence shows that sNT can be freely extracted from and reinserted into the membrane reservoir (Fig. 6A). Fitting  $G_{NT}(L_{NT})$  obtained experimentally with Eq.4 yielded the sNT radius  $r_s$  (Fig. 6B, -U).<sup>18</sup> Upon voltage-induced formation of a stable AnV coverage on the sNT surface (Fig. 5, +U\*), the  $G_{NT}(L_{NT})$  dependence became nonsmooth with visible jumps and inflexion points, indicating a barrier for AnV transfer from sNT to the reservoir (Fig. 5C, purple). Fitting of the dependence yielded higher  $r_s$  (Fig. 5B, +U), in agreement with the sNT expansion by AnV accumulated on the sNT membrane (Fig. 5B).

Furthermore, at short lengths (ranging between 90 and 220nm)  $G_{NT}(L_{NT})$  reached a plateau (Fig. 6C, arrowhead), indicating the appearance of a protein scaffold encaging the sNT and preventing further decrease of the tube length (Fig. 6C, purple arrow). On the PS-containing sNT such a plateau was detected at the beginning of the shortening (Fig. 5C, green). In this case, the protein scaffold covering the whole sNT maintained  $L_{NT}$  and  $r_s$ , and thus  $G_{NT}$ , constant and could only bend upon the sNT shortening (Fig 6C, green path), eventually leading to the tube rupture. Hence, slow spontaneous entry of AnV into sNT resulted in more complete and stable protein coverage, indicating that the formation of the AnV lattice on the sNT membrane is kinetically regulated.

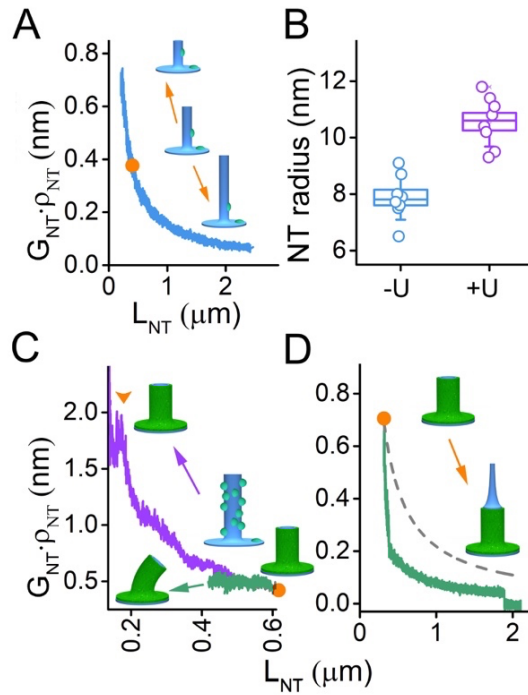


**Figure 6.** AnV scaffolds limit both the shortening and extension of sNT. (A) A characteristic example of  $G_{NT}\rho_{NT}$  changes with the  $L_{NT}$  variations measured with sNT containing **4** and AnV prior to AnV polymerization. (B) The boxplot shows the sNT radii calculated from fitting  $G_{NT}(L_{NT})$  dependences using Eq. 4. (C) A characteristic example of  $G_{NT}\rho_{NT}$  increase with the sNT shortening measured with sNT containing **4** (purple) and PS (green) and AnV upon AnV polymerization. (D) An example of the sNT extension-fission in the presence of AnV scaffold. The  $G_{NT}(L_{NT})$  shows faster decay than that predicted by Eq. 4 (grey dash line).

Similar stepwise conductance changes, albeit less frequent and reversible, were detected with PS-containing sNTs prior to AnV polymerization (Fig. 6A green). As AnV coverage of such sNTs is relatively high (Fig. 3D, lower panel), the stepwise changes were interpreted as spontaneous entries and exits of AnV oligomers. The sNT conductance increase was associated with the local expansion of the sNT lumen, parametrized by the luminal volume increment ( $\Delta v$ , Fig. 6B,<sup>18</sup>). AnV entry produced extremely small  $\Delta v$  consistent with molecular deformations (Fig. 6B). Crucially,  $\Delta v\varphi_U$  correctly estimated the total increase of the sNT volume upon AnV entry measured at the end of the sNT expansion (Fig. 4B, Supplementary Model 3.3). Similar quantification for the steps detected during the sNT shortening (Fig. 5C) yielded much bigger  $\Delta v$ , in agreement with the formation of small elements of the AnV lattice (Fig. 6, violet)

To relate  $\Delta v$  to the size of AnV oligomers in the membrane plane, a simple *ad hoc* model for a local sNT deformation by a flat and rigid disk of an area  $a$ , mimicking slightly concave AnV oligomers, was used (Supplementary Model 3.2, Fig. S10). In the linear

approximation, we obtained the following equation:  $a \approx r/\Delta v$ . Using this approximation, we found that the  $\Delta v$  measured on the PS-containing sNT corresponded to AnV monomer ( $a \sim 30 \text{ nm}^2$ ,<sup>44</sup>) while  $\Delta v$  measured with **4** corresponded to a mixture of AnV monomers and trimers, known precursors of AnV polymerization of the flat surface.<sup>42</sup>

Comparison of spontaneous and voltage-driven entry of AnV into sNTs (Fig. 6B, green and apricot) revealed that the curvature barrier between the planar reservoir membrane and the sNT is surmountable only for the smallest AnV oligomers with  $a$  comparable to the AnV monomers. The barrier is to be relatively low to account for substantial coverage of PS-containing NTs and sNTs by AnV (Fig. 3B, D, lower panel). Nevertheless, using the rigid disk model we found that, even for the smallest  $\Delta v$  associated with AnV monomers, the barrier was around  $5 k_B T$ , that is, prohibitively high for spontaneous crossing (Supplementary Model 3.2). As the model correctly predicted the size of AnV monomers, a correction factor not related to the molecular shape or rigidity was needed to explain the spontaneous AnV partitioning into the sNT membrane. We found that such a correction could be associated with the membrane curvature dependency of the hydrophobic interaction between AnV and lipids (Supplementary Model 3.2).<sup>21</sup>

Interestingly, such a dependency is formally equivalent to the introduction of an *effective* positive  $J_s^*$  (Supplementary Model 3.2), in agreement with the experiment. We next found that with  $J_s^* \sim 0.05 \text{ nm}^{-1}$  the energy barrier for AnV monomer entry to sNT reduced to the values ( $\sim 2 k_B T$ ) fully compatible with the experiment (Supplementary Model 3.2). The same  $J_s^*$  value was used to fit the dependence of  $k_{NT}$  on the sNT curvature measured on sNTs containing **4** in the presence of AnV (Fig. S7). While more is to be done to unravel the complexity of AnV interactions with the lipid bilayer, these results highlight the capabilities of ROFT-sNTs in obtaining fine molecular details of the proteo-lipid interactions.

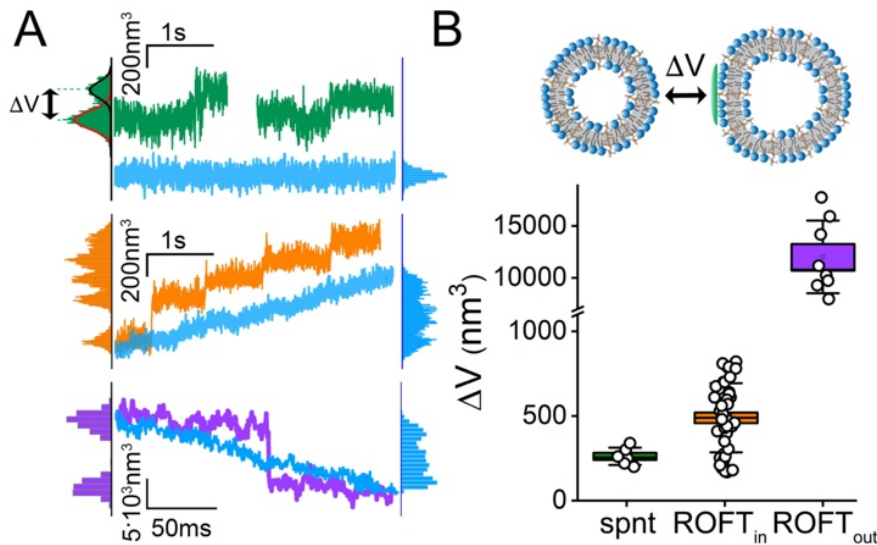


**Figure 7.** Detection of the entry/exit of individual AnV oligomers to/from the sNT. (A). Stepwise conductance changes were detected upon spontaneous (green) and voltage-driven (apricot) AnV entry into sNT, as well as upon AnV exit driven by the length decrease (violet). No stepwise changes were detected without AnV when sNTs contained only 4 (blue traces). (B) Boxplot shows the changes of the luminal volume of sNT corresponding to individual conductance steps seen in A; the cartoon shows how the sNT cross-section is expanded by a bound AnV monomer.

### 3.3 Results and Discussion

The ability to create shapes through molecular self-assembly is essential in both life and technology.<sup>5</sup> However, few methods are available to study this process with molecular precision and establish a connection between the resulting mesoscale shapes and their elementary molecular precursors. Within cells, protein oligomerization and self-assembly can be facilitated and guided by soft membrane templates, where the shape of the membrane changes with the protein binding and self-assembly.<sup>11,14</sup> We showed here that the shape changes induced by AnV bound to sNTs can be used to track in real time the oligomeric state of AnV on the sNT membrane. Both the molecular-scale deformations caused by small oligomeric precursors of AnV polymerization and the mesoscale expansion and stiffening of sNT by the AnV lattice self-assembled on the sNT surface were resolved. Simple elastic modeling indicated that the small stepwise deformations (Fig. 6B) could be produced by rigid AnV oligomers, monomers and trimers, known elementary precursors of the planar AnV lattice.<sup>42,44</sup> In turn, the moderate rigidity increase upon AnV accumulation on the sNT membrane indicated that these rigid oligomers self-assemble into a flexible cylindrical lattice.<sup>23</sup>

Spontaneous and unexpected partitioning of AnV oligomers to positively curved NTs was detected by both fluorescence microscopy and conductance measurements (Fig. 3), in contrast with earlier association of their shape with negative membrane curvature.<sup>49</sup> Furthermore, the analysis of membrane deformations imposed by AnV oligomers confirmed their close-to-planar geometry. To explain their partitioning to NTs, hydrophobic interaction stimulated by packing defects associated with increasing membrane curvature were invoked.<sup>21,50</sup> Introduction of a curvature-dependent hydrophobic interaction explained the spontaneous size-dependent entry of AnV, indicating a novel intricate mechanism of the curvature sensing by AnV relevant to the overall complexity of membrane interactions by annexins.<sup>51</sup> The sensing is defined by two antagonistic factors, the concave molecular shape of AnV and its interaction with the hydrophobic core of the lipid bilayer, which can be parametrized by an effective positive  $J_s^*$  (as summarized by Eq.1). As a result, AnV monomers are ambivalent toward the positive mean membrane curvature: they can be both attracted to or repelled from the membrane templates of positive curvature, depending on the ratio between the membrane curvature value and  $J_s^*$ .

Spontaneous, or ROFT-assisted, partitioning of small AnV oligomers into the sNT was effective enough to enable further AnV self-assembly into a curved lattice. Importantly, the self-assembly process is kinetically controlled, with the faster ROFT-assisted assembly leading to less regular, fragmented lattices (Fig. 5C, 6A, purple). The differences between the lattices forming on the sNT containing PS and 4 can be interpreted in terms of the number of the nucleation events.<sup>42,43</sup> The slow, sigmoidal time dependence of the lattice formation on the PS-NTs (Fig. 4D, green) indicates that the nucleation is a rate-limiting step, with a single nucleation event leading to the complete lattice. In turn, the AnV crowding on the sNT enforced by 4-mediated electrophoresis triggered the formation of multiple nucleation points and, as a result, rival polymerization processes leading to more fragmented sNT coverage.

Our major criterion for the lattice appearance was the impairment, followed by complete obstruction, of the sNT retraction to the reservoir membrane (Fig. 5B, C). Such obstruction, also observed by fluorescence microscopy, is characteristic for protein scaffolds encaging sNT.<sup>17</sup> The experiments with the sNT extension further confirmed formation of the scaffold restricting the material exchange between the reservoir membrane and the sNT. The extension caused fast constriction and fission of the sNT (Fig. 5C), a behavior earlier associated with the frictional drag imposed by the

protein scaffold.<sup>24,25</sup> The ability of AnV to form such a scaffolding suggests its direct involvement in membrane fission during membrane recycling and repair.<sup>52</sup>

While we detected spontaneous self-assembly of AnV on the sNT membrane, synthetic ROFT BAs played a key role in the mechanistic assessment of the self-assembly process. ROFT-mediated AnV entry to sNTs from the planar membrane reservoir revealed the well-characterized small oligomeric precursors of the planar AnV lattice (Fig. 6, apricot),<sup>42,44</sup> thus validating our detection method. In turn, the ROFT-mediated exit of AnV confirmed the oligomerization seen as the increase in the conductance signal (Fig. 6, violet). Our interpretation of the conductance changes, as well as our understanding of the mechanisms of protein binding by ROFTs, are presently basic and incomplete. However, we note that the above proof-of-principle analyses were conducted using simple symmetric ROFT prototypes. Further modification of ROFTs directed toward shape/rigidity variations and chemical recognition of proteins is possible. Indeed, the control of OF shape has found extensive use in the field of molecular recognition,<sup>53-56</sup> and several reports describe OF self-assembly into vesicles, fibers, gels and liquid crystals.<sup>57-65</sup> Controlled alterations of the shape and molecular rigidity of ROFT could reveal how local mechanical properties of the membrane change upon the protein adsorption and, in turn, affect the protein functions. The shape flexibility might further encode complex responses to membrane stresses,<sup>66,67</sup> with additional experimental readouts and means of regulation of the ROFT membrane partitioning enabled.

### **3.4 Outlook**

Label-free real time interrogation of protein interactions is imperative for understanding their functions in the cell and unraveling complex and dynamic protein interactomes. Here, we showed that tiny lipid membrane nanotubes constricted to almost molecular dimensions and equipped with ROFTs can be operated as primitive externally controlled nanoreactors that can contain, control, and report protein interactions on the membrane. In its simplest form, the ROFT-sNT prototype demonstrated its capabilities to resolve molecular details of AnV oligomerization and membrane interactions. Advancing the ROFT chemistry, sNT design and the means of the interpretation of the current changes detected by the ROFT-sNT shall greatly expand its detection capabilities potentially making it a highly selective tool for affinity

and size recognition of molecular species and investigation of their interactions on and with the membrane.

## **ASSOCIATED CONTENT**

### **Supporting Information**

The Supporting Information is available free of charge on the ACS Publications website. Experimental procedures and characterization of new compounds, materials and methods and additional biophysical experiments are described in a supplementary pdf file. Crystallographic data is available in a supplementary cif file.

## **AUTHOR INFORMATION**

### **Corresponding Author**

Correspondence should be addressed to I.H. (ivan.huc@cup.lmu.de) or V.A.F (vadim.frolov@ehu.eus).

### **Author Contributions**

‡These authors contributed equally.

### **Notes**

The authors declare no competing financial interests.

## **ACKNOWLEDGMENT**

This work was partially supported by NIGMS of the National Institutes of Health under award R01GM121725 (the content is solely the responsibility of the authors and does not necessarily represent the official views of the National Institutes of Health) and Spanish Ministry of Science and Innovation grant PID2020-117497GB-I00 to V.A.F, the Basque Government grant IT1270-19, the Russian Science Foundation (grant # N<sup>o</sup> 22-15-00265) to P.V.B. We thank Dr. Brice Kauffmann (IECB, Bordeaux) for assistance with crystallographic studies and Dr. Emilio Gonzalez-Ramirez for the help with AFM imaging. We thank the Center for Precision Genome Editing and Genetic Technologies for Biomedicine, Federal Research and Clinical Center of Physical-Chemical Medicine of Federal Medical Biological Agency for providing laboratory facilities.

### 3.5 References Manuscript

- (1) Wang, F.; Burrage, A. M.; Postel, S.; Clark, R. E.; Orlova, A.; Sundberg, E. J.; Kearns, D. B.; Egelman, E. H. A Structural Model of Flagellar Filament Switching across Multiple Bacterial Species. *Nat. Commun.* **2017**, *8* (1), 960. <https://doi.org/10.1038/s41467-017-01075-5>.
- (2) Unger, E.; Böhm, K. J.; Vater, W. Structural Diversity and Dynamics of Microtubules and Polymorphic Tubulin Assemblies. *Electron Microsc. Rev.* **1990**, *3* (2), 355–395. [https://doi.org/10.1016/0892-0354\(90\)90007-f](https://doi.org/10.1016/0892-0354(90)90007-f).
- (3) Mesarec, L.; Drab, M.; Penič, S.; Kralj-Iglič, V.; Iglič, A. On the Role of Curved Membrane Nanodomains, and Passive and Active Skeleton Forces in the Determination of Cell Shape and Membrane Budding. *Int. J. Mol. Sci.* **2021**, *22* (5), 2348. <https://doi.org/10.3390/ijms22052348>.
- (4) Gao, C.; Chen, G. Exploring and Controlling the Polymorphism in Supramolecular Assemblies of Carbohydrates and Proteins. *Acc. Chem. Res.* **2020**, *53* (4), 740–751. <https://doi.org/10.1021/acs.accounts.9b00552>.
- (5) Luo, Q.; Hou, C.; Bai, Y.; Wang, R.; Liu, J. Protein Assembly: Versatile Approaches to Construct Highly Ordered Nanostructures. *Chem. Rev.* **2016**, *116* (22), 13571–13632. <https://doi.org/10.1021/acs.chemrev.6b00228>.
- (6) McManus, J. J.; Charbonneau, P.; Zaccarelli, E.; Asherie, N. The Physics of Protein Self-Assembly. *Curr. Opin. Colloid Interface Sci.* **2016**, *22*, 73–79. <https://doi.org/https://doi.org/10.1016/j.cocis.2016.02.011>.
- (7) Pak, A. J.; Grime, J. M. A.; Sengupta, P.; Chen, A. K.; Durumeric, A. E. P.; Srivastava, A.; Yeager, M.; Briggs, J. A. G.; Lippincott-Schwartz, J.; Voth, G. A. Immature HIV-1 Lattice Assembly Dynamics Are Regulated by Scaffolding from Nucleic Acid and the Plasma Membrane. *Proc. Natl. Acad. Sci. U. S. A.* **2017**, *114* (47), E10056–E10065. <https://doi.org/10.1073/pnas.1706600114>.
- (8) Pellarin, R.; Schuetz, P.; Guarnera, E.; Caflich, A. Amyloid Fibril Polymorphism Is under Kinetic Control. *J. Am. Chem. Soc.* **2010**, *132* (42), 14960–14970. <https://doi.org/10.1021/ja106044u>.
- (9) Kochovski, Z.; Chen, G.; Yuan, J.; Lu, Y. Cryo-Electron Microscopy for the Study of Self-Assembled Poly(Ionic Liquid) Nanoparticles and Protein Supramolecular Structures. *Colloid Polym. Sci.* **2020**, *298* (7), 707–717. <https://doi.org/10.1007/s00396-020-04657-w>.
- (10) Heddle, J. G.; Chakraborti, S.; Iwasaki, K. Natural and Artificial Protein Cages: Design, Structure and Therapeutic Applications. *Curr. Opin. Struct. Biol.* **2017**, *43*, 148–155. <https://doi.org/10.1016/j.sbi.2017.03.007>.
- (11) Zhu, J.; Avakyan, N.; Kakkis, A.; Hoffnagle, A. M.; Han, K.; Li, Y.; Zhang, Z.; Choi, T. S.; Na, Y.; Yu, C.-J.; Tezcan, F. A. Protein Assembly by Design. *Chem. Rev.* **2021**, *121* (22), 13701–13796. <https://doi.org/10.1021/acs.chemrev.1c00308>.
- (12) Majewski, J.; Jones, E. M.; Vander Zanden, C. M.; Biernat, J.; Mandelkow, E.; Chi, E. Y. Lipid Membrane Templated Misfolding and Self-Assembly of Intrinsically Disordered Tau Protein. *Sci. Rep.* **2020**, *10* (1), 13324. <https://doi.org/10.1038/s41598-020-70208-6>.
- (13) Hu, R.; Diao, J.; Li, J.; Tang, Z.; Li, X.; Leitz, J.; Long, J.; Liu, J.; Yu, D.; Zhao, Q. Intrinsic and Membrane-Facilitated  $\alpha$ -Synuclein Oligomerization Revealed by Label-Free Detection through Solid-State Nanopores. *Sci. Rep.* **2016**, *6*, 20776. <https://doi.org/10.1038/srep20776>.

- (14) Bozelli, J. C. J.; Epand, R. M. Membrane Shape and the Regulation of Biological Processes. *J. Mol. Biol.* **2020**, *432* (18), 5124–5136. <https://doi.org/10.1016/j.jmb.2020.03.028>.
- (15) Antonny, B. Membrane Deformation by Protein Coats. *Curr. Opin. Cell Biol.* **2006**, *18* (4), 386–394. <https://doi.org/10.1016/j.ceb.2006.06.003>.
- (16) Tagiltsev, G.; Haselwandter, C. A.; Scheuring, S. Nanodissected Elastically Loaded Clathrin Lattices Relax to Increased Curvature. *Sci. Adv.* **2021**, *7* (33), eabg9934. <https://doi.org/10.1126/sciadv.abg9934>.
- (17) Shnyrova, A. V.; Bashkirov, P. V.; Akimov, S. A.; Pucadyil, T. J.; Zimmerberg, J.; Schmid, S. L.; Frolov, V. A. Geometric Catalysis of Membrane Fission Driven by Flexible Dynamin Rings. *Science* (80-. ). **2013**, *339* (6126), 1433–1436. <https://doi.org/10.1126/science.1233920>.
- (18) Bashkirov, P. V.; Kuzmin, P. I.; Chekashkina, K.; Arrasate, P.; Vera Lillo, J.; Shnyrova, A. V.; Frolov, V. A. Reconstitution and Real-Time Quantification of Membrane Remodeling by Single Proteins and Protein Complexes. *Nat. Protoc.* **2020**, *15* (8), 2443–2469. <https://doi.org/10.1038/s41596-020-0337-1>.
- (19) Bashkirov, P. V.; Kuzmin, P. I.; Vera Lillo, J.; Frolov, V. A. Molecular Shape Solution for Mesoscopic Remodeling of Cellular Membranes. *Annu. Rev. Biophys.* **2022**, *51*, 473–497. <https://doi.org/10.1146/annurev-biophys-011422-100054>.
- (20) Antonny, B. Mechanisms of Membrane Curvature Sensing. *Annu. Rev. Biochem.* **2011**, *80*, 101–123. <https://doi.org/10.1146/annurev-biochem-052809-155121>.
- (21) Jeppesen, B.; Smith, C.; Gibson, D. F.; Tait, J. F. Entropic and Enthalpic Contributions to Annexin V-Membrane Binding: A Comprehensive Quantitative Model. *J. Biol. Chem.* **2008**, *283* (10), 6126–6135. <https://doi.org/10.1074/jbc.M707637200>.
- (22) Lu, J.; Le Brun, A. P.; Chow, S. H.; Shiota, T.; Wang, B.; Lin, T.-W.; Liu, G.-S.; Shen, H.-H. Defining the Structural Characteristics of Annexin V Binding to a Mimetic Apoptotic Membrane. *Eur. Biophys. J.* **2015**, *44* (8), 697–708. <https://doi.org/10.1007/s00249-015-1068-z>.
- (23) Wilson-Kubalek, E. M.; Brown, R. E.; Celia, H.; Milligan, R. A. Lipid Nanotubes as Substrates for Helical Crystallization of Macromolecules. *Proc. Natl. Acad. Sci. U. S. A.* **1998**, *95* (14), 8040–8045. <https://doi.org/10.1073/pnas.95.14.8040>.
- (24) Simunovic, M.; Manneville, J. B.; Renard, H. F.; Evergren, E.; Raghunathan, K.; Bhatia, D.; Kenworthy, A. K.; Voth, G. A.; Prost, J.; McMahon, H. T.; Johannes, L.; Bassereau, P.; Callan-Jones, A. Friction Mediates Scission of Tubular Membranes Scaffolded by BAR Proteins. *Cell* **2017**, *170* (1), 172–184. <https://doi.org/10.1016/j.cell.2017.05.047>.
- (25) Espadas, J.; Pendin, D.; Bocanegra, R.; Escalada, A.; Misticioni, G.; Trevisan, T.; Velasco del Olmo, A.; Montagna, A.; Bova, S.; Ibarra, B.; Kuzmin, P. I.; Bashkirov, P. V.; Shnyrova, A. V.; Frolov, V. A.; Daga, A. Dynamic Constriction and Fission of Endoplasmic Reticulum Membranes by Reticulon. *Nat. Commun.* **2019**, *10* (1), 5327. <https://doi.org/10.1038/s41467-019-13327-7>.
- (26) Fuhrhop, J.-H.; Wang, T. Bolaamphiphiles. *Chem. Rev.* **2004**, *104* (6), 2901–2938. <https://doi.org/10.1021/cro30602b>.
- (27) Gong, B. Hollow Crescents, Helices, and Macrocycles from Enforced Folding and Folding-Assisted Macrocyclization. *Acc. Chem. Res.* **2008**, *41* (10), 1376–1386. <https://doi.org/10.1021/ar700266f>.

- (28) Saraogi, I.; Hamilton, A. D. Recent Advances in the Development of Aryl-Based Foldamers. *Chem. Soc. Rev.* **2009**, *38* (6), 1726–1743. <https://doi.org/10.1039/b819597h>.
- (29) Huc, I. Aromatic Oligoamide Foldamers. *Eur. J. Org. Chem.* **2004**, *2004* (1), 17–29. <https://doi.org/https://doi.org/10.1002/ejoc.200300495>.
- (30) Qi, S.; Zhang, C.; Yu, H.; Zhang, J.; Yan, T.; Lin, Z.; Yang, B.; Dong, Z. Foldamer-Based Potassium Channels with High Ion Selectivity and Transport Activity. *J. Am. Chem. Soc.* **2021**, *143* (9), 3284–3288. <https://doi.org/10.1021/jacs.oc12128>.
- (31) Roy, A.; Joshi, H.; Ye, R.; Shen, J.; Chen, F.; Aksimentiev, A.; Zeng, H. Polyhydrazide-Based Organic Nanotubes as Efficient and Selective Artificial Iodide Channels. *Angew. Chem. Int. Ed.* **2020**, *59* (12), 4806–4813. <https://doi.org/https://doi.org/10.1002/anie.201916287>.
- (32) Shen, J.; Fan, J.; Ye, R.; Li, N.; Mu, Y.; Zeng, H. Polypyridine-Based Helical Amide Foldamer Channels: Rapid Transport of Water and Protons with High Ion Rejection. *Angew. Chem. Int. Ed. Engl.* **2020**, *59* (32), 13328–13334. <https://doi.org/10.1002/anie.202003512>.
- (33) Lang, C.; Deng, X.; Yang, F.; Yang, B.; Wang, W.; Qi, S.; Zhang, X.; Zhang, C.; Dong, Z.; Liu, J. Highly Selective Artificial Potassium Ion Channels Constructed from Pore-Containing Helical Oligomers. *Angew. Chem. Int. Ed. Engl.* **2017**, *56* (41), 12668–12671. <https://doi.org/10.1002/anie.201705048>.
- (34) Wei, X.; Zhang, G.; Shen, Y.; Zhong, Y.; Liu, R.; Yang, N.; Al-Mkhaizim, F. Y.; Kline, M. A.; He, L.; Li, M.; Lu, Z.-L.; Shao, Z.; Gong, B. Persistent Organic Nanopores Amenable to Structural and Functional Tuning. *J. Am. Chem. Soc.* **2016**, *138* (8), 2749–2754. <https://doi.org/10.1021/jacs.5b12698>.
- (35) Gong, B.; Shao, Z. Self-Assembling Organic Nanotubes with Precisely Defined, Sub-Nanometer Pores: Formation and Mass Transport Characteristics. *Acc. Chem. Res.* **2013**, *46* (12), 2856–2866. <https://doi.org/10.1021/ar400030e>.
- (36) Zhang, D.-W.; Zhao, X.; Hou, J.-L.; Li, Z.-T. Aromatic Amide Foldamers: Structures, Properties, and Functions. *Chem. Rev.* **2012**, *112* (10), 5271–5316. <https://doi.org/10.1021/cr300116k>.
- (37) Choma, C.; Gratkowski, H.; Lear, J. D.; DeGrado, W. F. Asparagine-Mediated Self-Association of a Model Transmembrane Helix. *Nat. Struct. Biol.* **2000**, *7* (2), 161–166. <https://doi.org/10.1038/72440>.
- (38) Velasco-Olmo, A.; Ormaetxea Gisasola, J.; Martinez Galvez, J. M.; Vera Lillo, J.; Shnyrova, A. V. Combining Patch-Clamping and Fluorescence Microscopy for Quantitative Reconstitution of Cellular Membrane Processes with Giant Suspended Bilayers. *Sci. Rep.* **2019**, *9* (1), 7255. <https://doi.org/10.1038/s41598-019-43561-4>.
- (39) García-Arribas, A. B.; Alonso, A.; Goñi, F. M. Cholesterol Interactions with Ceramide and Sphingomyelin. *Chem. Phys. Lipids* **2016**, *199*, 26–34. <https://doi.org/10.1016/j.chemphyslip.2016.04.002>.
- (40) Werner, S.; Ebenhan, J.; Poppe, M.; Poppe, S.; Ebert, H.; Tschierske, C.; Bacia, K. Effects of Lateral and Terminal Chains of X-Shaped Bolapolyphiles with Oligo(Phenylene Ethynylene) Cores on Self-Assembly Behavior. Part 2: Domain Formation by Self-Assembly in Lipid Bilayer Membranes. *Polymers*. **2017**, *9* (10), 471. <https://doi.org/10.3390/polym9100471>.
- (41) Schmid, S. L.; Frolov, V. A. Dynamins: Functional Design of a Membrane Fission Catalyst. *Annu. Rev. Cell Dev. Biol.* **2011**, *27* (1), 79–105. <https://doi.org/10.1146/annurev-cellbio-100109-104016>.

- (42) Richter, R. P.; Him, J. L. K.; Tessier, B.; Tessier, C.; Brisson, A. R. On the Kinetics of Adsorption and Two-Dimensional Self-Assembly of Annexin A5 on Supported Lipid Bilayers. *Biophys. J.* **2005**, *89* (5), 3372–3385. <https://doi.org/10.1529/biophysj.105.064337>.
- (43) Lin, Y.-C.; Chipot, C.; Scheuring, S. Annexin-V Stabilizes Membrane Defects by Inducing Lipid Phase Transition. *Nat. Commun.* **2020**, *11* (1), 230. <https://doi.org/10.1038/s41467-019-14045-w>.
- (44) Miyagi, A.; Chipot, C.; Rangl, M.; Scheuring, S. High-Speed Atomic Force Microscopy Shows That Annexin V Stabilizes Membranes on the Second Timescale. *Nat. Nanotechnol.* **2016**, *11* (9), 783–790. <https://doi.org/10.1038/nnano.2016.89>.
- (45) Capraro, B. R.; Yoon, Y.; Cho, W.; Baumgart, T. Curvature Sensing by the Epsin N-Terminal Homology Domain Measured on Cylindrical Lipid Membrane Tethers. *J. Am. Chem. Soc.* **2010**, *132* (4), 1200–1201. <https://doi.org/10.1021/ja907936c>.
- (46) Tian, A.; Baumgart, T. Sorting of Lipids and Proteins in Membrane Curvature Gradients. *Biophys. J.* **2009**, *96* (7), 2676–2688. <https://doi.org/10.1016/j.bpj.2008.11.067>.
- (47) Frolov, V. A.; Lizunov, V. A.; Dunina-Barkovskaya, A. Y.; Samsonov, A. V.; Zimmerberg, J. Shape Bistability of a Membrane Neck: A Toggle Switch to Control Vesicle Content Release. *Proc. Natl. Acad. Sci. U. S. A.* **2003**, *100* (15), 2962100. <https://doi.org/10.1073/pnas.1432962100>.
- (48) Chekashkina, K. V.; Galimzyanov, T. R.; Kuzmin, P. I.; Akimov, S. A.; Romanov, S. A.; Pozmogova, G. E.; Klinov, D. V.; Bashkirov, P. V. Detection of DNA Molecules in a Lipid Nanotube Channel in the Low Ion Strength Conditions. *Biochem. (Moscow), Suppl. Ser. A Membr. Cell Biol.* **2017**, *11* (3), 217–224. <https://doi.org/10.1134/S1990747817030047>.
- (49) Oling, F.; Santos, J. S.; Govorukhina, N.; Mazères-Dubut, C.; Bergsma-Schutter, W.; Oostergetel, G.; Keestra, W.; Lambert, O.; Lewit-Bentley, A.; Brisson, A. Structure of Membrane-Bound Annexin A5 Trimers: A Hybrid Cryo-EM - X-Ray Crystallography Study. *J. Mol. Biol.* **2000**, *304* (4), 561–573. <https://doi.org/10.1006/jmbi.2000.4183>.
- (50) Bigay, J.; Antonny, B. Curvature, Lipid Packing, and Electrostatics of Membrane Organelles: Defining Cellular Territories in Determining Specificity. *Dev. Cell* **2012**, *23* (5), 886–895. <https://doi.org/10.1016/j.devcel.2012.10.009>.
- (51) Rescher, U.; Gerke, V. Annexins – Unique Membrane Binding Proteins with Diverse Functions. *J. Cell Sci.* **2004**, *117* (13), 2631–2639. <https://doi.org/10.1242/jcs.01245>.
- (52) Cooper, S. T.; McNeil, P. L. Membrane Repair: Mechanisms and Pathophysiology. *Physiol. Rev.* **2015**, *95* (4), 1205–1240. <https://doi.org/10.1152/physrev.00037.2014>.
- (53) Ferrand, Y.; Huc, I. Designing Helical Molecular Capsules Based on Folded Aromatic Amide Oligomers. *Acc. Chem. Res.* **2018**, *51* (4), 970–977. <https://doi.org/10.1021/acs.accounts.8b00075>.
- (54) Plante, J. P.; Burnley, T.; Malkova, B.; Webb, M. E.; Warriner, S. L.; Edwards, T. A.; Wilson, A. J. Oligobenzamide Proteomimetic Inhibitors of the P53-HDM2 Protein-Protein Interaction. *Chem. Commun.* **2009**, No. 34, 5091–5093. <https://doi.org/10.1039/b908207g>.
- (55) Reddy, P. S.; Langlois d'Estaintot, B.; Granier, T.; Mackereth, C. D.; Fischer, L.; Huc, I. Structure Elucidation of Helical Aromatic Foldamer-Protein Complexes with Large Contact Surface Areas. *Chemistry* **2019**, *25* (47), 11042–11047. <https://doi.org/10.1002/chem.201902942>.

- (56) Liu, Y.; Parks, F. C.; Sheetz, E. G.; Chen, C.-H.; Flood, A. H. Polarity-Tolerant Chloride Binding in Foldamer Capsules by Programmed Solvent-Exclusion. *J. Am. Chem. Soc.* **2021**, *143* (8), 3191–3204. <https://doi.org/10.1021/jacs.0c12562>.
- (57) Cai, W.; Wang, G.-T.; Xu, Y.-X.; Jiang, X.-K.; Li, Z.-T. Vesicles and Organogels from Foldamers: A Solvent-Modulated Self-Assembling Process. *J. Am. Chem. Soc.* **2008**, *130* (22), 6936–6937. <https://doi.org/10.1021/ja801618p>.
- (58) Sawato, T.; Arisawa, M.; Yamaguchi, M. Reversible Formation of Self-Assembly Gels Containing Giant Vesicles in Trifluoromethylbenzene Using Oxymethylenehelicene Oligomers with Terminal C16 Alkyl Groups. *Bull. Chem. Soc. Jpn.* **2020**, *93* (12), 1497–1503. <https://doi.org/10.1246/bcsj.20200164>.
- (59) Yan, T.; Li, F.; Tian, J.; Wang, L.; Luo, Q.; Hou, C.; Dong, Z.; Xu, J.; Liu, J. Biomimetic Pulsating Vesicles with Both PH-Tunable Membrane Permeability and Light-Triggered Disassembly–Re-Assembly Behaviors Prepared by Supra-Amphiphilic Helices. *ACS Appl. Mater. Interfaces* **2019**, *11* (34), 30566–30574. <https://doi.org/10.1021/acsami.9b09632>.
- (60) Chen, Y.; Zhao, Z.; Bian, Z.; Jin, R.; Kang, C.; Qiu, X.; Guo, H.; Du, Z.; Gao, L. Hexagonal Lyotropic Liquid Crystal from Simple “Abiotic” Foldamers. *ChemistryOpen* **2016**, *5* (4), 386–394. <https://doi.org/https://doi.org/10.1002/open.201600007>.
- (61) He, Y.; Xu, M.; Gao, R.; Li, X.; Li, F.; Wu, X.; Xu, D.; Zeng, H.; Yuan, L. Two-Component Supramolecular Gels Derived from Amphiphilic Shape-Persistent Cyclo[6]Aramids for Specific Recognition of Native Arginine. *Angew. Chem. Int. Ed. Engl.* **2014**, *53* (44), 11834–11839. <https://doi.org/10.1002/anie.201407092>.
- (62) Gan, Q.; Wang, Y.; Jiang, H. Twisted Helical Microfibers by Hierarchical Self-Assembly of an Aromatic Oligoamide Foldamer. *Chin. J. Chem.* **2013**, *31* (5), 651–656. <https://doi.org/https://doi.org/10.1002/cjoc.201300240>.
- (63) Yang, Y.; Feng, W.; Hu, J.; Zou, S.; Gao, R.; Yamato, K.; Kline, M.; Cai, Z.; Gao, Y.; Wang, Y.; Li, Y.; Yang, Y.; Yuan, L.; Zeng, X. C.; Gong, B. Strong Aggregation and Directional Assembly of Aromatic Oligoamide Macrocycles. *J. Am. Chem. Soc.* **2011**, *133* (46), 18590–18593. <https://doi.org/10.1021/ja208548b>.
- (64) Cuccia, L. A.; Ruiz, E.; Lehn, J.-M.; Homo, J.-C.; Schmutz, M. Helical Self-Organization and Hierarchical Self-Assembly of an Oligoheterocyclic Pyridine–Pyridazine Strand into Extended Supramolecular Fibers. *Chem. – Eur. J.* **2002**, *8* (15), 3448–3457. [https://doi.org/https://doi.org/10.1002/1521-3765\(20020802\)8:15<3448::AID-CHEM3448>3.0.CO;2-#](https://doi.org/https://doi.org/10.1002/1521-3765(20020802)8:15<3448::AID-CHEM3448>3.0.CO;2-#).
- (65) Zhou, C.; Cai, W.; Wang, G.-T.; Zhao, X.; Li, Z.-T. Hydrogen-Bonded Shape-Persistent Aryl Hydrazide Polymers: Side-Chain-Tuned Formation of Vesicles and Organogels. *Macromol. Chem. Phys.* **2010**, *211* (19), 2090–2101. <https://doi.org/https://doi.org/10.1002/macp.201000259>.
- (66) Piazzolla, F.; Mercier, V.; Assies, L.; Sakai, N.; Roux, A.; Matile, S. Fluorescent Membrane Tension Probes for Early Endosomes. *Angew. Chem. Int. Ed. Engl.* **2021**, *60* (22), 12258–12263. <https://doi.org/10.1002/anie.202016105>.
- (67) Colom, A.; Derivery, E.; Soleimanpour, S.; Tomba, C.; Molin, M. D.; Sakai, N.; González-Gaitán, M.; Matile, S.; Roux, A. A Fluorescent Membrane Tension Probe. *Nat. Chem.* **2018**, *10* (11), 1118–1125. <https://doi.org/10.1038/s41557-018-0127-3>.

## 3.6

### SUPPORTING INFORMATION

for

# Molecular sensing and manipulation of protein oligomerization in membrane nanotubes with bolaamphiphilic foldamers

Kathrin Aftahy,<sup>a,‡</sup> Pedro Arrasate,<sup>b,c,‡</sup> Pavel V. Bashkirov,<sup>d,‡</sup> Petr I. Kuzmin,<sup>e</sup> Victor Maurizot,<sup>f</sup> Ivan Huc,<sup>a,\*</sup> Vadim A. Frolov<sup>b,c,g,\*</sup>

<sup>a</sup> Department of Pharmacy, Ludwig-Maximilians-Universität, Munich, 81377, Germany

<sup>b</sup> Biofisika Institute (CSIC, UPV/EHU), University of the Basque Country, Leioa, 48940, Spain

<sup>c</sup> Department of Biochemistry and Molecular Biology, University of the Basque Country, Leioa, 48940, Spain

<sup>d</sup> Research Institute for Systems Biology and Medicine, Moscow, 117246, Russia

<sup>e</sup> A.N. Frumkin Institute of Physical Chemistry and Electrochemistry, Moscow, 119071, Russia.

<sup>f</sup> Univ. Bordeaux, CNRS, Bordeaux Institut National Polytechnique, CBMN (UMR 5248), Pessac, 33600, France

<sup>g</sup> Ikerbasque, Basque Foundation for Science, Bilbao, 48009, Spain

## 1. ABBREVIATIONS

Boc<sub>2</sub>O: di-*tert*-butyl dicarbonate.

DCM: dichloromethane.

DIAD: diisopropyl azodicarboxylate.

DIEA: *N,N*-diisopropylethylamine.

DMF: *N,N*-dimethylformamide.

DTT: dithiothreitol

EDTA: Ethylenediaminetetraacetic acid.

ESI: electrospray ionization.

EtOAc: ethyl acetate.

HCl: hydrogen chloride.

HRMS: high-resolution mass spectrometry.

*i*PrOH: 2-propanol.

MeOH: methanol.

NMR: nuclear magnetic resonance.

PFP: pentafluorophenol.

PyBOP: benzotriazol-1-yl-oxytripyrrolidinophosphonium hexafluorophosphate.

1,1,2,2-TCE-*d*<sub>2</sub>: 1,1,2,2-tetrachloroethane-*d*<sub>2</sub>.

TFA: trifluoro acetic acid.

THF: tetrahydrofuran.

TLC: thin layer chromatography.

Trt: trityl.

## 2. SUPPLEMENTARY TABLE AND FIGURES

**Table S1.** Lipid-dependence of ROFT incorporation into GSB.

ROFT compound #	LIPID COMPOSITION						
	PC		PC:PE (7:3)		DOTA P	SM	PC:poly-PE (7:3)*
	<input type="checkbox"/> 20mol 1%ROFT	>20mol % ROFT	<input type="checkbox"/> 20mol 1% ROFT	>20mol % ROFT	up to 45mol% ROFT		
<b>1</b>	Yes	No	Yes	Yes	Yes	Yes	Yes
<b>2</b>	Yes	No	-	-	Yes	Yes	-
<b>3</b>	No	No	-	-	No	Yes	-
<b>4</b>	Yes	No	Yes	Yes	Yes	-	Yes

\*addition of >10mol% of cholesterol to all lipid mixtures but PC:polyPE inhibited the GSB formation and completely suppressed incorporation of all ROFT compounds into GSBs. Up to 30mol% Chol could be added to PC:polyPE mixture (substituting PC for Chol).

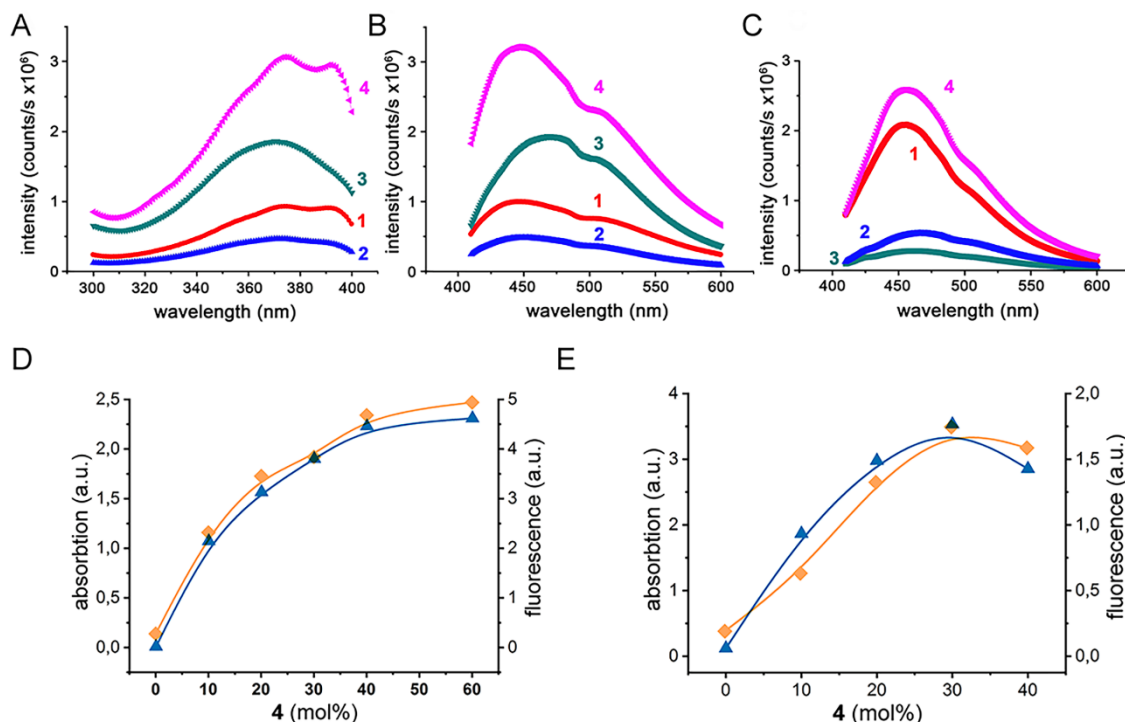


**Figure S1.** Incorporation of ROFTs into multilamellar lipid vesicles (MLVs). (A-C) The excitation (A) and emission (B, C) spectra of the indicated ROFT compounds in chloroform (A, B) and in PC/PE MLVs (C). The excitation spectra were collected at 450 nm emission, the emission spectra were collected with 370 nm excitation. (D-E) The light absorption (apricot) and fluorescence of DOTAP (D) and PC/PE (E) MLVs containing different amounts of **4**. The absorption was measured at 370 nm, the fluorescence was calculated as the total area under the emission curve (C).

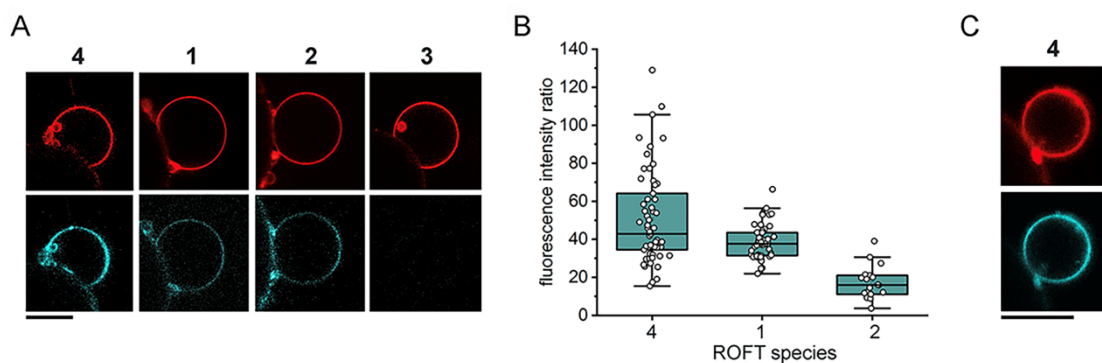


**Figure S2.** The incorporation of ROFT into GSBs. (A). The fluorescence microscopy images of DOTAP:Rh-PE-ROFT 79:1:20 mol/mol GSBs containing indicated ROFT species, the ROFT ( $F_{\text{ROFT}}$ , blue) and Rh-PE ( $F_{\text{lipid}}$ , red) fluorescence is shown. (B). The membrane incorporation efficiency, calculated as the fluorescence intensity ratio  $F_{\text{ROFT}}/F_{\text{lipid}}$  for different ROFT species. (C) An example of a GSB made of 99:1 mol/mol mixture of **4** and Rh-PE mol% following the detergent removal procedure (see Material and Methods). Scale bars 10  $\mu\text{m}$ .

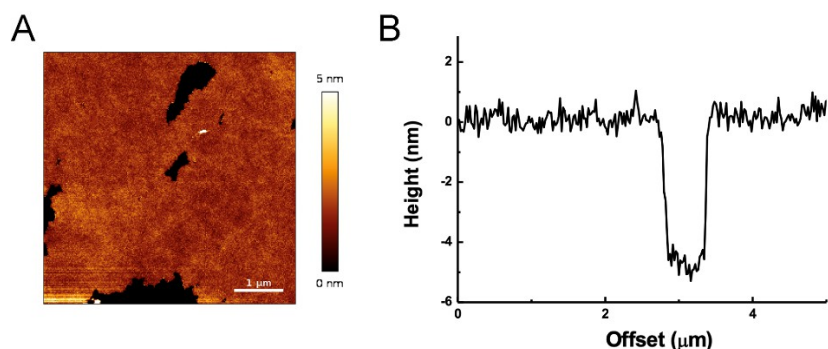


**Figure S3.** Atomic Force Microscopy imaging of ROFT-containing supported membranes. **A.** An AFM image of a glass-supported membrane patch produced by crushing a GSB containing 30 mol% of **4** against a pretreated glass coverslip. **B.** A linear height scan across a pore in the supported membrane demonstrating the membrane height typical for pure lipid bilayer patches.

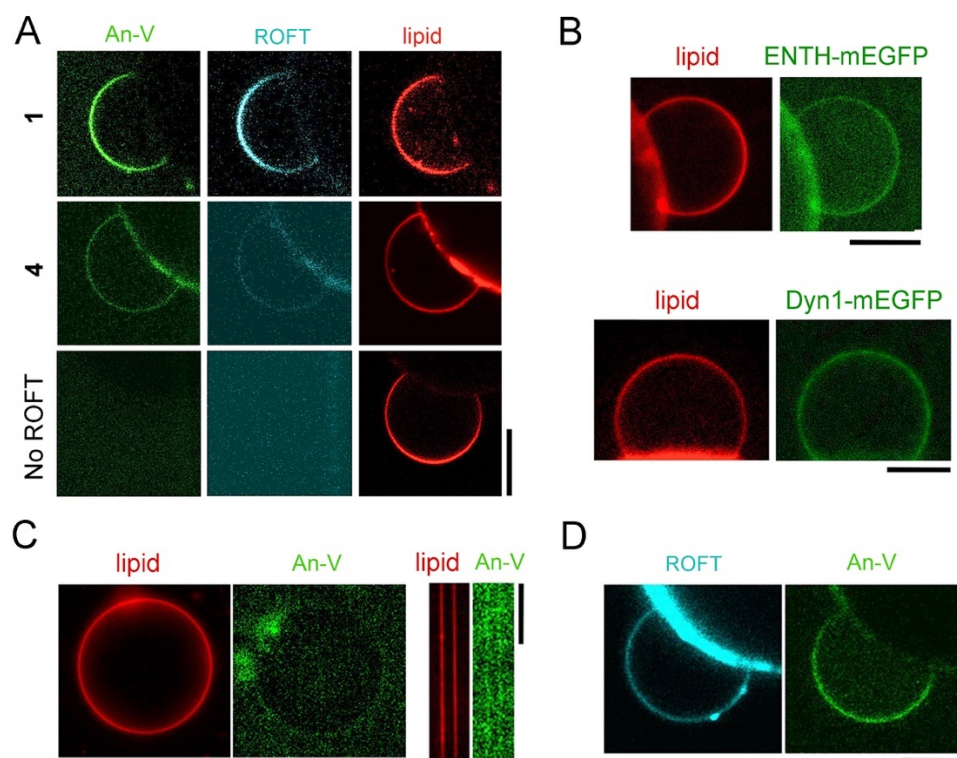


**Figure S4.** Protein binding to PC/PE and pure PC GSBs, GUVs and NTs containing **1** and **4**. (A). Representative fluorescence micrographs showing AnV-Alexa488 (2 $\mu$ M in the bulk) binding to GSBs containing ROFTs in the presence of Ca<sup>++</sup>. The lipid (red), ROFT (blue) and Alexa488 (green) fluorescence channels are shown, scale bar 10  $\mu$ m. (B,C). Dyn1-mEGFP (left) and ENTH-mEGFP (right) binding to PC/PE GSBs containing **4**, scale bars 10  $\mu$ m. (C). AnV remains on both GUVs (left) and NTs (right) after Ca<sup>++</sup> chelating by EDTA (5 mM, 30 min). Scale bars 5 $\mu$ m (D) AnV remains on GSBs containing **4** after Ca<sup>++</sup> chelating by EDTA (5 mM, 30 min). Scale bar 10  $\mu$ m.

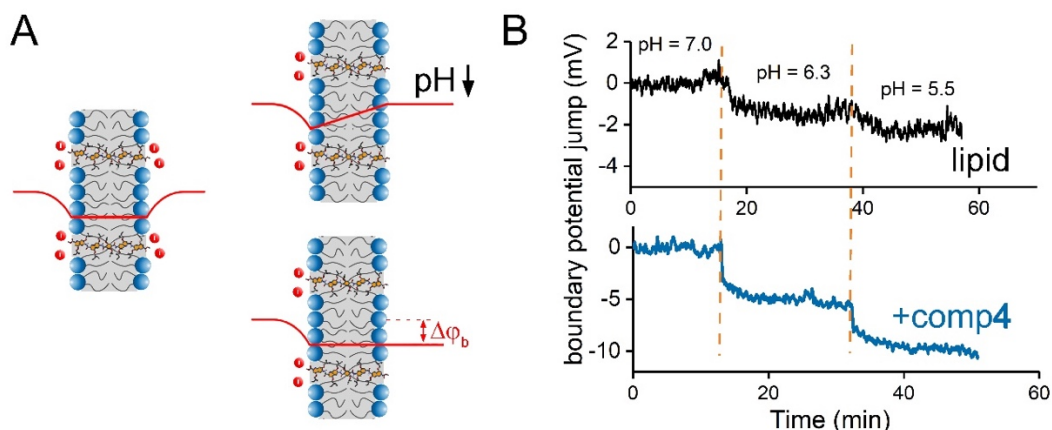


**Figure S5.** Measurements of the boundary potential of a planar lipid (PC/PE) membrane containing 20 mol% of **4**. (A). Schematic figure demonstrating the measurement of the potential compensating the membrane boundary potential jump  $\Delta\phi_b$ , which appears upon the pH increase on one side of the membrane. (B). Dynamics of the pH-dependent boundary potential changes in the control membrane (black) and the membrane containing **4** (blue). The decrease of pH from 7 to 5 should cause almost twofold reduction of the water/hydrophobic interface charge density.<sup>1</sup> We used it to recalculate the surface charge density,  $\sigma$  from the boundary potential value change,<sup>2</sup> and found  $\sigma \approx -0.15 \frac{e}{\text{nm}^2}$  for the membrane containing 10 mol% of **4**.

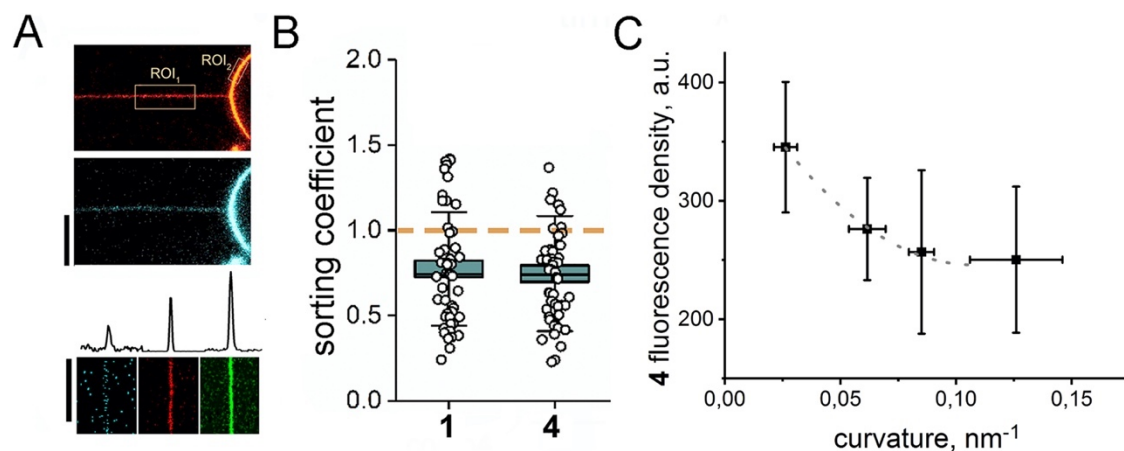


**Figure S6.** Quantification of the ROFTs distribution between GSB and NT. (A) The upper panel shown a typical selection of the regions of interest (ROIs) for calculation of the fluorescence intensities of fluorophores in the NT (ROI<sub>1</sub>) and GSB (ROI<sub>2</sub>) membranes. The average intensity values were obtained using 2 independent  $10 \times 3 \mu\text{m}$  ROI<sub>1</sub> on the NT, near and far from the GSB, and 2 independent  $5 \times 2 \mu\text{m}$  ROI<sub>2</sub> on the GSB placed a few microns from the NT. The lower panel shows a representative example of the fluorescence intensity profiles (black peaks) obtained from ROI<sub>1</sub>. The fluorescence intensity was integrated over the profiles. AnV-Alexa488 (green), Rh-DOPE (red) and **4** (blue) fluorescence signals are shown. Scale bars  $5 \mu\text{m}$ . (B) Both **1** and **4** are expelled from NT, measured as sorting coefficient  $q < 1$ . (C) The dependence of the fluorescence density ( $F_{\text{ROFT}}$ , Fig. 2), proportional to the ROFT concentration in the NT ( $\phi_{\text{NT}}$ ) on the sNT curvature ( $1/r_s$ ). The dash line shows the 2<sup>nd</sup> order polynomial fit, following Eq.1 rewritten at  $J_s = 0$  as  $\phi_{\text{NT}} = \phi_0(1 - \beta/r_s^2)$ .

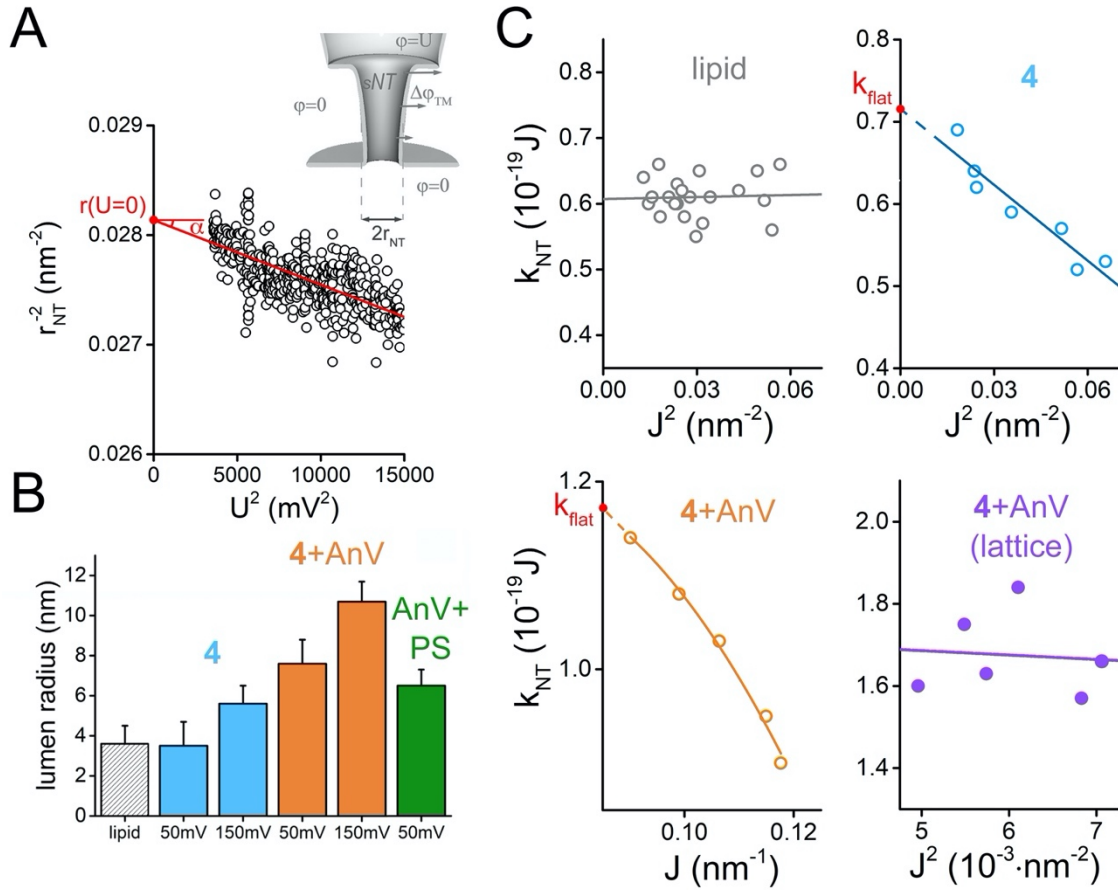


**Figure S7.** Measurements of  $k_{NT}$ . (A). The cartoon shows the sNT expansion by trans-membrane electric field ( $\Delta\varphi_{TM}$ ) coupled with the voltage bias (from  $\varphi = 0$  to  $\varphi = U$ ) driving the ionic current through the sNT lumen. The corresponding increase of the ionic current through the sNT was used to calculate the  $r_s^{-2}(U^2)$  dependence. The dependence was subsequently fitted by  $r_s^{-2}(U^2) = \frac{2\sigma}{k_{NT}} - \frac{cU^2}{3k_{NT}}$ , with  $k_{NT}$  and the sNT radius determined from the linear regression (see Methods for details).<sup>3</sup> The dependence obtained from an sNT pulled from the reservoir membrane containing 10 mol% of **4** by applying a voltage ramp is shown. (B) The sNT radii at  $U = 0$  measured for the reference pure lipid sNT (PC/PE, grey), upon addition of **4** (blue, measured at different holding potentials at the conductance plateau, see Fig. 4B), **4**+AnV (apricot, measured at different holding potentials at the conductance plateau, see Fig. 4B) and PS and AnV (green). (C) The dependences of  $k_{NT}$  on the sNT curvature ( $J = 1/r_s$ ) measured for the pure lipid (PC/PE) sNT (grey), the sNT containing 10mol% of **4** (blue), the **4**-sNT with bound AnV measured at low  $U$  (orange) and upon prolonged application of  $+U$  triggering appearance of stable AnV lattice on the sNT membrane (magenta, corresponding to the stage indicated by  $U^*$  in Fig. 4B). The solid lines are fits, with linear regression ( $k_{NT} = k_{flat}(1 - \epsilon J^2)$ ) used in all cases (the slope is not significantly different from 0 (at  $p = 0.05$ ) for pure lipid NT (grey), the slope is significantly different from 0 (at  $p = 0.05$ ) in the presence of **4** (blue)) but with comp**4**+AnV (where, following Eq. 3,  $k_{NT} = k_{flat} \left(1 - \epsilon J^2 \left(1 - \frac{2J_s}{3J}\right)\right)$  with  $J_s = 0.05 \text{ nm}^{-1}$  was used), the fits confirm the linear dependence of  $k_{NT}$  on  $J^2$  in the presence of **4** ( $R^2 > 0.88$ , blue), and the dependence becomes parabolic in the presence of AnV ( $R^2 > 0.99$ , orange). For **4**  $k_{flat} = (0.72 \pm 0.02) \cdot 10^{-19} \text{ J}$  was obtained while for **4**+AnV  $k_{flat} = (1.1 \pm 0.05) \cdot 10^{-19} \text{ J}$  was obtained (similar to the  $k_{flat}$  value obtained from the conductance decrease shown in Fig. 3C).

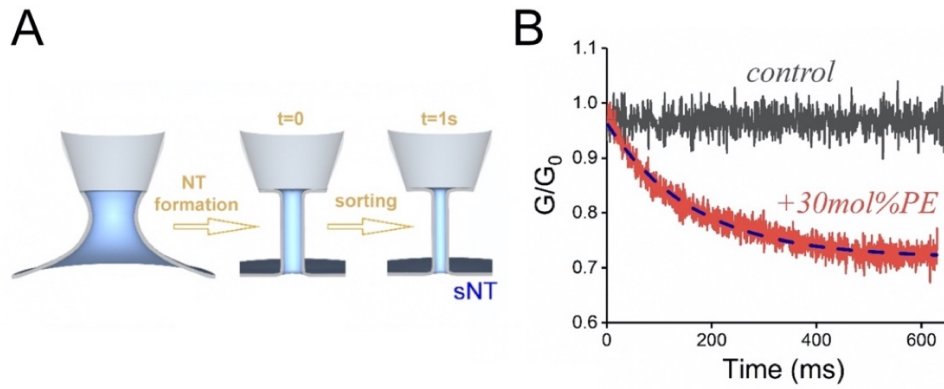


**Figure S8.** Detection of the adjustment of the sNT composition via molecular exchange with the reservoir membrane. (A) The cartoon shows an instantaneous sNT formation from a microscopic catenoidal membrane tube followed by the constriction due to the PE distribution.<sup>4-6</sup> (B) The time dependence of the sNT conductance ( $G_{NT}$ , normalized to the initial conductance  $G_0$ ) recorded immediately after the sNT formation upon the sNT formation from the reservoir membrane composed of cylindrical lipids having zero spontaneous curvature (control, dark grey) and from the membrane containing 30mol% of PE (red), which has high negative spontaneous curvature.<sup>4,6</sup> Curvature-driven redistribution of PE between highly curved NT monolayers and flat reservoir membrane results in slow-kinetic decrease of NT lumen ionic conductance  $G$  displaying relaxation of apparent bending rigidity of NT membrane. Gradual relaxation of  $\frac{G}{G_0} = \frac{k}{k_{flat}}$  was approximated by an exponent function  $\frac{k}{k_{flat}} = \frac{k_{NT}}{k_{flat}} + \frac{k_{flat} - k_{NT}}{k_{flat}} \exp\left(-\frac{t}{\tau}\right)$  (deep blue dashed curve) used to figure out  $k_{flat}$ .

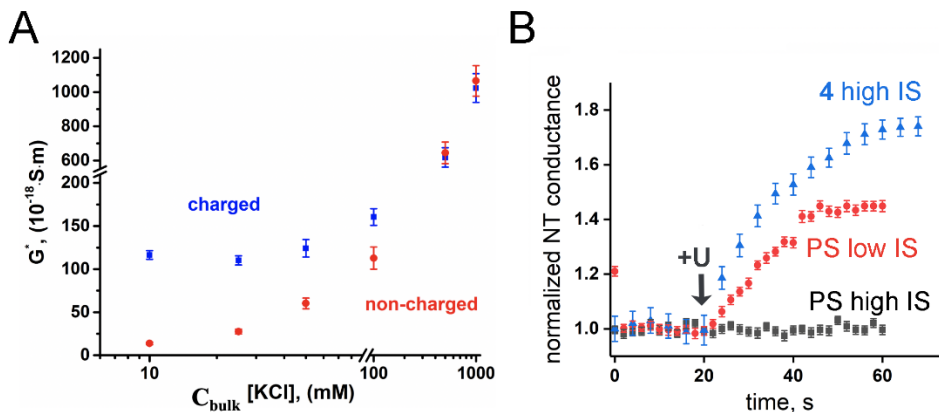


**Figure S9.** The contribution of the inner lipid monolayer charge to the sNT luminal conductance  $G_{NT}$ . (A) Dependence of sNT conductance per unit length,  $G^* = G_{NT}L_{NT}$  on the ion strength (IS) measured for membrane sNT composed of electrically neutral lipids (red) and containing 20 mol% of negatively charged PS lipids (blue). At low IS ( $[KCl] \leq 100$  mM), the contribution of ions of the screening layer to the total conductivity becomes significant for NTs with a lumen radius of about 5 nm.<sup>7</sup> (B) The sNT conductance changes due to voltage-driven incorporation of **4** (red) and PS (grey) measured at different IS.

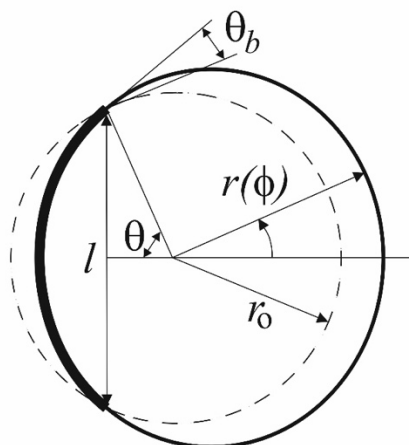


**Figure S10.** Schematic of the local sNT deformation produced by a curved rigid inclusion. The sNT cross-section is shown, the thick black arc shows the inclusion of a characteristic linear size  $l$  and spontaneous curvature  $J_s$ . The thin black contour line defined by radius vector  $r(\phi)$  shows the lipid membrane part. The dashed line shows a circular cross-section of a stationary cylindrical sNT with the luminal radius  $r_s$ ;  $\theta$  is the angular size of the inclusion from the center of the reference sNT contour and  $\theta_b$  is the boundary angle set on the inclusion ends.

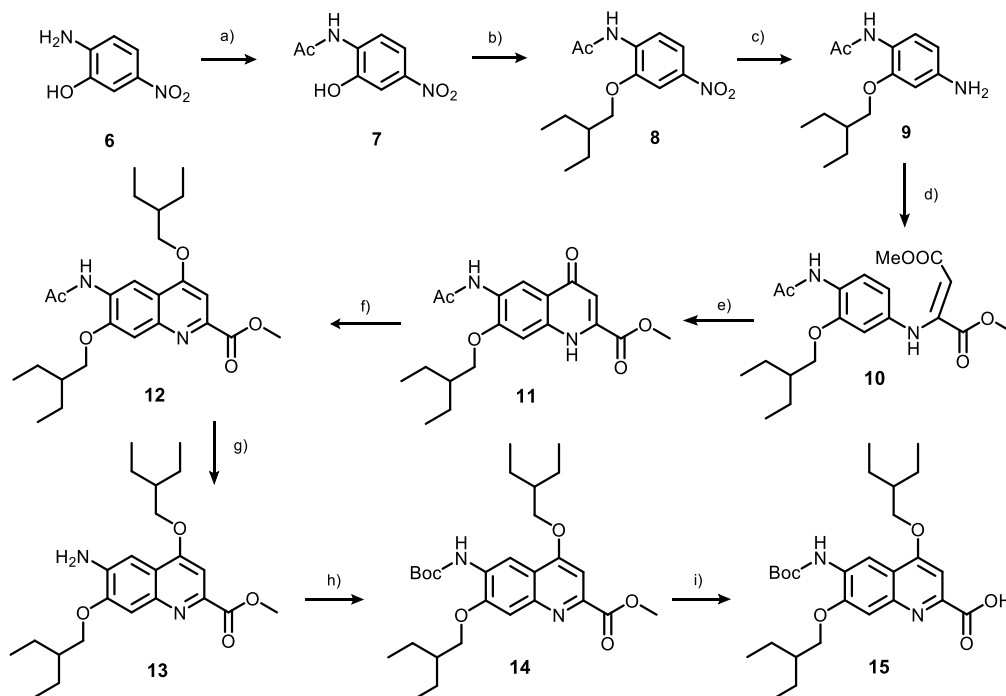


**Figure S11.** Synthetic pathway to 7-14. Reagents and conditions: (a)  $\text{Ac}_2\text{O}$  (b) DIAD,  $\text{PPh}_3$ , 2-ethyl-1-butanol, THF; (c)  $\text{H}_2$ , Pd/C, THF, (d) DMAD, MeOH, (e)  $\text{Ph}_2\text{O}$ , 260 °C, 10 min; (f) DIAD,  $\text{PPh}_3$ , 2-ethyl-1-butanol, THF; (g)  $\text{H}_2\text{SO}_4$ , MeOH; (h)  $\text{Boc}_2\text{O}$ , DIEA, DCM; (i) NaOH, 1,4-Dioxane

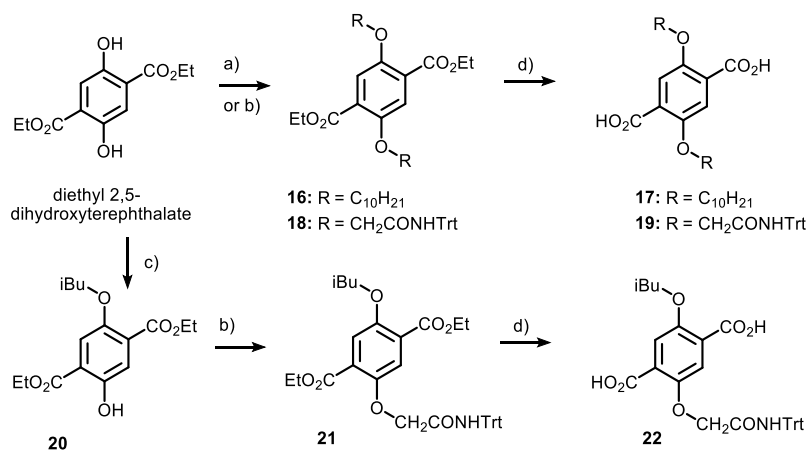


**Figure S12.** Synthetic pathway of **17**, **19**, and **22**. Reagents and conditions: (a) DIAD, PPh<sub>3</sub>, THF, 1-decanol; (b) 2-bromo-*N*-tritylacetylamine, K<sub>2</sub>CO<sub>3</sub> acetone, 60 °C; (c) DIAD, PPh<sub>3</sub>, THF, *i*BuOH; (d) KOH, 1,4-dioxane.

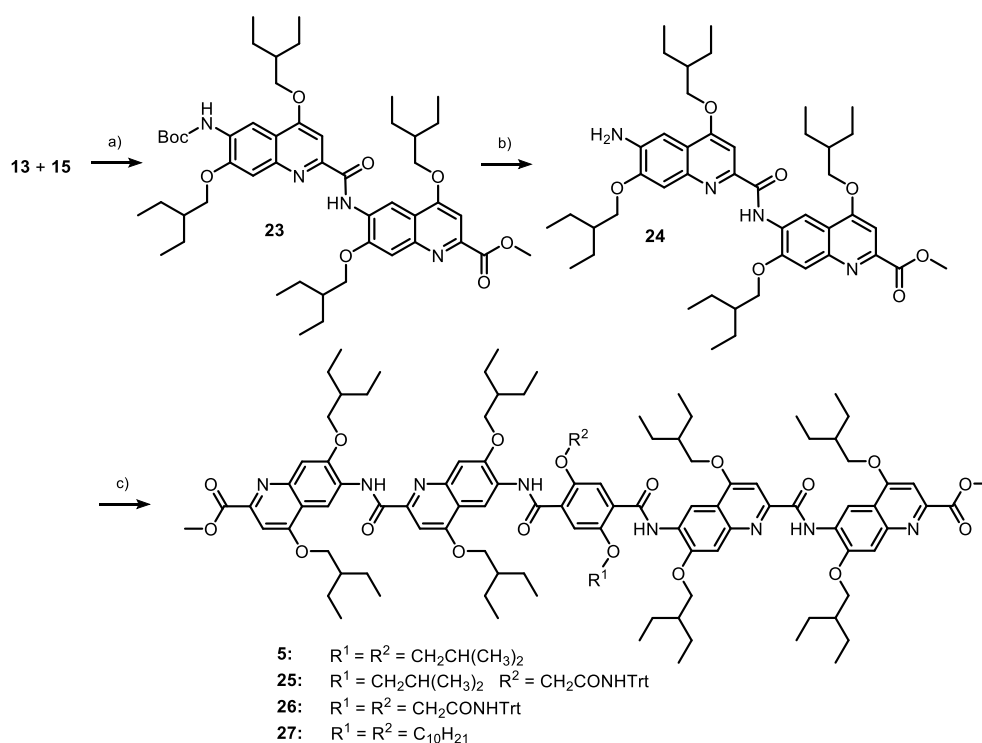


**Figure S13.** Synthetic pathway to **5**, **25**, **26** and **27**. Reagents and conditions: (a) **15**, **13**, PyBOP, DIEA, CHCl<sub>3</sub>; (b) TFA, DCM; (c) **5**: 2,5-diisobutoxyterephthalic acid activated with (COCl)<sub>2</sub>, DIEA, DCM; **25**: **22** activated with 1-chloro-*N,N*,-2-trimethyl-1-propenylamine, DIEA, DCM; **26**: **19** activated with 1-chloro-*N,N*,-2-trimethyl-1-propenylamine, DIEA, DCM; **27**: **17** activated with (COCl)<sub>2</sub>, DIEA, DCM.

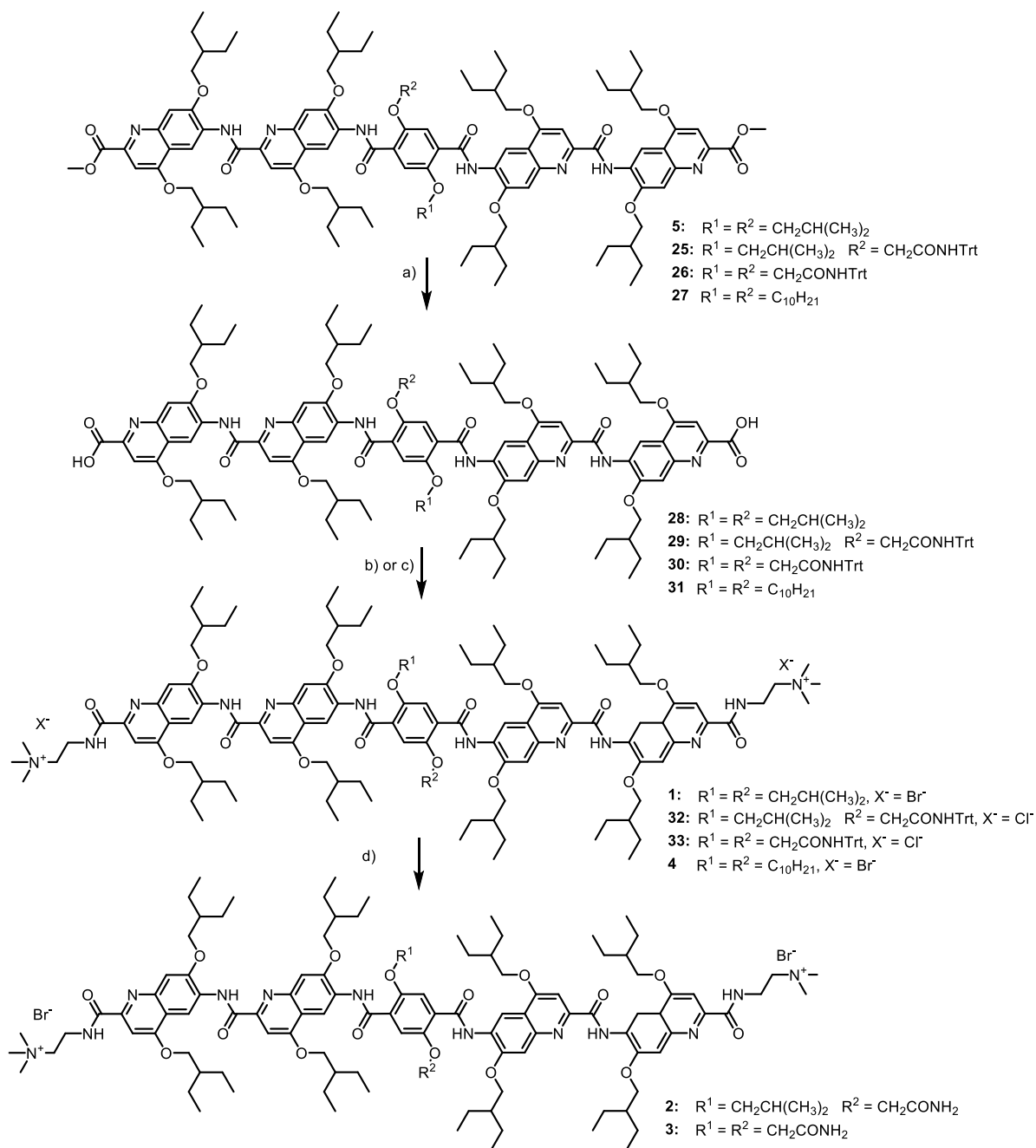


**Figure S14.** Synthetic pathway to **1-4**. Reagents and conditions: (a) NaOH, 1,4-Dioxane (b) for **28**, **29** and **30**: PFP, EDT, rt, followed by 2-Aminoethyltrimethylammoniumchloride, DIEA, THF, 40 °C, followed by RP HPLC purification and ion-exchange chromatography for **1** and **4**; (c) for **31**: 2-aminoethyl-trimethylammonium chloride, PyBOP, DIEA, DCM; (d) TFA/DCM (1:1 vol/vol), TIS, rt, followed by ion-exchange chromatography.

### 3.6.3. Theoretical Models

3.6.3.1 We considered individual ROFTs, AnV oligomers and ROFT-AnV quasi-particles as rigid membrane inclusions incorporated in the lipid bilayer at low surface density  $\varphi$ . The inclusions induce spontaneous membrane curvature  $J_s$ .<sup>6,8,9</sup> We consider the membrane area occupied by the inclusions “unbendable” so that the bending rigidity modulus of the inclusion-containing reference bilayer,  $k$ , could be determined from the relationship  $k = \frac{k_l}{1-\varphi}$  where  $k_l$  bending modulus character for pure lipid bilayer. Neglecting the deviatropic part, the free energy density,  $w$  of an inclusion-containing NT connected to a planar membrane reservoir is:

$$(S1) \quad w = 2\pi r \left( \sigma + \frac{k_l}{1-\varphi} \frac{1}{r^2} - \frac{k_l}{1-\varphi} \frac{\varphi J_s}{r} + \frac{k_B T}{a} \left[ \varphi \ln \frac{\varphi}{\varphi_0} + (1-\varphi_0) \ln \frac{1-\varphi}{1-\varphi_0} \right] \right)$$

where  $r$  is the NT radius,  $\sigma$  is the lateral tension of the reservoir membrane,  $a$  is the membrane area occupied by a single inclusion,  $\varphi_0$  is the area fraction occupied by the inclusions in the reservoir and  $J_s$  is the spontaneous curvature of the inclusions defined at  $\varphi_0 = 1$  (note that  $k(\varphi_0) = \frac{k_l}{1-\varphi_0} = k_{flat}$ ). Expansion and minimization of Eq.S1 over  $\varphi$  (assuming  $\varphi - \varphi_0 < \varphi_0$ ,  $\varphi_0 \ll 1$ ) yielded:

$$(S2) \quad \varphi(r) = q(r)\varphi_0 \approx \left( 1 - \frac{k_{flat} a}{2k_B T} \frac{1}{r} \left( \frac{1}{r} - 2J_s \right) \right) \varphi_0$$

where  $q(r) = \varphi(r)/\varphi_0$  is the sorting coefficient measuring the difference of the inclusion concentrations (surface coverage) in the reservoir and NT membranes. Note that Eq.S2 is essentially Eq.1 of the main text. Substituting Eq. S2 into S1 and minimizing over  $r$  we obtained the stationary radius  $r_s$ :

$$(S3) \quad r_s^2 \approx r_0^2 \left( 1 + \frac{3\varphi_0}{2} (q(r_0) - 1) \left( 1 - \frac{2}{3} r_0 J_s \right) \right),$$

where  $r_0^2 = \frac{k_{flat}}{2\sigma}$ . Assuming  $r_s^2 = \frac{k_{NT}}{2\sigma}$ ,<sup>4,6</sup> we found the relationship between the apparent bending rigidity of the NT membrane,  $k_{NT}$ , and  $k_{flat}$ :

$$(S4) \quad k_{NT} \approx k_{flat} \left( 1 + \frac{3\varphi_0}{2} (q(r_0) - 1) \left( 1 - \frac{2}{3} r_0 J_s \right) \right).$$

Note, that from Eqs. S2 and S4 we obtain  $k_{NT} = k_{flat} \left( 1 - \frac{\alpha \varphi_0 (1 - \varphi_0) k_{flat}^3 \left( \frac{\Delta k}{k_{ROFT} k_l} \right)^2}{4 k_{BT}} j^2 \right) =$

$k_{flat} (1 - \varepsilon j^2)$ , that it, Eq.(2) of the main text.

For  $\varphi_0 \ll 1$ ,  $r_0$  could be substituted by  $r_s$  in Eq.S4 yielding Eq.3 in the main text. Eq.S4 can be rewritten to relate the effective softening of the NT membrane due to the expulsion of rigid inclusions ( $\Delta k = k_{flat} - k_{NT}$ , see Figure 3D, S8) to the sorting coefficient  $q$ :

$$(S5) \quad q = 1 - \frac{2}{3} \frac{\Delta k}{k_{flat}} \frac{(1 - \varphi_0)}{\varphi_0}$$

**3.2 Estimation of the geometry and elastic energy of the local sNT deformation produced by a single rigid inclusion.**

We used a simple 1D approximation of the sNT deformation depicted in Fig. S10, where the inclusion is considered as a curved rigid arc of a small angular size, the arc curvature  $J_s$  defining the membrane radial curvature at the arc ends. The membrane shape is parameterized by the contour radius  $r(\alpha)$ :

$$(S6) \quad r(\alpha) = r_s (1 + u(\alpha))$$

where  $u(\alpha)$  measures the small deviation of the contour from the reference cylinder of the radius  $r_s$  (Fig. S10). The membrane shape is found by minimizing the contour energy:

$$(S7) \quad w_{NT} = \int \left( \frac{1}{2} k_{NT} \frac{1}{(r(\alpha))^2} + \sigma \right) dA,$$

In the small deformation limit ( $u \ll 1$ ), we obtained the Euler-Lagrange equation:

$$(S8) \quad \frac{d^4 u}{d\alpha^4} + 2 \frac{d^2 u}{d\alpha^2} + u = 0$$

by solving which  $u(\alpha)$  could be found. To set boundary conditions, we placed the inclusion center at  $\alpha = 0$  and considered  $u(\theta) = u(-\theta) = 0$ , where  $\theta = \frac{l}{2r_0}$  is the angular size of the inclusion (Fig. S10). We further assumed that the inclusion set the membrane curvature at its ends as:

$$(S9) \quad \theta_b = \frac{du}{d\alpha} \Big|_{\alpha=\theta} = -\frac{du}{d\alpha} \Big|_{\alpha=-\theta} = \frac{1}{2} l \left( \frac{1}{r_s} - J_s \right)$$

Using Eqs. S8 and S9, we estimated the change of the sNT luminal volume caused by the inclusion as:

$$(S10) \quad \Delta v = \frac{1}{2} l \int_{-\pi}^{\pi} r(\alpha)^2 d\alpha - l\pi r_s^2$$

For  $l \ll 2r_s$

$$(S11) \quad \Delta v = 2lr_s^2 \left(1 + \frac{l}{\pi r_s}\right) \theta_b \approx l^2 r_s^2 \left(\frac{1}{r_s} - J_s\right)$$

For estimation of the area ( $a$ ) of a flat and rigid AnV monomer, we used the simplified form of Eq.S11  $\Delta v = ar_s$ , where  $a=l^2$  and  $J_s=0$ . The area was calculated as  $a = \frac{r_s}{\Delta v}$  where  $\Delta v$  and  $r_s$  were determined experimentally as described below (see 5.6).

Using Eq.S7 we found the change of the sNT elastic energy due to the inclusion incorporation as:

$$(S12) \quad \Delta w_{NT} \approx k_{NT} \frac{l^2}{r_s} \left(\frac{1}{r_s} - 2J_s\right)$$

Eq.S12 was used to estimate the energy barrier for the AnV entry into the sNT. For flat AnV oligomers of the area  $a$  Eq.S12 was reduced to

$$(S12a) \quad \Delta w_{NT} = k_{NT} \frac{a}{r_s^2},$$

yielding  $\Delta w_{NT} = 5k_B T$  for the AnV monomer.

To account for the hydrophobic interaction of AnV with the lipid bilayer core, we assumed that the corresponding interaction energy  $\Delta w_h$  is proportional to the density of hydrophobic defects on the membrane surface proportional to the membrane curvature.<sup>10</sup> In the linear approximation,  $\Delta w_h \sim \frac{\gamma}{r_s}$ , where  $\gamma$  is phenomenological parameter. Using this approximation, we rewrote Eq. S12a as:

$$(S13) \quad \Delta W = \Delta w_{NT} + \Delta w_{protein} = k_{NT} \frac{l^2}{r_s^2} - \frac{\gamma l^2}{r_s} = k_{NT} \frac{l^2}{r_s} \left(\frac{1}{r_s} - \frac{\gamma}{k_{NT}}\right)$$

We note that the resulting energy correction is formally equivalent to positive  $J_s$  (compare Eq. S.12 and S.13), in agreement with the experiments. With  $\frac{\gamma}{k_{NT}} \approx 0.05 \text{ nm}^{-1}$  (corresponding to the lower curvature limit of the NTs pulled from GSB, Fig. S4C), the curvature barrier for AnV entry into sNT is reduced to  $\sim 2 \text{ k}_B T$ .

### 3.3 Estimation of the sNT and reservoir membrane coverage by rigid inclusions.

For NTs pulled from ROFT-containing membranes we obtained  $k_{flat} = 0.75 \cdot 10^{-19}J$ . Taking into consideration that measured for ROFT free NT  $k_l = 0.63 \cdot 10^{-19}J$ , we could estimate the area fraction occupied by ROFT in the flat reservoir membrane as  $\varphi_0 = 1 - \frac{k_l}{k_{flat}} = 0.16 \pm 0.05$  (SD, n=5), that was very close to expected value according to ROFT to lipid 1:9 molar mixture. Normal orientation of ROFT should lead to  $\varphi_0 = 0.18$ . For extremely narrow NTs ( $r_s \approx 2 - 3 \text{ nm}$ )  $\Delta k = 0.25 \cdot 10^{-19}J$  so sorting coefficient calculated by Eq. S5,  $q \approx 0$ , indicating that almost all ROFT molecules squeezed out of NT. For wider NTs ( $r_s \approx 4 - 5 \text{ nm}$ )  $\Delta k = 0.15$  and  $q = 0.4$  thus the average area fraction of ROFT in NT membrane was  $\varphi_{NT} = 0.04 \pm 0.06$  (SD n=5). The same calculations made for AnV revealed  $\varphi_0 = 0.34 \pm 0.05$  (SD n=6) and  $\varphi_{NT} = 0.28 \pm 0.07$  (SD n=6) for PS containing membranes; and  $\varphi_0 = 0.38 \pm 0.05$  (SD n=5) and  $\varphi_{NT} = 0.29 \pm 0.06$  (SD n=5) for **4** containing membranes. After AnV polymerization its area fraction on NT membrane increased to  $\varphi_{NT}^* = 0.46 \pm 0.04$  (SD n=6) and  $\varphi_{NT}^* = 0.50 \pm 0.04$  (SD n=5) respectively for PS and **4** containing NT. Importantly approximately the same values were obtained by extrapolation of sNT volume changes induced by single AnV molecules. Assuming the additivity and independence of sNT shape deformations locally caused by individual AnV, we estimated how many AnV molecules are additionally recruited to the membrane surface from the ratio of the total change in NT volume:

$$(S14) \quad \Delta\varphi_{NT}^* = \frac{1}{2} \left( \frac{k_{NT}^*}{k_{NT}} - 1 \right),$$

where asterisk marks conditions after polymerization.

Using Eq.S14 we found  $\Delta\varphi_{NT}^* = 0.23 \pm 0.07$  and  $\Delta\varphi_{NT}^* = 0.3 \pm 0.1$  respectively for PS and **4** containing sNTs.

## 4. METHODS FOR SYNTHESIS

### 4.1 General methods for chemical synthesis

**NMR** spectroscopic experiments were carried out on different instruments. NMR instruments of the analytical division at the Faculty for Chemistry and Pharmacy in LMU: **(1)** Avance III HD 400 MHz Bruker BioSpin (400 MHz for  $^1\text{H}$  observation) equipped with a broadband probe; **(2)** Avance III HD 500 MHz Bruker BioSpin (500 MHz for  $^1\text{H}$  observation) equipped with a CryoProbe<sup>TM</sup> Prodigy broadband probe; **(3)** VNMRS 400 Varian (400 MHz for  $^1\text{H}$  observation) equipped with a room-temperature

AutoX Dual Broadband probe; and **(4)** Avance III HD 800 MHz Bruker BioSpin (800 MHz for  $^1\text{H}$  observation) equipped with a cryogenic probe. Chemical shifts ( $\delta$ ) are reported in parts per million (ppm) relative to trimethylsilane (TMS), and coupling constants ( $J$ ) are reported in Hertz (Hz).  $^1\text{H}$  NMR splitting patterns are designated as singlet (s), broad singlet (brs), doublet (d), doublet of doublets (dd), triplet (t), quartet (q), multiplet (m) and broad multiplet (brm). Samples were not degassed.

**HRMS (ESI+)** experiments were performed at the LMU Mass Spectrometry facility, using a Thermo Finnigan LTQ FT Ultra Fourier Transform Ionen Cyclotron Resonance mass spectrometry instrument. The resolution was set to 100,000 at  $m/z$  400. Depending on the sample, mass ranges from 50 to 2000 u were measured. The spray capillary voltage at the IonMax ESI head was 4 kV, the heater capillary temperature 250 °C, the nitrogen sheath gas flow 20 and the sweep gas flow 5 units.

Moisture or oxygen sensitive experiments were performed under a nitrogen atmosphere. Solvents used for reactions involving metals such as palladium or nickel were degassed via nitrogen bubbling or freezing-defrosting cycles. All solvents were reagent grade. Commercial reagents were purchased from Sigma-Aldrich, TCI Chemicals or Alfa-Aesar and were used without further purification. Tetrahydrofuran and DCM were dried over alumina columns (MBRAUN SPS-800 solvent purification system) whereas chloroform and diisopropylethylamine were distilled over  $\text{CaH}_2$  prior to use. Reactions were monitored by TLC on Merck silica gel 60  $F_{254}$  plates and observed under UV light. Column chromatography purifications were carried out on Merck GEDURAN Si60 (40-63  $\mu\text{m}$ ).

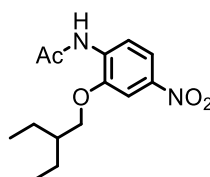
2-Amino-5-nitrophenol and diethyl 2,5-dihydroxyterephthalate were commercially available. Diethyl 2,5-diisobutoxyterephthalate and 2,5-diisobutoxyterephthalic acid were synthesized according to reported procedures,<sup>11</sup> as well as compound 7,<sup>12</sup> and 2-bromo-*N*-tritylacetamide.<sup>13</sup>

#### **Ion exchange chromatography of compounds 1-4.**

Commercially available resin Amberlite IRA 400 Cl was used packing 20 mL of cartridge and swelling the resin beads in water. The swelled resin was then flushed 3 times the column volume (CV) with 2 M HCl solution followed by neutralizing the resin with 3 times CV with pure water. Then the target solution was prepared using 2M HBr

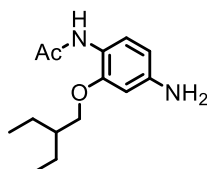
solution, the resin flushed (3x CV) followed by neutralizing the resin with water (3x CV). Afterwards pure MeOH was flushed (3x CV) and compound was loaded on the resin, dissolved in chloroform (200  $\mu$ L). At gravity flow, eluted fraction was collected and eluted with more chloroform (1.5x CV). The fractions were then evaporated to obtain compounds **1-4**.

#### 4.2. Synthetic procedures



Chemical Formula: C<sub>14</sub>H<sub>20</sub>N<sub>2</sub>O<sub>4</sub>

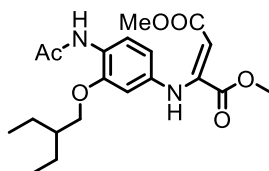
**Compound 8.** *N*-(2-hydroxy-4-nitrophenyl)acetamide **7** (19.6 g, 1.0 eq., 0.10 mol), PPh<sub>3</sub> (31.4 g, 1.2 eq., 0.12 mol) and 2-ethyl-1-butanol (14.8 mL, 1.2 eq., 0.12 mol) were suspended in 150 mL of THF. At 0 °C DIAD (24.2 mL 1.2 eq., 0.12 mol) were added dropwise over 30 min to the reaction mixture. The mixture was left stirring at room temperature during overnight. THF was then partially removed and 200 ml of MeOH was added. The solid was filtered and washed with MeOH and dried over vacuum to give 23.9 g (yield: 85.4 %) of compound **8**. <sup>1</sup>H NMR (500 MHz, chloroform-*d*)  $\delta$  8.56 (d, *J* = 9.0 Hz, 1H), 7.93 (s, 1H), 7.91 (dd, *J* = 9.0, 2.4 Hz, 1H), 7.75 (d, *J* = 2.4 Hz, 1H), 4.05 (d, *J* = 5.7 Hz, 2H), 2.25 (s, 3H), 1.80 (p, *J* = 6.2 Hz, 1H), 1.58 – 1.46 (m, 4H), 0.99 (t, *J* = 7.5 Hz, 6H). <sup>13</sup>C NMR (101 MHz, chloroform-*d*)  $\delta$  168.5, 146.8, 143.1, 134.0, 118.3, 117.7, 106.1, 71.8, 40.8, 25.2, 23.8, 11.3. HRMS (ESI-) calcd. for C<sub>14</sub>H<sub>19</sub>N<sub>2</sub>O<sub>4</sub> [M-H]<sup>-</sup> (m/z): 279.1320, found: 279.13519.



Chemical Formula: C<sub>14</sub>H<sub>22</sub>N<sub>2</sub>O<sub>2</sub>

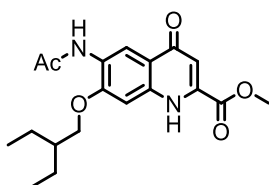
**Compound 9.** Compound **8** (23.9 g, 1.0 eq., 0.09 mol) was dissolved in a mixture of 200 mL of THF and 200 mL of MeOH. 2.4 g of Pd/C (10 % m/m) were added to the mixture and placed under H<sub>2</sub> atmosphere until no more starting material was detected by TLC. The solution was then filtered through a pad of silate and solvents were evaporated to give 19.4 g (yield: 90.6 %) of compound **9**. <sup>1</sup>H NMR (400 MHz,

chloroform-*d*)  $\delta$  8.06 – 8.00 (m, 1H), 7.44 (s, 1H), 6.29 (d,  $J = 2.4$  Hz, 1H), 6.26 (s, 1H), 3.87 (d,  $J = 5.7$  Hz, 2H), 3.67 (bs, 2H), 2.14 (s, 3H), 1.71 (m,  $J = 12.3, 6.2$  Hz, 1H), 1.53 – 1.42 (m, 4H), 0.96 (t,  $J = 7.5$  Hz, 6H).  $^{13}\text{C}$  NMR (101 MHz, chloroform-*d*)  $\delta$  167.6, 148.9, 143.2, 121.5, 119.8, 107.0, 99.5, 70.8, 51.34, 41.0, 24.8, 23.8, 11.4. HRMS (ESI+) calcd. for  $\text{C}_{14}\text{H}_{23}\text{N}_2\text{O}_4$   $[\text{M}+\text{H}]^+$  (m/z): 251.1780, found: 251.17539.



Chemical Formula:  $\text{C}_{20}\text{H}_{28}\text{N}_2\text{O}_6$

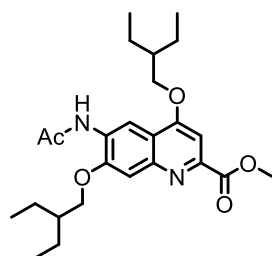
**Compound 10.** In a 500 ml round bottom flask, compound **9** (23.9 g, 1.0 eq., 0.078 mole) was dissolved in 220 mL of MeOH and DMAD (10.45 mL, 1.1 eq., 0.085 mol) were added slowly over 30 min to the reaction mixture. The solution was stirred at room temperature until no starting material was detectable by TLC. After 3 h a precipitate forms slowly. The solid was filtered and washed with some more MeOH to give 24.3 g (yield: 85.0 %) of compound **10**.  $^1\text{H}$  NMR (400 MHz, chloroform-*d*)  $\delta$  9.62 (s, 1H), 8.25 (d,  $J = 8.6$  Hz, 1H), 7.62 (s, 1H), 6.63 – 6.22 (m, 1H), 5.34 (s, 1H), 3.88 (d,  $J = 5.7$  Hz, 2H), 3.72 (d,  $J = 16.1$  Hz, 6H), 2.17 (s, 3H), 1.73 (p,  $J = 6.1$  Hz, 1H), 1.59 – 1.39 (m, 4H), 0.96 (t,  $J = 7.5$  Hz, 6H).  $^{13}\text{C}$  NMR (126 MHz, chloroform-*d*)  $\delta$  207.1, 170.1, 167.9, 165.0, 148.5, 148.0, 136.2, 124.8, 120.0, 113.10, 104.8, 93.0, 71.1, 52.9, 51.3, 40.8, 31.0, 24.9, 23.8, 11.3. HRMS (ESI+) calcd. for  $\text{C}_{20}\text{H}_{29}\text{N}_2\text{O}_6$   $[\text{M}+\text{H}]^+$  (m/z): 393.1980, found: 393.20197



Chemical Formula:  $\text{C}_{19}\text{H}_{24}\text{N}_2\text{O}_5$

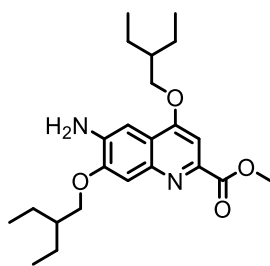
**Compound 11.** Into a 1000 mL round bottom flask containing 310 mL of boiling  $\text{Ph}_2\text{O}$  (260 °C) compound **10** (17.9 g, 1 eq., 0.049 mol) was added in small portions over 2 min The temperature was kept for 11 min. After cooling to room temperature a chewy solid was formed. 400 mL of cyclohexane were added to the reaction mixture and the

solvents were removed. Then 300 mL of Et<sub>2</sub>O was added and after harsh trituration with spatula and strong sonication the chewy solid became filterable. The olive green solid was filtered and washed with some more Et<sub>2</sub>O. The solid was then dried under vacuum to give 15.1 g (yield: 92.0 %) of compound **11**. <sup>1</sup>H NMR (400 MHz, DMSO-*d*<sub>6</sub>) δ 11.80 (s, 1H), 9.02 (s, 1H), 8.51 (d, *J* = 9.0 Hz, 1H), 7.50 (s, 1H), 6.54 (s, 1H), 3.99 (d, *J* = 6.0 Hz, 2H), 3.95 (s, 3H), 2.10 (s, 3H), 1.81 (m, *J* = 12.6, 6.3 Hz, 1H), 1.58 – 1.38 (m, *J* = 6.8 Hz, 4H), 0.92 (t, *J* = 7.5 Hz, 6H). <sup>13</sup>C NMR (101 MHz, DMSO-*d*<sub>6</sub>) δ 176.91, 168.91, 163.13, 154.12, 138.41, 137.07, 130.45, 126.05, 120.39, 117.58, 110.19, 100.44, 71.46, 53.83, 24.24, 23.17, 23.06, 11.33, 11.23. HRMS (ESI+) calcd. for C<sub>19</sub>H<sub>25</sub>N<sub>2</sub>O<sub>5</sub> [M+H]<sup>+</sup> (m/z): 361.1780, found: 361.17572.



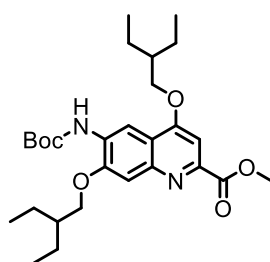
Chemical Formula: C<sub>25</sub>H<sub>36</sub>N<sub>2</sub>O<sub>5</sub>

**Compound 12.** Compound **11** (13.6 g 1.0 eq., 0.041 mole), PPh<sub>3</sub> (12.9 g, 1.2 eq., 0.049 mol) and 2-ethyl-1-butanol (6.04 mL, 1.2 eq., 0.049 mol) were suspended in 50 mL of dry THF. The reaction mixture was cooled to 0 °C using an ice bath and DIAD (9.7 mL, 1.2 eq., 0.049 mol) were added dropwise over 25 min. The mixture was left stirring at room temperature for overnight. The solvent was removed and the solid purified by column chromatography using cyclohexane / ethyl acetate as eluent to give 14.3 g (yield: 78.9 %) of compound **12**. <sup>1</sup>H (500 MHz, chloroform-*d*) δ 7.47 (s, 2H), 7.45 (s, 1H), 7.25 (s, 1H), 4.35 (s, 3H), 4.12 (d, *J* = 5.6 Hz, 2H), 4.05 (d, *J* = 5.9 Hz, 2H), 4.04 (s, 8H), 1.80 (m, *J* = 8.7, 6.2 Hz, 1H), 1.65 – 1.44 (m, 1H), 0.98 (d, *J* = 7.5 Hz, 3H), 0.94 (d, *J* = 7.5 Hz, 12H). <sup>13</sup>C NMR (126 MHz, chloroform-*d*) δ 206.77, 168.15, 166.33, 162.29, 150.33, 147.76, 146.16, 129.11, 117.49, 109.59, 108.23, 100.05, 71.37, 70.71, 52.97, 40.58, 40.29, 30.76, 26.75, 24.90, 23.56, 23.50, 21.79, 11.09, 10.99. HRMS (ESI+) calcd. for C<sub>25</sub>H<sub>37</sub>N<sub>2</sub>O<sub>5</sub> [M+H]<sup>+</sup> (m/z): 445.2680, found: 445.26927.



Chemical Formula: C<sub>23</sub>H<sub>34</sub>N<sub>2</sub>O<sub>4</sub>

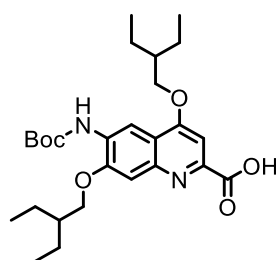
**Compound 13.** Compound **12** (14.3 g, 1 eq. 0.032 mol) were dissolved in 50 mL MeOH and pure H<sub>2</sub>SO<sub>4</sub> (0.65mL, 2.0 eq., 0.064 mole) were added to this solution. The reaction mixture was allowed to stir for 3 days at room temperature. After the starting material was consumed completely, an aqueous solution of saturated sodium bicarbonate was added to the mixture to reach neutral pH and the solution was extracted with ethyl acetate. The organic layers were combined and washed 2 times with water and dried over MgSO<sub>4</sub> and concentrated under reduced pressure to give 9.7 g (yield: 75.2 %) of compound **13**. <sup>1</sup>H NMR (500 MHz, chloroform-*d*) δ 8.71 (s, 1H), 7.89 (s, 1H), 7.50 (d, *J* = 16.2 Hz, 1H), 4.14 (d, *J* = 5.9 Hz, 3H), 4.09 – 4.02 (m, 2H), 3.68 (s, 2H), 1.87 (m, *J* = 32.9, 6.2 Hz, 1H), 1.61 – 1.53 (m, 1H), 1.51 (s, 8H), 0.96 (m, *J* = 14.7, 7.4 Hz, 12H). <sup>13</sup>C NMR (126 MHz, chloroform-*d*) δ 166.67, 160.24, 150.92, 144.89, 144.37, 138.60, 118.33, 108.31, 100.70, 99.72, 70.64, 70.26, 69.89, 52.78, 40.69, 40.42, 23.40, 23.36, 21.78, 11.05, 10.94. HRMS (ESI+) calcd. for C<sub>23</sub>H<sub>34</sub>N<sub>2</sub>O<sub>4</sub>Na [2M+Na]<sup>+</sup> (m/z): 828.5198, found: 828.49351.



Chemical Formula: C<sub>28</sub>H<sub>42</sub>N<sub>2</sub>O<sub>6</sub>

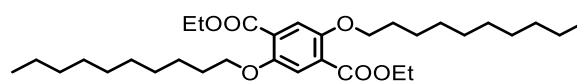
**Compound 14.** In a 100 mL round bottom flask, compound **13** (9.7 g, 1 eq. 0.024 mol) and Boc<sub>2</sub>O (26.4 g, 5 eq., 0.121 mol) were dissolved in 50 mL 1,4-Dioxane and placed at 90°C for 4 days. The solvent was then removed and the reaction mixture was purified by flash chromatography using DCM/ethyl acetate (9/1) mixture as eluent to give 8.0 g (yield: 66 %) of the protected amine **14**. <sup>1</sup>H NMR (500 MHz, chloroform-*d*) δ 8.72 (s, 1H), 7.53 (s, 1H), 7.49 (s, 1H), 7.29 (s, 1H), 4.15 (d, *J* = 6.0 Hz, 3H), 4.09 –

4.03 (m, 4H), 1.91 (p,  $J = 6.3$  Hz, 1H), 1.84 (p,  $J = 6.2$  Hz, 1H), 1.58 (s, 9H), 1.65 – 1.46 (m, 8H), 0.97 (dt,  $J = 14.1, 7.5$  Hz, 12H).  $^{13}\text{C}$  NMR (126 MHz, chloroform- $d$ )  $\delta$  174.07, 166.90, 162.53, 153.36, 152.53, 149.29, 138.48, 131.24, 117.04, 107.95, 102.84, 100.41, 81.89, 73.26, 72.88, 40.93, 40.79, 31.33, 29.56, 28.68, 24.00, 23.75, 11.64, 11.40, 1.42. HRMS (ESI+) calcd. for  $\text{C}_{28}\text{H}_{43}\text{N}_2\text{O}_6$   $[\text{M}+\text{H}]^+$  (m/z): 503.3080, found: 503.31116



Chemical Formula:  $\text{C}_{27}\text{H}_{40}\text{N}_2\text{O}_6$

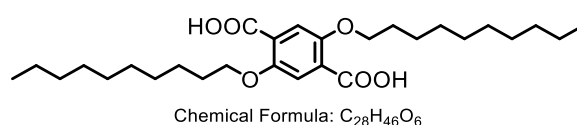
**Compound 15.** Compound **14** (0.8 g, 1 eq. 1.59 mmol) was dissolved in 10 mL 1,4-dioxane and NaOH (0.35 g, 5.5 eq. 8.75 mmol), dissolved in 1 mL of water, was added to the solution. The reaction mixture was stirred 12h until no starting material could be detected on TLC. 10 mL of a 5 % aqueous. citric acid solution is then added to the reaction mixture to neutralize the excess of NaOH. The solid was filtered and re-dissolved in EtOAc. This organic phase was washed with brine and was dried over  $\text{MgSO}_4$ . The solvent was then removed to give 1.8 g of **15**.  $^1\text{H}$  NMR (400 MHz, chloroform- $d$ )  $\delta$  8.81 (s, 1H), 8.34 (s, 1H), 7.72 (s, 1H), 7.34 (s, 1H), 4.35 (d,  $J = 5.6$  Hz, 2H), 4.30 (d,  $J = 6.1$  Hz, 2H), 1.93 (m,  $J = 24.8, 6.2$  Hz, 1H), 1.66 – 1.50 (m, 1H), 1.58 (s, 19H), 1.00 (m,  $J = 10.3, 7.5$  Hz, 12H).  $^{13}\text{C}$  (101 MHz, chloroform- $d$ )  $\delta$  167.05, 162.57, 152.83, 151.73, 151.04, 147.75, 146.32, 130.49, 118.21, 109.66, 108.85, 108.01, 100.62, 83.02, 81.49, 77.68, 71.96, 71.56, 53.52, 41.20, 41.02, 40.82, 28.79, 28.30, 23.99, 11.57, 11.48. HRMS (ESI+) calcd. for  $\text{C}_{27}\text{H}_{41}\text{N}_2\text{O}_6$   $[\text{M}+\text{H}]^+$  (m/z): 489.2980, found: 489.295



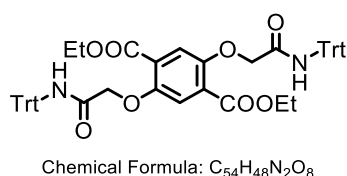
Chemical Formula:  $\text{C}_{32}\text{H}_{54}\text{O}_6$

**Compound 16.** Dimethyl 2,5-dihydroxyterephthalate (0.5 g, 1 eq. 1.97 mmol) and Triphenyl phosphine (1.1 g 2.1 eq. 4.2 mmol) were dissolved in 15 mL of dry THF. 1-Decanol (0.79 mL, 2.1 eq., 4.2 mmol) were added to this solution and followed by dropwise addition of DIAD (0.81 mL, 2.1 eq., 4.2 mmol) at 0 °C. The solution was

allowed to reach room temperature and was left stirring for 2h. The solvents were removed and the crude material was purified by flash chromatography using pure DCM as eluent. After purification 0.46 g (yield: 39.5 %) of **16** were obtained.  $^1\text{H}$  NMR (400 MHz,  $\text{DMSO-}d_6$ )  $\delta$  7.27 (s, 2H), 4.27 (q,  $J = 7.1$  Hz, 4H), 4.09 (q,  $J = 5.2$  Hz, 4H), 3.97 (t,  $J = 6.2$  Hz, 4H), 3.17 (d,  $J = 5.2$  Hz, 28H), 1., 1.28 (dd,  $J = 16.9, 8.1$  Hz, 6H), 0.85 (t,  $J = 6.6$  Hz, 6H).  $^{13}\text{C}$  NMR (101 MHz,  $\text{DMSO-}d_6$ )  $\delta$  150.45, 124.73, 115.42, 93.81, 85.60, 69.11, 60.84, 48.55, 31.22, 28.94, 28.84, 28.62, 25.31, 22.02, 14.00, 13.89. HRMS (ESI+) calcd. for  $\text{C}_{32}\text{H}_{55}\text{O}_6\text{Na}$   $[\text{M}+\text{H}]^+$  (m/z): 535.3978, found: 535.39951

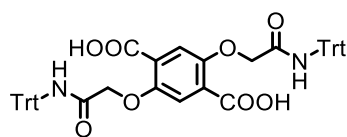


**Compound 17.** Compound **16** (0.41 g, 1 eq., 0.775 mmol) was dissolved in 2 mL of 1,4-dioxane and KOH (0.44 g 10 eq., 7.75 mmol) dissolved in 200  $\mu\text{L}$  of water were added to the solution. The reaction mixture was left stirring overnight. The solvent was concentrated and the solution acidified with 1 N HCl to pH = 1 and extracted with 50 mL of EtOAc. The organic layers were combined and washed with water (3 x 15mL). It was dried over  $\text{MgSO}_4$ , filtrated and concentrated under reduced pressure to give 0.35 g (yield: 94.1 %) of **17**.  $^1\text{H}$  (400 MHz,  $\text{DMSO-}d_6$ )  $\delta$  12.85 (s, 2H), 7.25 (s, 2H), 3.97 (t,  $J = 6.4$  Hz, 4H), 1.67 (p,  $J = 6.6$  Hz, 4H), 1.26 (d,  $J = 9.5$  Hz, 28H), 0.89 – 0.81 (m, 6H)  $^{13}\text{C}$  (101 MHz,  $\text{DMSO-}d_6$ )  $\delta$  166.81, 150.43, 125.47, 115.54, 96.0, 92.65, 69.13, 31.26, 28.99, 28.90, 28.66, 25.28, 22.07, 13.93. HRMS (ESI-) calcd. for  $\text{C}_{28}\text{H}_{45}\text{O}_6$   $[\text{M}-\text{H}]^-$  (m/z): 477.3229, found: 477.32289



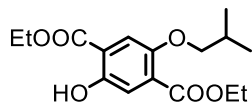
**Compound 18.** Dimethyl 2,5-dihydroxyterephthalate (1 g, 1 eq., 0.039 mmol) was dissolved in 80 mL of dry acetone and of  $\text{K}_2\text{CO}_3$  (2.17 g, 4 eq. 0.156 mol) were added. At 60  $^\circ\text{C}$  2-bromo-*N*-tritylacetamide (3.28 g, 2.2 eq. 0.086 mol) were added and the reaction mixture was stirred overnight. After 2 h, a precipitate formed and after no starting material was detected, 10 mL of  $\text{H}_2\text{O}$  were added to complete precipitation.

The solid was filtered off and purified by silica gel chromatography using 4/1 cyclohexane/EtOAc to obtain 3.3 g of pure compound **18** (yield = 98.0 %). <sup>1</sup>H NMR (400 MHz, chloroform-*d*) δ 8.56 (s, 2H), 7.42 (s, 2H), 7.26 (d, *J* = 4.1 Hz, 30H), 4.53 (s, 4H), 4.18 (q, *J* = 7.1 Hz, 4H), 1.27 (t, *J* = 7.1 Hz, 6H). <sup>13</sup>C NMR (126 MHz, chloroform-*d*) δ 181.18, 173.41, 171.57, 166.97, 163.78, 151.79, 144.86, 136.81, 129.36, 128.30, 127.43, 124.51, 123.62, 117.31, 106.56, 104.53, 89.59, 73.10, 71.64, 71.00, 69.29, 61.90, 30.18, 29.79, 25.95, 23.19, 14.70. HRMS (ESI-) calcd. for C<sub>54</sub>H<sub>47</sub>N<sub>2</sub>O<sub>8</sub> [M-H]<sup>-</sup> (m/z): 851.33216, found: 851.33488



Chemical Formula: C<sub>50</sub>H<sub>40</sub>N<sub>2</sub>O<sub>8</sub>

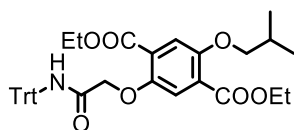
**Compound 19.** Compound **18** (3.3 g, 1 eq. 3.9 mmol) was dissolved in 20 mL of 1,4-dioxane and KOH (2.16 g 10 eq., 38.5 mmol) dissolved in 2 mL of water were added to the solution. The reaction mixture was left stirring overnight. The solvent was concentrated and the solution acidified with 1 N HCl to pH = 1 and extracted with 50 mL of EtOAc. The organic layers were combined and washed with water (3 x 15mL). It was dried over MgSO<sub>4</sub>, filtrated and concentrated under reduced pressure to give 1.79 g (yield: 66.4 %) of **19**. <sup>1</sup>H NMR (500 MHz, DMSO-*d*<sub>6</sub>) δ 8.64 (s, 2H), 7.41 (s, 2H), 7.36 – 7.14 (m, 30H), 6.44 (s, 2H), 4.73 (d, *J* = 3.8 Hz, 4H). <sup>13</sup>C NMR (101 MHz, Methanol-*d*<sub>4</sub>) δ 189.88, 177.51, 173.13, 145.38, 145.08, 141.80, 129.44, 128.57, 127.60, 122.09, 117.92, 79.72, 79.39, 79.06, 67.52, 40.43, 40.23, 40.02, 39.80, 39.59, 39.37, 39.17, 22.45, 15.09, 14.53. HRMS (ESI-) calcd. for C<sub>50</sub>H<sub>39</sub>N<sub>2</sub>O<sub>6</sub> [M-H]<sup>-</sup> (m/z): 795.27216, found: 795.27487



Chemical Formula: C<sub>16</sub>H<sub>22</sub>O<sub>6</sub>

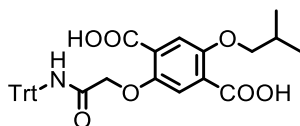
**Compound 20.** Dimethyl 2,5-dihydroxyterephthalate (2.0 g, 1 eq., 7.87 mmol) and Triphenylphosphine (2.48 g 1.2 eq., 9.44 mmol) were dissolved in 15mL of dry THF. *i*PrOH (0.85 mL 1.2 eq., 9.44 mmol) were added to this solution and followed by dropwise addition of 1.9 mL of DIAD (1.2 eq., 9.44 mmol) at 0 °C. The solution was allowed to reach room temperature and was left stirring for 2h. The solvents were removed and the crude material is purified by flash chromatography using pure DCM

as eluent. After purification 0.96 g (yield: 38.1 %) of **20** are obtained.  $^1\text{H}$  NMR (500 MHz,  $\text{DMSO-}d_6$ )  $\delta$  7.57 (s, 1H), 7.43 (s, 1H), 7.41 (s, 1H), 4.53 (s, 6H), 4.32 (q,  $J = 7.0$  Hz, 1H), 1.31 (t,  $J = 7.1$  Hz, 12H).  $^{13}\text{C}$  NMR (126 MHz,  $\text{DMSO-}d_6$ )  $\delta$  170.15, 165.15, 151.10, 149.52, 124.86, 124.33, 117.47, 68.84, 67.60, 61.88, 60.98, 22.73, 19.93, 14.50, 13.60, 10.24 HRMS (ESI $^-$ ) calcd. for  $\text{C}_{16}\text{H}_{21}\text{O}_6$   $[\text{M-H}]^-$  (m/z): 309.13216, found: 309.13485



Chemical Formula:  $\text{C}_{37}\text{H}_{39}\text{NO}_7$

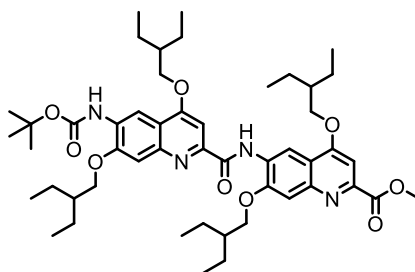
**Compound 21.** Compound **20** (0.94 g, 1 eq. 3.1 mmol) was dissolved in 5 mL of dry acetone and  $\text{K}_2\text{CO}_3$  (0.856 g, 2 eq. 6.2 mmol) were added. At 60 °C 2-bromo-*N*-tritylacetamide (1.41 g, 1.2 eq. 3.72 mmol) were added and the reaction mixture was stirred overnight. After no starting material was detected, 10 mL of  $\text{H}_2\text{O}$  were added to precipitate the reaction mixture. The solid was filtered off and purified by silica gel chromatography using 4/1 cyclohexane/EtOAc to obtain 210 mg of pure compound **21** after drying (yield: 11.2 %)  $^1\text{H}$  NMR (500 MHz,  $\text{DMSO-}d_6$ )  $\delta$  8.61 (s, 1H), 7.39 – 7.31 (m, 2H), 7.33 – 7.14 (m, 15H), 4.70 (d,  $J = 3.8$  Hz, 2H), 4.31 (q,  $J = 7.1$  Hz, 2H), 4.18 (q,  $J = 7.1$  Hz, 2H), 3.79 (dd,  $J = 6.3, 2.0$  Hz, 2H), 2.00 (m,  $J = 6.6$  Hz, 1H), 1.30 (t,  $J = 7.1$  Hz, 6H), 0.98 (d,  $J = 6.6$  Hz, 6H).  $^{13}\text{C}$  NMR (126 MHz,  $\text{DMSO-}d_6$ )  $\delta$  221.60, 194.34, 192.47, 184.74, 179.16, 166.68, 165.83, 164.51, 156.40, 149.72, 144.37, 132.68, 128.42, 127.65, 126.66, 124.90, 121.95, 115.86, 103.81, 100.41, 94.60, 85.67, 75.11, 73.41, 69.34, 68.15, 61.04, 60.62, 58.29, 31.00, 27.90, 26.33, 25.03, 18.88, 14.06, 7.13, 1.55. HRMS (ESI $^+$ ) calcd. for  $\text{C}_{37}\text{H}_{40}\text{NO}_7$   $[\text{M+H}]^+$  (m/z): 610.27784, found: 610.27985.



Chemical Formula:  $\text{C}_{33}\text{H}_{31}\text{NO}_7$

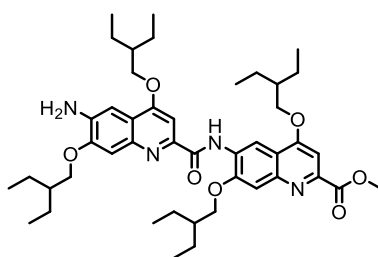
**Compound 22.** Compound **21** (0.20 g, 1 eq. 3.3 mmol) was dissolved in 2 mL of 1,4-dioxane and KOH (0.18 g 10 eq., 33.0 mmol) dissolved in 200  $\mu\text{L}$  of water were added to the solution. The reaction mixture was left stirring overnight. The solvent was concentrated and the solution acidified with 1 N HCl to pH = 1 and extracted with 5 mL

of EtOAc. The organic layers were combined and washed with water (3 x 15mL). It was dried over MgSO<sub>4</sub>, filtrated and concentrated under reduced pressure to give 0.18 g (yield: 97.5 %) of **22**. <sup>1</sup>H NMR (400 MHz, chloroform-*d*) δ 8.01 (s, 1H), 7.77 (s, 1H), 7.61 (s, 1H), 7.32 – 7.16 (m, 15H), 4.63 (s, 2H), 4.04 (d, *J* = 6.5 Hz, 2H), 1.31 – 1.22 (m, 1H), 1.10 (d, *J* = 6.7 Hz, 6H). <sup>13</sup>C NMR (126 MHz, chloroform-*d*) δ 196.55, 194.95, 181.48, 179.30, 179.12, 172.88, 157.32, 156.49, 153.39, 146.22, 145.70, 106.46, 106.20, 105.94, 105.02, 101.00, 99.11, 97.63, 94.58, 77.67, 77.50, 77.33, 77.16, 76.99, 76.82, 76.65, 59.10, 56.92, 47.48, 43.39. HRMS (ESI-) calcd. for C<sub>16</sub>H<sub>21</sub>O<sub>6</sub> [M-H]<sup>-</sup> (m/z): 309.20977, found: 389.19340 HRMS (ESI+) calcd. for C<sub>20</sub>H<sub>31</sub>O<sub>6</sub>Na [M+Na]<sup>+</sup> (m/z): 389.20977, found: 389.19340



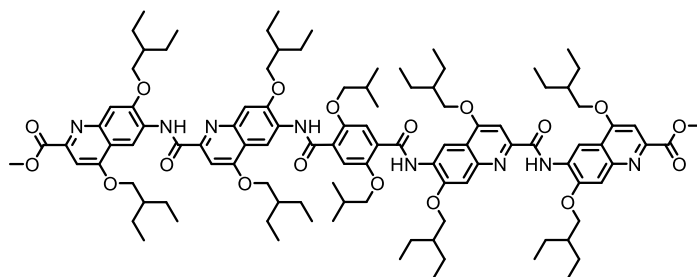
Chemical Formula: C<sub>50</sub>H<sub>72</sub>N<sub>4</sub>O<sub>9</sub>

**Compound 23.** Compound **15** (10.9 g 1.0 eq., 0.02 mol), compound **13** (9.0 g 1.0 eq., 0.02 mol), PyBOP (31.2 g 3.0 eq. 0.06 mol) and DIPEA (13.6 mL 4.0 eq., 0.08 mol) were mixed in 100 mL of CHCl<sub>3</sub> and left stirring for 3 days at room temperature. The solvent was removed and the crude material purified by flash chromatography using cyclohexane / ethyl acetate (7/3) as an eluent. The impure fractions were recrystallized in MeOH overnight in the fridge to obtain 12.1 g (yield: 69.2 %) of pure compound **23**. <sup>1</sup>H NMR (500 MHz, chloroform-*d*) δ 11.30 (s, 1H), 9.37 (s, 1H), 8.72 (s, 1H), 7.70 (s, 1H), 7.61 (s, 1H), 7.51 (s, 1H), 7.34 (s, 1H), 4.24 – 4.16 (m, 4H), 4.07 (d, *J* = 13.3 Hz, 4H), 3.45 (s, 3H), 1.93 (m *J* = 6.3 Hz, 2H), 1.83 (m, *J* = 21.4, 14.2, 6.7 Hz, 2H), 1.72 (d, *J* = 8.9 Hz, 1H), 1.62 (m, *J* = 17.8, 8.9, 4.8 Hz, 16H), 1.40 (s, 9H), 1.07 – 0.94 (m, 24H). <sup>13</sup>C NMR (126 MHz, chloroform-*d*) δ 165.98, 163.69, 162.61, 161.21, 151.91, 151.34, 149.80, 148.44, 147.71, 146.64, 145.78, 143.72, 140.65, 138.40, 129.97, 127.49, 124.99, 118.50, 118.03, 113.47, 109.33, 108.41, 107.52, 101.57, 100.34, 98.99, 97.47, 95.15, 77.41, 77.16, 76.91, 73.11, 71.09, 70.88, 70.79, 70.26, 60.55, 53.26, 41.25, 40.98, 40.75, 39.46, 37.54, 34.21, 29.84, 28.48, 23.91, 23.70, 15.55, 14.35, 11.33, 11.24. HRMS (ESI+) calcd. for C<sub>50</sub>H<sub>73</sub>N<sub>4</sub>O<sub>9</sub> [M+H]<sup>+</sup> (m/z): 873.5378, found: 873.5378. The structure of **23** was also characterized by x-ray crystallography (see section 5)



Chemical Formula: C<sub>45</sub>H<sub>64</sub>N<sub>4</sub>O<sub>7</sub>

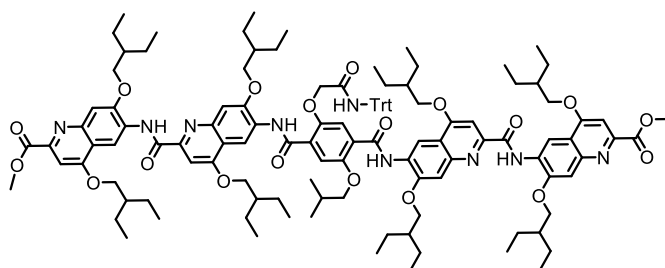
**Compound 24.** Dimer **23** (1.0 g, 1.0 eq., 1.15 mmol), were dissolved in 13 mL of DCM and 3 mL TFA was added. The reaction mixture was stirred overnight at RT. The solution was then diluted with 20 mL EtOAc and 15 mL of saturated aqu. NaHCO<sub>3</sub> solution was carefully added. The organic layer was washed a second time with a 10 mL of saturated aqu. NaHCO<sub>3</sub> and finally with water. The organic layers were combined and dried over MgSO<sub>4</sub>. The solvents were removed using reduced pressure to give 870 mg (yield: 98.3 %) of compound **24**. <sup>1</sup>H NMR (500 MHz, chloroform-*d*) δ 11.32 (s, 1H), 9.40 (d, *J* = 3.6 Hz, 1H), 7.65 (d, *J* = 11.5 Hz, 2H), 7.54 (d, *J* = 4.7 Hz, 1H), 7.50 (s, 0H), 7.44 (d, *J* = 7.5 Hz, 1H), 7.31 (d, *J* = 3.3 Hz, 2H), 5.30 (s, 2H), 4.21 (q, *J* = 5.3 Hz, 6H), 4.17 – 4.02 (m, 10H), 2.17 (s, 1H), 2.04 (s, 2H), 1.96 (p, *J* = 6.1 Hz, 2H), 1.85 (dt, *J* = 14.0, 7.0 Hz, 4H), 1.81 (s, 2H), 1.76 (dd, *J* = 13.9, 6.9 Hz, 1H), 1.68 – 1.47 (m, 10H), 1.42 (s, 4H), 1.34 – 1.23 (m, 6H), 1.09 – 0.92 (m, 30H). <sup>13</sup>C NMR (126 MHz, chloroform-*d*) δ 170.00, 167.01, 163.60, 163.12, 162.89, 152.83, 152.13, 151.09, 150.06, 148.09, 146.97, 145.31, 130.06, 129.98, 118.26, 118.08, 109.78, 108.73, 108.46, 107.68, 100.63, 98.05, 81.82, 71.77, 71.68, 71.37, 70.53, 66.01, 53.53, 41.48, 41.01, 40.99, 28.76, 27.32, 24.17, 24.01, 23.94, 23.89, 15.81, 11.76, 11.58, 11.50, 11.44, 11.40, 10.93. HRMS (ESI+) calcd. for C<sub>45</sub>H<sub>65</sub>N<sub>4</sub>O<sub>7</sub> [M+H]<sup>+</sup> (m/z): 773.4880, found: 773.48363



Chemical Formula: C<sub>106</sub>H<sub>146</sub>N<sub>9</sub>O<sub>18</sub>

**Compound 5.** 2,5-diisobutoxyterephthalic acid (60 mg 1.0 eq., 0.25 mmol), was suspended in 2 mL of DCM and oxalylchloride (170 μL 10 eq., 2.0 mmol) were added

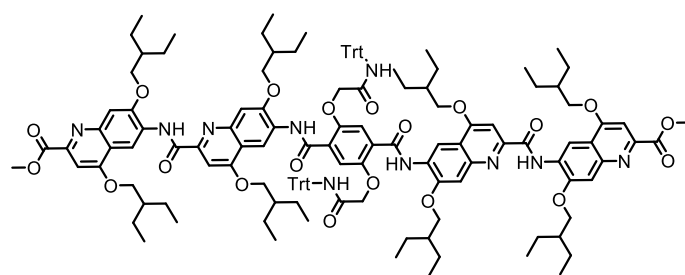
followed by the addition of DMF (5  $\mu$ L 0.1 eq., 0.02 mmol) and the solution was left stirring at room temperature. This solution was then evaporated to dryness under vacuum and dried for 2 h under high vacuum. The solid was then re-dissolved in 1 mL of dry DCM and transferred to a prepared solution of 190 mg of **24** (2.0 eq., 0.50 mmol) containing 167  $\mu$ L of DIPEA (4 eq., 1.0 mmol) in dry DCM. The reaction mixture was stirred at RT for 2h. 10 mL of DCM and EtOAc are added to this solution and then washed with water (3 x 5 mL). The organic phase is collected and dried over MgSO<sub>4</sub>. DCM is evaporated slowly and 82 mg (yield: 30.5 %) of compound **5** was obtained by recrystallization in EtOAc. <sup>1</sup>H NMR (500 MHz, chloroform-*d*)  $\delta$  11.33 (s, 2H), 10.37 (s, 2H), 9.42 (s, 2H), 9.37 (s, 2H), 7.96 (s, 2H), 7.77 (s, 2H), 7.65 (s, 2H), 7.55 (s, 2H), 7.46 (s, 2H), 4.28 (d, *J* = 5.8 Hz, 4H), 4.26 – 4.20 (m, 4H), 4.15 (d, *J* = 6.8 Hz, 4H), 4.11 (t, *J* = 7.1 Hz, 4H), 4.08 (s, 6H), 2.23 (m, *J* = 13.6, 6.9 Hz, 4H), 2.04 (s, 6H), 2.00 – 1.94 (m, 18H), 1.91 – 1.79 (m, 4H), 1.77 (m, *J* = 13.9, 6.9 Hz, 4H), 1.66 (p, *J* = 8.7, 7.9 Hz, 8H), 1.56 – 1.49 (m, 10H), 1.26 (t, *J* = 7.1 Hz, 16H), 1.06 (dd, *J* = 13.6, 6.2 Hz, 12H), 1.05 – 1.00 (m, 24H), 0.97 (t, *J* = 7.5 Hz, 12H). <sup>13</sup>C-NMR NMR (126 MHz, chloroform-*d*)  $\delta$  173.94, 166.64, 165.85, 163.56, 162.48, 161.09, 155.34, 153.21, 151.79, 151.21, 149.67, 148.30, 147.59, 146.51, 143.59, 138.28, 133.26, 129.84, 128.94, 127.36, 122.55, 118.37, 117.90, 113.33, 109.20, 108.28, 107.39, 101.44, 100.21, 97.35, 93.12, 81.86, 70.95, 70.70, 70.13, 65.49, 60.42, 59.73, 53.13, 50.32, 43.15, 41.12, 40.86, 37.40, 30.13, 29.71, 28.34, 26.94, 14.22, 11.38. HRMS (ESI+) calcd. for C<sub>106</sub>H<sub>147</sub>N<sub>8</sub>O<sub>18</sub> [M+H]<sup>+</sup> (m/z): 1820.08784, found: 1820.08275.



Chemical Formula: C<sub>123</sub>H<sub>155</sub>N<sub>9</sub>O<sub>19</sub>

**Compound 25.** Diacid **22** (150 mg, 1.0 eq., 0.03 mmol), was suspended in 2 mL of DCM and 120  $\mu$ L of 1-chloro-N,N-2-trimethyl-1-propenylamine (4 eq., 0.12 mmol) were added and the solution was left stirring at room temperature for 2 h. This solution was then evaporated to dryness under vacuum and dried for 2 h under high vacuum. The solid was then re dissolved in 1 mL of dry DCM and transferred to a prepared solution of dimer **24** (349 mg 2.0 eq., 0.06 mmol) containing DIPEA (153  $\mu$ L 4 eq.,

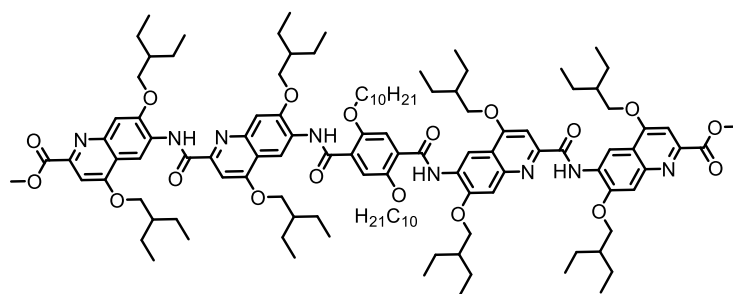
0.12 mmol) in dry DCM. After 4h no more starting material was left and the crude mixture was purified by MeOH precipitation to give 176 mg of pure compound **25** (yield 42.2 %).  $^1\text{H}$  NMR (500 MHz, chloroform-*d*)  $\delta$  11.39 (s, 1H), 10.38 (s, 1H), 9.49 (s, 1H), 9.39 (s, 1H), 8.24 (s, 1H), 7.96 (d,  $J = 10.9$  Hz, 1H), 7.76 (d,  $J = 5.3$  Hz, 2H), 7.47 (s, 1H), 4.48 (s, 2H), 4.35 (d,  $J = 6.0$  Hz, 3H), 4.29 (d,  $J = 5.7$  Hz, 2H), 4.14 (dd,  $J = 22.8, 6.6$  Hz, 4H), 2.24 (dt,  $J = 13.6, 6.6$  Hz, 1H), 2.00 (dt,  $J = 11.5, 6.5$  Hz, 1H), 1.97 – 1.88 (m, 1H), 1.84 (dt,  $J = 14.3, 7.1$  Hz, 4H), 1.67 (q,  $J = 7.3$  Hz, 8H), 1.57 (t,  $J = 8.1$  Hz, 6H), 1.42 (s, 1H), 1.26 (s, 1H), 1.13 (d,  $J = 7.5$  Hz, 5H), 1.12 – 1.00 (m, 19H), 1.01 (s, 1H), 0.99 (s, 9H), 0.97 (d,  $J = 7.4$  Hz, 3H), 0.84 (s, 1H).  $^{13}\text{C}$  NMR (126 MHz, chloroform-*d*)  $\delta$  166.48, 165.37, 163.09, 162.99, 162.88, 162.41, 162.21, 162.07, 151.74, 151.60, 151.57, 151.47, 150.76, 150.49, 150.41, 148.69, 147.69, 147.64, 146.50, 145.71, 145.65, 129.49, 129.42, 128.88, 128.47, 128.24, 127.85, 127.13, 127.10, 126.97, 117.75, 117.53, 117.47, 116.54, 111.97, 111.38, 109.41, 108.29, 107.68, 107.62, 100.16, 97.75, 97.67, 71.68, 71.04, 70.95, 70.87, 70.44, 69.99, 69.07, 53.04, 45.35, 45.21, 45.20, 45.19, 40.97, 40.94, 40.56, 40.52, 40.34, 40.18, 37.33, 37.00, 36.78, 32.68, 31.33, 30.83, 30.21, 29.95, 29.61, 27.96, 27.62, 27.60, 27.42, c 27.40, 27.33, 27.23, 27.01, 26.84, 24.37, 23.71, 23.51, 22.94, 22.86, 21.30, 21.25, 21.01, 20.81, 20.76, 19.90, 19.72, 19.41, 19.10, 14.09, 11.30, 11.26, 11.09, 10.70, 10.59, 1.80, 0.91. HRMS (ESI+) calcd. for  $\text{C}_{123}\text{H}_{156}\text{N}_9\text{O}_{19}$   $[\text{M}+2\text{H}]^{2+}$  (m/z): 1031.57392, found: 1031.54628.



Chemical Formula:  $\text{C}_{140}\text{H}_{164}\text{N}_{10}\text{O}_{20}$

**Compound 26.** 2,5-bis(2-oxo-2-(tritylamino)ethoxy)terephthalic acid (200 mg 1 eq., 0.25 mmol) was suspended in 2.5 mL of DCM and 1-chloro-N,N-2-trimethyl-1-propenylamine (133  $\mu\text{L}$ , 4 eq., 0.1 mmol) was added and the solution was left stirring at room temperature. This solution was then evaporated to dryness under vacuum and dried for 2 h under high vacuum. The solid was then re-dissolved in 1 mL of dry DCM and transferred to a prepared solution containing dimer **24** (388 mg 2.0 eq., 0.50 mmol) containing DIPEA (170  $\mu\text{L}$  4 eq., 0.1 mmol) in dry DCM. After 4 h no more starting material was left and the crude mixture was purified by MeOH precipitation to give 70

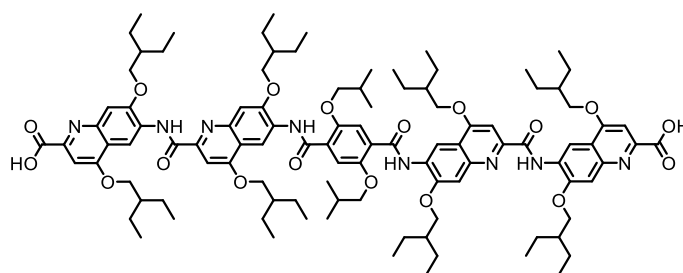
mg of pure compound **26** (yield: 12.4 %).  $^1\text{H}$  NMR (400 MHz)  $\delta$  10.89 (s, 2H), 9.92 (s, 2H), 9.03 (s, 2H), 8.92 (d,  $J = 12.8$  Hz, 2H), 7.59 (s, 2H), 7.52 (s, 4H), 7.45 (d,  $J = 10.5$  Hz, 6H), 6.98 (d,  $J = 8.6$  Hz, 6H), 4.94 (s, 4H), 4.04 (s, 6H), 3.68 (dd,  $J = 17.3, 6.7$  Hz, 18H), 3.27 (t,  $J = 6.5$  Hz, 18H), 1.40 – 1.32 (m, 20H), 1.20 (m,  $J = 7.5$  Hz, 24H), 0.68 – 0.46 (m, 48H).  $^{13}\text{C}$  (126 MHz, chloroform- $d$ )  $\delta$  171.55, 165.58, 163.50, 163.01, 162.70, 161.86, 152.41, 151.20, 150.95, 150.11, 147.23, 146.15, 145.04, 144.35, 142.80, 140.77, 130.74, 129.88, 129.16, 128.96, 128.73, 128.43, 128.40, 128.15, 127.92, 127.56, 118.08, 117.21, 112.00, 109.83, 108.85, 108.11, 101.53, 98.30, 72.23, 71.58, 71.46, 71.03, 70.70, 69.64, 68.16, 41.47, 41.15, 41.05, 40.67, 39.40, 27.90, 33.75, 32.32, 31.84, 30.51, 30.10, 29.91, 29.67, 29.24, 25.17, 24.21, 24.10, 24.05, 23.37, 23.09, 21.45, 14.56, 11.79, 11.69, 11.65, 11.63, 11.49, 11.08, 1.42 HRMS (ESI+) calcd. for  $\text{C}_{140}\text{H}_{165}\text{N}_{10}\text{O}_{20}$   $[\text{M}+2\text{H}]^{2+}$  (m/z): 1153.61284, found: 1153.6160.



Chemical Formula:  $\text{C}_{118}\text{H}_{170}\text{N}_8\text{O}_{18}$

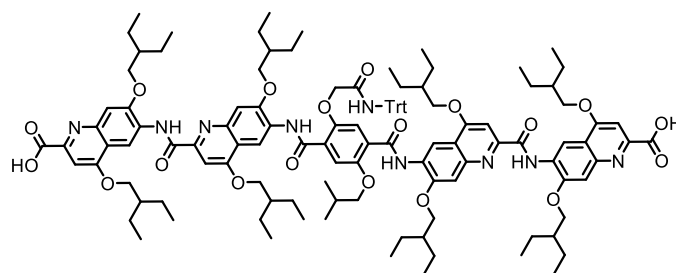
**Compound 27.** 2,5-bis(decyloxy)terephthalic acid (51 mg 1 eq., 0.11 mmol) was suspended in 2 mL of DCM and oxalyl chloride (92  $\mu\text{L}$  10 eq., 1.1 mmol) was added followed by 5  $\mu\text{L}$  of DMF and the solution was left stirring at room temperature. This solution was then evaporated to dryness under vacuum and dried for 2 h under high vacuum. The solid was then re dissolved in 1 mL of dry DCM and transferred to a prepared solution of dimer **24** (150 mg 2.0 eq., 0.22 mmol) containing DIPEA (132  $\mu\text{L}$  4 eq., 0.44 mmol) in dry DCM. After 4 h, no more starting material was left and the crude mixture was purified by MeOH precipitation to give 92 mg of pure compound **27** (yield 47.2 %).  $^1\text{H}$  NMR (400 MHz, chloroform- $d$ )  $\delta$  11.27 (s, 2H), 10.43 (s, 2H), 9.35 (d,  $J = 10.5$  Hz, 4H), 7.93 (s, 2H), 7.69 (s, 2H), 7.58 (s, 2H), 7.49 (s, 2H), 7.39 (s, 2H), 5.23 (s, 2H), 4.27 (t,  $J = 6.9$  Hz, 4H), 4.21 (d,  $J = 5.8$  Hz, 2H), 4.17 (s, 8H), 4.09 (d,  $J = 6.5$  Hz, 4H), 4.02 (s, 6H), 1.94 (s, 6H), 2.00 – 1.86 (m, 2H), 1.86 – 1.64 (m, 8H), 1.67 – 1.53 (m, 14H), 1.53 – 1.44 (m, 10H), 1.36 (dd,  $J = 16.9, 7.2$  Hz, 6H), 1.28 – 1.16 (m, 4H), 0.96 (m,  $J = 22.8, 14.9, 7.5$  Hz, 70H), 0.72 (t,  $J = 7.0$  Hz, 6H).  $^{13}\text{C}$  NMR (126 MHz,

chloroform-*d*)  $\delta$  163.16, 162.92, 151.74, 150.98, 150.71, 150.38, 145.82, 129.18, 126.91, 117.87, 117.70, 117.62, 116.6, 116.21, 111.96, 109.45, 107.73, 100.29, 97.73, 71.77, 71.18, 71.14, 70.15, 70.10, 70.00, 60.51, 53.60, 53.30, 53.20, 41.87, 41.10, 41.08, 40.63, 40.61, 40.44, 31.79, 29.51, 29.46, 29.33, 29.25, 29.08, 25.85, 23.83, 23.62, 23.57, 23.05, 23.01, 22.61, 18.66, 17.40, 14.04, 12.10, 12.00, 11.39, 11.20, 11.16, 11.0 10.80, 1.93, 1.03. HRMS (ESI+) calcd. for  $C_{118}H_{171}N_8O_{18}$  [ $2M+H$ ]<sup>+</sup> (*m/z*): 994.1339, found: 994.63954.



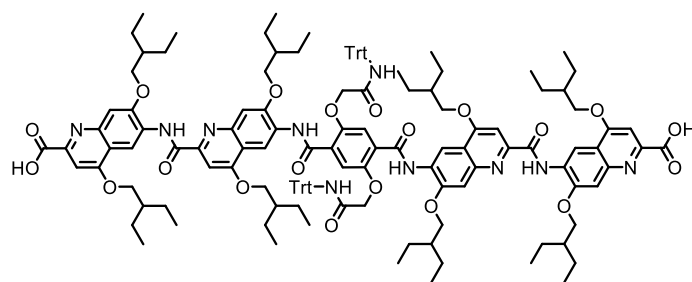
Chemical Formula:  $C_{104}H_{142}N_8O_{18}$

**Compound 28.** Oligomer **5** (82 mg, 1.0 eq., 0.045 mmol) was dissolved in 3 mL of a mixture of THF/MeOH (4/1). NaOH (25 mg, 10 eq., 0.45 mmol) dissolved in 100  $\mu$ L of water were added to this mixture. The suspension was left stirring for 5 h at room temperature. 1M aqueous HCl solution was added to neutralize the excess of NaOH. The organic solvents were then removed using the evaporator and H<sub>2</sub>O is added. The precipitate was filtered and washed with water. The solid was then suspended in toluene and evaporated using reduced pressure to remove resting amount of water as an azeotrope. This was repeated 3 times to dry the solid completely and to obtain 72 mg of product **28** (yield: 90.3 %). <sup>1</sup>H NMR (500 MHz, chloroform-*d*)  $\delta$  11.39 (s, 2H), 10.38 (s, 2H), 9.49 (s, 2H), 9.39 (s, 2H), 8.24 (s, 2H), 7.97 (s, 2H), 7.76 (d, *J* = 5.2 Hz, 2H), 7.65 (d, *J* = 8.9 Hz, 2H), 7.48 (s, 2H), 4.48 (s, 4H), 4.35 (d, *J* = 6.0 Hz, 4H), 4.29 (d, *J* = 5.7 Hz, 4H), 4.20 (d, *J* = 5.2 Hz, 4H), 4.16 (d, *J* = 6.4 Hz, 4H), 4.11 (d, *J* = 6.9 Hz, 2H), 2.23 (m, *J* = 6.6 Hz, 2H), 1.94 – 1.82 (m, 32H), 1.69 – 1.63 (m, 8H), 1.12 (t, *J* = 7.6 Hz, 12H), 1.07 – 0.94 (m, 48H). <sup>13</sup>C (126 MHz, chloroform-*d*)  $\delta$  171.54, 167.56, 167.27, 167.06, 158.40, 155.94, 155.00, 153.81, 153.66, 149.86, 142.00, 134.26, 133.03, 130.54, 121.59, 121.35, 120.68, 120.55, 116.29, 113.96, 111.64, 104.42, 101.58, 76.93, 75.78, 75.05, 74.81, 71.81, 57.36, 53.53, 52.27, 52.10, 50.21, 44.95, 44.61, 44.52, 44.39, 44.21, 31.97, 30.72, 30.23, 29.35, 27.58, 27.37, 26.94, 25.56, 22.94, 15.15, 14.90, 14.85, 14.57, 5.10. HRMS (ESI+) calcd. for  $C_{104}H_{143}N_8O_{18}$  [ $M+H$ ]<sup>+</sup> (*m/z*): 1792.04784, found: 1792.02214.



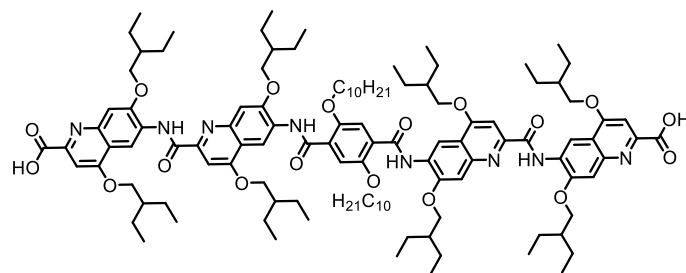
Chemical Formula: C<sub>121</sub>H<sub>151</sub>N<sub>9</sub>O<sub>19</sub>

**Compound 29.** Compound **25** (20 mg 1 eq., 9.69 mmol) was dissolved in 1 mL of a mixture of THF/MeOH (4/1). 3.9 mg of NaOH (10 eq., 96.9 mmol) dissolved in 20  $\mu$ L of water were added to this mixture. The suspension was left stirring for 5 h at room temperature. 1M aqueous. HCl solution was added to neutralize the excess of NaOH. The organic solvents are then removed using the evaporator and H<sub>2</sub>O is added. The precipitate was filtered and washed with water. The solid was then suspended in toluene and evaporated using reduced pressure to remove resting amount of water as an azeotrope. This was repeated 3 times to dry the solid completely and to obtain 18 mg of pure compound **29** (yield: 86.0 %). <sup>1</sup>H NMR (400 MHz, chloroform-*d*)  $\delta$  11.30 (d, *J* = 6.5 Hz, 1H), 10.31 (d, *J* = 11.8 Hz, 1H), 10.29 (s, 1H), 9.93 (dd, *J* = 10.4, 6.2 Hz, 1H), 9.43 (d, *J* = 1.8 Hz, 1H), 9.42 (s, 1H), 9.41 (s, 1H), 9.40 – 9.38 (m, 1H), 9.35 (d, *J* = 2.4 Hz, 1H), 9.30 (d, *J* = 2.3 Hz, 1H), 8.01 (t, *J* = 1.3 Hz, 1H), 8.00 (s, 1H), 7.87 (s, 1H), 7.85 (s, 1H), 7.84 (s, 1H), 7.79 (d, *J* = 1.2 Hz, 1H), 7.76 (t, *J* = 1.3 Hz, 1H), 7.64 (d, *J* = 1.5 Hz, 1H), 7.62 (d, *J* = 4.0 Hz, 1H), 7.54 (s, 1H), 7.45 (d, *J* = 1.8 Hz, 1H), 7.43 (dd, *J* = 3.5, 1.3 Hz, 1H), 7.37 (s, 1H), 7.35 (d, *J* = 1.9 Hz, 1H), 7.33 (d, *J* = 1.3 Hz, 1H), 7.16 – 7.08 (m, 6H), 7.09 – 7.05 (m, 6H), 7.05 – 6.96 (m, 6H), 5.07 – 5.00 (m, 2H), 4.99 (s, 2H), 4.99 – 4.93 (m, 4H), 4.84 (dd, *J* = 5.3, 3.5 Hz, 4H), 4.63 (s, 4H), 4.36 (s, 4H), 4.34 – 4.15 (m, 4H), 4.12 (dd, *J* = 7.2, 1.6 Hz, 6H), 4.12 – 4.00 (m, 4H), 3.98 – 3.85 (m, 6H), 3.65 – 3.59 (m, 1H), 3.06 – 2.99 (m, 1H), 2.93 (d, *J* = 1.6 Hz, 6H), 2.02 (d, *J* = 1.7 Hz, 16H), 1.81 (m, *J* = 23.3, 13.3, 7.0 Hz, 6H), 1.71 – 1.59 (m, 6H), 1.59 – 1.43 (m, 6H), 1.24 (m, *J* = 7.0, 1.6 Hz, 18H), 1.19 – 0.84 (m, 8H). HRMS (ESI-) calcd. for C<sub>121</sub>H<sub>150</sub>N<sub>9</sub>O<sub>19</sub> [M-2H]<sup>2-</sup> (m/z): 1016.04716, found: 1016.04212. Note: compound **29** showed poor solubility and a <sup>13</sup>C NMR spectrum could not be measured.



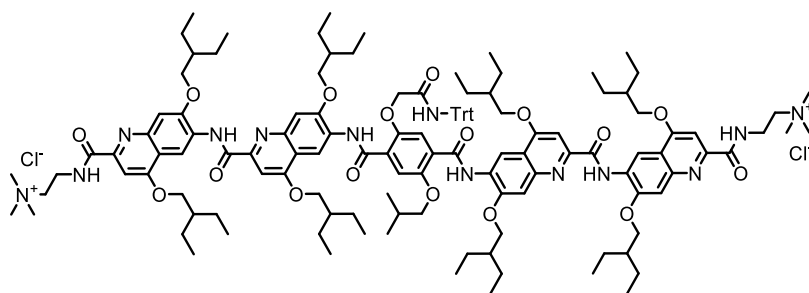
Chemical Formula: C<sub>138</sub>H<sub>160</sub>N<sub>10</sub>O<sub>20</sub>

**Compound 30.** Compound **26** (70mg, 1 eq., 0.03 mmol) was dissolved in 2 mL of a mixture of THF/MeOH (4/1). NaOH (12.1 mg 10 eq., 0.3 mmol) dissolved in 20  $\mu$ L of water are added to this mixture. The suspension was left stirring for 5 h at room temperature. 1 M aqueous. HCl solution was added to neutralize the excess of NaOH. The organic solvents were then removed using the evaporator and H<sub>2</sub>O was added. The precipitate was filtered and washed with water. The solid was then suspended in toluene and evaporated using reduced pressure to remove resting amount of water as an azeotrope. This was repeated 3 times to dry the solid completely and to obtain 40 mg of pure compound **30** (yield: 60.1 %). <sup>1</sup>H NMR (400 MHz, chloroform-*d*)  $\delta$  11.38 (s, 2H), 9.91 (s, 2H), 9.50 (s, 2H), 9.44 (s, 2H), 8.37 (s, 2H), 7.94 (d, *J* = 5.9 Hz, 2H), 7.80 (s, 4H), 7.52 (s, 2H), 7.39 (s, 2H), 7.17 – 7.01 (m, 30H), 4.86 (s, 2H), 4.50 (s, 2H), 4.36 (dd, *J* = 10.9, 5.5 Hz, 4H), 4.29 – 4.24 (m, 2H), 4.10 (dd, *J* = 14.9, 6.9 Hz, 4H), 2.07 – 1.97 (m, 4H), 1.87 (m, *J* = 27.2, 13.8, 6.8 Hz, 6H), 1.69 (m, *J* = 14.7, 7.4 Hz, 7H), 1.51 (t, *J* = 7.1 Hz, 8H), 1.36 – 1.19 (m, 8H), 1.16 – 0.93 (m, 24H), 0.93 (d, *J* = 7.4 Hz, 12H), 0.93 – 0.79 (m, 12H). <sup>13</sup>C NMR (126 MHz, chloroform-*d*)  $\delta$  173.72, 166.39, 165.08, 163.13, 162.37, 161.39, 153.73, 150.78, 150.15, 149.61, 148.83, 145.64, 143.85, 139.60, 130.15, 128.55, 127.40, 127.06, 117.63, 116.89, 116.72, 111.49, 109.55, 107.56, 103.02, 99.80, 97.74, 72.54, 71.75, 70.97, 70.88, 70.53, 69.13, 60.29, 41.02, 40.65, 40.38, 40.19, 37.35, 37.00, 32.70, 29.95, 29.59, 27.43, 23.83, 23.59, 23.41, 22.97, 22.85, 21.89, 20.95, 20.41, 14.10, 11.48, 11.14, 10.99, 10.75, 10.58, 0.92. HRMS (ESI<sup>-</sup>) calcd. for C<sub>138</sub>H<sub>159</sub>N<sub>10</sub>O<sub>20</sub> [M-2H]<sup>2-</sup> (m/z): 1138.08608, found: 1138.08451.



Chemical Formula: C<sub>116</sub>H<sub>166</sub>N<sub>8</sub>O<sub>18</sub>

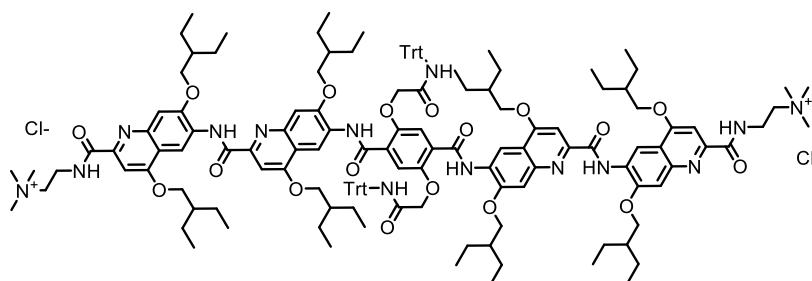
**Compound 31.** Compound **27** (73 mg 1 eq., 0.04 mmol) was dissolved in 3 mL of a mixture of THF/MeOH (4/1). NaOH (14.7 mg, 10 eq., 0.4 mmol) dissolved in 100  $\mu$ L of water was added to this mixture. The suspension was left stirring for 5 h at room temperature. 1 M aqueous HCl solution was added to neutralize the excess of NaOH. The organic solvents were then removed using the evaporator and H<sub>2</sub>O was added. The precipitate was filtered and washed with water. The solid was then suspended in toluene and evaporated using reduced pressure to remove resting amount of water as an azeotrope. This was repeated 3 times to dry the solid completely and to obtain 67.1 mg of pure compound **31** (yield: 93.2 %). <sup>1</sup>H NMR (500 MHz, chloroform-*d*) <sup>1</sup>H NMR (500 MHz, chloroform-*d*)  $\delta$  11.41 (s, 2H), 11.31 (s, 2H), 9.50 (s, 2H), 9.44 (d,  $J$  = 30.3 Hz, 2H), 8.07 (d,  $J$  = 21.9 Hz, 2H), 7.99 (d,  $J$  = 9.0 Hz, 2H), 7.80 – 7.70 (m, 4H), 7.53 (d,  $J$  = 8.6 Hz, 2H), 7.35 (d,  $J$  = 4.3 Hz, 2H), 7.13 (dd,  $J$  = 8.6, 2.4 Hz, 2H), 6.98 (s, 4H), 5.58 (s, 2H), 5.12 – 4.93 (m, 4H), 4.45 – 4.25 (m, 24H), 4.21 – 4.11 (m, 8H), 4.04 – 3.93 (m, 4H), 3.87 – 3.73 (m, 2H), 3.66 (m,  $J$  = 12.0, 7.8, 7.3, 4.1 Hz, 4H), 3.09 (qd,  $J$  = 7.4, 4.1 Hz, 3H), 2.92 – 2.79 (m, 4H), 2.61 (d,  $J$  = 8.3 Hz, 3H), 2.36 (t,  $J$  = 7.5 Hz, 3H), 2.30 – 2.19 (m, 9H), 1.93 – 1.76 (m, 28H), 1.71 – 1.37 (m, 24H), 1.22 – 0.92 (m, 14H). <sup>13</sup>C NMR (126 MHz, chloroform-*d*)  $\delta$  173.03, 167.53, 162.53, 154.70, 152.40, 151.35, 150.21, 149.22, 148.06, 147.46, 146.13, 143.56, 138.92, 136.24, 130.99, 129.71, 128.08, 127.23, 125.11, 124.60, 119.51, 118.10, 117.15, 102.59, 101.40, 98.07, 73.31, 72.30, 71.60, 62.68, 46.78, 46.37, 45.97, 45.81, 45.55, 42.32, 41.44, 41.06, 40.87, 38.67, 38.41, 37.85, 37.30, 36.94, 32.19, 31.84, 30.75, 30.45, 30.12, 27.94, 27.75, 21.01, 20.77, 17.81, 14.82, 14.45, 11.88, 11.53, 11.20. HRMS (ESI-) calcd. for C<sub>115</sub>H<sub>163</sub>N<sub>8</sub>O<sub>18</sub> [M-H]<sup>-</sup> (m/z): 1958.22216, found: 1958.20139.



Chemical Formula:  $C_{131}H_{177}N_{13}O_{17}^{2+}$

**Compound 32.** Compound **29** (100 mg, 1 eq., 0.049 mmol) was dissolved in 1.5 mL of dry DCM, followed by the addition of pentafluorophenol (45 mg, 5eq., 0.24 mmol), EDC (47 mg, 5 eq. 0.24 mmol) and DIPEA (59  $\mu$ L, 7 eq. 0.34 mmol). The reaction was stirred at room temperature for 7 days. The solution was then evaporated and the crude material purified by flash chromatography using DCM as eluent to give 27 mg of PFP ester (yield: 15.6 %) It was directly then used for the next step. The purified PFP ester (20mg 1.0 eq., 0.008 mmol), was solubilized in 2.5 mL of a dry THF/DCM mixture (1:1 vol/vol) containing (2-aminoethyl)-trimethyl-ammonium chloride hydrochloride (14.8 mg 10 eq., 0.08 mmol) and DIPEA (28.7  $\mu$ L, 20 eq. 0.16 mmol) and stirred at 40 °C for 3 days. Solvents were evaporated and the solid suspended in acetonitrile and filtered. The solid was then suspended in water and washed 2 times with water. The suspension was then centrifuged 10 minutes with 4300 rpm and the supernatant removed. This process was repeated 3 times. The solid is finally suspended in water and freeze dried to give 1.6 mg of **32** (yield: 8.6 %) as a white powder.  $^1H$  NMR (500 MHz, DMSO- $d_6$ )  $\delta$  11.26 (s, 1H), 11.24 (s, 1H), 10.63 (s, 1H), 10.59 (s, 1H), 10.43 (s, 1H), 9.66 (t,  $J = 1.8$  Hz, 1H), 9.42 (s, 1H), 9.35 – 9.31 (m, 1H), 9.20 (s, 1H), 9.14 (s, 1H), 8.18 (s, 1H), 7.90 (s, 1H), 7.87 (s, 1H), 7.73 (d,  $J = 7.0$  Hz, 1H), 7.53 (s, 1H), 7.51 (d,  $J = 7.8$  Hz, 1H), 7.45 – 7.38 (m, 1H), 7.36 (d,  $J = 8.0$  Hz, 1H), 7.34 – 7.28 (m, 1H), 7.29 – 7.24 (m, 1H), 7.19 (s, 6H), 7.18 (d,  $J = 2.1$  Hz, 6H), 7.16 (dd,  $J = 5.8, 3.6$  Hz, 6H), 7.13 (s, 1H), 7.11 – 7.09 (m, 1H), 5.65 (d,  $J = 4.0$  Hz, 2H), 5.60 (s, 2H), 5.57 (s, 2H), 5.33 – 5.28 (m, 2H), 5.16 (s, 2H), 4.32 (s, 2H), 4.28 (s, 9H), 4.25 (d,  $J = 5.2$  Hz, 3H), 4.17 – 4.13 (m, 4H), 4.12 – 4.09 (m, 2H), 3.97 (d,  $J = 5.1$  Hz, 12H), 3.92 – 3.81 (m, 1H), 3.62 (dt,  $J = 13.0, 5.9$  Hz, 2H), 3.19 (s, 12H), 3.14 – 3.09 (m, 12H), 2.63 (m,  $J = 1.9$  Hz, 8H), 2.54 (m,  $J = 2.0$  Hz, 8H), 2.46 (m,  $J = 1.9$  Hz, 1H), 2.36 (m,  $J = 1.9$  Hz, 1H), 2.29 – 2.25 (m, 1H), 2.15 (d,  $J = 7.4$  Hz, 1H), 2.08 (d,  $J = 2.2$  Hz, 1H), 1.89 – 1.77 (m, 1H), 1.65 – 1.60 (m, 1H), 1.51 (dd,  $J = 14.5, 9.6$  Hz, 4H), 1.37 – 1.34 (m, 1H), 1.18 (t,  $J = 7.1$  Hz, 48H), 1.09 – 1.05 (m, 9H), 1.04 – 0.97  $^{13}C$  NMR (126 MHz, chloroform- $d$ )  $\delta$  179.00, 171.55,

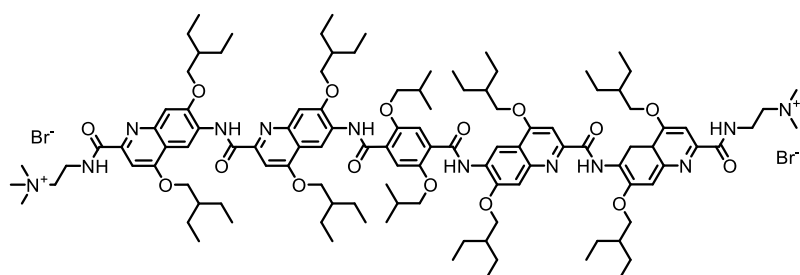
165.58, 163.59, 163.50, 163.01, 162.70, 161.86, 156.72, 156.11, 153.31, 153.10, 152.41, 151.20, 150.95, 150.11, 147.23, 146.15, 145.04, 144.35, 143.30, 142.21, 140.82, 139.42, 136.30, 127.62, 130.74, 129.88, 129.16, 128.96, 128.73, 128.40, 127.92, 127.56, 126.21, 125.31, 120.52, 120.75, 118.91, 118.08, 117.21, 112.00, 109.83, 108.85, 108.11, 101.53, 98.30, 72.23, 71.58, 71.46, 71.03, 70.70, 69.64, 68.16, 60.79, 41.47, 41.15, 41.05, 40.81, 40.75, 40.60, 40.67, 39.11, 38.61, 37.90, 37.65, 34.90, 33.75, 32.32, 31.84, 30.97, 30.59, 30.44, 30.10, 30.06, 29.76, 29.53, 29.39, 29.25, 27.91, 25.17, 24.20, 24.10, 24.05, 23.37, 23.09, 21.45, 20.71, 20.14, 20.11, 19.90, 19.75, 19.10, 18.80, 14.60, 14.52, 11.79, 11.65, 11.49, 11.08, 1.42. HRMS (ESI+) calcd. for  $C_{131}H_{178}N_{13}O_{17}$   $[M+2H]^{2+}$  (m/z): 1102.16892, found: 1102.17201



Chemical Formula:  $C_{148}H_{186}N_{14}O_{18}^{2+}$

**Compound 33.** Compound **30** (40 mg, 1 eq., 0.02 mmol) was dissolved in 1 mL of dry DCM, followed by the addition of pentafluorophenol (16 mg 5eq. 0.1 mmol), EDC (17 mg, 5 eq. 0.1 mmol) and DIPEA (21  $\mu$ L, 7 eq., 0.14 mmol). The reaction mixture was stirred at room temperature for 7 days. The solution was then evaporated and the crude material purified by flash chromatography using 100 % EtOAc as eluent to give 31 mg of PFP ester (yield: 67.6 %). It was then directly used for the next step. The purified PFP ester (31 mg, 1 eq., 0.012 mmol) was solubilized in 2.5 mL of a dry THF/DCM mixture (1:1 vol/vol) containing (2-aminoethyl)-trimethyl-ammonium chloride hydrochloride (20.8 mg 10 eq., 0.12 mmol) and DIPEA (40  $\mu$ L 20 eq. 0.24 mmol) and stirred at 40 °C for 3 days. Solvents were evaporated and the solid suspended in acetonitrile and filtered. The solid was then suspended in water and washed 2 times with water. The suspension was then centrifuged 10 minutes with 4300 rpm and the supernatant removed. This process was repeated 3 times. The solid was finally suspended in water and freeze dried to give 3.2 mg of **33** (yield: 10.2 %) as a white powder.  $^1H$  NMR (400 MHz, )  $\delta$  10.89 (s, 2H), 9.92 (s, 2H), 9.03 (s, 4H), 8.90 (s, 2H), 7.59 (s, 2H), 7.52 (s, 2H), 7.45 (d,  $J$  = 10.5 Hz, 4H), 6.99 (s, 2H), 4.04 (s, 4H), 3.85 (s,

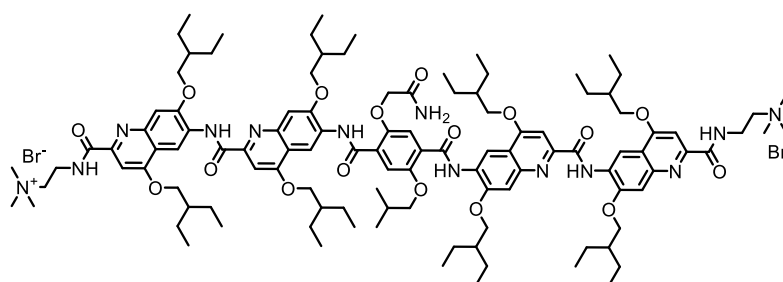
10H), 3.71 – 3.63 (m, 6H), 3.52 (s, 4H), 3.27 (t,  $J = 6.5$  Hz, 6H), 1.67 (s, 12H), 1.55 (s, 6H), 1.49 (s, 2H), 1.40 (s, 2H), 1.35 (dd,  $J = 14.8, 7.3$  Hz, 4H), 1.20 (q,  $J = 7.4$  Hz, 18H), 1.08 (t,  $J = 7.3$  Hz, 2H), 0.81 (s, 9H), 0.77 (s, 14H), 0.64 (t,  $J = 7.5$  Hz, 14H), 0.58 (d,  $J = 7.8$  Hz, 16H), 0.52 (dd,  $J = 16.2, 8.7$  Hz, 22H), 0.38 (d,  $J = 10.7$  Hz, 14H).  $^{13}\text{C}$  NMR (126 MHz,  $\text{CDCl}_3$ )  $\delta$  165.32, 163.34, 163.25, 162.76, 162.45, 152.16, 150.94, 150.70, 149.85, 146.98, 145.89, 144.79, 144.10, 142.54, 140.52, 139.20, 139.13, 137.20, 137.10, 130.49, 129.63, 129.51, 128.81, 128.71, 128.47, 128.15, 127.30, 126.11, 125.94, 120.30, 118.66, 117.83, 116.96, 111.75, 109.57, 108.60, 107.86, 101.27, 98.04, 71.98, 71.33, 71.21, 70.77, 70.45, 69.39, 60.54, 41.22, 40.90, 40.80, 40.42, 33.50, 32.07, 31.58, 30.34, 30.18, 29.84, 29.51, 29.27, 28.99, 23.95, 23.85, 23.80, 23.11, 22.84, 21.20, 14.34, 14.27, 11.54, 11.39, 11.37, 11.34, 10.83, 1.17. HRMS (ESI+) calcd. for  $\text{C}_{148}\text{H}_{187}\text{N}_{14}\text{O}_{18}^{2+}$   $[\text{M}+2\text{H}]^{2+}$  (m/z): 1223.70392, found: 1223.70864.



Chemical Formula:  $\text{C}_{114}\text{H}_{170}\text{N}_{12}\text{O}_{16}^{2+}$

**Compound 1.** Compound **28** (72 mg, 1 eq., 0.04 mmol) was dissolved in 3 mL of dry DCM, followed by the addition of pentafluorophenol (36 mg 5 eq. 0.2 mmol), EDC (39 mg 5 eq. 0.2 mmol) and DIPEA (34  $\mu\text{L}$ , 5 eq. 0.2 mmol). The reaction mixture was stirred at room temperature for 7 days. The solution was then evaporated and the crude material purified by flash chromatography using DCM as eluent to give 41 mg of PFP ester intermediate (yield: 48.0 %). It was then directly used for the next step. The purified PFP ester (50 mg 1.0 eq., 0.028 mmol), was solubilized in 4 mL of a dry THF/DCM mixture (1:1 vol/vol) containing (2-Aminoethyl)-trimethylammonium chloride hydrochloride (49 mg, 10 eq., 0.28 mmol) and DIPEA (95  $\mu\text{L}$ , 20 eq., 0.56 mmol) and stirred at 40  $^{\circ}\text{C}$  for 3 days. Solvents were evaporated and the solid suspended in acetonitrile and filtered. The solid was then suspended in water and washed 2 times with water. The suspension was then centrifuged 10 minutes with 4300 rpm and the supernatant removed. This process was repeated 3 times. The solid was finally suspended in water and freeze dried to give 58 mg of **1** (yield:84.4 %). The white powder was further used for Ion exchange chromatography.  $^1\text{H}$  NMR  $\delta$  11.31 (d,  $J = 6.4$

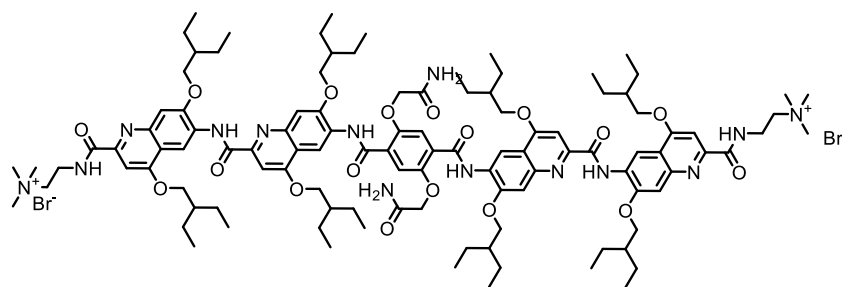
Hz, 2H), 10.31 (s, 2H), 9.93 (s, 2H), 9.44 (s, 2H), 9.42 (d,  $J = 2.6$  Hz, 2H), 9.36 (s, 2H), 8.02 (s, 2H), 7.87 (s, 2H), 7.79 (s, 2H), 7.77 (s, 2H), 7.65 (d,  $J = 1.2$  Hz, 2H), 7.55 (s, 2H), 7.46 (s, 2H), 7.36 (s, 2H), 7.14 (s, 2H), 7.13 (d,  $J = 2.0$  Hz, 2H), 7.11 (s, 2H), 7.09 (d,  $J = 1.5$  Hz, 2H), 7.07 (s, 2H), 7.05 – 7.03 (m, 2H), 4.30 (dd,  $J = 9.6, 5.7$  Hz, 2H), 4.23 (t,  $J = 6.1$  Hz, 2H), 4.16 (d,  $J = 6.5$  Hz, 2H), 4.11 (s, 4H), 4.07 (s, 4H), 2.17 (s, 24H), 2.00 (s, 18H), 1.90 – 1.85 (m, 8H), 1.84 (d,  $J = 4.6$  Hz, 8H), 1.77 (dd,  $J = 12.2, 7.2$  Hz, 6H), 1.65 (d,  $J = 9.2$  Hz, 12H), 1.51 (dq,  $J = 13.9, 7.1$  Hz, 12H), 1.13 – 1.01 (m, 4H), 1.05 – 0.98 (m, 24H), 0.94 (dt,  $J = 9.2, 7.5$  Hz, 12H).  $^{13}\text{C}$  (126 MHz, chloroform-*d*)  $\delta$  165.58, 164.46, 162.18, 162.09, 161.98, 161.50, 161.30, 161.17, 150.83, 150.69, 150.56, 149.85, 149.58, 149.51, 147.78, 128.55 (d,  $J = 9.3$  Hz), 127.97, 126.15 (d,  $J = 19.4$  Hz), 116.84, 116.63, 115.63, 111.07, 110.48, 108.51, 107.38, 106.77, 99.25, 96.81 (d,  $J = 10.4$  Hz), 70.78, 70.14, 70.04, 69.97, 69.53, 69.08, 68.16, 52.13, 40.07, 40.03, 39.66, 39.62, 39.43, 39.28, 29.30, 29.04, 28.71, 27.06, 22.81, 22.79, 22.03, 21.95, 18.18, 10.39, 10.35, 10.18, 9.79, 9.69, 0.01. HRMS (ESI+) calcd. for  $\text{C}_{114}\text{H}_{172}\text{N}_{12}\text{O}_{16}$   $[\text{M}+2\text{H}]^{2+}$  (m/z): 980.6378, found: 980.88647.



Chemical Formula:  $\text{C}_{112}\text{H}_{163}\text{N}_{13}\text{O}_{17}^{2+}$

**Compound 2.** Compound **32** (1.6 mg, 1 eq.) was solubilized in 4 mL of a dry TFA/DCM mixture (3/1), containing 1 eq. TRIS scavenger and stirred at room temperature for 3 hours. Solvents were evaporated and the solid was suspended in 5 mL of diethyl ether and centrifuged. The pellet was then suspended in water and lyophilized to obtain 1.4 mg of **2** (yield: quant. %). The white powder was further used for Ion exchange chromatography.  $^1\text{H}$  NMR (500 MHz, DMSO-*d*<sub>6</sub>)  $\delta$  11.19 (s, 1H), 10.70 (s, 1H), 9.33 (s, 1H), 9.28 (s, 1H), 9.19 (s, 1H), 7.82 (s, 1H), 7.78 (s, 1H), 7.75 (s, 1H), 7.49 (s, 1H), 7.33 (s, 1H), 4.89 (s, 2H), 4.38 (d,  $J = 5.7$  Hz, 2H), 4.26 (d,  $J = 9.4$  Hz, 4H), 4.14 (d,  $J = 6.4$  Hz, 2H), 3.80 (d,  $J = 7.9$  Hz, 2H), 3.58 (t,  $J = 6.3$  Hz, 2H), 1.97 (m,  $J = 15.6, 10.2, 6.1$  Hz, 2H), 1.86 (m,  $J = 10.8, 5.4, 4.9$  Hz, 2H), 1.77 (m,  $J = 17.3, 7.2$  Hz, 3H), 1.65 – 1.58 (m, 7H), 1.52 (m,  $J = 14.0, 7.0$  Hz, 12H), 1.25 (s, 12H), 1.22 (d,  $J = 7.1$

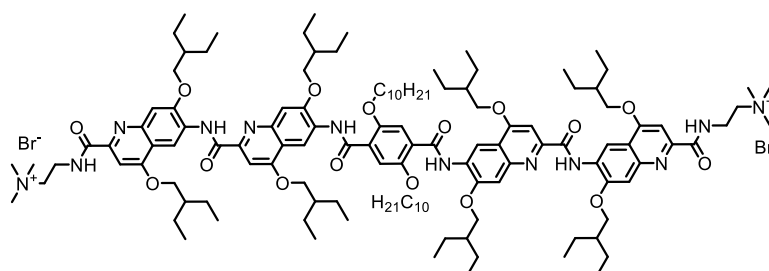
Hz, 12H), 1.18 (d,  $J = 6.6$  Hz, 12H), 1.16 – 1.11 (m, 9H), 1.05 (d,  $J = 3.3$  Hz, 6H), 1.02 (m,  $J = 10.2, 7.2, 3.4$  Hz, 24H), 0.96 (m,  $J = 7.2, 4.2$  Hz, 24H).  $^{13}\text{C}$  NMR (126 MHz, chloroform- $d$ )  $\delta$  166.99, 165.87, 163.59, 163.50, 163.39, 162.91, 162.72, 162.58, 152.24, 152.10, 152.08, 151.97, 151.27, 150.99, 150.92, 149.20, 148.20, 148.15, 147.01, 146.22, 146.15, 144.41, 130.00, 129.92, 129.38, 128.98, 128.75, 128.36, 127.64, 127.61, 127.48, 125.50, 125.46, 125.00, 124.86, 124.80, 118.26, 118.05, 117.98, 117.05, 112.48, 111.89, 109.92, 108.80, 108.19, 108.13, 100.66, 98.40, 98.26, 98.18, 72.19, 71.55, 71.45, 71.38, 70.95, 70.50, 69.58, 53.55, 45.70, 45.63, 45.61, 45.60, 45.00, 41.48, 41.44, 41.07, 41.03, 40.84, 40.69, 37.85, 37.51, 37.29, 34.82, 34.80, 33.19, 31.84, 31.34, 30.72, 30.46, 30.12, 28.47, 27.93, 27.76, 27.51, 27.34, 24.88, 24.60, 24.22, 24.02, 23.45, 23.37, 22.12, 21.40, 21.38, 21.35, 21.01, 20.76, 20.60, 20.50, 20.15, 19.59, 14.60, 14.40, 11.81, 11.76, 11.60, 11.21, 11.10, 2.31, 1.42, 1.12. HRMS (ESI+) calcd. for  $\text{C}_{112}\text{H}_{164}\text{N}_{13}\text{O}_{17}$   $[\text{M}+2\text{H}]^{2+}$  (m/z): 981.61892, found: 981.59484.



Chemical Formula:  $\text{C}_{110}\text{H}_{158}\text{N}_{14}\text{O}_{18}^{2+}$

**Compound 3.** Compound **33** (3.2 mg, 1 eq.) was solubilized in 4 mL of a dry TFA/DCM mixture (3/1), containing 1 eq. TRIS scavenger and stirred at room temperature for 3 hours. Solvents were evaporated and the solid suspended in 5 mL of diethyl ether and centrifuged. The pellet was then suspended in water and lyophilized to obtain 1.4 mg of 3.0 mg of **3** (yield: quant. %) as a white powder with low solubility. The white powder was further used for Ion exchange chromatography.  $^1\text{H}$  NMR (500 MHz, DMSO- $d_6$ )  $\delta$  8.71 (s, 2H), 8.46 (s, 2H), 7.91 (d,  $J = 7.6$  Hz, 4H), 7.73 (d,  $J = 7.5$  Hz, 4H), 7.58 (s, 2H), 7.47 (s, 2H), 7.43 (t,  $J = 7.5$  Hz, 4H), 7.32 (t,  $J = 7.4$  Hz, 4H), 4.47 (d,  $J = 7.2$  Hz, 6H), 4.34 (t,  $J = 7.1$  Hz, 6H), 4.22 (d,  $J = 5.6$  Hz, 8H), 4.11 (d,  $J = 5.7$  Hz, 8H), 1.79 (m,  $J = 18.6, 6.2$  Hz, 8H), 1.49 (m,  $J = 14.0, 6.8$  Hz, 32H), 1.17 (t,  $J = 7.1$  Hz, 18H), 0.93 (m,  $J = 7.5, 2.7$  Hz, 48H).  $^{13}\text{C}$  NMR (126 MHz, DMSO- $d_6$ )  $\delta$  185.70, 179.43, 172.05, 169.99, 168.70, 165.29, 157.03, 155.38, 143.04, 142.23, 140.21, 139.16, 135.36,

133.47, 132.01, 129.91, 128.61, 127.16, 119.60, 115.30, 110.44, 108.46, 106.94, 104.36, 99.14, 97.35, 95.04, 91.87, 90.72, 86.82, 84.68, 78.48, 77.05, 75.88, 73.99, 70.41, 69.99, 68.41, 68.05, 65.84, 60.07, 58.22, 47.19, 45.86, 42.33, 34.24, 22.37, 22.28, 20.38, 18.62, 16.07, 14.69, 13.47, 12.49, 10.40. HRMS (ESI+) calcd. for C<sub>110</sub>H<sub>158</sub>N<sub>14</sub>O<sub>18</sub> [2M+H]<sup>+</sup> (m/z): 982.09784, found: 982.09636



Chemical Formula: C<sub>126</sub>H<sub>192</sub>N<sub>12</sub>O<sub>16</sub><sup>2+</sup> 2Br<sup>-</sup>

**Compound 4.** Compound **31** (67 mg 1.0 eq., 0.034 mmol), was solubilized in 5 mL CHCl<sub>3</sub> containing (2-aminoethyl)-trimethyl-ammonium chloride hydrochloride (18 mg 3 eq., 0.102 mmol), PyBOP (80 mg, 4.5 eq., 0.153 mmol) and DIPEA (58 μL, 10 eq. 0.34 mmol) and stirred at 40 °C for 3 days. Solvents were evaporated and the solid suspended in acetonitrile and filtered. The solid was then suspended in water and washed 2 times with water. The suspension was then centrifuged 10 minutes with 4300 rpm and the supernatant removed. This process was repeated 3 times. The solid was finally suspended in water and freeze dried to give 30 mg of **4** (yield: 41.2 %) as a white powder. The white powder was further used for Ion exchange chromatography. <sup>1</sup>H NMR (500 MHz, DMSO- *d*<sub>6</sub>) δ 11.05 (s, 2H), 10.36 (s, 2H), 9.28 (s, 2H), 9.16 (s, 2H), 8.03 (s, 2H), 7.82 (s, 2H), 7.74 (s, 2H), 7.42 (d, *J* = 16.5 Hz, 4H), 7.17 (s, 2H), 4.35 (s, 4H), 4.26 (s, 4H), 4.21 (s, 4H), 4.12 (s, 4H), 3.20 (s, 17H), 3.13 (s, 6H), 1.97 – 1.91 (m, 2H), 1.88 – 1.71 (m, 6H), 1.62 (h, *J* = 7.0 Hz, 14H), 1.53 (dt, *J* = 14.6, 7.4 Hz, 6H), 1.37 (d, *J* = 17.6 Hz, 2H), 1.37 (s, 6H), 1.26 (dd, *J* = 19.5, 15.7 Hz, 6H), 1.23 (s, 18H), 1.01 (ddt, *J* = 31.7, 28.4, 7.4 Hz, 60H), 0.85 (dt, *J* = 13.4, 5.0 Hz, 4H), 0.64 (t, *J* = 7.2 Hz, 6H). <sup>13</sup>C NMR (101 MHz, chloroform-*d*) δ 206.81, 182.68, 178.48, 173.13, 170.97, 166.40, 163.02, 162.73, 162.32, 159.10, 157.31, 151.51, 151.19, 150.71, 147.60, 146.44, 146.00, 142.85, 138.77, 137.85, 136.17, 129.35, 127.33, 117.65, 117.21, 110.82, 109.32, 108.20, 107.37, 100.07, 97.69, 90.34, 88.70, 83.00, 71.13, 70.79, 70.00, 69.17, 68.15, 65.40, 62.66, 60.21, 52.95, 44.95, 43.64, 40.95, 40.80, 40.46, 34.88, 33.13, 30.75, 27.58, 23.61, 23.47, 20.87, 17.87, 14.02, 11.21, 11.04, 7.59, 5.56, 4.73, 2.13. HRMS (ESI+) calcd. for C<sub>126</sub>H<sub>193</sub>N<sub>12</sub>O<sub>16</sub> [M+2H]<sup>2+</sup> (m/z): 1064.72892, found: 1064.73200



## 5. METHODS FOR BIOPHYSICAL STUDIES

### 5.1. ROFT-lipid mixtures for the membrane template production

#### *ROFT-lipid mixtures in chloroform*

1,2-dioleoyl-*sn*-glycero-3-phosphocholine (PC), 1,2-dioleoyl-*sn*-glycero-3-phosphoethanolamine (PE), 1,2-dioleoyl-*sn*-glycero-3-phospho-L-serine (PS), 1,2-dioleoyl-3-trimethylammonium-propane (DOTAP), Sphingomyelin (Brain) (SM), 1,2-dioleoyl-*sn*-glycero-3-phosphoethanolamine-*N*-(lissaminerhodamine B sulfonyl) (Rh-PE), 1-stearoyl-2-docosahexaenoyl-*sn*-glycero-3-phosphoethanolamine (poly-PE) and cholesterol (Chol) were from Avanti Polar Lipids (USA). Lipid stock solutions in chloroform (10mg/mL) were used. ROFT derivatives were first dissolved in a chloroform/methanol solution (1:1) and then mixed with the chloroform solution of lipids in desired proportions. The excitation/emission spectra of the intrinsic ROFT fluorescence in chloroform are shown in Fig. S1A, B. The stock solutions, stored at -20C°, were further used to prepare, on daily basis, multilamellar ROFT-lipid vesicles and ROFT-lipid solution in squalene or decane.

#### *ROFT-lipid mixtures in squalene/decane*

Appropriate volumes of ROFT-lipid stock solution in chloroform were placed in a 1.5 ml safe-lock Eppendorf tube and dried under vacuum for 30 minutes, to evaporate solvent, with ROFT-lipid mix forming a dry film on the tube wall. Squalene or decane (both HPLC grade, SigmaAldrich) was added to the tube and dissolved the film, the final concentration of ROFT-lipid mixture in squalene was ~20mg/mL.

#### *Lipid-ROFT Multi-lamellar Vesicles (MLVs)*

The dry ROFT-lipid film was formed in the Eppendorf tube. MLVs were formed after hydrating lipid film with 1mM HEPES pH 7.0 solution and vortexing until removing all the film from the tube wall <sup>14</sup>. For the production of GUVs containing high amounts of ROFTs (99:1 4:Rh-DOPE) the detergent (Triton x100, 2-10v/v) was added to the hydrating solution. ROFT incorporation to MLVs was verified by fluorometry (on PTI QuantaMaster fluorometer, Horriba Scientific) using the intrinsic fluorescence of the ROFT species (370/450 nm excitation/emission wavelengths, Fig. S1C).

## 5.2. Membrane templates

### *Giant Suspended Bilayer (GSB) and unilamellar vesicles (GUVs)*

GSBs and GUVs were prepared by the MLV deposition on silica microbeads as described earlier<sup>14</sup>. 16 ul of MLV sample were deposited on a Teflon film split into 4 drops. A small amount of 40 um silica beads (Microspheres-Nanospheres, USA) was added to each drop. The drops were dried in vacuum for 30-50 minutes to evaporate liquid and obtain the beads covered with ROFT-lipid multilamellar films. Next the dry beads were picked from the Teflon film and placed into a microchamber containing 6 ul of 1M trehalose + 1mM HEPES solution, pH 7. The microchamber was placed for 15 minutes at 60° in a humidity chamber to prehydrate the ROFT-lipid lamellas. After prehydration, the beads were transferred to the working buffer (150 mM KCl 20 mM HEPES 1 mM EDTA, pH 7) in the observation chamber. The coverslip bottom of the observation chamber was pre-treated with bovine serum albumin (BSA) at 0.2 g/l concentration, for 20 minutes at room temperature, to avoid lipids "spilling" from the beads to the glass surface<sup>14</sup>. GSB spontaneously form ("swell") from the ROFT-lipid lamellas on the beads. The swelling was monitored by fluorescence microscopy

(described below). The extent of the swelling was regulated by the amount of ROFT-lipid lamellar deposited on the beads<sup>14</sup>. For small-moderate bead coverage, GSB half-spheres formed and remained attached to the beads throughout the experiments. When the ROFT-lipid amount on the bead was further increased, the swelling resulted in formation of spherical GUVs which spontaneously detached from the beads. Incorporation of ROFTs into GSB and GUV membranes was verified by fluorescence microscopy. For all lipid composition tested, the GSB and GUV membranes contained a small (0.5mol%) amount of Rh-PE (referred to as to "lipid fluorescence").

### *Glass-supported ROFT-lipid bilayers*

To explore the nanostructure of the ROFT-lipid membranes we made glass-supported ROFT-lipid bilayers directly from GUVs. Negatively-charged membranes of ROFT-lipid GUVs stick spontaneously to the glass surface (24 mm glass coverslip (Glasswarefabrik Karl Hecht GmbH, Sondheim, Germany were used) and crush leaving patches of glass-adhered material. After cleaning the glass surface with ethanol followed by plasma-cleaning for 1-2min (Harrick Plasma, Ithaca, NY), the GUV-glass adhesion areas became large and uniform. To achieve that, the following procedure was used. 120  $\mu$ L working buffer containing 150 mM KCL, 20 mM HEPES and 1 mM EDTA were added onto previously prepared 24 mm glass coverslip mounted onto a BioCell coverslip-based liquid cell for the atomic force microscopy measurements (described below). 80  $\mu$ L GUV solution were then added to the glass and vesicles were left to adsorb and extend for 30 min keeping the sample temperature at 60 °C. In order to avoid sample evaporation and ion concentration, after the first 5 min the buffer was constantly exchanged with working buffer at 60 °C for the remaining time. Additional 30 min were left for the samples to equilibrate at room temperature, discarding the

non-adsorbed vesicles by washing the samples 10 times with buffer. The efficiency of repeated rinsing to obtain proper and clean supported lipid bilayers has been reported.<sup>15</sup> This extension and cleaning procedure allowed the formation of bilayers that did not cover the entire substrate surface. The presence of lipid-depleted areas helped with the quantification of bilayer thicknesses. Planar bilayers were then left to equilibrate at room temperature for 20 minutes prior to measurements in order to avoid the presence of possible artifacts.<sup>16</sup> Finally, the BioCell was set to 23 °C to start the AFM measurements

### *Planar Lipid Bilayer*

Horizontal planar lipid bilayers were formed by "painting" technique on Transmission Electron Microscopy (TEM) grids as described earlier.<sup>3</sup> Briefly, a guilder TEM copper grid (200 mesh, Ted Pella, US) was attached to the glass coverslip bottom of the observation chamber using PDMS spacers. The ROFT-lipid solution in squalene was deposited to the grid using a small brush. The solution formed a thick film covering the holes in the grid. Planar lipid bilayers formed by spontaneous thinning of the film in each hole. Vertical lipid bilayers, also known as black lipid membranes (BLM), were formed in a standard two-compartment BLM chamber.<sup>17</sup> The compartments were separated by with a Teflon film partition containing a 100mm circular orifice. The planar bilayers were formed on the orifice from decane-based ROFT-lipid mixtures as described elsewhere.<sup>18,19</sup>

### *Membrane nanotubes (NTs)*

Membrane nanotubes were pulled vertically (from the planar lipid bilayers) and horizontally (from GSBs) by borosilicate patch-pipettes, the tip (diameter of ~1mm) of which was put into tight contact with the reservoir membrane as described elsewhere.<sup>5,14</sup> Formation of the tight contact between the pipette tip and the membrane was monitored by measuring the electrical resistance of the pipette, which shall increase to 1-10GOhm upon formation of the contact.<sup>5</sup> In the GSB system, membrane nanotubes were then pulled by slowly moving the pipette horizontally away from the GSB. The NT formation was controlled by fluorescence microscopy. In the planar bilayer system, before the pulling the membrane patch isolated inside the pipette was ruptured to enable the electrical access to the NT lumen. The pipette then was moved vertically away from the planar bilayer. The NT formation was controlled by conductance measurements as described earlier.<sup>3</sup> The NT length was controlled with 30 nm accuracy by a precise nanopositioning system consisting of a calibrated piezo linear actuator and controller (Newport, model no. ESA-CSA). To create ultra-short NT (sNT<sup>3</sup>) the length of NT was set in the range of 100-300 nm.

### 5.3. Protein expression and purification

Dynamin1 conjugated to monomeric EGFP (Dyn1-mEGFP) was expressed in Sf9 cells transiently transfected with pIEX6 constructs. The protein was purified by affinity chromatography using immobilized GST tagged amphiphysin-II SH3 domain as affinity ligand. Cell pellet was resuspended in buffer containing 20 mM Hepes, pH 7.4, 150 mM NaCl, 1 mM DTT and lysed by sonication. The lysate was clarified by ultracentrifugation and after incubation with amphiphysin-SH3 beads the protein-bound resin was extensively washed in the previous buffer. The elution of the protein was done using the buffer containing 20 mM PIPES, pH 6.1-6.5, 1.2 M NaCl, 10 mM

CaCl<sub>2</sub>, 1 mM DTT and then dialyzed overnight in buffer containing 20 mM Hepes (pH 7.2), 150mM KCl, 1 mM DTT, 1mM EDTA, 1 mM EGTA. The protein was aliquoted in 5 % of glycerol, flash-frozen in liquid nitrogen and stored at -80 °C.

ENTH-meGFP domain was expressed in BL21 *E.coli*. Cell pellet was resuspended in lysis buffer containing 150 mMm KCL, 50 mM HEPES 5 mM imidazole, protease inhibitor and 1 mM DTT and lysed by sonication; the lysate was then centrifuged at 38000 g for 30 minutes, at 4° C. Supernatant was applied to a Ni-NTA resin, eluted with an Imidazol gradient and then dialyzed overnight in buffer containing 150 mMm KCL, 20 mMm HEPES, 1 Mm edta AND 1 mM DTT. Protein was aliquoted in 5 % of glycerol, frozen in liquid nitrogen and stored at -80 °C.

Anexin-V, Alexa fluor™ 488 Ready Flow™ was from Thermo Fisher Scientific.

#### 5.4. Confocal and fluorescence microscopy

TCS SP5 II confocal microscope (Leica Microsystems Gmbh) with 63X/1.2NA oil immersion objective and Nikon Eclipse Ti-E motorized inverted microscope (Nikon) with a CoolLed pE-4000 light source, 100x/1.49 NA oil immersion objective, equipped with Zyla 4.2 sCMOS camera (Andor, Oxford Instruments) were used. The following excitation/emission filter combinations (single band, Semrock) were used: 405/450 nm for ROFTs, 543/590 nm for Rh-PE and 488/510 nm for Dyn1-mEGFP, ENTH-mEGFP and Annexin-V-Alexa488. Images were processed with ImageJ software, as described elsewhere.<sup>20</sup> For the qualitative (yes/no, Table 1) assessment of the ROFT incorporation into GSBs the Intensity Profile tool of ImageJ was used. Detection of the ROFT fluorescence peak with the intensity >3s was scored as incorporation. For the quantitative assessment of the ROFT incorporation at different ROFT:lipid ratios, the ROFT and Rh-PE fluorescence were compared as shown in Fig. S2.

## 5.5. Atomic Force Microscopy

Planar bilayer topography was performed in an UltraSpeed AFM (JPK Instruments, Berlin, Germany) using the 'QI Mode', an imaging mode that performs force curves simultaneously at a low force ( $< 1$  nN). The AFM was coupled to a Leica fluorescence microscope and mounted onto an anti-vibration table and inside an acoustic enclosure (JPK Instruments), in a similar setup and experimental approach as described previously.<sup>21</sup> The BioCell liquid sample holder (JPK Instruments) was used to regulate the temperature at the assay was performed. V-shaped MLCT  $\text{Si}_3\text{N}_4$  cantilevers (Bruker, Billerica, MA) with nominal spring constants of 0.1 or 0.5 N/m were used for bilayer imaging, obtaining  $256 \times 256$  pixel images through 'QI Mode'

## 5.6. Conductance measurements

### *Quantification of the radius and the mean curvature bending rigidity modulus of the NT membrane*

The current through the NT lumen and the trans-membrane potential were simultaneously controlled by the measuring electrode applying a holding potential to the patch-pipette interior and upper NT end (Fig. 3A). The ground electrode held the NT exterior and lower end at zero potential. Axopatch 200B (Molecular Devices, Sunnyvale, CA) patch-clamp amplifier set in the voltage-clamp mode was used to apply the holding potential and simultaneously record the ionic current flowing through the NT lumen. The voltage and the ion current were digitized by the analog-to-digit converter of DigitData 1550 acquisition board (Molecular Devices, Sunnyvale, CA). Radius of NT was evaluated from fitting the dependence of the measured conductance

on NT length with Ohm law for cylindrical conductor, for more details see<sup>3</sup>. The bending rigidity of the NT was measured using nanoscale electro-actuation as described earlier.<sup>3</sup> Briefly, a voltage ramp (50 to 200 mV, 10 mV/s) was applied to the ends of a fixed length sNT, the axial voltage bias coupled with the trans-membrane potential gradient (Fig. S7).<sup>3</sup> The trans-membrane electric field caused transient expansion of the sNT, recorded as the increase of the sNT conductance parameterized by the apparent radius  $r_{NT}$  (Fig. S7).<sup>3</sup> The  $k_{NT}$  and  $r_s$  (the stationary sNT radius at  $U=0$ ) were obtained from the linear regression of  $r_{NT}^{-2}(U^2) = \frac{2\sigma}{k_{NT}} - \frac{cU^2}{3k_{NT}}$  (Fig. S7), where  $c = 1\mu F \cdot sm^{-2}$  – specific capacitance of lipid bilayer, and  $\sigma$  - lateral tension of the reservoir membrane. The dependence of  $k_{NT}$  on the sNT curvature  $J=1/r_s$  was obtained and further analyzed to extract  $k_{flat}$  (Fig. S7C).

The voltage ramp duration was much shorter than the characteristic time ( $\tau$ ) of the field-driven changes of the sNT composition (e.g. in Fig. 4). The time is set by the (quasi-stationary) flux,  $J_f$  of charged membrane species

$$(S15) J_f = -2\pi r D \frac{\partial c}{\partial x} + 2\pi r \frac{Dq\varphi(1-\varphi)}{k_{BT}} \frac{U}{L_p}$$

where,  $D$  is the diffusion coefficient ( $D = \frac{k_{BT}}{4\pi\eta l_{ROFT}}$ ),  $q$  is the elementary charge and  $\varphi$  is the molar (area) fraction of the charged species (**4** molecules) in the inner monolayer of the sNT membrane. The time required to achieve the stationary concentration in the monolayer is:

$$(S16) \tau \sim \frac{S}{J} \approx \frac{2SL_p\eta l_{ROFT}}{r\varphi qU} \approx 5s$$

where  $S \approx 1\mu m^2$  is the total area of the sNT and the membrane patch inside the patch pipette,  $l_4 = 4.5 nm$ ,  $\eta = 84 \cdot 10^{-3} Pa \cdot s$ ,  $L_p \approx 100 nm$ ,  $r \approx 8 nm$ ,  $U \approx 200 mV$ ,  $q = e$ ,  $\varphi \approx 0.1$ .

#### *Estimation of the sNT deformation caused by a single rigid molecule.*

Following our analysis of the small deformations of sNT (see above: 3.2 sNT shape change caused by a single rigid protein molecule),<sup>3</sup> the changes of the sNT luminal volume due to molecular incorporation are related to the conductance change as  $\Delta v = \Delta G \rho L_{NT}^2$ . This equation was used to obtain  $\Delta v$  from the amplitude of the conductance steps measured in the experiment (Fig. 6).

## 5.7 Quantification of the bulk curvature-composition adjustment in newly formed sNT

To measure curvature-driven expulsion of AnV and **4**, we recorded changes of the sNT conductance immediately after its formation (Fig. 3D, S8).<sup>4,6</sup> The conductance changes reflect the diffusion adjustment of the sNT composition driven by curvature stress. The adjustment caused effective softening of the sNT, seen as the gradual constriction (Fig. 3D, S8).<sup>4,6</sup> The corresponding reduction of the luminal conductance was well approximated by an exponential function  $\frac{\delta G}{G_0} = g \left[ \exp\left(-\frac{t}{\tau}\right) - 1 \right]$ , with the fitting yielding  $g$  (Fig. S8). Assuming that the initial sNT composition is similar to that of the reservoir membranes,<sup>6</sup> the fitting parameter  $G$  quantifies the reduction of the effective bending rigidity modulus as  $g = \frac{k_{flat} - k_{NT}}{k_{flat}}$ . This relation was used to calculate  $k_{flat}$  using  $g$  and  $k_{NT}$  measured as described above (see 5.6). If the membrane contained DOPE, the sNT membrane curvature relaxation associated with DOPE redistribution (such as shown in Fig. S8) was measured and subtracted from the total relaxation amplitude measured with AnV and **4**.

## 5.8. Boundary potential measurements

The intermembrane electric field compensation method was used to measure the electrical boundary potential of planar lipid bilayers containing ROFTs membrane.<sup>22</sup> The method relies on the non-monotonous voltage dependence of the specific membrane capacitance  $C_{sp}$  due to membrane electrostriction:

$$(S17) \quad C_{sp} = C_{sp,0} + \alpha V_{TM}^2$$

where  $C_{o,sp}$  is the initial membrane capacitance,  $V_{TM}$  is boundary potential difference, and  $\alpha$  is the electrostriction coefficient.  $V_{TM}$  changes could be measured in real time by applying the sinewave electric potential  $v \sin(\omega t)$  across the membrane.<sup>18,22</sup> It follows from Eq.16 that the resulting capacitive current contains higher harmonics, with the second harmonic amplitude could be expressed as  $3\alpha\omega V_{TM} v^2$ . When the electrolytes in the two compartments of the chamber have similar composition and pH, no trans-membrane potential is generated as the boundary potentials caused by ROTFs in the two membrane monolayers cancel each other (Fig. S4A). In this case, the amplitude of

the second harmonic signal is zero. Increasing the pH on one side of the membrane leads to the emergence of the boundary potential  $V_{TM}$  due to the asymmetrical charging of membrane leaflets (Fig. S4A). The amplitude of the second harmonic current could be measured by applying a compensatory holding potential across the membrane.<sup>18</sup> The measurements were performed on vertical decane-based ROFT-lipid membranes. A low-frequency sinewave holding potential with  $\omega = 300$  Hz and  $v = 50$  mV was used. The second harmonic of capacitance current was measured with the aid of a lock-in amplifier (Model SR830 Stanford Research Systems, USA). The in-house controlling software provided negative feedback that maintained zero second harmonics by adjusting the compensatory holding potential every 0.5 s. The changes of the compensatory potential with time are shown in Fig. S4B.

## 6. METHODS FOR CRYSTALLOGRAPHY

Single crystal X-ray diffraction data for **23** and **5** were collected with a Rigaku FRX rotating anode (2.97 kW) diffractometer at the IECB x-ray facility (CNRS UMS 3033 – INSERM US001, University of Bordeaux). CuK $\alpha$  radiation monochromated with high flux Osmic Varimax mirrors was used for data collection. The x-ray source is equipped with a Dectris Pilatus 200K detector and an AFC11 partial chi goniometer allowing omega scans. The crystals were mounted on a cryoloop and flashfrozen under a nitrogen gas stream at 130(2) K. Data were processed with the CrysAlis PRO software.<sup>23</sup> The structures were solved with the ShelXT<sup>24</sup> structure solution program using Intrinsic Phasing. The Olex2 suite<sup>25</sup> was used for models building and structures refinement with the ShelXL<sup>24</sup> package running Least Squares minimization. Only non-H atoms were refined with anisotropic displacement parameters. H atoms were positioned geometrically and constrained depending on their environment. Those H-atoms were refined in the riding-model approximation, with  $U_{iso}(H)=1.2U_{eq}$  (CH, CH<sub>2</sub>, NH). DFIX, AFIX, and SIMU restraints were apply to model geometry of the molecules and thermal motion parameters for structure **5**.

The checkcif analysis of the final structure of **5** contained a number of A-level alerts that are inherent to the poor quality of the data and to disorder in the structure. These alerts and what they correspond to are listed below:

*Alerts due to the inherent low quality of the data. All crystals measured yielded similar results:*

SHFSU01\_ALERT\_2\_A The absolute value of parameter shift to su ratio > 0.20. Absolute value of the parameter shift to su ratio given 2.012. Additional refinement cycles may be required.

THETM01\_ALERT\_3\_A The value of  $\sin(\theta_{\max})/\text{wavelength}$  is less than Calculated  $\sin(\theta_{\max})/\text{wavelength} = 0.4177$

PLAT023\_ALERT\_3\_A Resolution (too) Low [ $\sin(\theta)/\text{Lambda}$ ]

PLAT088\_ALERT\_3\_A Poor Data / Parameter Ratio

*Alerts related to refinement cycles: additional refinement cycles did not improve the results:*

PLAT080\_ALERT\_2\_A Maximum Shift/Error

*Alerts related to the fact that the structure is large with disordered regions*

PLAT234\_ALERT\_4\_A Large Hirshfeld Difference O1J --

PLAT234\_ALERT\_4\_A Large Hirshfeld Difference C2 --C033

PLAT234\_ALERT\_4\_A Large Hirshfeld Difference C018 --C02U .

PLAT234\_ALERT\_4\_A Large Hirshfeld Difference C02E --C02G .

PLAT234\_ALERT\_4\_A Large Hirshfeld Difference C02P --C03E .

PLAT234\_ALERT\_4\_A Large Hirshfeld Difference C02U --C03B .

PLAT234\_ALERT\_4\_A Large Hirshfeld Difference C031 --C032 .

PLAT234\_ALERT\_4\_A Large Hirshfeld Difference C034 --C03G .

PLAT410\_ALERT\_2\_A Short Intra H...H Contact H8..H01E . 1.78 Ang. x,y,z = 1\_555

PLAT412\_ALERT\_2\_A Short Intra XH3 .. XHn H3A ..H40 . x,y,z

PLAT412\_ALERT\_2\_A Short Intra XH3 .. XHn H8 ..H10 . x,y,z

### **Crystal data and structure refinement for 5:**

Identification code	<b>5</b>
Empirical formula	$\text{C}_{106}\text{H}_{146}\text{N}_8\text{O}_{18}$
Formula weight	1820.30
Temperature/K	130
Crystal system	monoclinic
Space group	C2/c
a/Å	13.365(3)

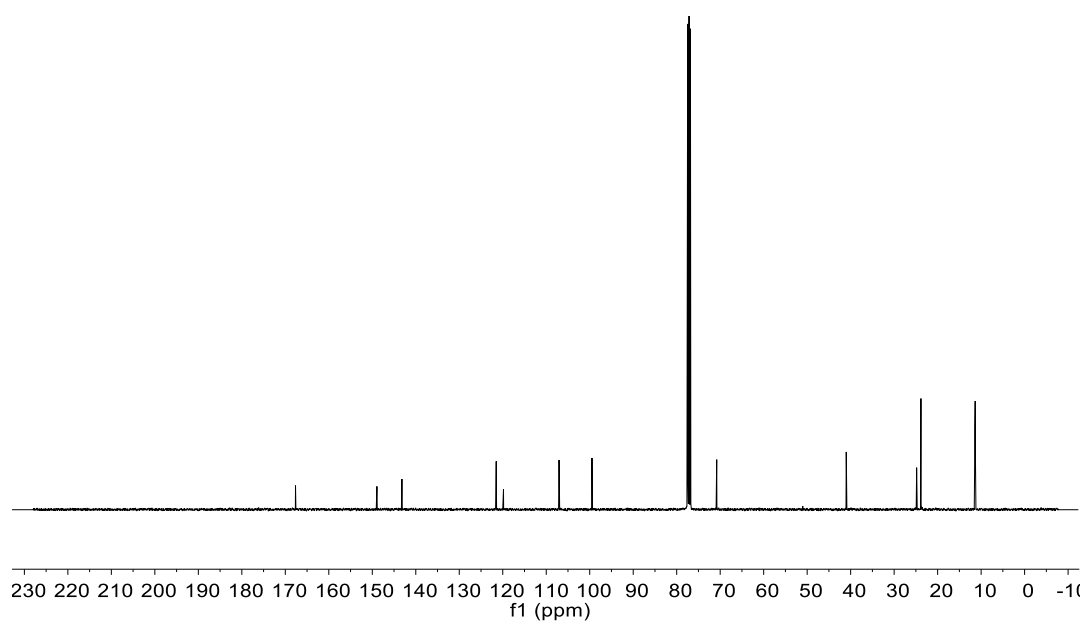
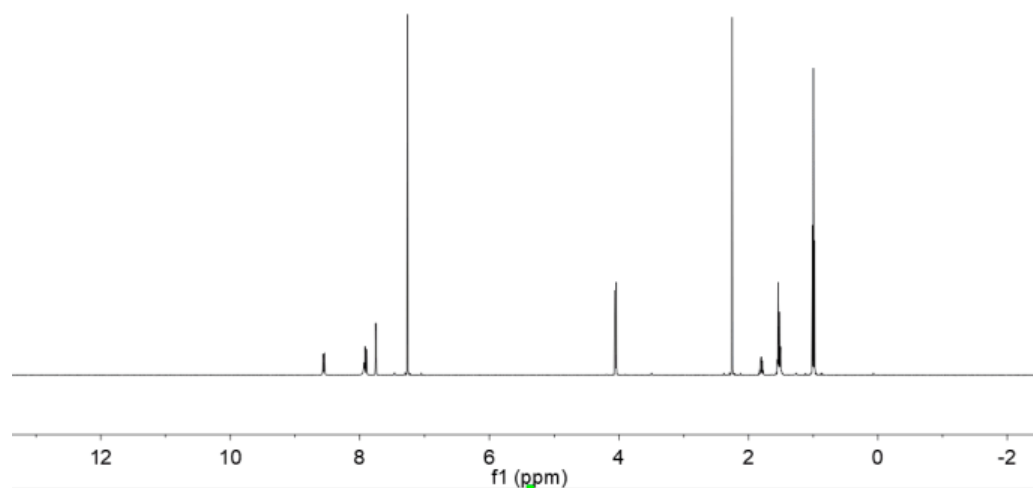
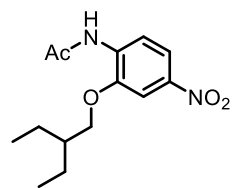
b/Å	54.642(11)
c/Å	30.633(6)
α/°	90
β/°	102.53(3)
γ/°	90
Volume/Å <sup>3</sup>	21837(8)
Z	8
ρ <sub>calc</sub> /cm <sup>3</sup>	1.107
μ/mm <sup>-1</sup>	0.604
F(000)	7856.0
Crystal size/mm <sup>3</sup>	0.1 × 0.1 × 0.1
Radiation	CuKα (λ = 1.54178)
2θ range for data collection/°	6.47 to 80.174
Index ranges	-11 ≤ h ≤ 11, -45 ≤ k ≤ 45, -25 ≤ l ≤ 23
Reflections collected	41832
Independent reflections	6552 [R <sub>int</sub> = 0.1345, R <sub>sigma</sub> = 0.0873]
Data/restraints/parameters	6552/2381/1211
Goodness-of-fit on F <sup>2</sup>	1.326
Final R indexes [I > 2σ (I)]	R <sub>1</sub> = 0.1311, wR <sub>2</sub> = 0.3425
Final R indexes [all data]	R <sub>1</sub> = 0.2002, wR <sub>2</sub> = 0.3977
CCDC #	2080181

### Crystal data and structure refinement for **23**:

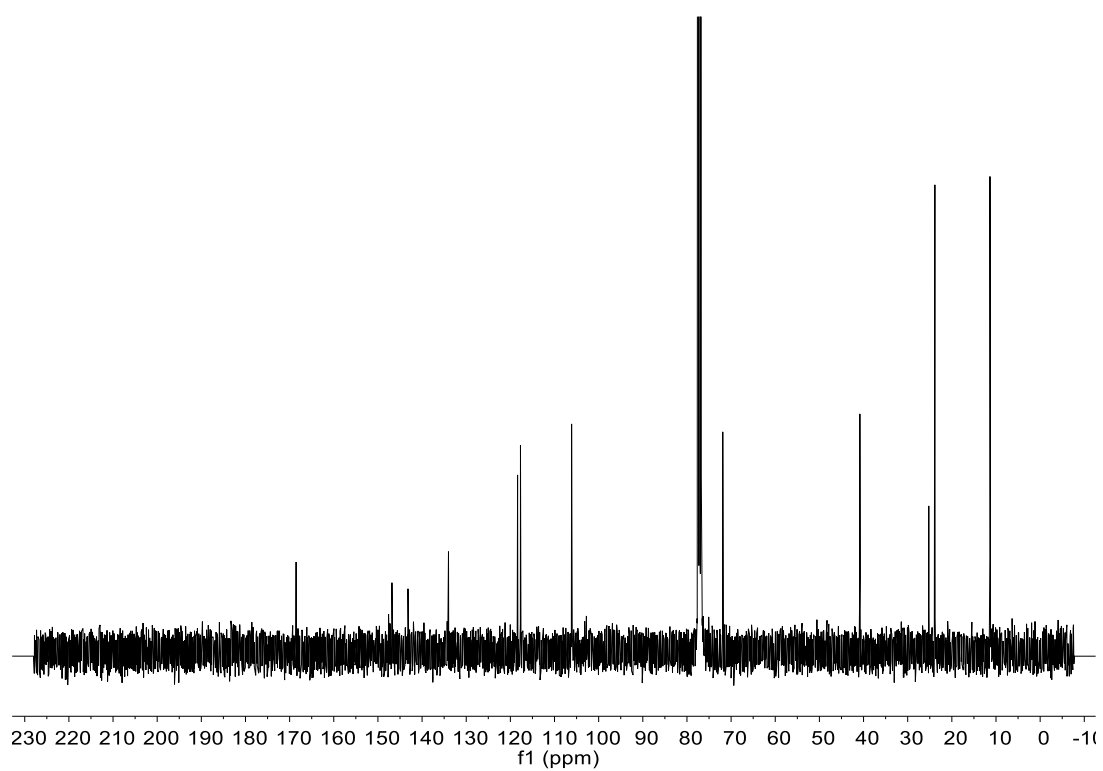
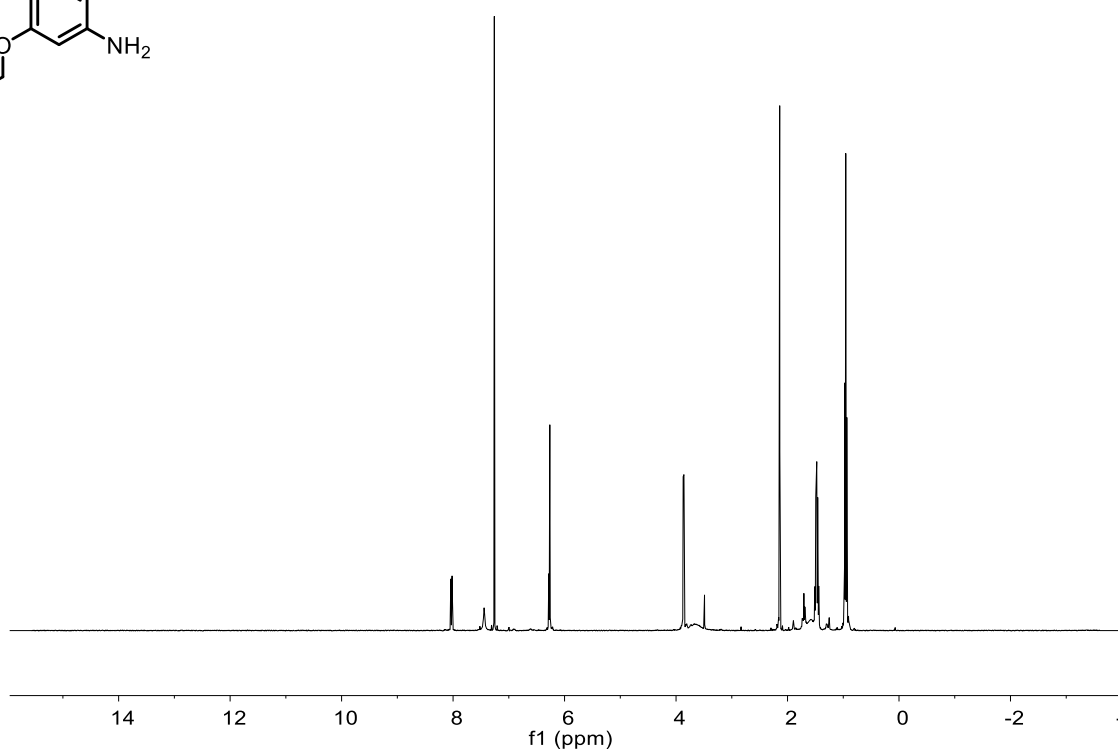
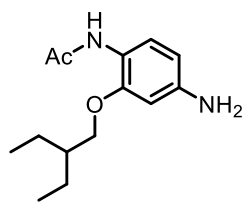
Identification code	<b>23</b>
Empirical formula	C <sub>50</sub> H <sub>72</sub> N <sub>4</sub> O <sub>9</sub>
Formula weight	873.11

Temperature/K	130
Crystal system	triclinic
Space group	P-1
a/Å	11.4426(7)
b/Å	14.5963(17)
c/Å	16.636(3)
$\alpha$ /°	92.51(5)
$\beta$ /°	105.16(3)
$\gamma$ /°	113.02(3)
Volume/Å <sup>3</sup>	2434.7(8)
Z	2
$\rho_{\text{calc}}$ /cm <sup>3</sup>	1.191
$\mu$ /mm <sup>-1</sup>	0.655
F(000)	944.0
Crystal size/mm <sup>3</sup>	0.2 × 0.2 × 0.2
Radiation	CuK $\alpha$ ( $\lambda$ = 1.54178)
2 $\theta$ range for data collection/°	5.58 to 136.484
Index ranges	-13 ≤ h ≤ 13, -17 ≤ k ≤ 17, -20 ≤ l ≤ 20
Reflections collected	33440
Independent reflections	8100 [ $R_{\text{int}}$ = 0.0230, $R_{\text{sigma}}$ = 0.0196]
Data/restraints/parameters	8100/0/580
Goodness-of-fit on F <sup>2</sup>	1.080
Final R indexes [ $I > 2\sigma$ (I)]	$R_1$ = 0.0470, $wR_2$ = 0.1385
Final R indexes [all data]	$R_1$ = 0.0524, $wR_2$ = 0.1430
CCDC #	2080180

## 7 NMR spectra of new compounds

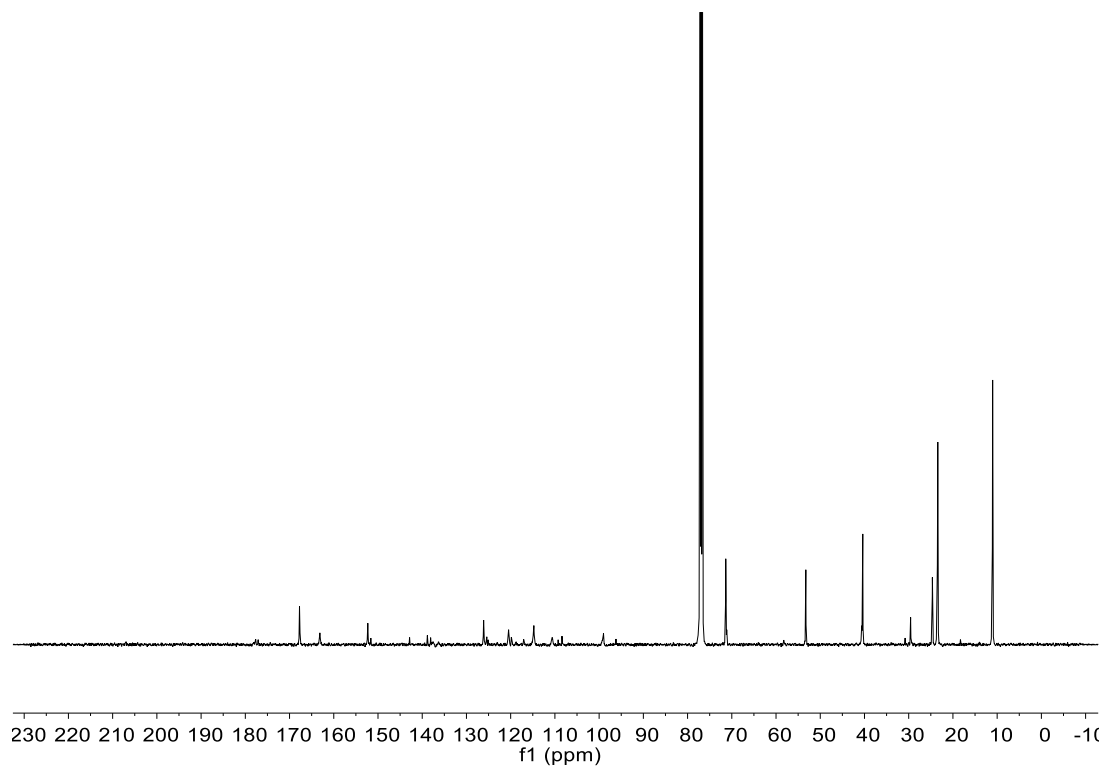
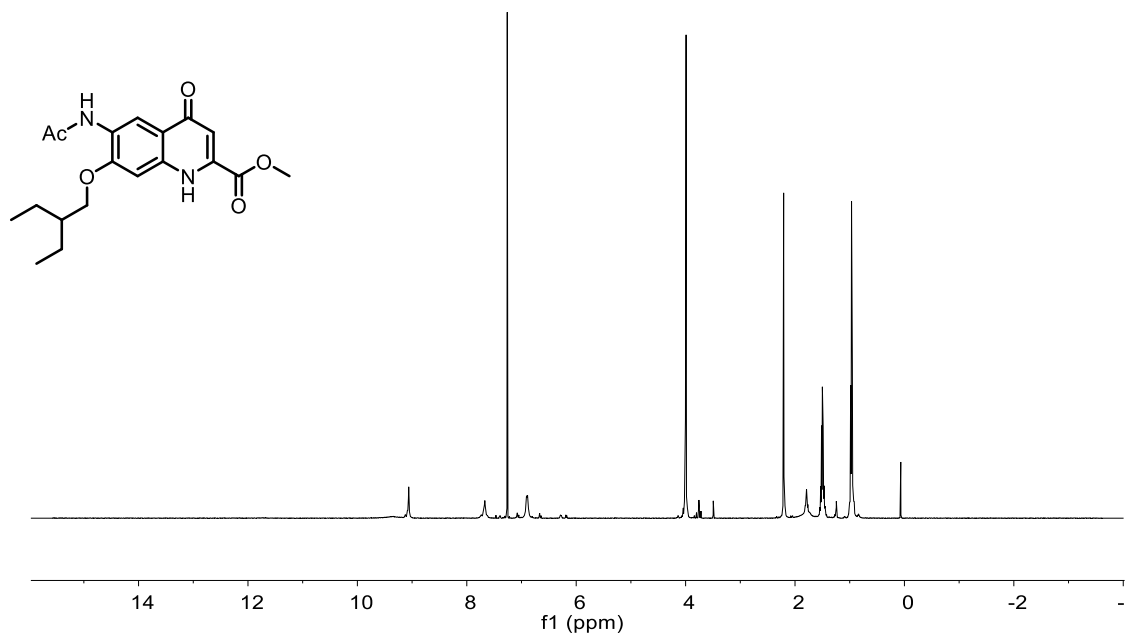


<sup>1</sup>H (500 MHz, CDCl<sub>3</sub>, 298 K) and <sup>13</sup>C (101 MHz, CDCl<sub>3</sub>, 298 K) NMR spectra of compound **8**

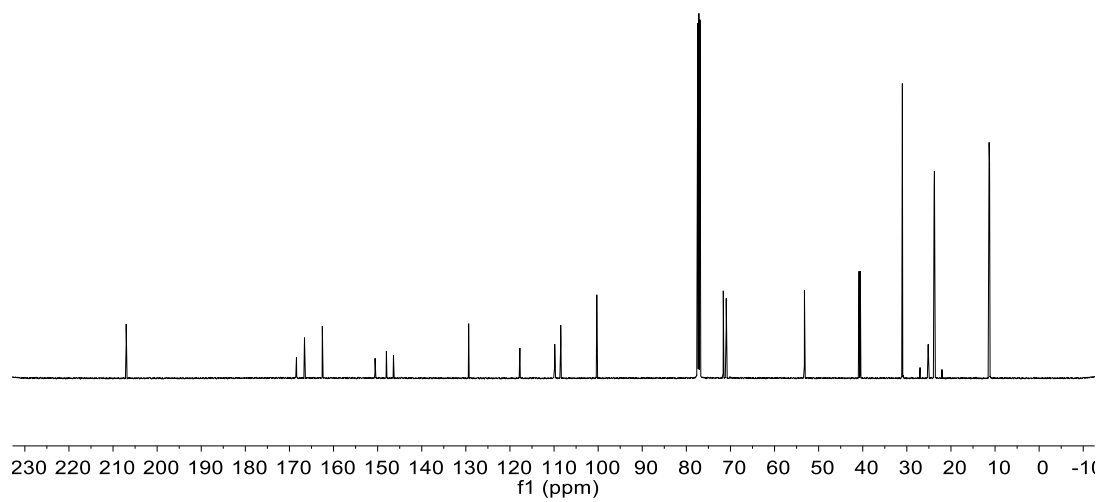
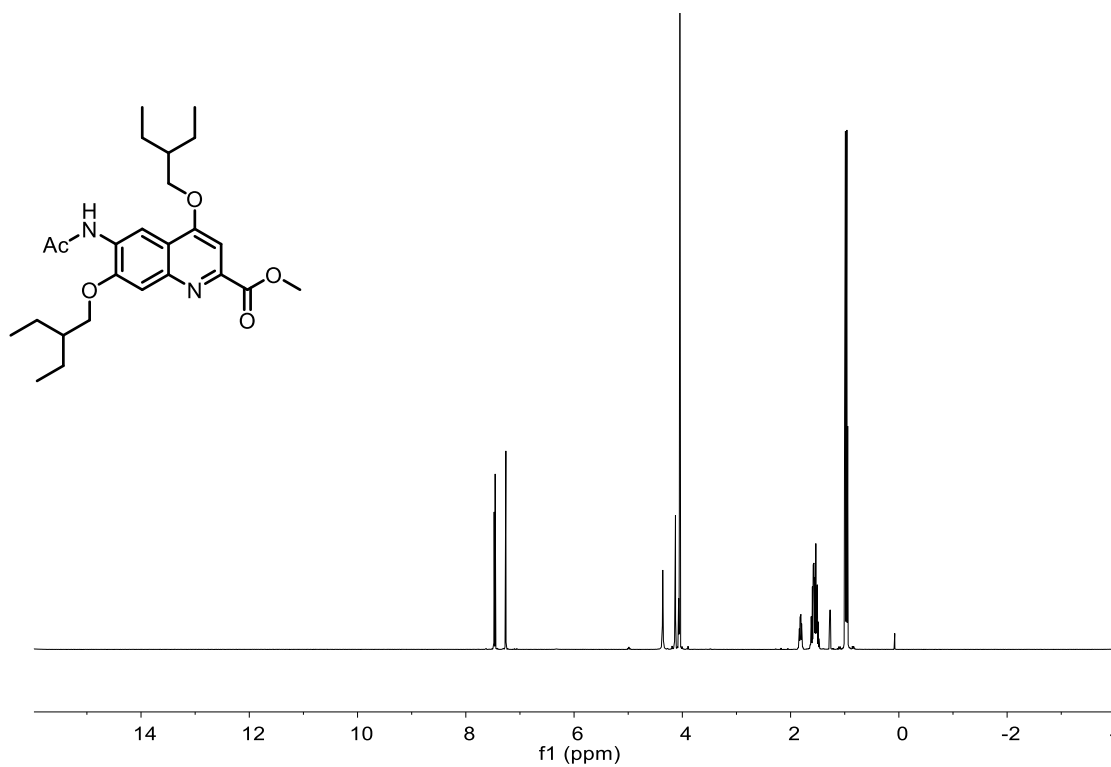


<sup>1</sup>H (400 MHz, Chloroform-d, 298 K) and <sup>13</sup>C (101 MHz, Chloroform-d, 298 K) NMR spectra of compound **9**.

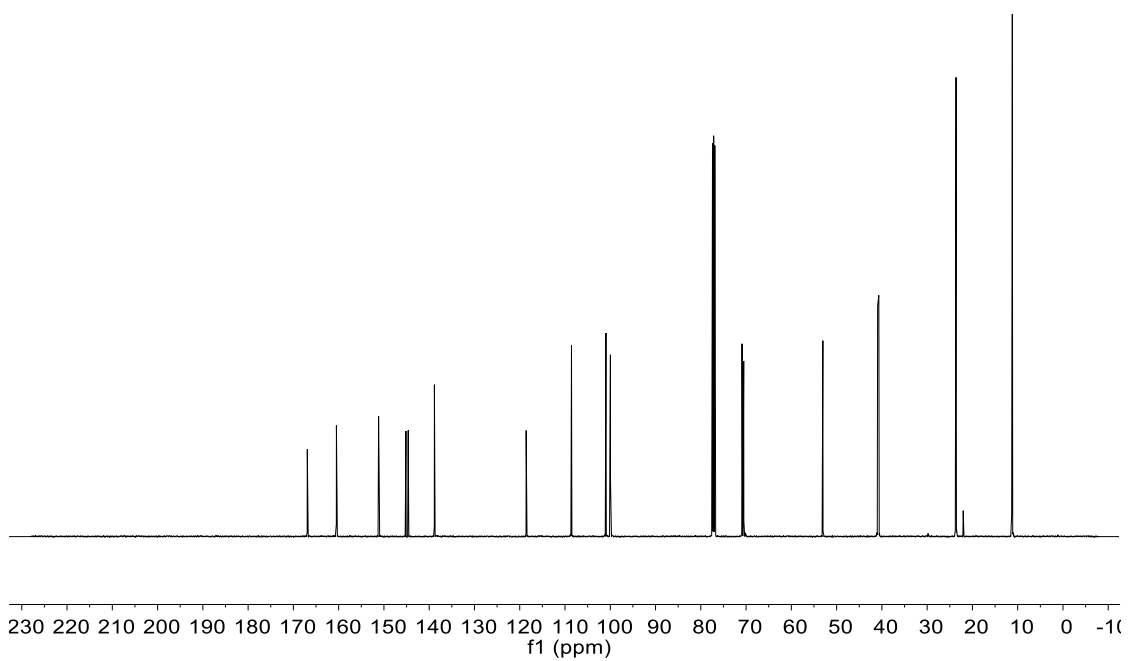
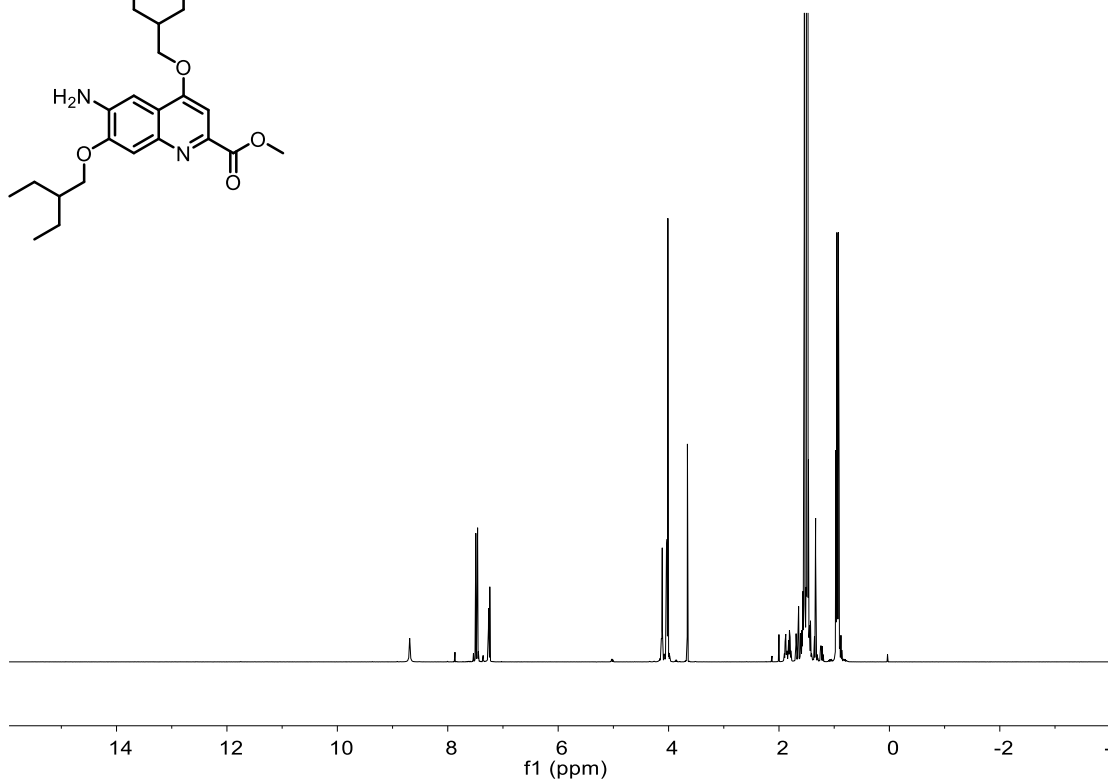
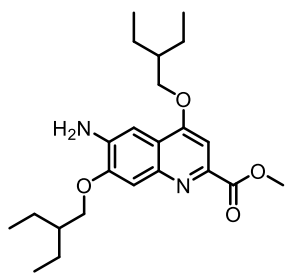




<sup>1</sup>H (500 MHz, CDCl<sub>3</sub>, 298 K) and <sup>13</sup>C (126 MHz, CDCl<sub>3</sub>, 298 K) NMR spectra of compound **11**.

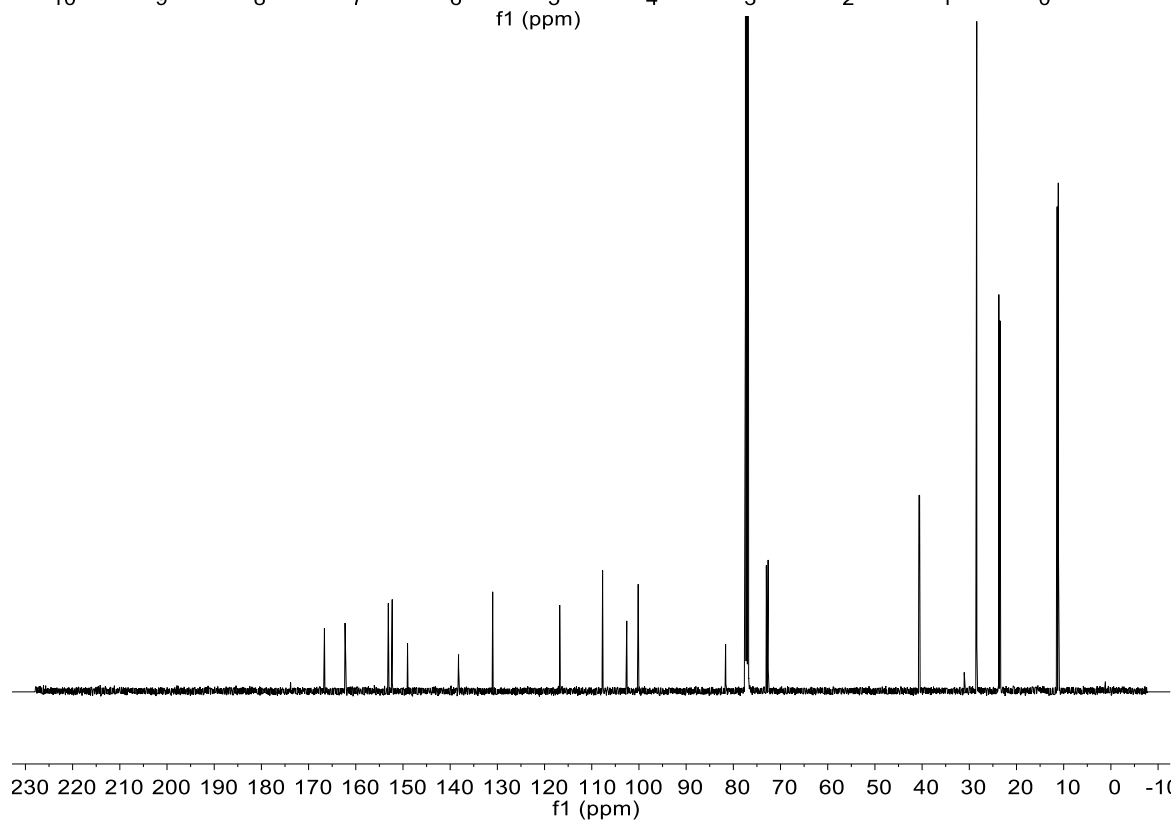
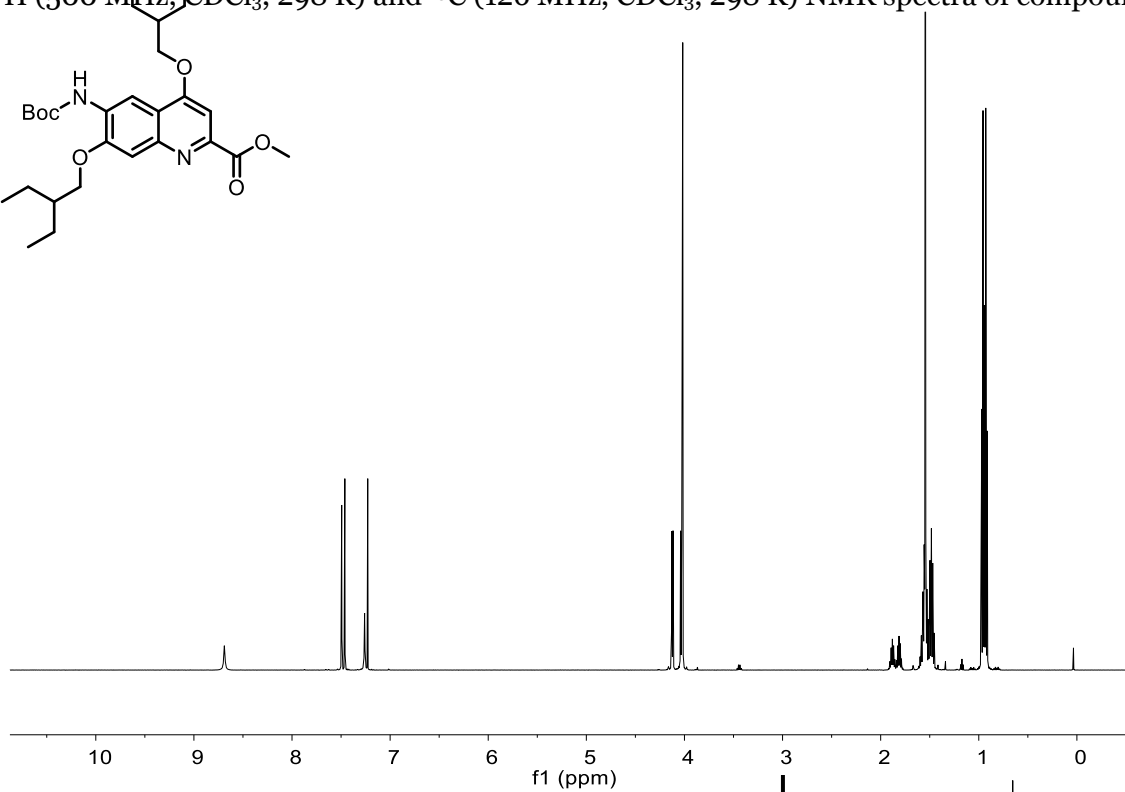
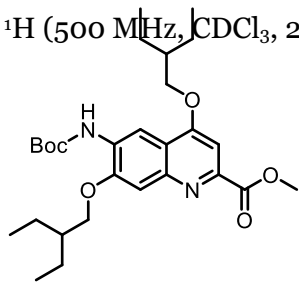


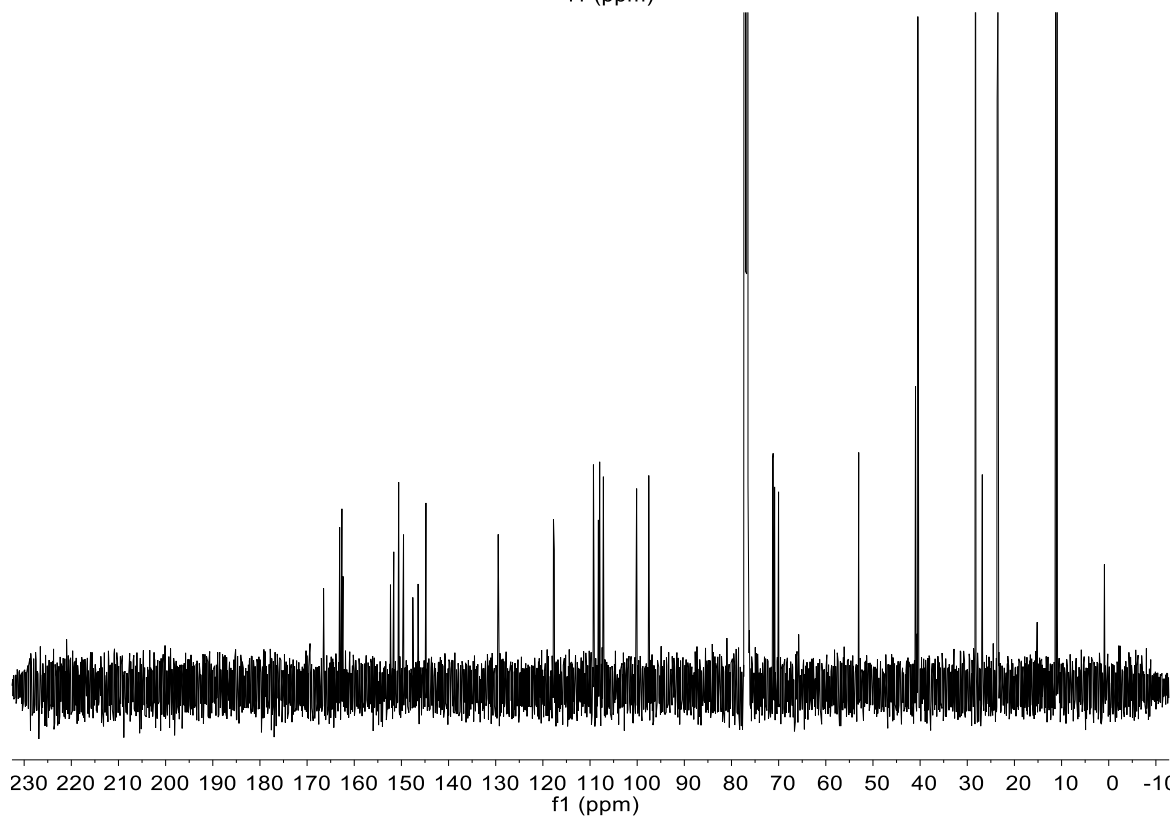
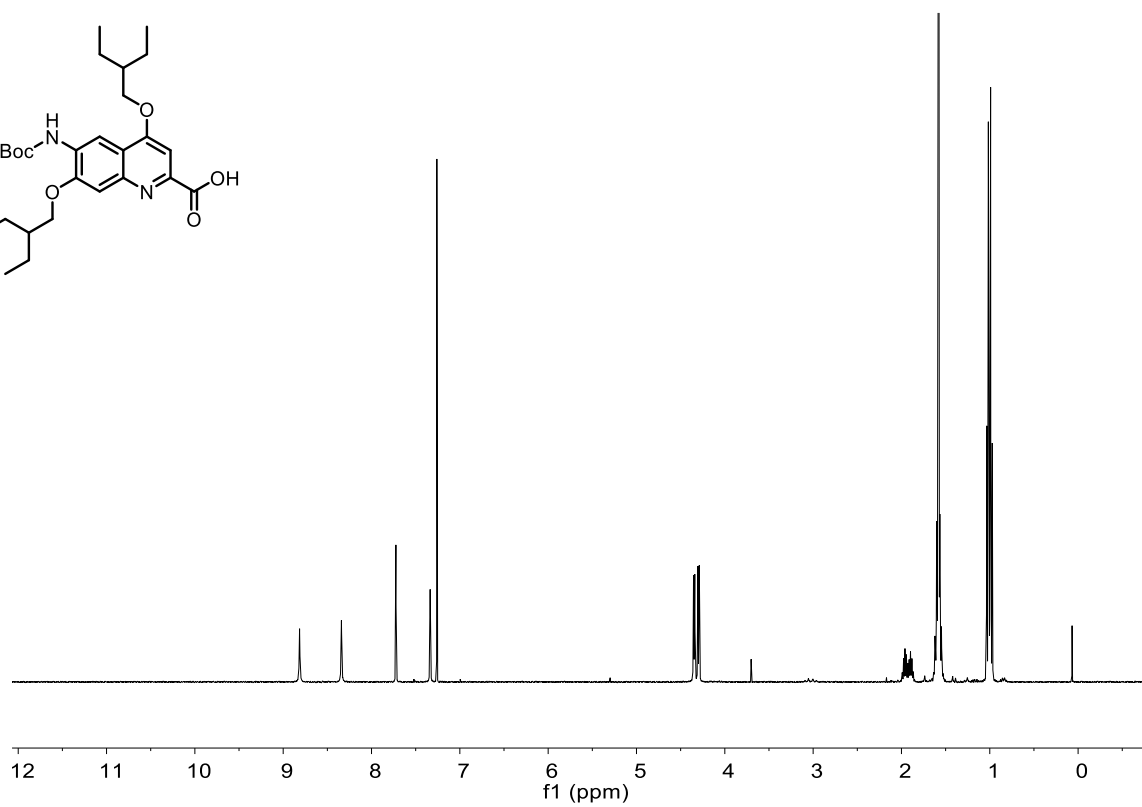
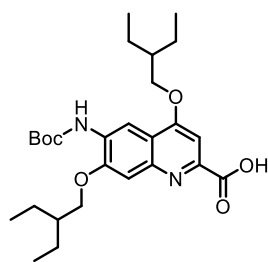
<sup>1</sup>H (500 MHz, CDCl<sub>3</sub>, 298 K) and <sup>13</sup>C (126 MHz, CDCl<sub>3</sub>, 298 K) NMR spectra of compound **12**.



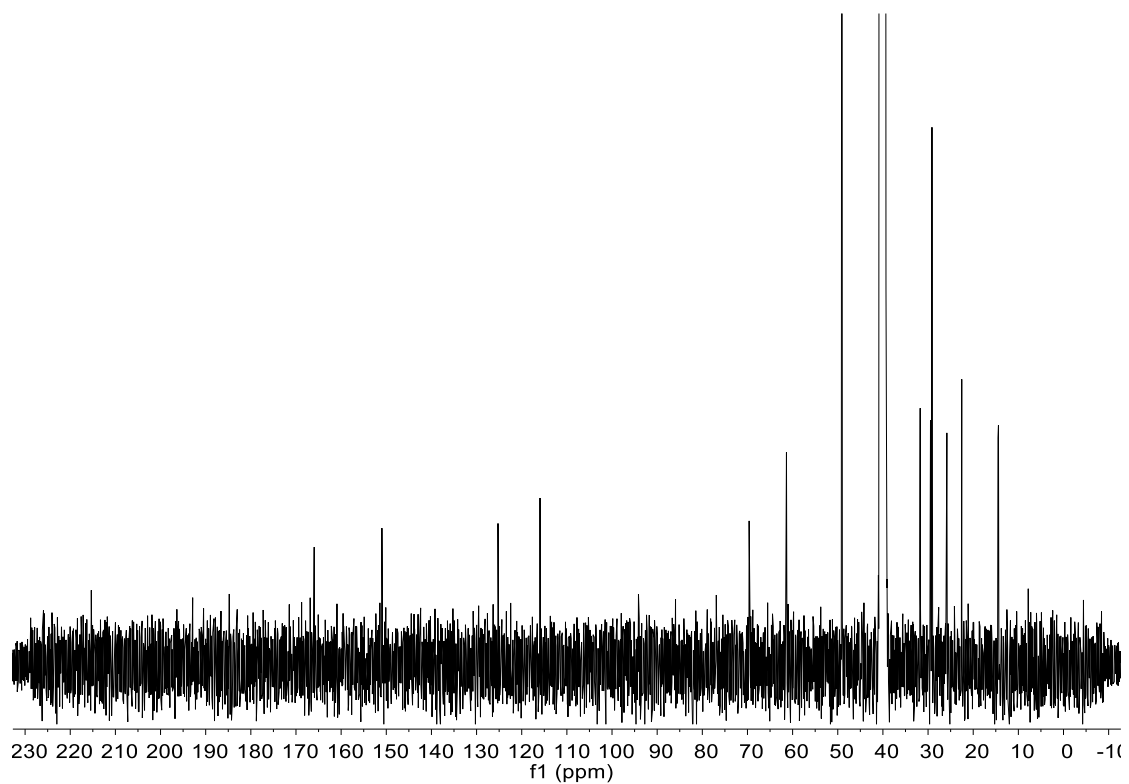
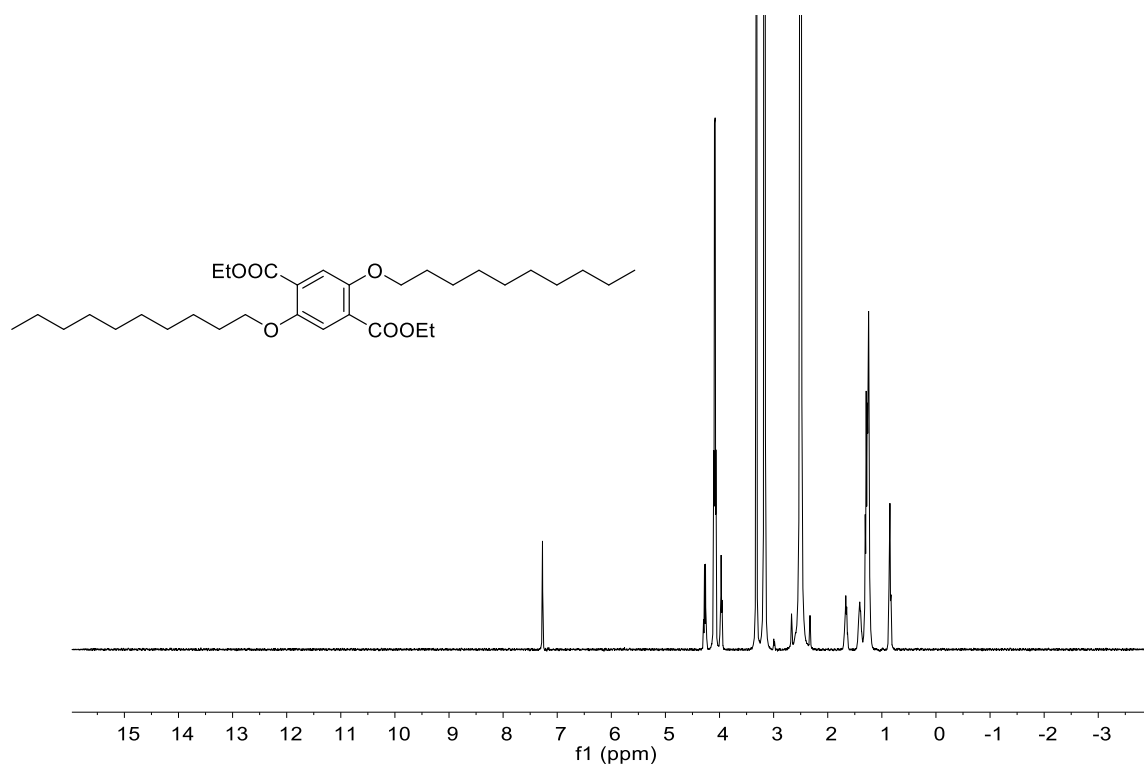
<sup>1</sup>H (500 MHz, CDCl<sub>3</sub>, 298 K) and <sup>13</sup>C (101 MHz, CDCl<sub>3</sub>, 298 K) NMR spectra of compound **13**.

$^1\text{H}$  (500 MHz,  $\text{CDCl}_3$ , 298 K) and  $^{13}\text{C}$  (126 MHz,  $\text{CDCl}_3$ , 298 K) NMR spectra of compound **14**.

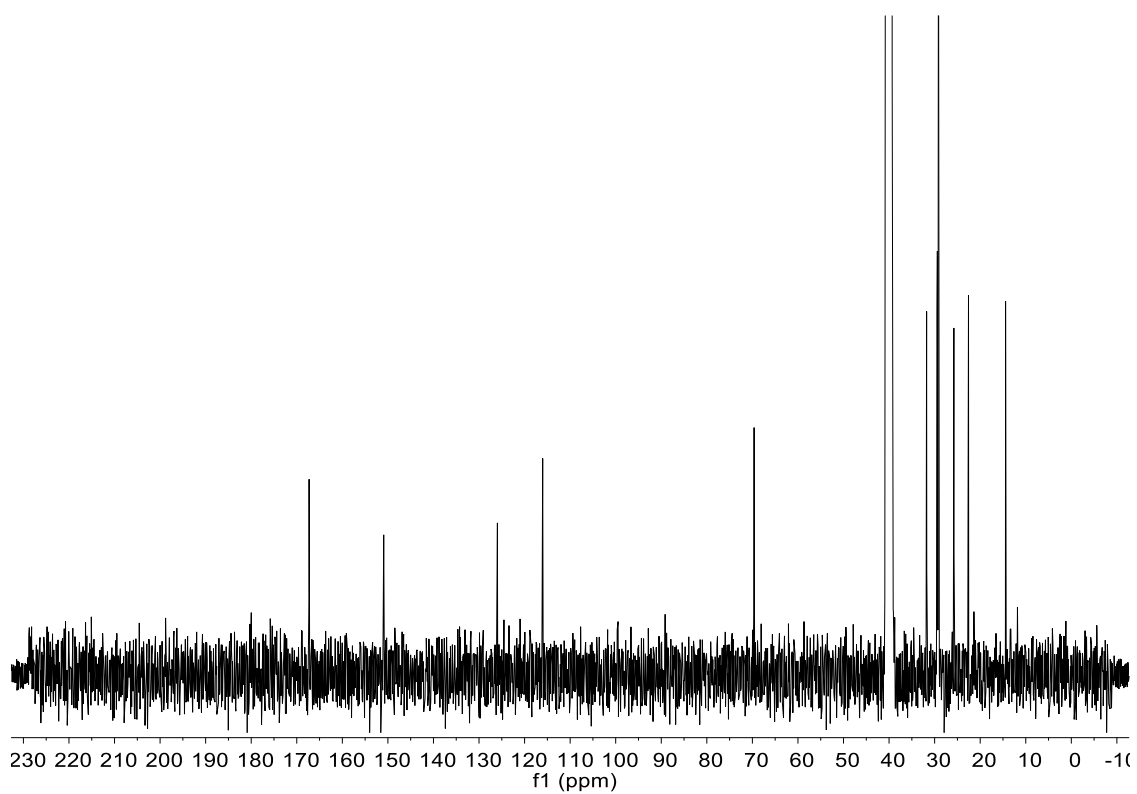
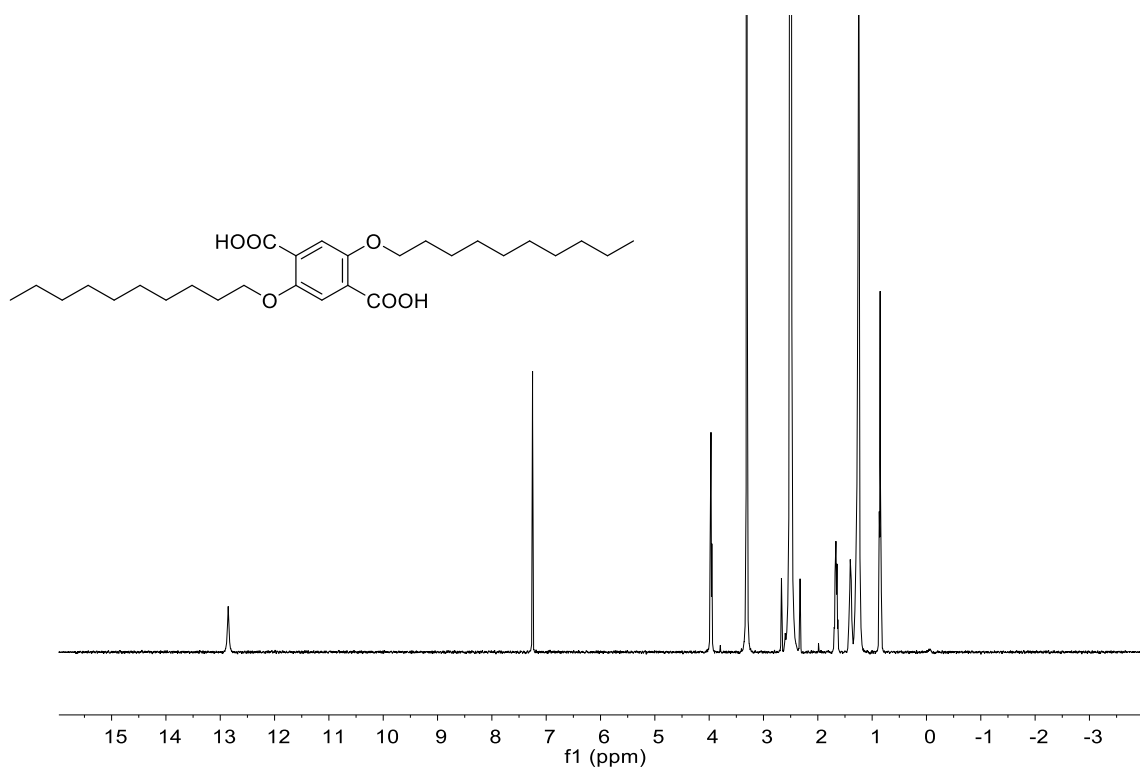




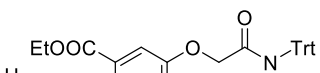
<sup>1</sup>H (500 MHz, CDCl<sub>3</sub>, 298 K) and <sup>13</sup>C (126 MHz, CDCl<sub>3</sub>, 298 K) NMR spectra of compound **15**.

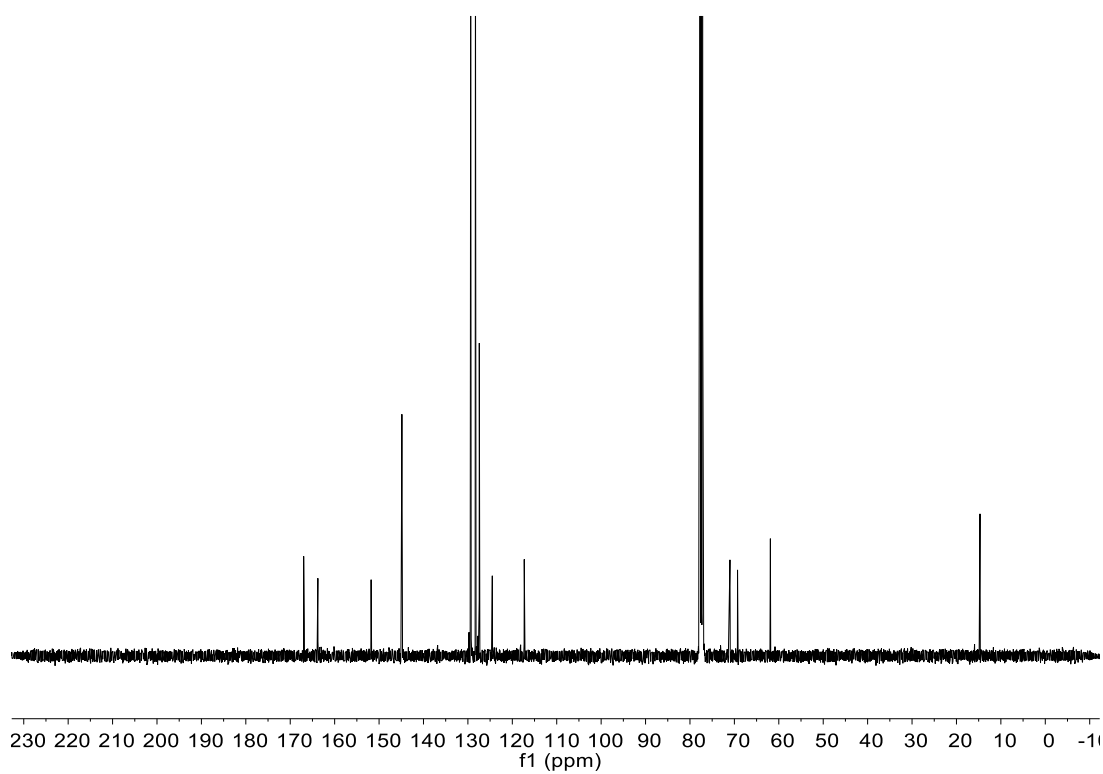
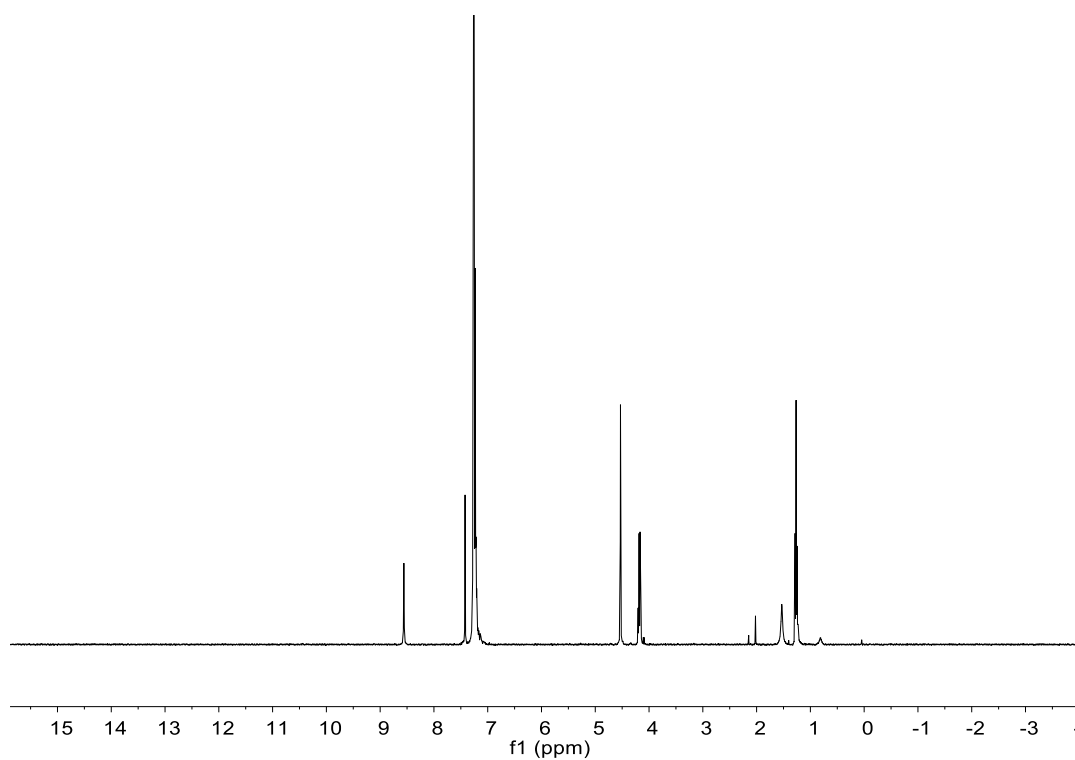


$^1\text{H}$  (500 MHz, DMSO- $d_6$ , 298 K) and  $^{13}\text{C}$  (126 MHz, DMSO- $d_6$ , 303 K) NMR spectra of compound **16**.

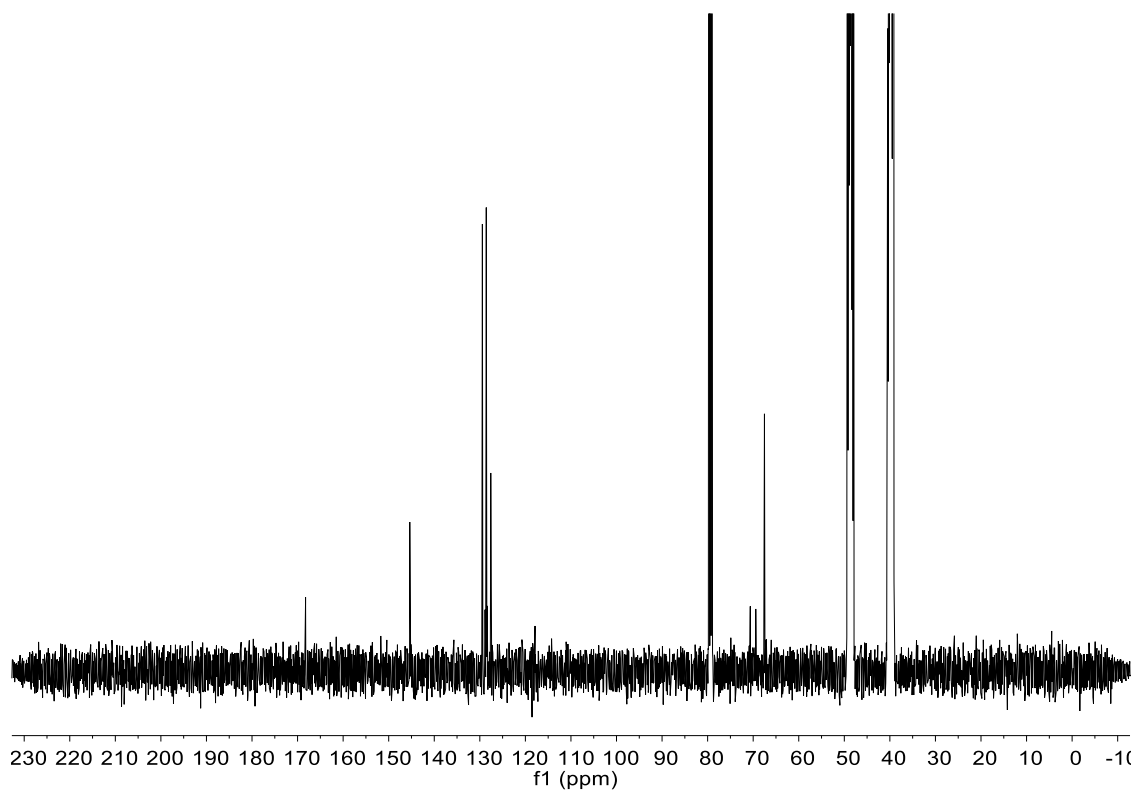
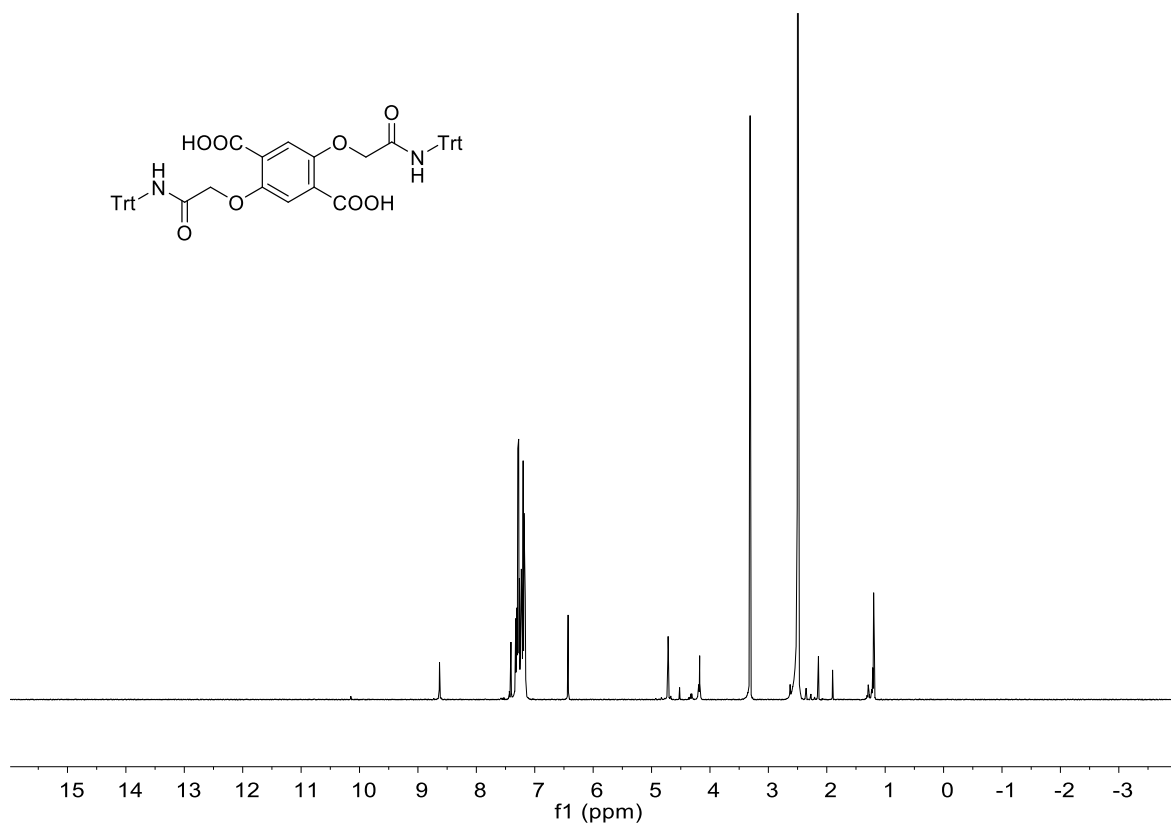


$^1\text{H}$  (500 MHz, DMSO- $d_6$ , 298 K) and  $^{13}\text{C}$  (126 MHz, DMSO- $d_6$ , 298 K) NMR spectra of compound **17**.

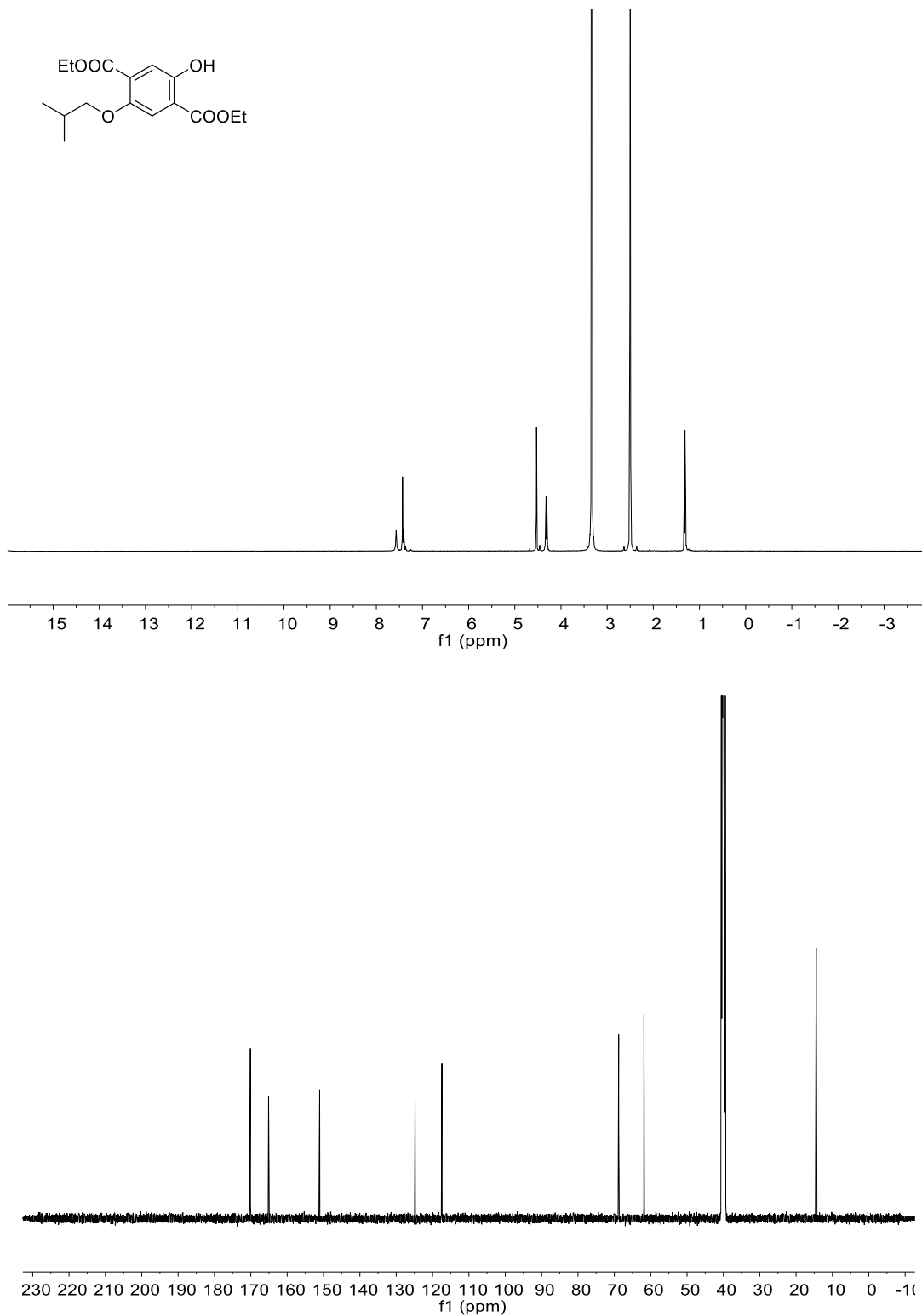




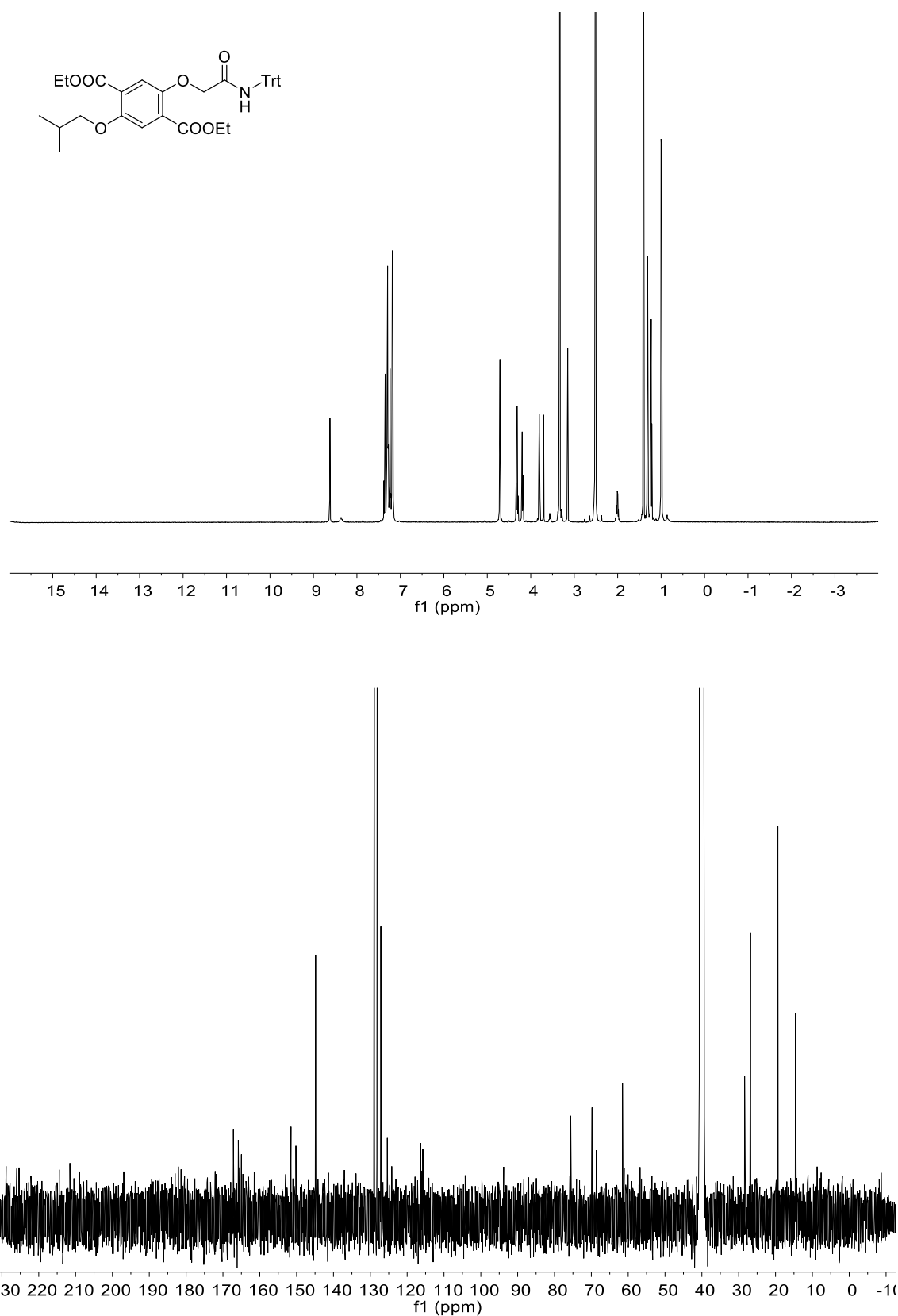
$^1\text{H}$  (400 MHz,  $\text{CDCl}_3$ , 298 K) and  $^{13}\text{C}$  (126 MHz,  $\text{CDCl}_3$ , 298 K) NMR spectra of compound **18**



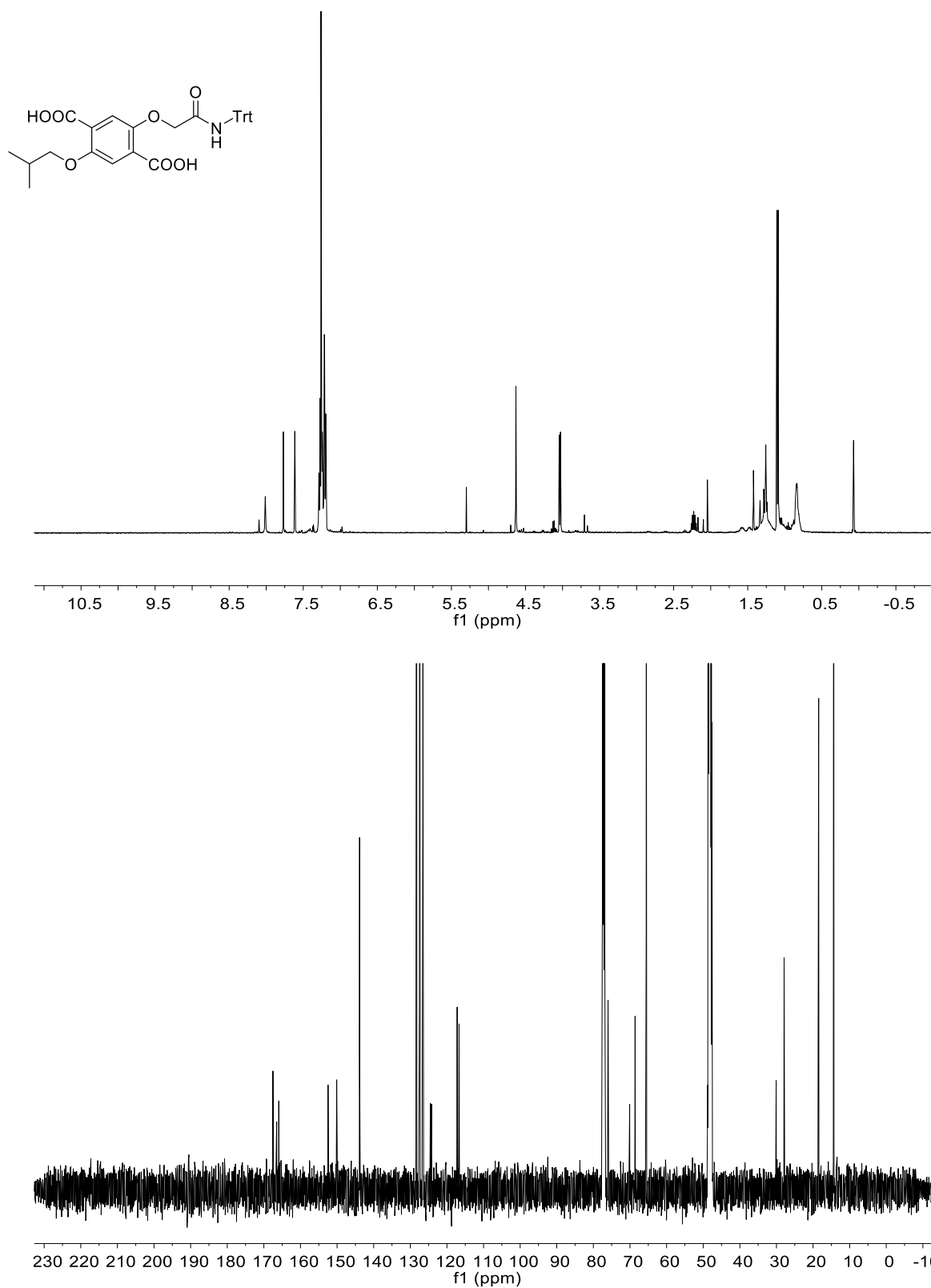
<sup>1</sup>H (500 MHz, DMSO-*d*<sub>6</sub>, 298 K) and <sup>13</sup>C (126 MHz, DMSO-*d*<sub>6</sub>, 298 K) NMR spectra of compound **19**.



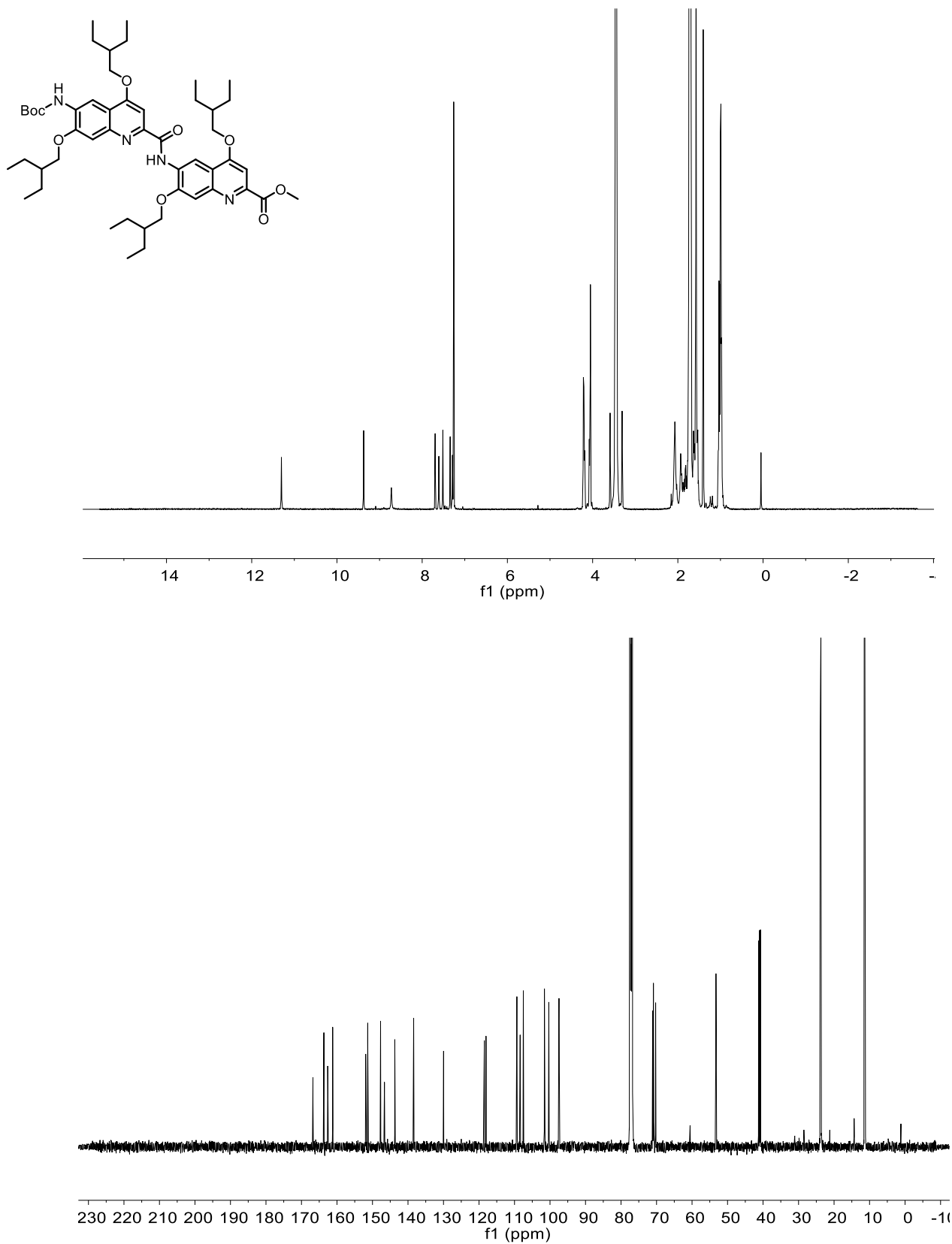
$^1\text{H}$  (500 MHz,  $\text{DMSO-}d_6$ , 298 K) and  $^{13}\text{C}$  (126 MHz,  $\text{DMSO-}d_6$ , 298 K) NMR spectra of compound **20**.



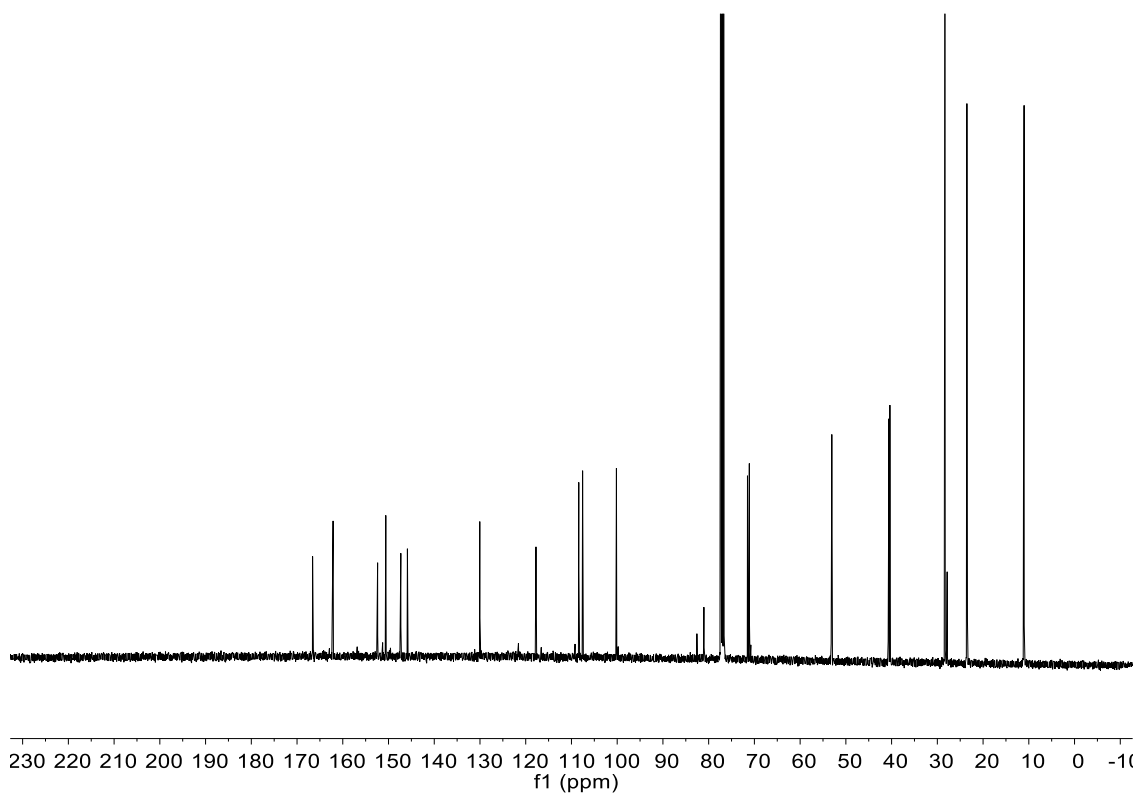
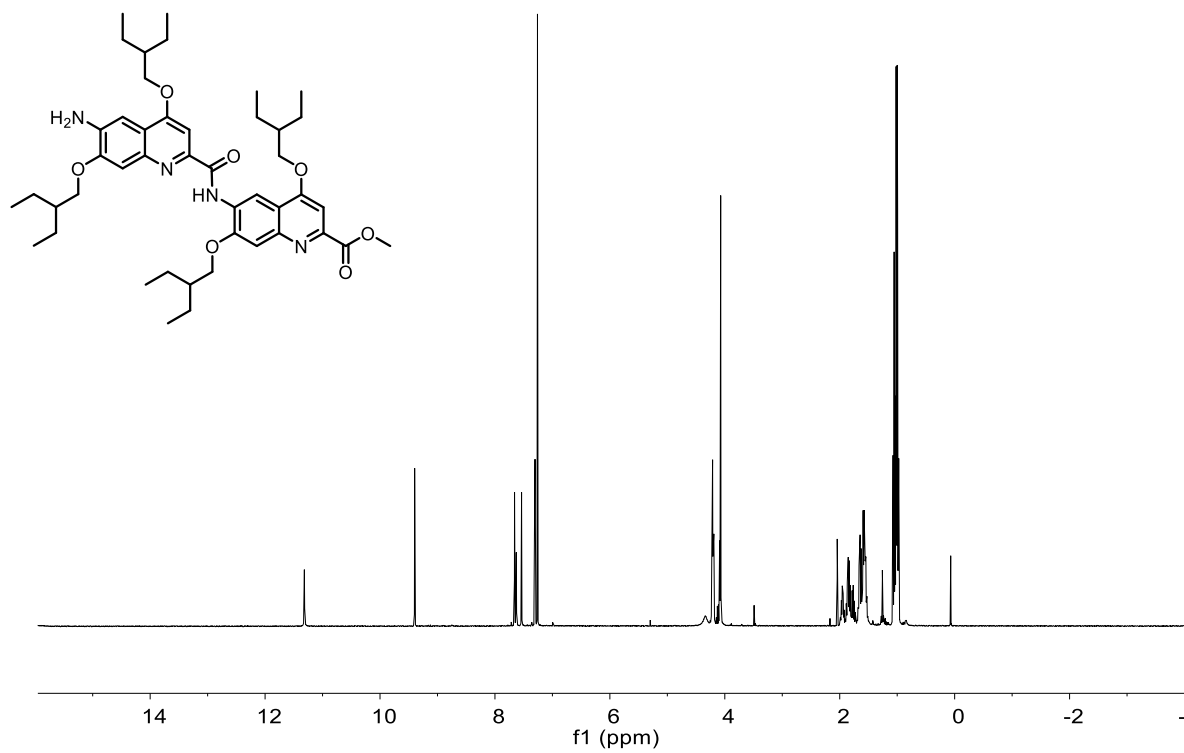
$^1\text{H}$  (500 MHz,  $\text{DMSO-}d_6$ , 298 K) and  $^{13}\text{C}$  (126 MHz,  $\text{DMSO-}d_6$ , 298 K) NMR spectra of compound **21**.



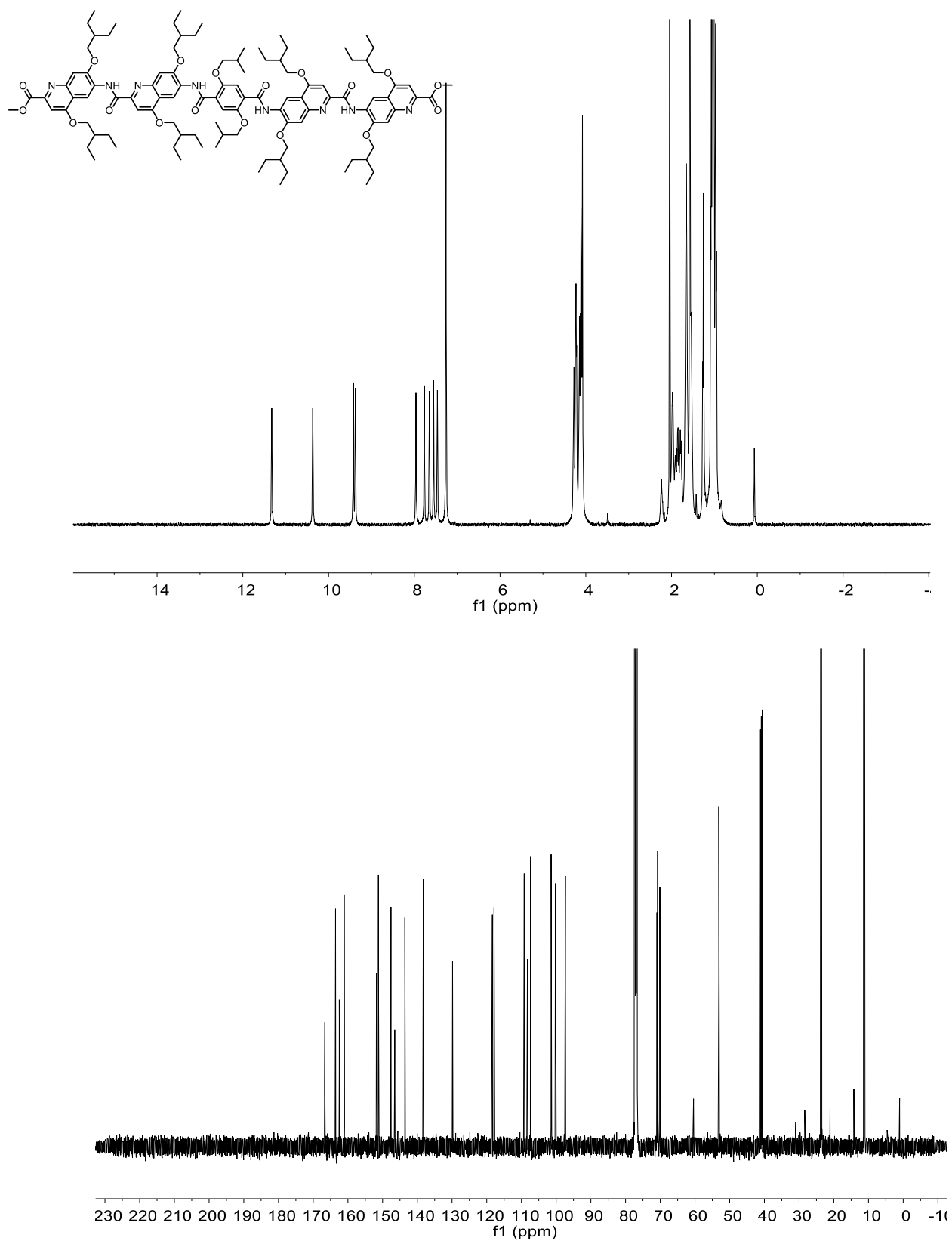
$^1\text{H}$  (500 MHz,  $\text{CDCl}_3$ , 298 K) and  $^{13}\text{C}$  (126 MHz,  $\text{CDCl}_3$ , 298 K) NMR spectra of compound **22**.



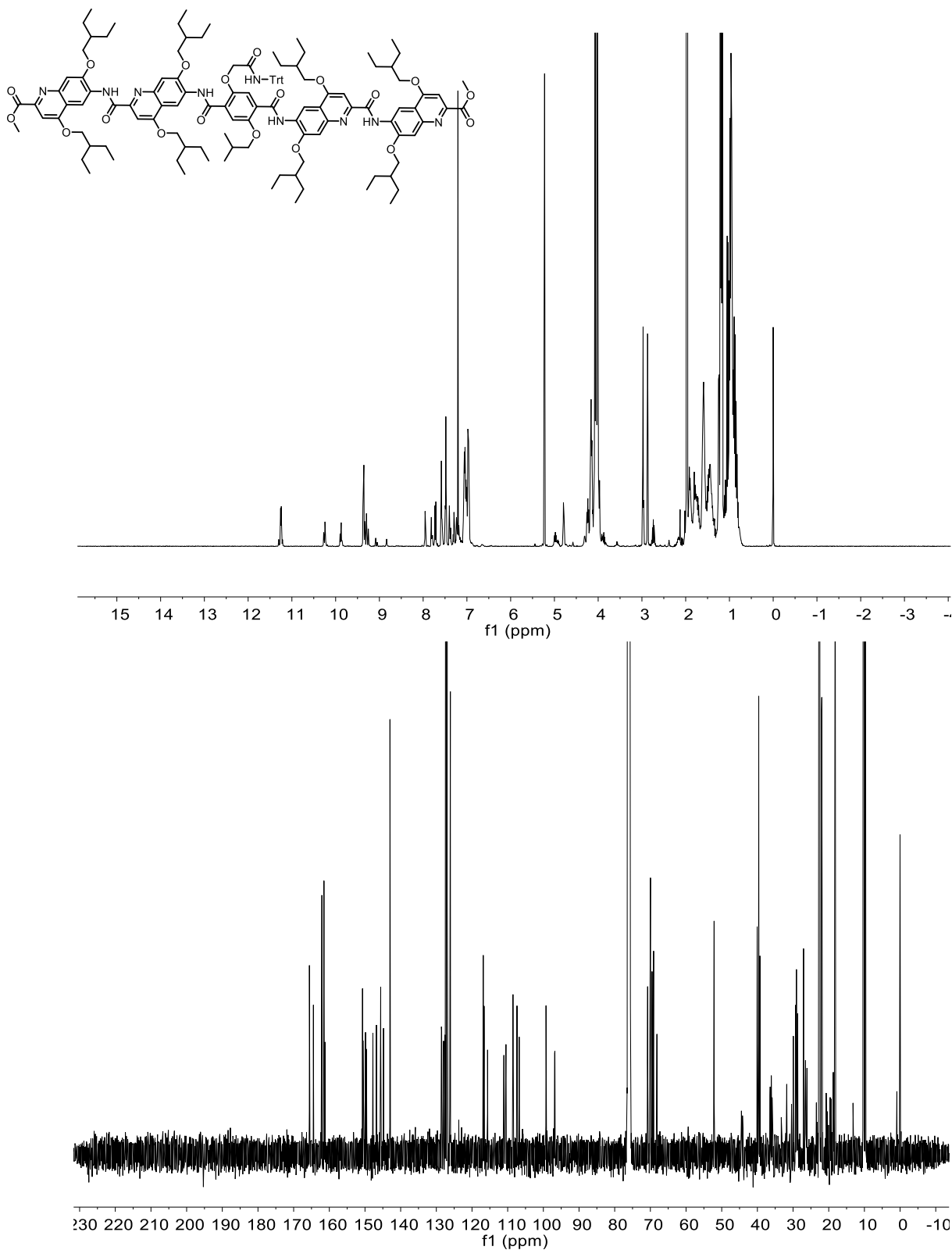
$^1\text{H}$  (500 MHz,  $\text{CDCl}_3$ , 298 K) and  $^{13}\text{C}$  (126 MHz,  $\text{CDCl}_3$ , 298 K) NMR spectra of compound **23**.



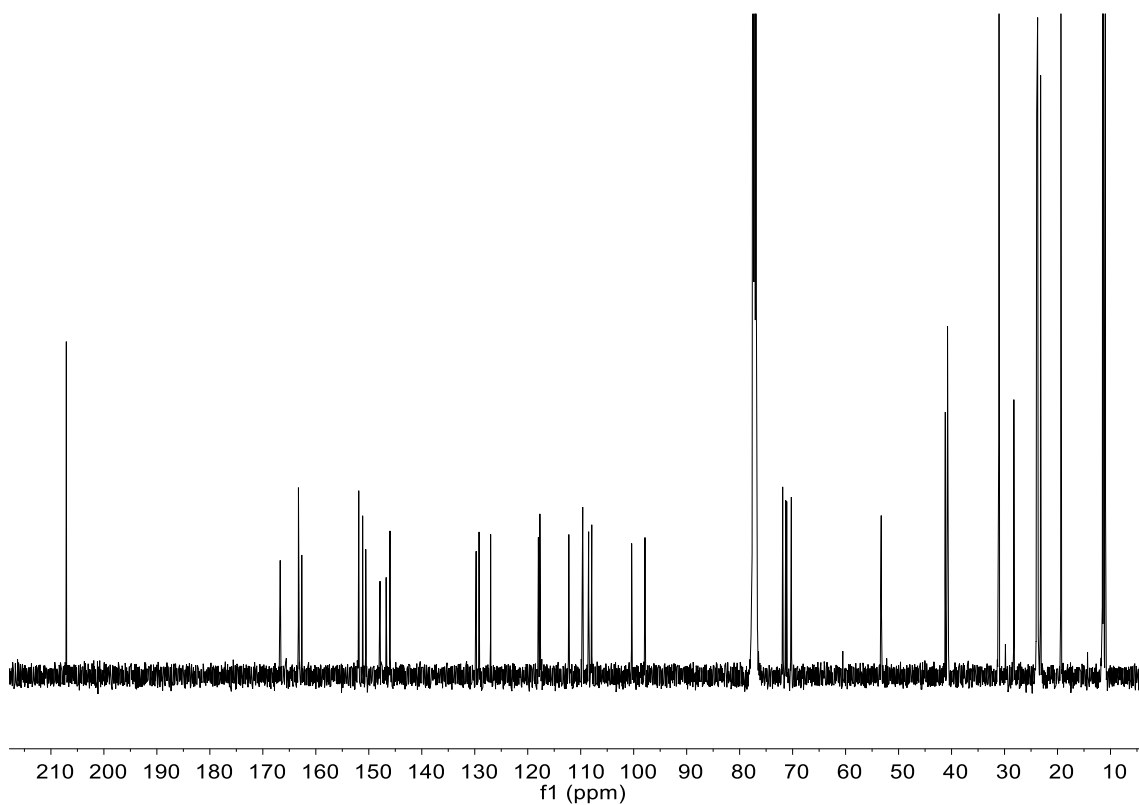
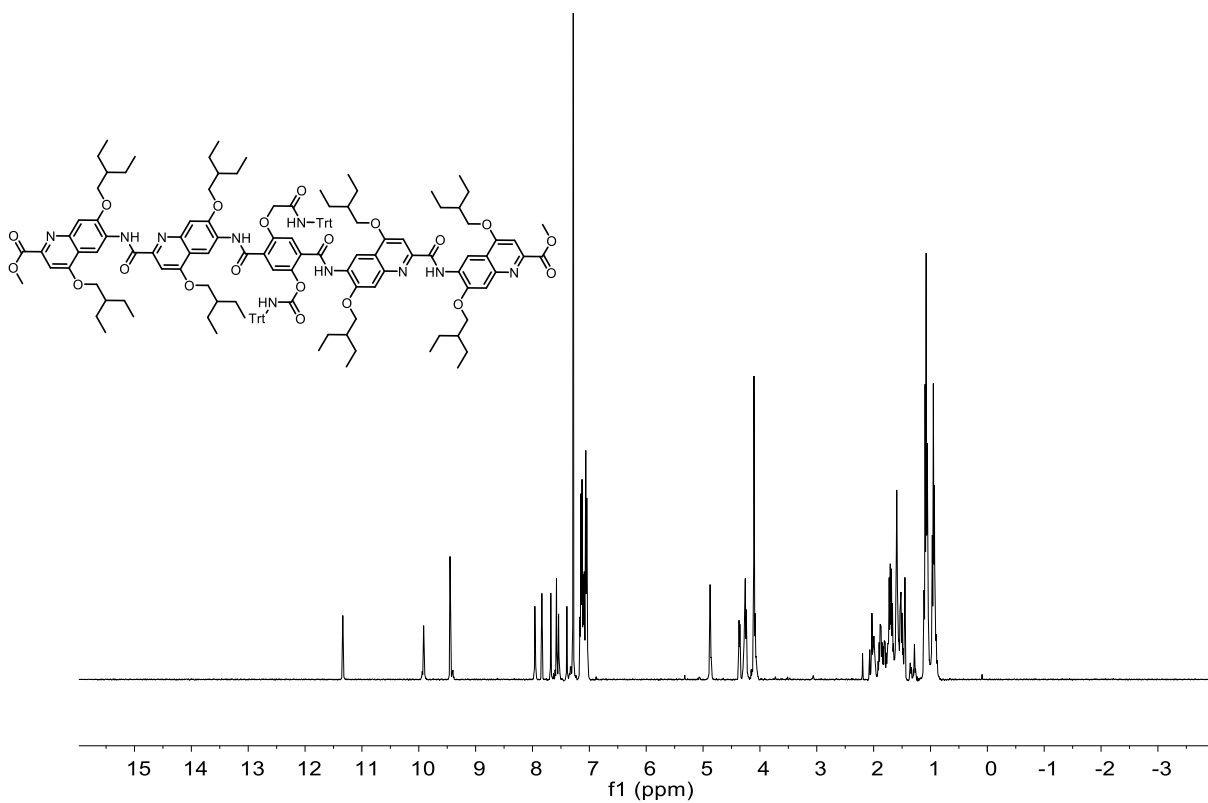
<sup>1</sup>H (500 MHz, CDCl<sub>3</sub>, 298 K) and <sup>13</sup>C (126 MHz, CDCl<sub>3</sub>, 298 K) NMR spectra of compound **24**.



$^1\text{H}$  (500 MHz,  $\text{CDCl}_3$ , 298 K) and  $^{13}\text{C}$  (126 MHz,  $\text{CDCl}_3$ , 298 K) NMR spectra of compound **5**

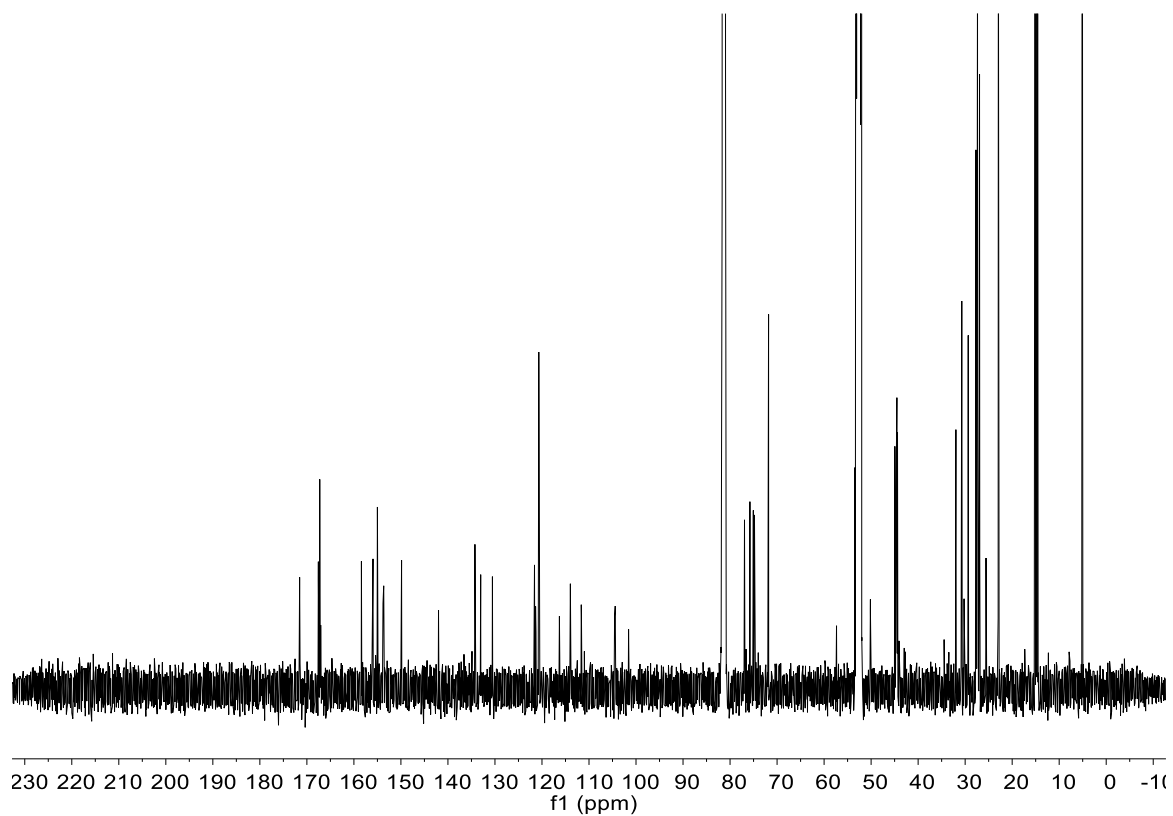
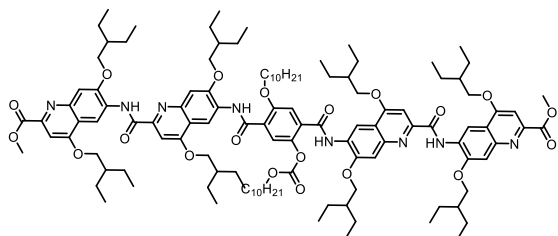


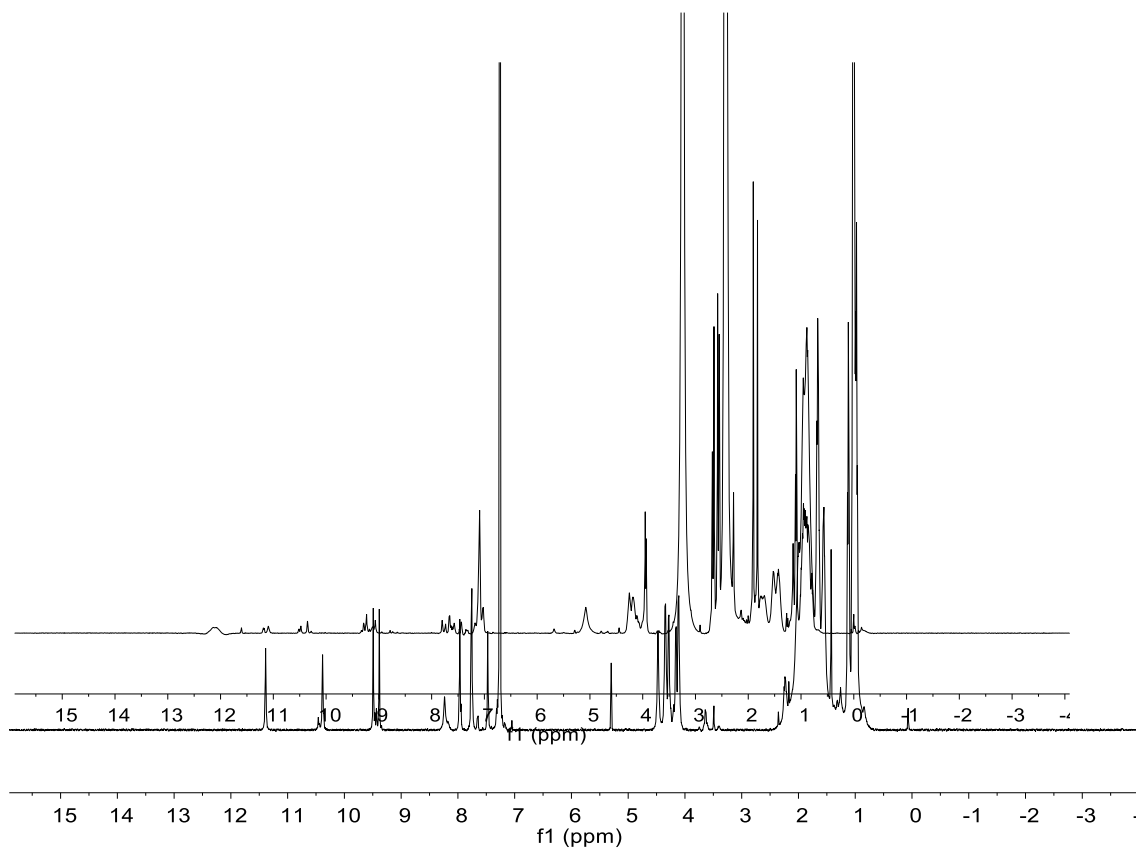
$^1\text{H}$  (500 MHz,  $\text{CDCl}_3$ , 298 K) and  $^{13}\text{C}$  (126 MHz,  $\text{CDCl}_3$ , 298 K) NMR spectra of compound 25.



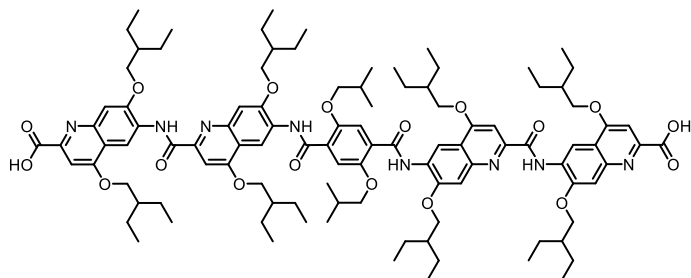
$^1\text{H}$  (500 MHz,  $\text{CDCl}_3$ , 298 K) and  $^{13}\text{C}$  (126 MHz,  $\text{CDCl}_3$ , 298 K) NMR spectra of compound **26**.

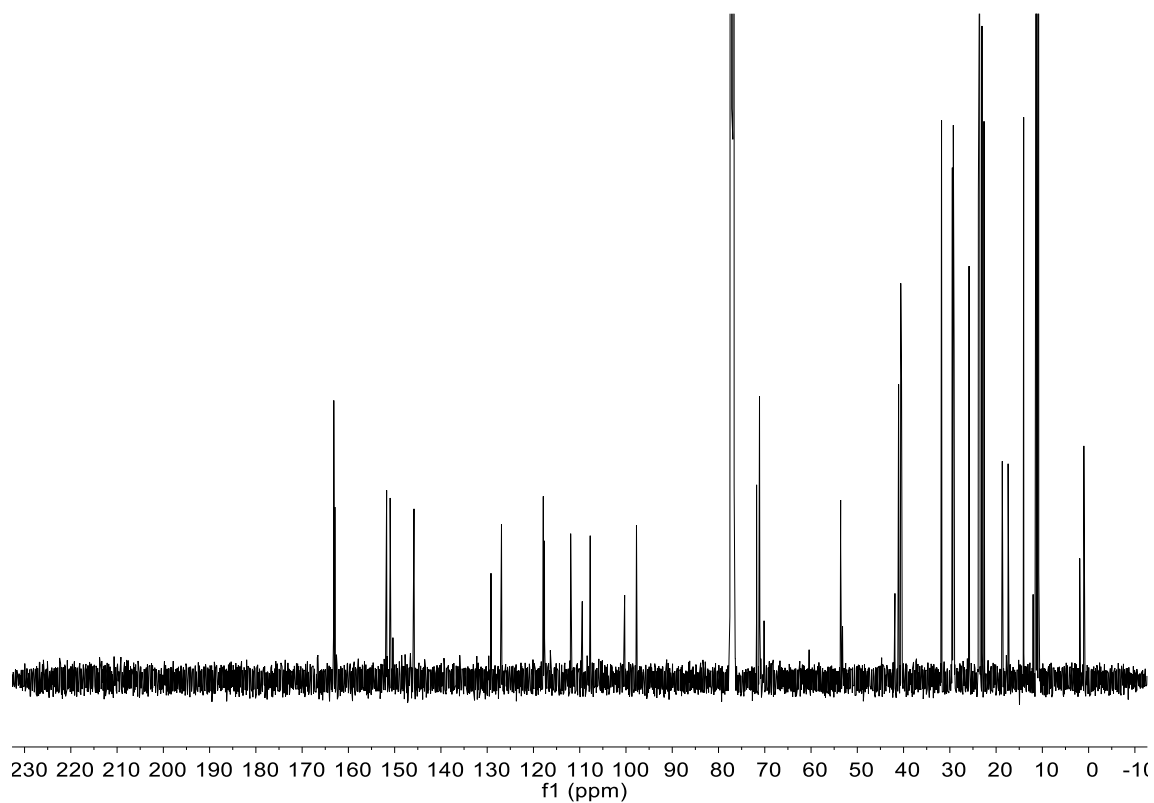
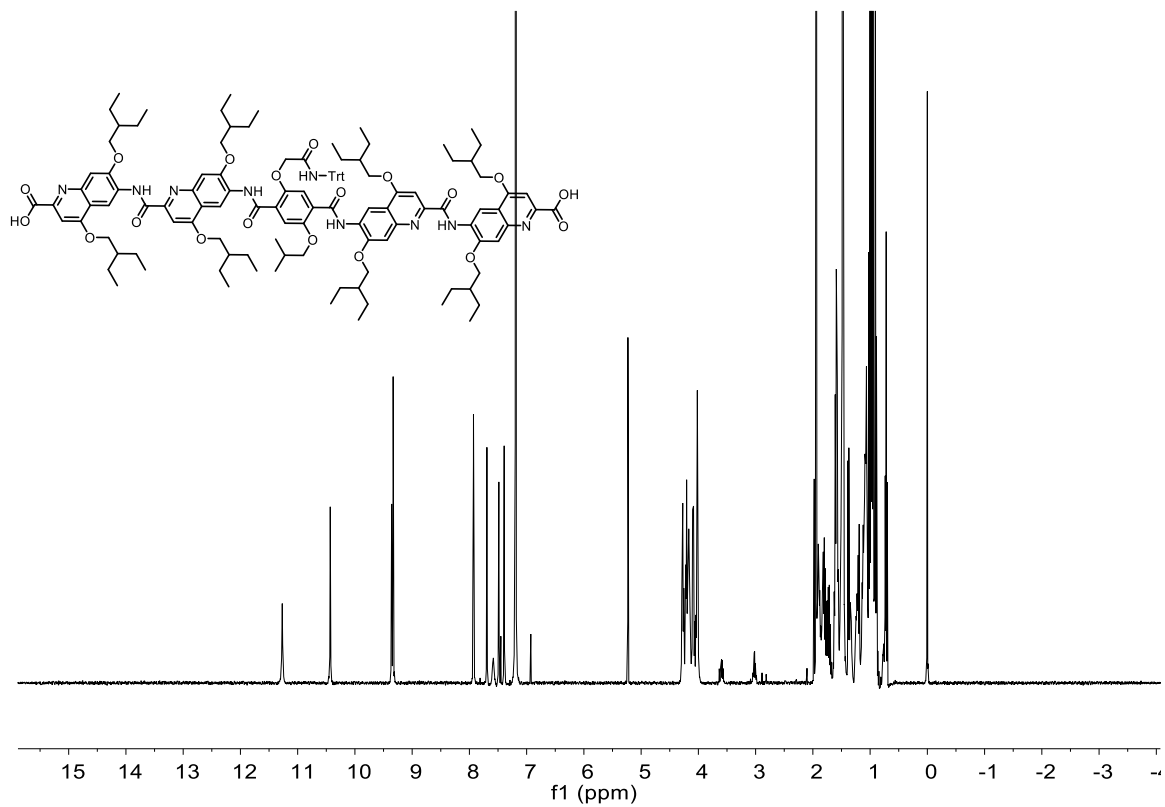
$^1\text{H}$  (500 MHz,  $\text{CDCl}_3$ , 298 K) and  $^{13}\text{C}$  (126 MHz,  $\text{CDCl}_3$ , 298 K) NMR spectra of compound **27**



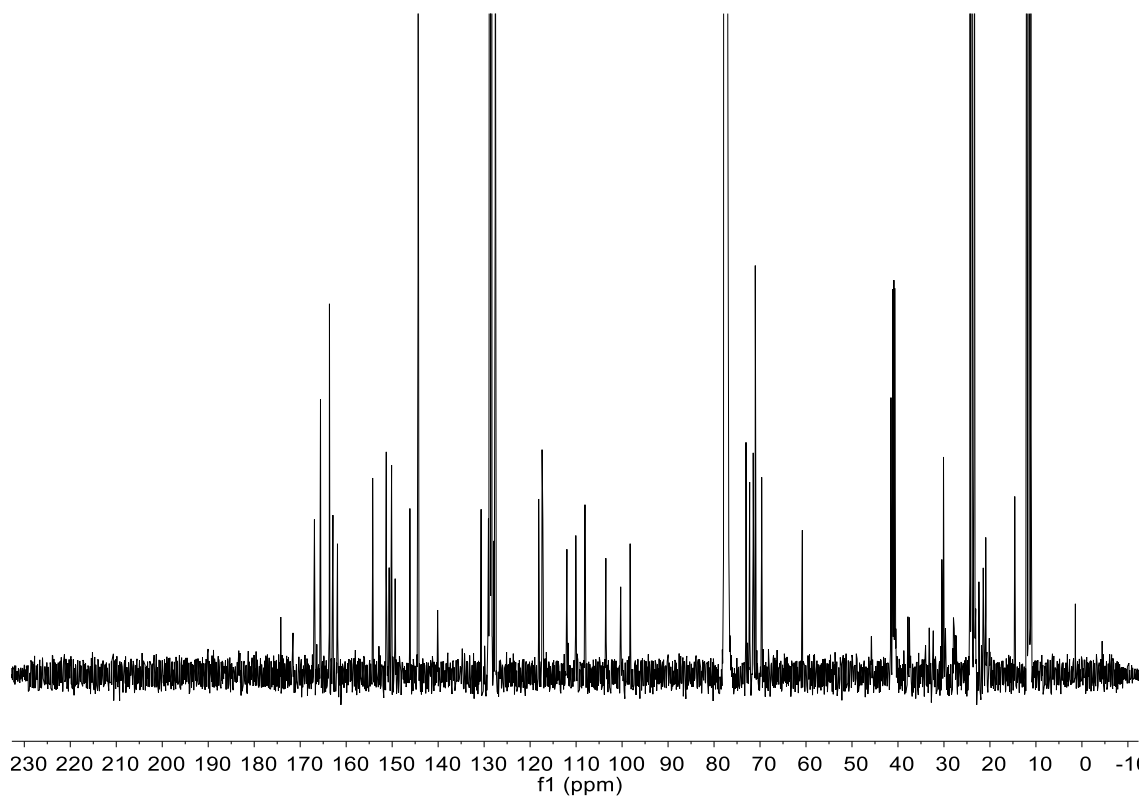
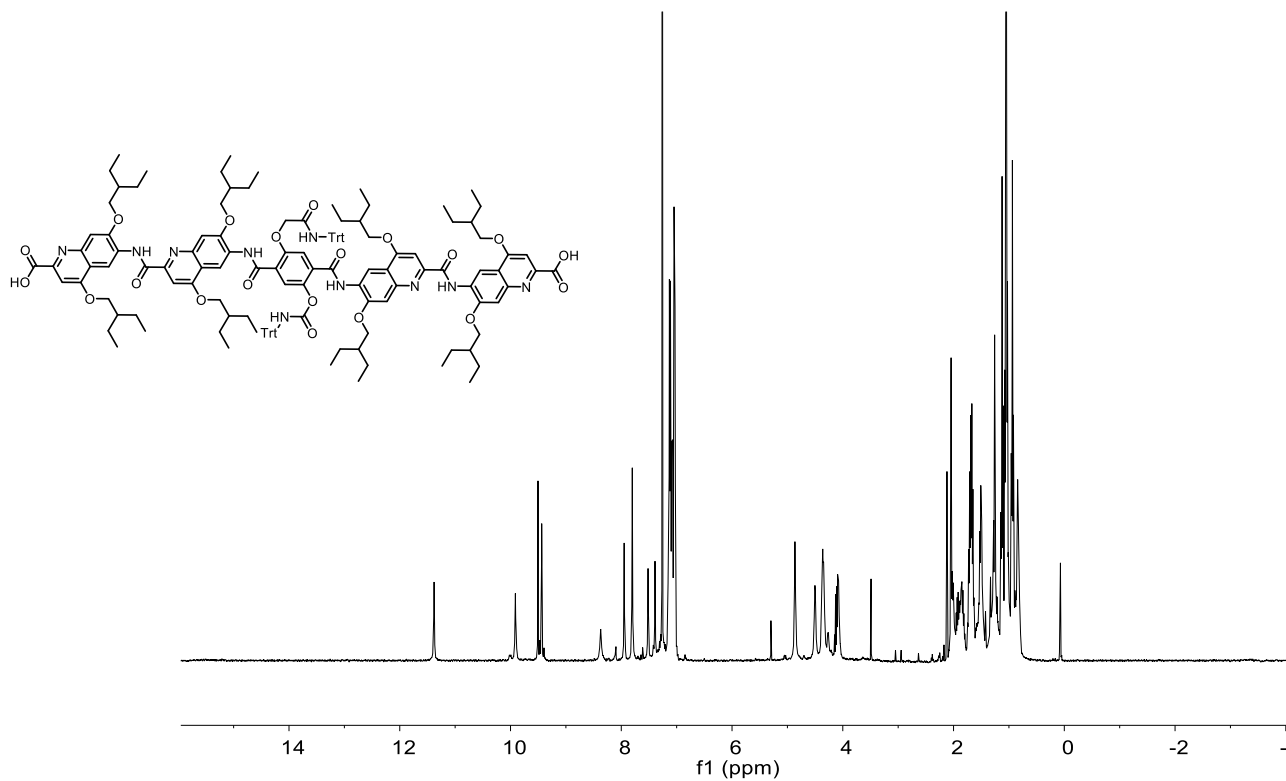


$^1\text{H}$  (500 MHz,  $\text{CDCl}_3$ , 298 K) and  $^{13}\text{C}$  (126 MHz,  $\text{CDCl}_3$ , 298 K) NMR spectra of compound **28**.



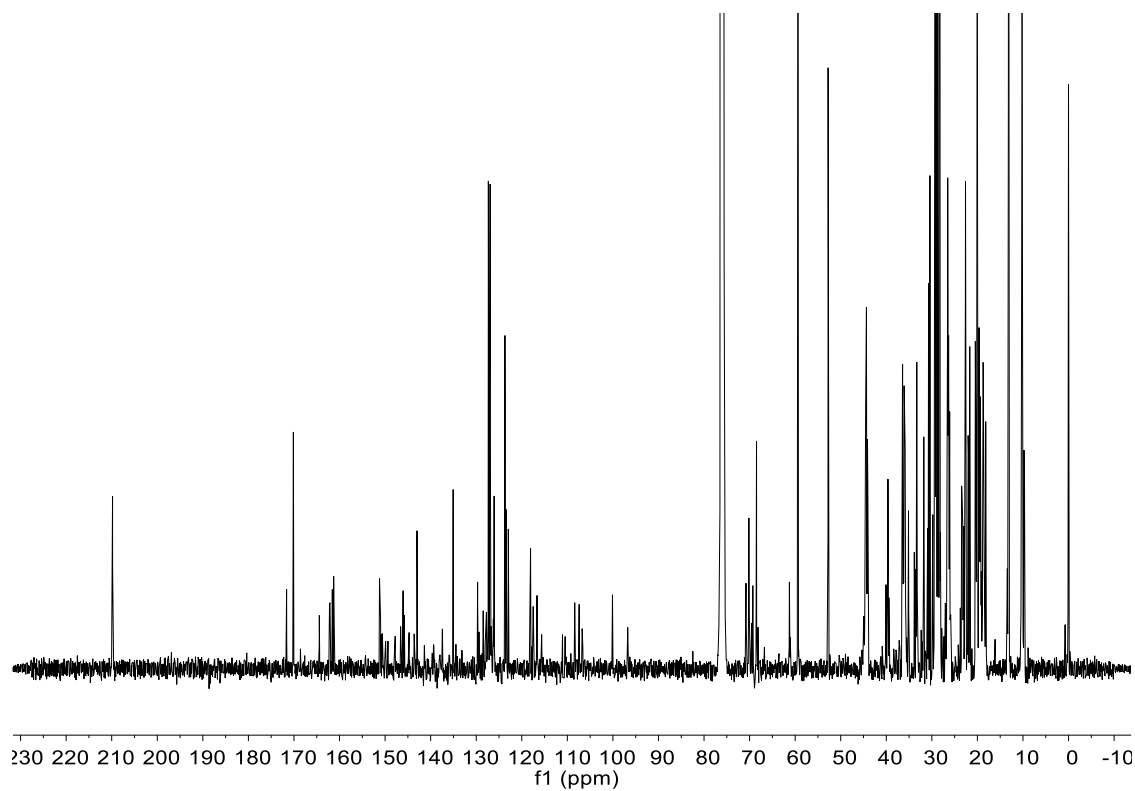
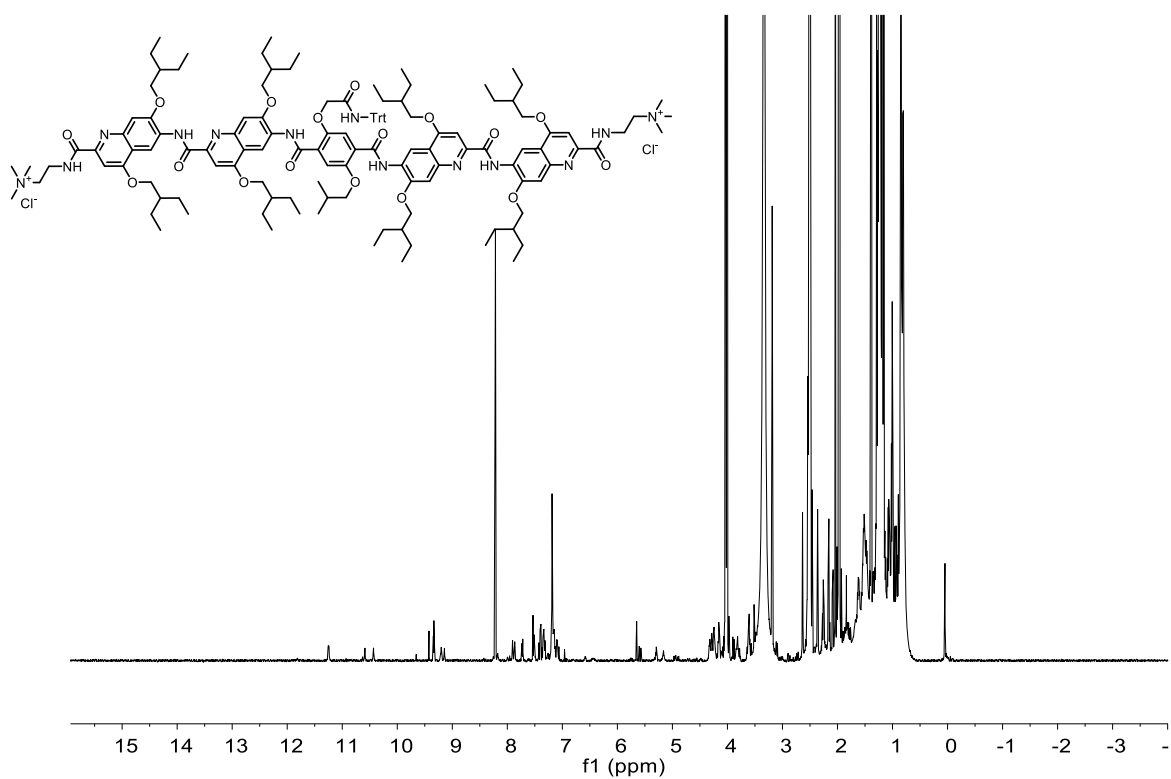


$^1\text{H}$  (500 MHz, DMSO, 298 K) and  $^{13}\text{C}$  (126 MHz,  $\text{CDCl}_3$ , 298 K) NMR spectra of compound **29**

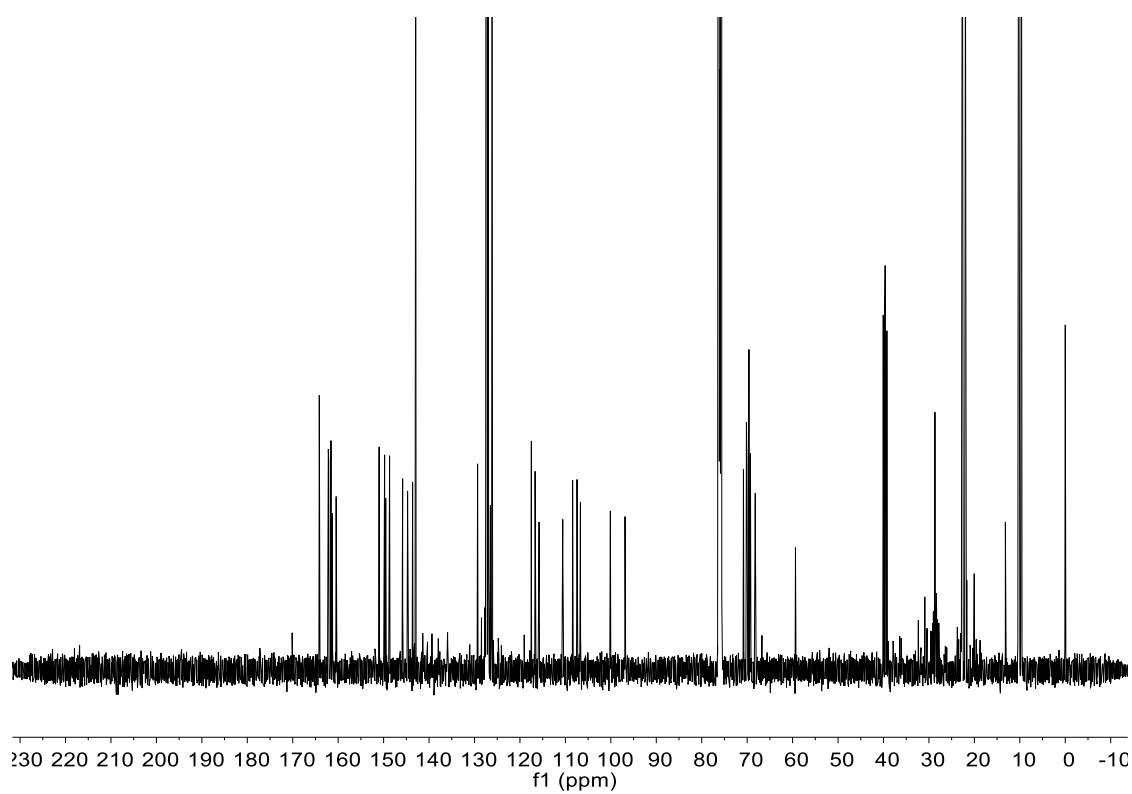
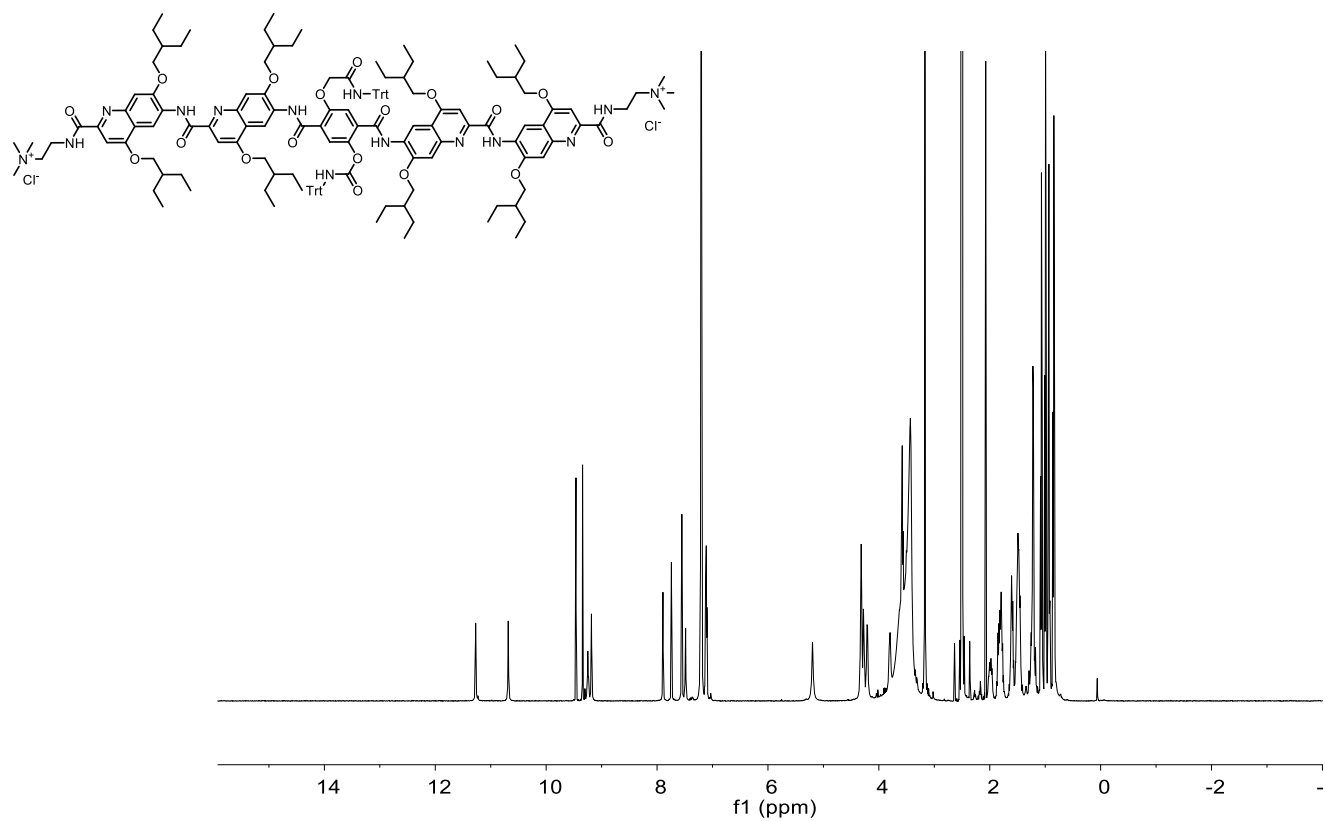


<sup>1</sup>H (500 MHz, CDCl<sub>3</sub>, 298 K) and <sup>13</sup>C (126 MHz, CDCl<sub>3</sub>, 298 K) NMR spectra of compound **30**

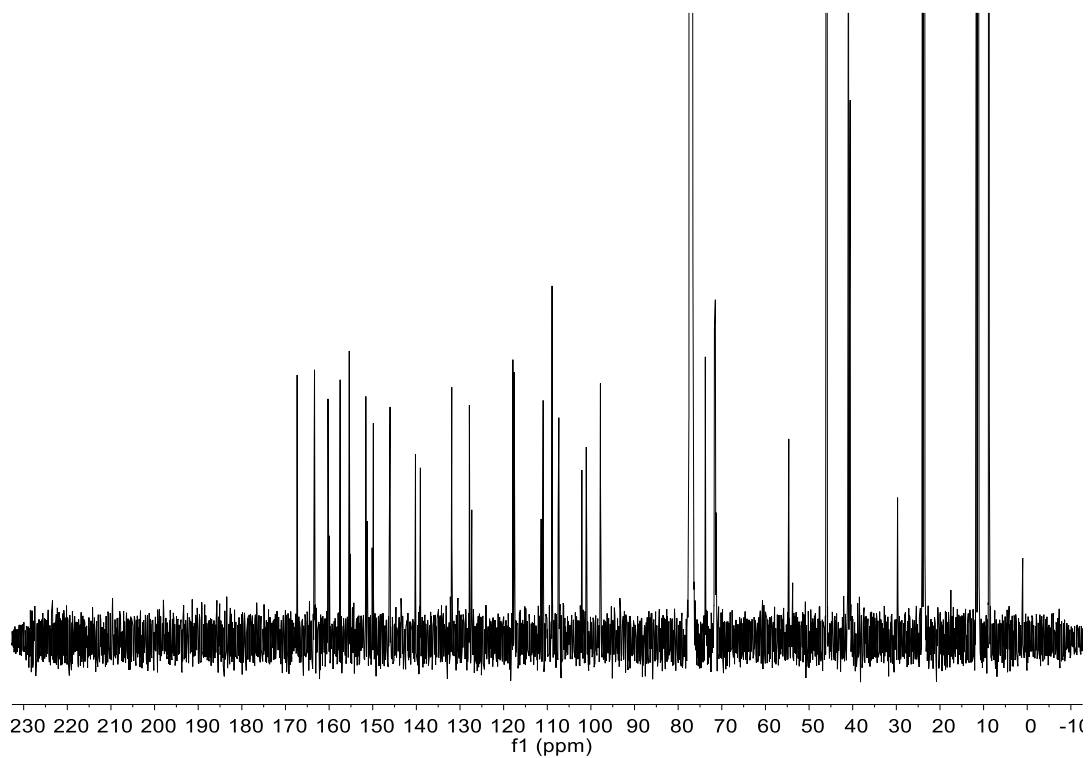
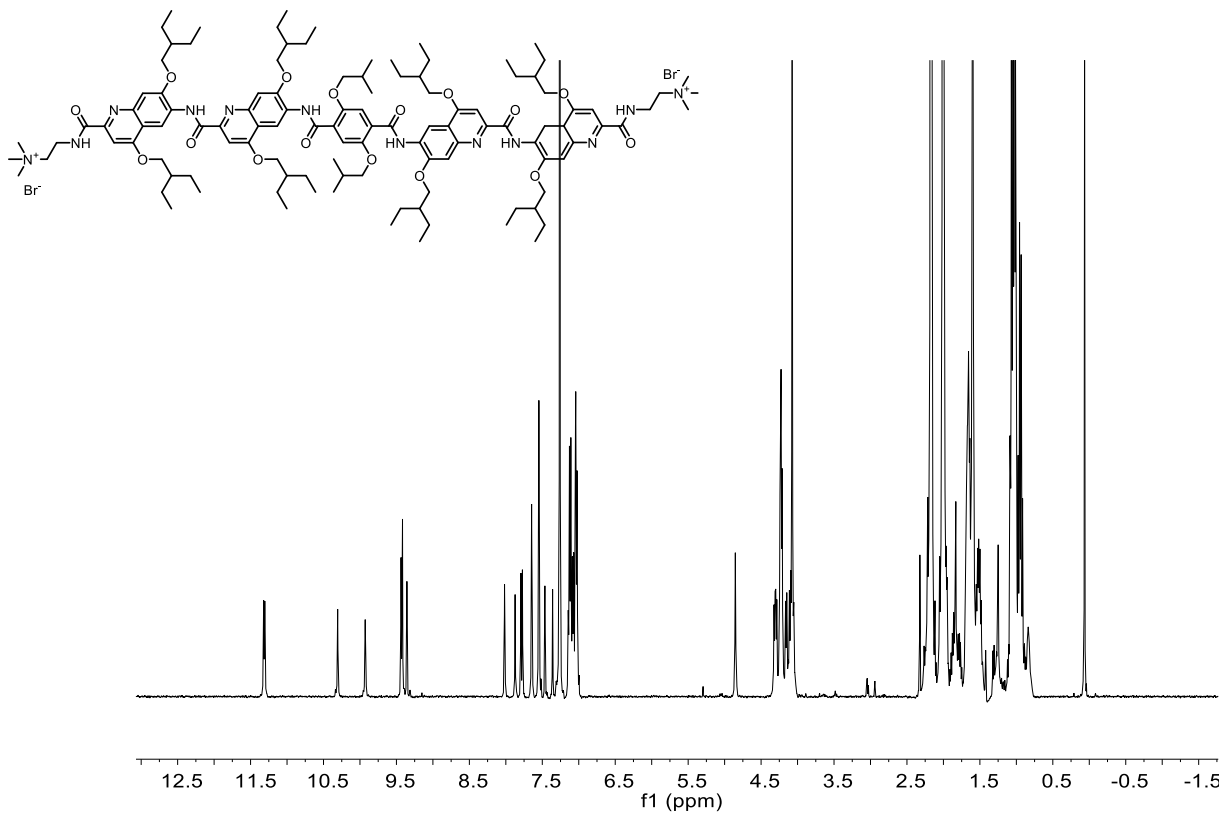




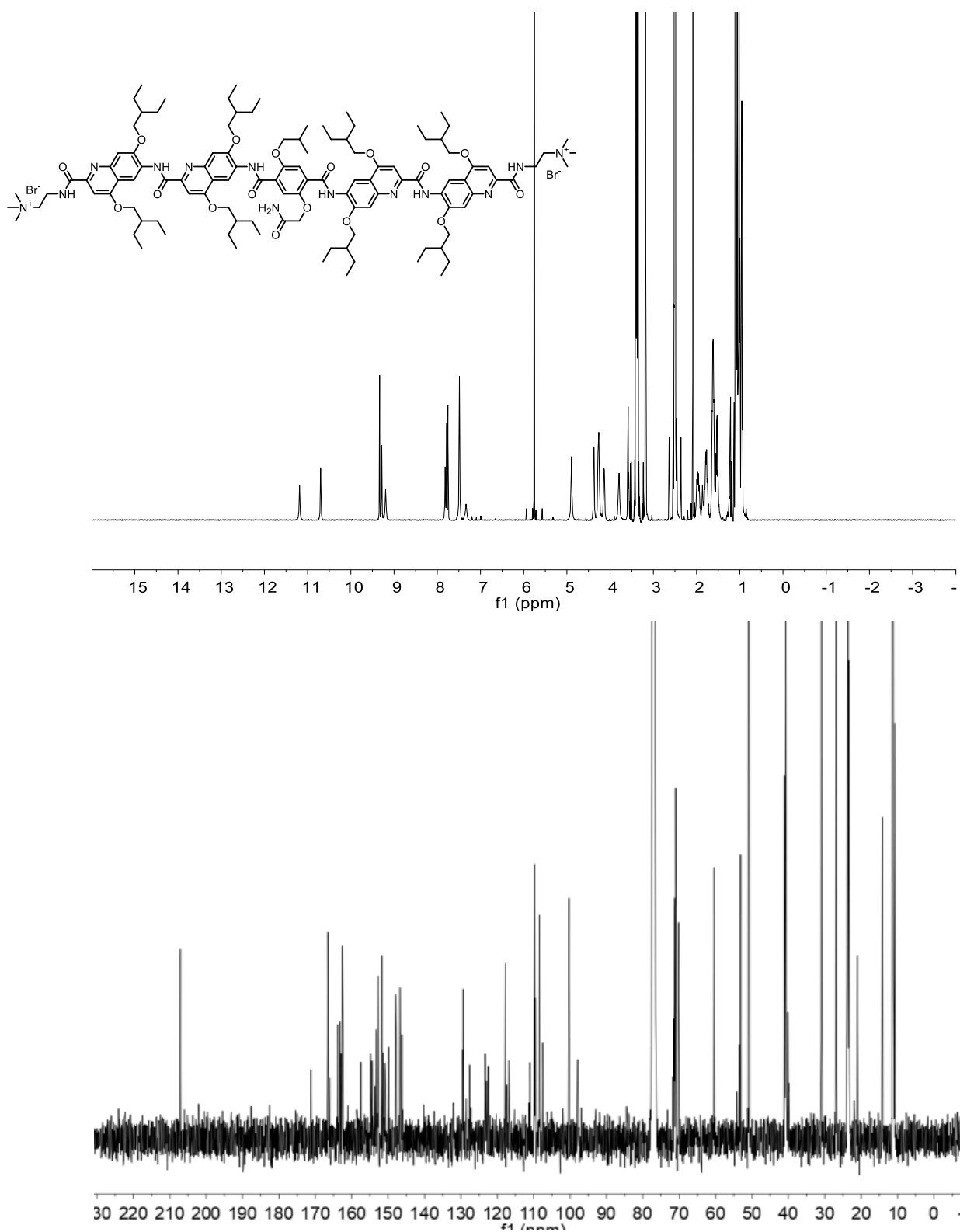
$^1\text{H}$  (500 MHz,  $\text{CDCl}_3$ , 298 K) and  $^{13}\text{C}$  (126 MHz,  $\text{CDCl}_3$ , 298 K) NMR spectra of compound **32**



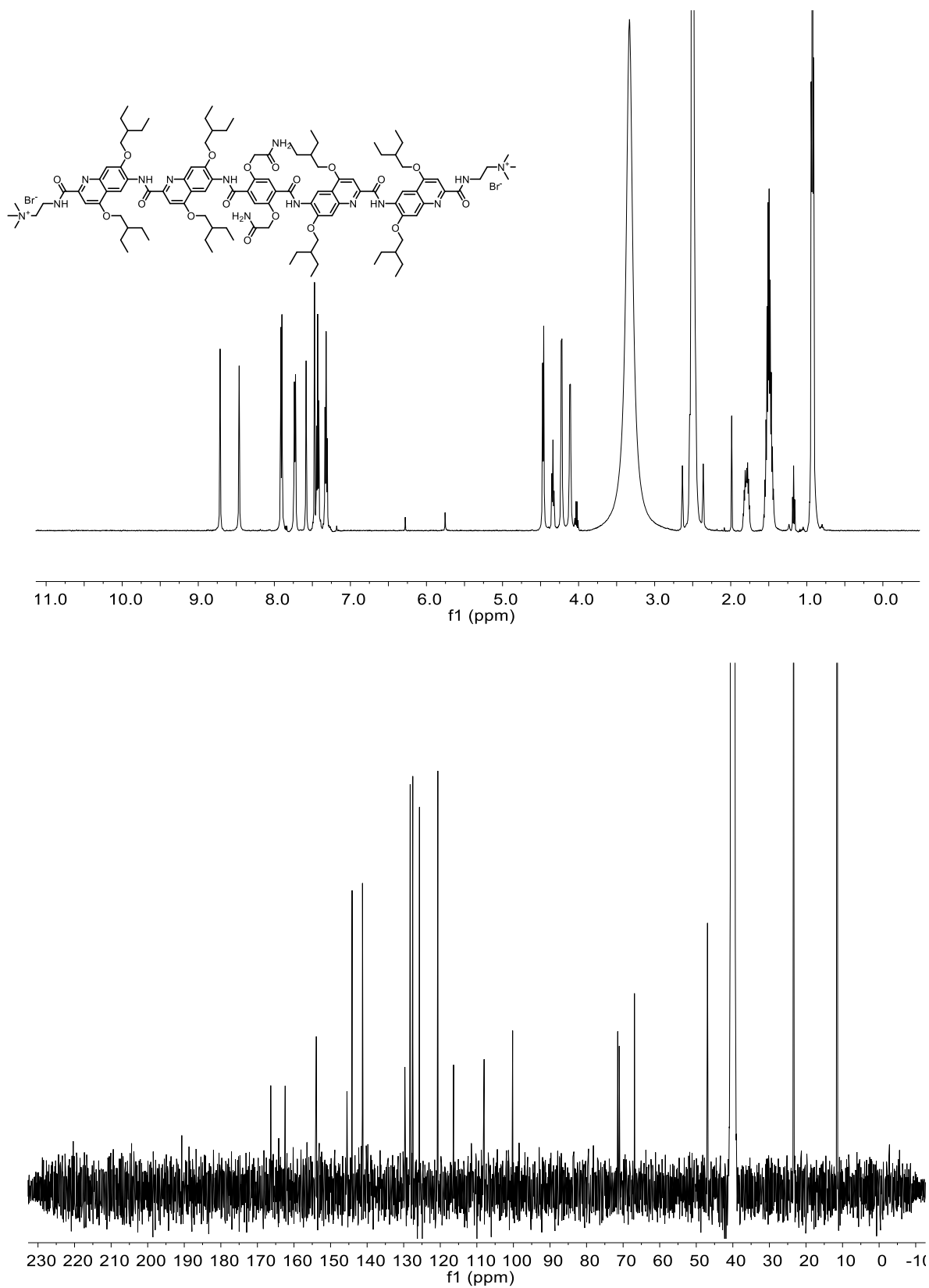
<sup>1</sup>H (500 MHz, CDCl<sub>3</sub>, 298 K) and <sup>13</sup>C (126 MHz, CDCl<sub>3</sub>, 298 K) NMR spectra of compound **33**



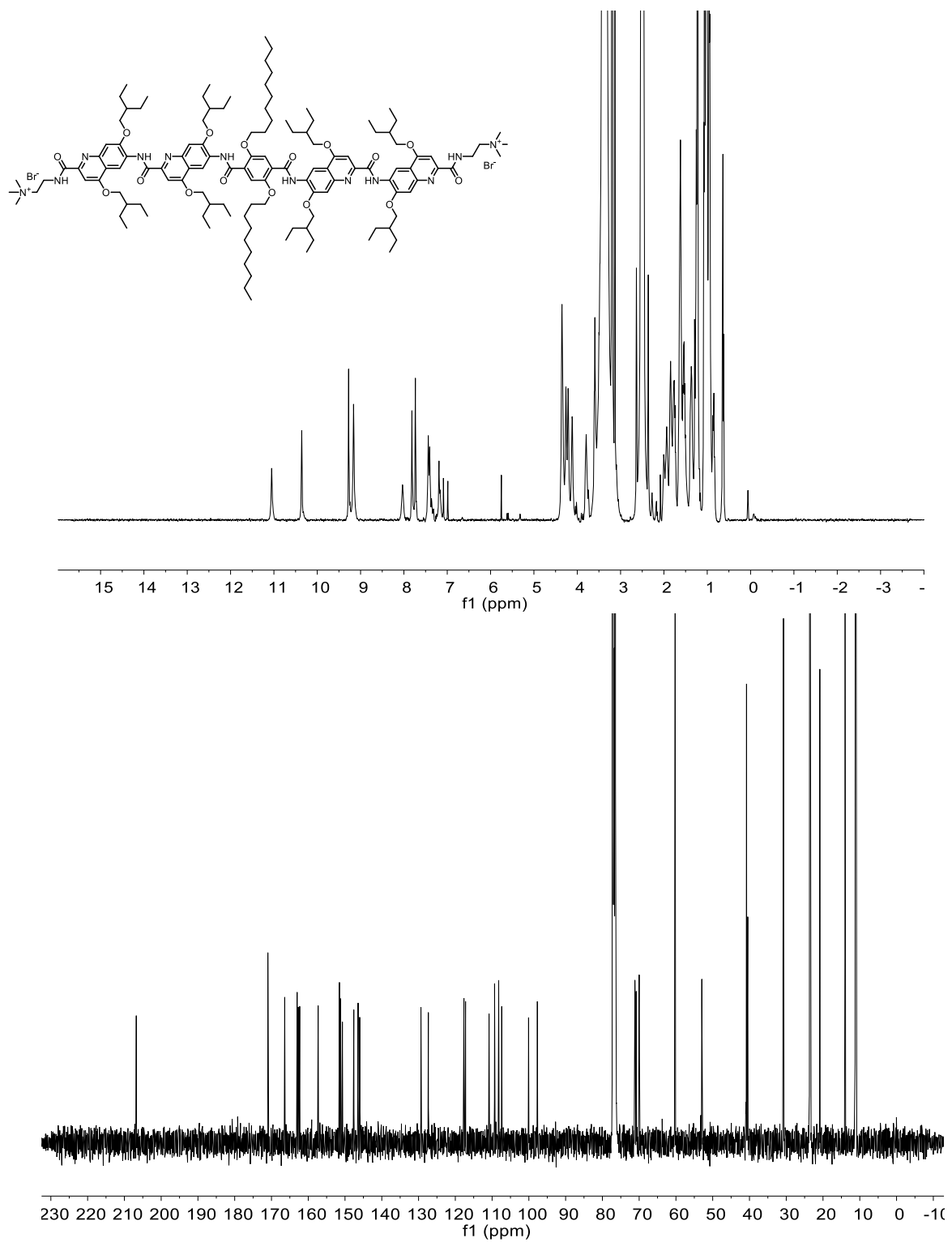
$^1\text{H}$ - (500 MHz,  $\text{CDCl}_3$ , 298 K) and  $^{13}\text{C}$  (500 MHz,  $\text{CDCl}_3$ , 298 K) NMR spectra of compound **1**.



$^1\text{H}$  (400 MHz,  $\text{CDCl}_3$ , 298 K) and  $^{13}\text{C}$  (126 MHz,  $\text{CDCl}_3$ , 298 K) NMR spectra of compound **2**.



$^1\text{H}$  (500 MHz,  $\text{CDCl}_3$ , 298 K) and  $^{13}\text{C}$  (126 MHz,  $\text{CDCl}_3$ , 298 K) NMR spectra of compound **3**.



$^1\text{H}$ - (500 MHz,  $\text{CDCl}_3$ , 298 K) and  $^{13}\text{C}$  (500 MHz,  $\text{CDCl}_3$ , 298 K) NMR spectra of compound 4

### 3.6.5.8 References – experimental section

- (1) Roger, K.; Cabane, B. Why Are Hydrophobic/Water Interfaces Negatively Charged? *Angew. Chemie Int. Ed.* **2012**, *51* (23), 5625–5628. <https://doi.org/https://doi.org/10.1002/anie.201108228>.
- (2) Ermakov, Y. A. The Determination of Binding Site Density and Association Constants for Monovalent Cation Adsorption onto Liposomes Made from Mixtures of Zwitterionic and Charged Lipids. *Biochim. Biophys. Acta - Biomembr.* **1990**, *1023* (1), 91–97. [https://doi.org/https://doi.org/10.1016/0005-2736\(90\)90013-E](https://doi.org/https://doi.org/10.1016/0005-2736(90)90013-E).
- (3) Bashkirov, P. V.; Kuzmin, P. I.; Vera Lillo, J.; Frolov, V. A. Molecular Shape Solution for Mesoscopic Remodeling of Cellular Membranes. *Annu. Rev. Biophys.* **2022**, *51*, 473–497. <https://doi.org/10.1146/annurev-biophys-011422-100054>.
- (4) Bashkirov, P. V.; Chekashkina, K. V.; Akimov, S. A.; Kuzmin, P. I.; Frolov, V. A. Variation of Lipid Membrane Composition Caused by Strong Bending. *Biochem. Suppl. Ser. A Membr. Cell Biol.* **2011**, *5* (2), 205–211. <https://doi.org/10.1134/S199074781101003X>.
- (5) Vlassiuk, I.; Smirnov, S.; Siwy, Z. Ionic Selectivity of Single Nanochannels. *Nano Lett.* **2008**, *8* (7), 1978–1985. <https://doi.org/10.1021/nl800949k>.
- (6) Markin, V. S. Lateral Organization of Membranes and Cell Shapes. *Biophys. J.* **1981**, *36* (1), 1–19. [https://doi.org/10.1016/S0006-3495\(81\)84713-3](https://doi.org/10.1016/S0006-3495(81)84713-3).
- (7) Fosnarić, M.; Igljć, A.; May, S. Influence of Rigid Inclusions on the Bending Elasticity of a Lipid Membrane. *Phys. Rev. E. Stat. Nonlin. Soft Matter Phys.* **2006**, *74* (5 Pt 1), 51503. <https://doi.org/10.1103/PhysRevE.74.051503>.
- (8) Antonny, B. Mechanisms of Membrane Curvature Sensing. *Annu. Rev. Biochem.* **2011**, *80*, 101–123. <https://doi.org/10.1146/annurev-biochem-052809-155121>.
- (9) Sebaoun, L.; Maurizot, V.; Granier, T.; Kauffmann, B.; Huc, I. Aromatic Oligoamide  $\beta$ -Sheet Foldamers. *J. Am. Chem. Soc.* **2014**, *136* (5), 2168–2174. <https://doi.org/10.1021/ja412729s>.
- (10) Hu, Liming; Rong, Jie; Mao, Zhijie; Wang, Yujie; Zeng, C. Preparation of 1-Substituted Benzyl-6-Substituted-9-Oxo-2,3,6,9-Tetrahydro-1H-[1,4]Oxazino[3,2-g]Quinoline-8-Carboxylic Acid Compounds and Their Application as HIV-1 Integrase Inhibitor.
- (11) Gourvest, J-F; Lesuisse, D; Teutsch, J.-G. Biphenyl Compounds, Process for Their Preparation, Intermediates for This Process, Their Use as 5-Alpha-Reductase

- Inhibitors, and Pharmaceutical Compositions Containing Them. *Eur. Pat. Appl.* **1997**, 47pp.
- (12) Velasco-Olmo, A.; Ormaetxea Gisasola, J.; Martinez Galvez, J. M.; Vera Lillo, J.; Shnyrova, A. V. Combining Patch-Clamping and Fluorescence Microscopy for Quantitative Reconstitution of Cellular Membrane Processes with Giant Suspended Bilayers. *Sci. Rep.* **2019**, 9 (1), 7255. <https://doi.org/10.1038/s41598-019-43561-4>.
- (13) Oncins, G.; Garcia-Manyes, S.; Sanz, F. Study of Frictional Properties of a Phospholipid Bilayer in a Liquid Environment with Lateral Force Microscopy as a Function of NaCl Concentration. *Langmuir* **2005**, 21 (16), 7373–7379. <https://doi.org/10.1021/la050644q>.
- (14) Garcia-Manyes, S.; Oncins, G.; Sanz, F. Effect of Temperature on the Nanomechanics of Lipid Bilayers Studied by Force Spectroscopy. *Biophys. J.* **2005**, 89 (6), 4261–4274. <https://doi.org/10.1529/biophysj.105.065581>.
- (15) Bashkirov, P. V; Kuzmin, P. I.; Chekashkina, K.; Arrasate, P.; Vera Lillo, J.; Shnyrova, A. V; Frolov, V. A. Reconstitution and Real-Time Quantification of Membrane Remodeling by Single Proteins and Protein Complexes. *Nat. Protoc.* **2020**, 15 (8), 2443–2469. <https://doi.org/10.1038/s41596-020-0337-1>.
- (16) Tien, H. T.; Ottova, A. Chapter 1 - The Lipid Bilayer Concept: Experimental Realization and Current Applications. In *Planar Lipid Bilayers (BLMs) and Their Applications*; Tien, H. T., Ottova-Leitmannova, A., Eds.; Membrane Science and Technology; Elsevier, 2003; Vol. 7, pp 1–73. [https://doi.org/https://doi.org/10.1016/S0927-5193\(03\)80025-6](https://doi.org/https://doi.org/10.1016/S0927-5193(03)80025-6).
- (17) Passechnik, V. I.; Sokolov, V. S. Estimation of Electrochrome Dyes Position in the Bilayer through the 2nd Harmonic of Capacitive Current. *Bioelectrochemistry* **2002**, 55 (1–2), 47–51. [https://doi.org/10.1016/s1567-5394\(01\)00167-0](https://doi.org/10.1016/s1567-5394(01)00167-0).
- (18) Mirsky, V. M.; Cherny, V. V; Sokolov, V. S.; Markin, V. S. Electrostatic Assay of Phospholipase A Activity: An Application of the Second Harmonic Method of Monitoring Membrane Boundary Potentials. *J. Biochem. Biophys. Methods* **1990**, 21(4), 277–284. [https://doi.org/10.1016/0165-022x\(90\)90002-t](https://doi.org/10.1016/0165-022x(90)90002-t).
- (19) Frolov, V. A.; Lizunov, V. A.; Dunina-Barkovskaya, A. Y.; Samsonov, A. V.; Zimmerberg, J. Shape Bistability of a Membrane Neck: A Toggle Switch to Control Vesicle Content Release. *Proc. Natl. Acad. Sci. U. S. A.* **2003**, 100 (15). <https://doi.org/10.1073/pnas.1432962100>.

- (20) Schneider, C. A.; Rasband, W. S.; Eliceiri, K. W. NIH Image to ImageJ: 25 Years of Image Analysis. *Nat. Methods* **2012**, *9*(7), 671–675. <https://doi.org/10.1038/nmeth.2089>.
- (21) García-Arribas, A. B.; González-Ramírez, E. J.; Sot, J.; Areso, I.; Alonso, A.; Goñi, F. M. Complex Effects of 24:1 Sphingolipids in Membranes Containing Dioleoylphosphatidylcholine and Cholesterol. *Langmuir* **2017**, *33* (22), 5545–5554. <https://doi.org/10.1021/acs.langmuir.7b00162>.
- (22) Sokolov, V. S.; Kuz'min, V. G. [Measurement of differences in the surface potentials of bilayer membranes according to the second harmonic of a capacitance current]. *Biofizika* **1980**, *25* (1), 170–172.
- (23) Rigaku OD (2019). CrysAlis PRO. Rigaku Oxford Diffraction Ltd, Yarnton, Oxfordshire, England.
- (24) Sheldrick, G. M. Crystal Structure Refinement with *{\it SHELXL}*. *Acta Crystallogr. Sect. C* **2015**, *71* (1), 3–8. <https://doi.org/10.1107/S2053229614024218>.
- (25) Dolomanov, O. V; Bourhis, L. J.; Gildea, R. J.; Howard, J. A. K.; Puschmann, H. *{\it OLEX2}*: A Complete Structure Solution, Refinement and Analysis Program. *J. Appl. Crystallogr.* **2009**, *42* (2), 339–341. <https://doi.org/10.1107/S0021889808042726>.

## **4. Strained shape persistent macrocycles**

**(to be submitted)**

### **Contributions:**

The project and the designs of the macrocycles was planned in collaboration with Prof. I. Huc. The synthetic routes and conditions for the synthesis of the Q<sup>p</sup> monomer with triethyleneglycol sidechains have been developed and established by me. DMB installation on the Q<sup>p</sup> intermediate was developed with the help of Sebastian Reiner, a master student in our group. The oligomer synthesis and subsequent analysis was performed by me. Automated synthesis of non-cyclic precursors was conducted with the help of Dr. Céline Douat. 2D-NMR experiments were performed with the help of Dr. Lars Allmendinger.

## 4.1 Introduction

One reason within many, why macrocycles are targets of interest, is due to the fact that macrocyclization can promote and stabilize conformations, which are unlikely to occur in non-cyclic derivatives. Macrocyclic structures are cyclic systems that may represent different conformations from those of their their non-cyclic precursors. These shapes can be found in nature in general and are frequently represented and used in the field of biology and pharmacology. Artificial macrocycles based on cyclodextrin,<sup>(1)</sup> crown ethers,<sup>(2)</sup> arylene ethylenes,<sup>(3)</sup> pillararenes<sup>(4)</sup> or callixarenes<sup>(5)</sup> and oligoamides<sup>(6)</sup> are widely described. Generally speaking, macrocycles comprise restricted conformational freedom compared to their non-cyclic derivatives due to their cyclic structure. Accordingly, these macrocycles are more rigid than their precursors. Moore et al. described oligomerization and cyclization using *ortho*, *meta* and *para* phenyl acetylene sequences in one synthetic step using Pd- catalyzed Sonogashira couplings.<sup>(6, 7)</sup> Gong et al. published oligoamide macrocycles with local conformational preferences<sup>(6)</sup> and proposed folding-assisted macrocyclization due to non-covalent interactions of the backbone.<sup>(8)</sup> These so-called shape-persistent macrocycles are based on units that are rather rigid and their overall shape does not differ (largely) from their initial shape compared to their non-cyclic precursors. Huc et al. described aromatic oligoamide macrocycles, using 8-aminoquinoline 2-carboxylate building blocks, which – due to their cyclic structure – are not able to exist in their preferred conformation and thus, are “frustrated”.<sup>(9-11)</sup> Consequently, these macrocycles are strained.

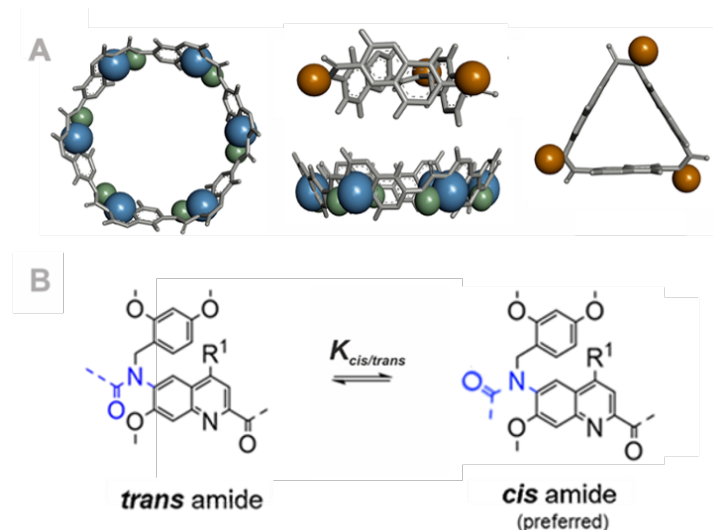


**Figure 1. Different strained macrocycles and their possible conformations (A)** Model of a chiral quinoline 6<sup>mer</sup> macrocycle based on 6-aminoquinoline 2-carboxylic acid building blocks, atoms involved in hydrogen bonding are represented in space filling mode; blue = nitrogen and green = hydrogen (**left**) and quinoline 3<sup>mer</sup> macrocycle; *cis* NH in orange (**right**), (**B**) *cis* and *trans* isomerism of a tertiary aromatic amide, R<sup>1</sup> = triethyleneglycol thioether)

In the following, this work will describe strained oligoamide macrocycles based on 6-aminoquinoline 2- carboxylic acid building blocks, which are obtained by “kinking” their shape. These macrocycles (**Figure 1A**) were synthesized by removable linearity-disruptor groups on the arylamide backbone, which lead to tertiary arylamides in *cis* conformation (**Figure 1B**). Their final conformations were studied in computational studies and further spectroscopically in solution.

## 4.2. Concept and experimental design

Short linear oligomers of 6-aminoquinoline 2- carboxylic acid (hereafter referred to as Q<sup>p</sup>) building blocks (see chapter 1 for more details on Q<sup>p</sup>) are *per se* too linear to cyclize. Specifically, due to their weak curvature sixteen units are approximately required per turn (**Figure 2A, 2B**). To obtain cyclic structures based on the same, the non-cyclic precursor needs to be “kinked” for reducing the number of units needed per turn. This is performed by introducing tertiary amides into the backbone which prefer a *cis*-conformation (**Figure 2C, right**; see also chapter 1 for more details on tertiary amides). Consequently, the final macrocycle with an “all-*trans*” conformation will be strained.

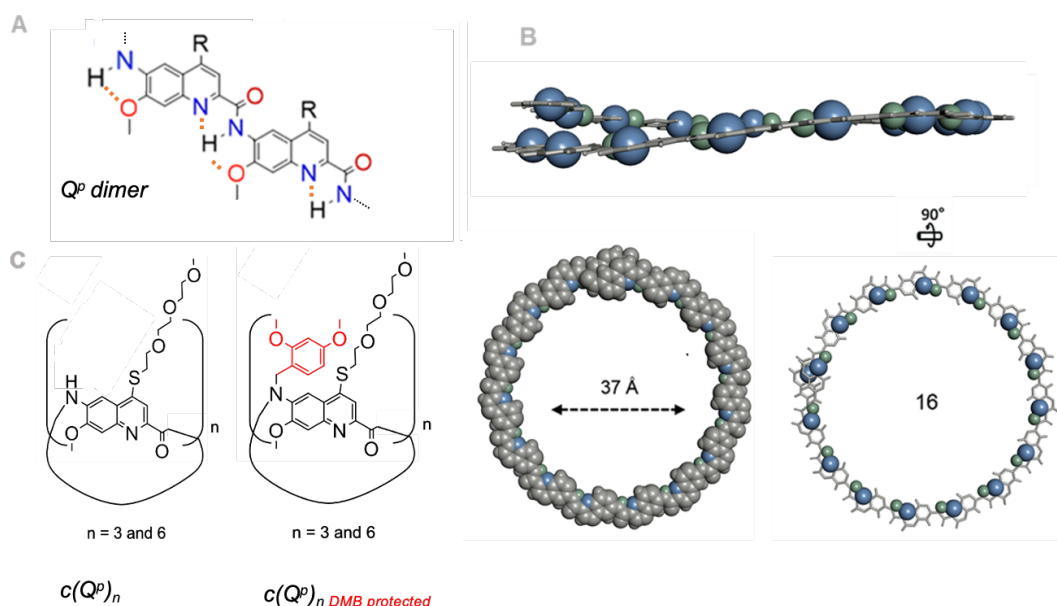


**Figure 2.** Q<sup>p</sup> (6-aminoquinoline 2-carboxylic acid) monomer used in this work and its natural curvature. (A) Chemical structure of Q<sup>p</sup> dimer, with methoxy groups on position 7 and R groups on position 4. Intramolecular hydrogen bonding shown in dotted lines in orange. (B) Molecular model of homogeneous 6-amino quinoline carboxylic acid oligomer with 16 units with 37 Å diameter size, atoms involved in hydrogen bonding in space filling mode in blue =nitrogen and green =hydrogen, sidechain and hydrogen atoms (except NH) were removed for clarity.

In detail, the oligomer of Q<sup>P</sup> (i.e. 6-aminoquinoline 2-carboxylic acid) building block (**Figure 2A**) shows hydrogen bonding interactions between the quinoline nitrogen and the arylamide NH on the inside of the foldamer curvature. When using this building block, sixteen units are required to achieve one full turn (**Figure 2B**, see chapter 1 for more details on the curvature of Q<sup>P</sup>). To reduce the number of building blocks and to simplify its cyclization, linearity disruptors are introduced on the backbone (**Figure 2C**, right). Hence, 2,4-dimethoxybenzyl groups (DMB) were installed on the all *trans* arylamide backbone of the oligomer (**Figure 2C**). The resulting tertiary arylamide bonds can exist in two different conformations, the *cis* and the *trans* isomer, whereas the *cis* isomer is strongly preferred. Therefore, the resulting *cis* amides between adjacent quinoline ring systems create kinking on the backbone chain obtaining an angle of 60° between adjacent quinoline rings (**Figure 1B**, see chapter 1 for more details regarding the conformation of tertiary arylamides).

Due to the disrupted hydrogen bonds and loss of planarity of the amide and quinoline ring, different conformational isomers were expected during the cyclization step. After successful cyclization, all DMB groups are removed and the tertiary *cis* amides on the backbone are transferred back to secondary aryl amides. The rotation of the latter is constricted – due to the double bond nature of the secondary aryl amide – and the *trans* isomer is preferred in principle. Macrocyclic sequences of cyclic Q<sup>P</sup> oligomers (hereafter referred to as c(Q<sup>P</sup>)<sub>n</sub> with n = 3 and 6; **c(Q<sup>P</sup>)<sub>3</sub>** for n = 3 and **c(Q<sup>P</sup>)<sub>6</sub>** for n = 6; see also chapter 1 for more details on Q<sup>P</sup>) were targeted (**Figure 2C**, left). The linear precursors were synthesized on solid support and macrocyclized in solution. The final macrocycle conformations were investigated in computational studies and further by <sup>1</sup>H-NMR spectroscopy.

## 4.3. Results and Discussion

### 4.3.1 Computational studies

After the removal of the linearity disruptors, the shortest macrocycle **c(Q<sup>P</sup>)<sub>3</sub>** with a length of three units was expected to be strained. The latter was expected to stay in an energy costly all *cis* conformation in a triangular shaped mode (**Figure 1A**, right). Molecular modelling for **c(Q<sup>P</sup>)<sub>3</sub>** suggests either a C<sub>3</sub> symmetrical triangular or unsymmetrical – tilted – triangular shape. The models suggest a restricted rotation around the arylamide bond due to steric hindrance of the sidechains in position 4 and 7. The interconversion between the symmetrical and the tilted conformation comprises

a barrier, which needs to be overcome between the two states. Moreover, the sidechains possibly need to pass within the cavity of the macrocycle.

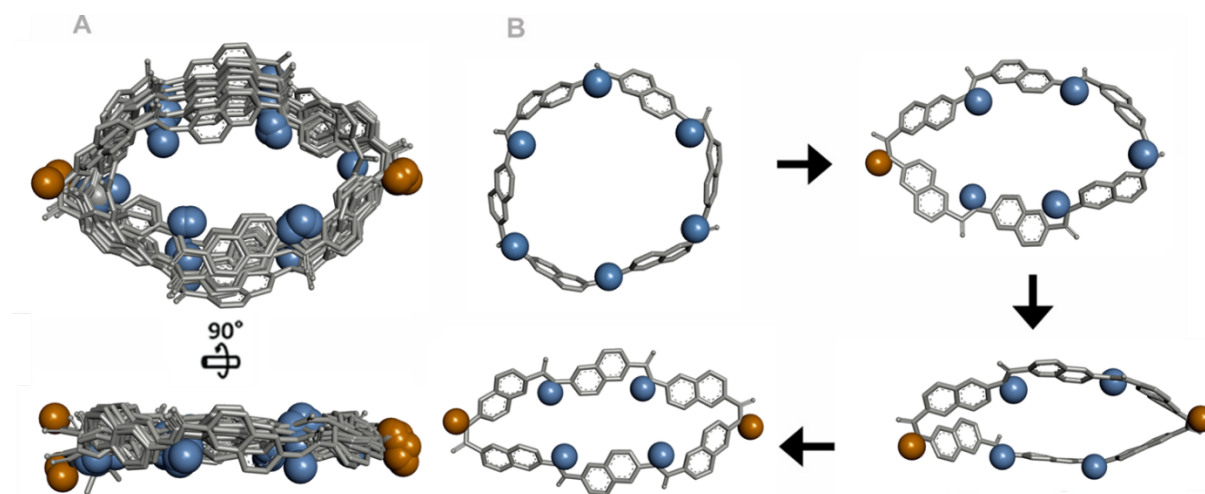


**Figure 3. MD simulation of the transition of a cone shaped  $c(QP)_6$  macrocycle.** (A) Overlay of 10 snapshots during the MD simulation. (B) MD models at 1, 19, 69 and 97 ps during the MD simulation (simulation time = 100 ps), sidechain and hydrogen atoms (except NH) were removed for clarity.

For the  $c(QP)_6$  conformation we first assumed to obtain a circular-shaped macrocycle with all secondary arylamides hydrogen bonded in preferred *trans* conformation. Interestingly, molecular dynamics (MD) simulations for  $c(QP)_6$  revealed the contrary – an ellipse shaped structure with 2 *cis* amides on the backbone (**Figure 3A, B**). During a 100 ps long MD simulation at 300 K we observed a conformational change of the two amide bonds from our initial circular  $c(QP)_6$  model. After 19 ps, we see disruption of the hydrogen bonding and amide bond rotation (**Figure 3B, 2<sup>nd</sup> snapshot**). After 69 ps, the second amide bond on contraposition undergoes *cis/trans* isomerism (**Figure 3B, 3<sup>rd</sup> snapshot**), supporting the final  $C_2$  symmetrical ellipse shaped conformation (**Figure 3B, 4<sup>th</sup> snapshot**). The latter stayed stable *in silico* during the remaining time of the computational simulation. MD simulations at higher temperature revealed similar outcomes. For both macrocycles these findings are in agreement with spectroscopic data obtained in this study.

For longer oligomers, e.g., a 10<sup>mer</sup>  $c(QP)_{10}$  or an 8<sup>mer</sup>  $c(QP)_8$ , molecular modelling revealed stable cone-shaped macrocycles with an all *trans* conformation on the backbone (**Figure 4A, B**).

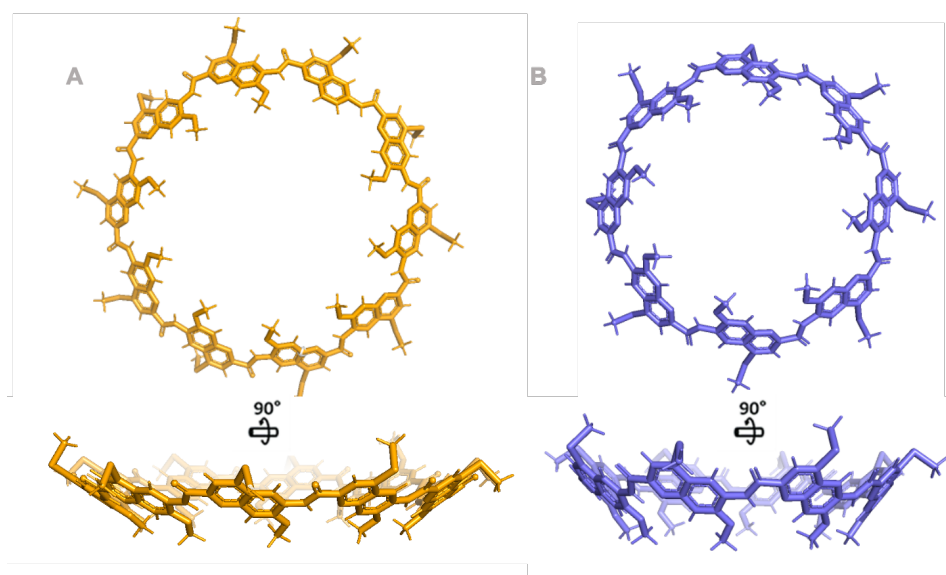


**Figure 4. Different conformers of  $cQP_n$**  (A) Model of a  $10^{\text{mer}} c(QP)_{10}$  in yellow; top (up) and side view (bottom). (B) Model of an  $8^{\text{mer}} c(QP)_8$  in blue; top (top) and side view (bottom).

#### 4.3.2 Compound synthesis

The  $Q^p$  monomer with a methoxy group on position 7 and a triethylene group on position 4 as sidechains from the commercially available 2-methoxy-4-nitroaniline was synthesized according to **Figure 5**.

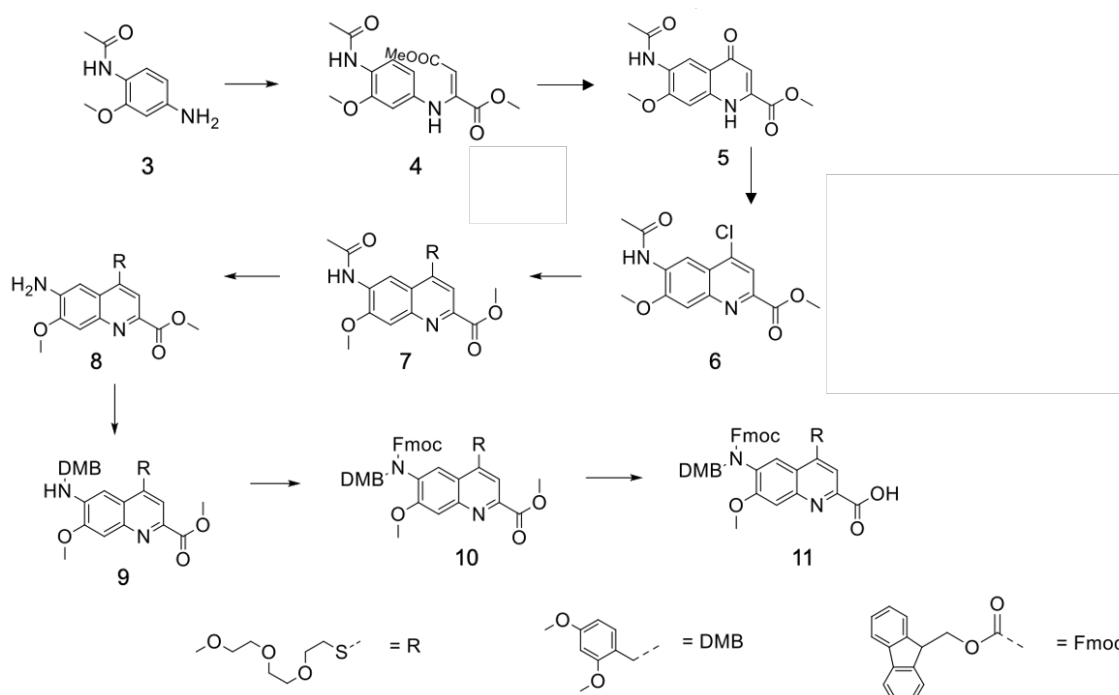


**Figure 5. Synthesis of the  $Q^p$  monomer with methoxy group on position 4 and triethylene groups on position 7.**

Oligomers were obtained using SPFS methodology using Fmoc strategy (**Figure 6**, see

experimental section for more details). SASRIN resin was loaded with the first amino acid building block, using HBTU and DIEA in DMF. The free active sites on the resin were capped using acetic anhydride in acetic acid and the first deprotection of the Fmoc group was performed by using 2% DBU in NMP (vol/vol %).

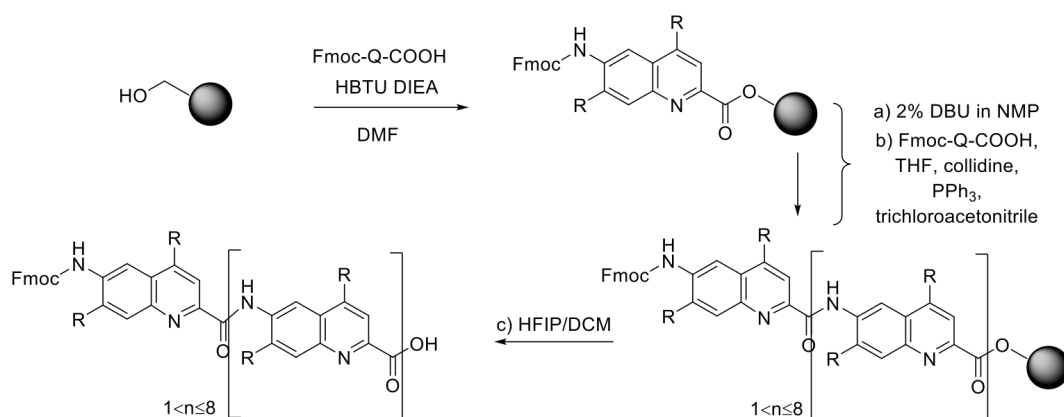


**Figure 6** Solid phase synthesis of Q<sup>p</sup> oligomers. Resin shown as black ball.

Thereafter, the coupling reaction was performed by firstly, activating the amino acid *via in situ* activation conditions, i.e., by using trichloroacetonitrile (TCAN), triphenylphosphine (PPh<sub>3</sub>) and secondly, mixing the activated acid in dry chloroform to the deprotected oligomer in dry THF in the presence of collidine as a base. After the desired target length has been reached on the resin, a final Fmoc deprotection was performed. Afterwards, the amino acid oligomer was cleaved from the resin. Macrocyclization of the kinked amino acid precursors was performed in solution phase, using earlier described *in situ* activation conditions.<sup>(12)</sup> The final removal of the DMB groups on the tertiary arylamides was achieved by treating the macrocycles with TFA at 60°C.

#### 4.3.3 Solvent dependent conformational behavior in solution

The <sup>1</sup>H NMR spectrum of **c(Q<sup>p</sup>)<sub>3</sub>** macrocycle in *d*<sub>6</sub>-DMSO showed two sets of signals, with a ratio of 1:3. The major species with nine C-Hs and three N-H signals suggests a unsymmetrical conformer, whereas the amide proton signals overlap. The second and minor species shows three C-Hs and one N-H, suggesting a C<sub>3</sub> symmetrical conformer. The amide proton signals were assigned by <sup>1</sup>H-<sup>15</sup>N-HSQC-NMR but surprisingly the three amide NH crosspeaks of the unsymmetrical conformer overlap (**Figure 7D** at

10.0 ppm, 121.4 ppm), as well. Nevertheless, we see signal splitting upon heating in  $d_6$ -DMSO, proving three individual N-H signals for the latter (**Figure 7B**).

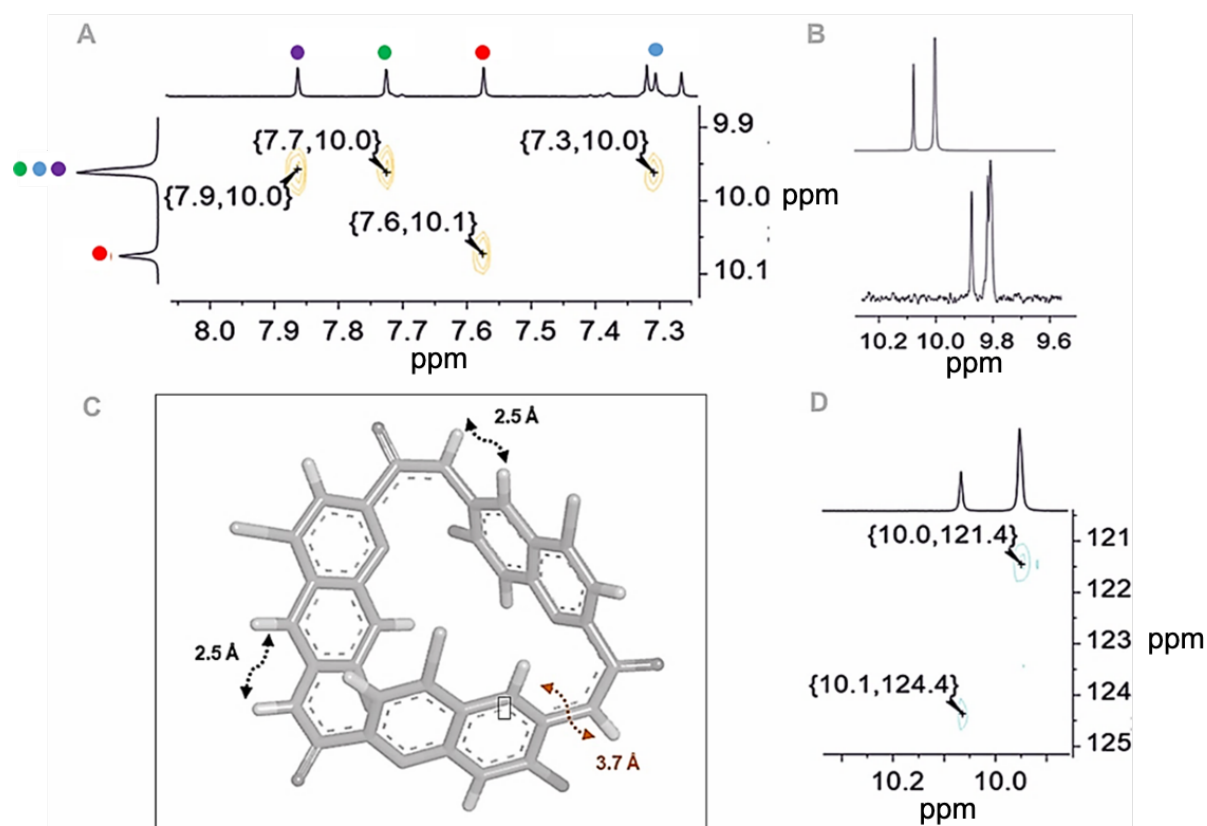


**Figure 7. Different conformers of  $c(QP)_3$**  (A)  $^1H$ - $^1H$ -NOESY NMR spectrum (500 MHz) in  $d_6$ -DMSO showing correlations with H5 for each individual NH signal. (B) Zoom of the  $^1H$  NMR spectrum (500 MHz) of  $c(QP)_3$  in  $d_6$ -DMSO at 45°C showing signal splitting of the amides (C) Model of unsymmetrical  $c(QP)_3$ , (black and orange arrow representing the distance). (D)  $^1H$ - $^{15}N$  NMR of the amide region, showing cross peaks overlapping.

The NOESY- $^1H$ - $^1H$  HSQC spectrum in  $d_6$ -DMSO at 25°C shows Nuclear Overhauser effects (NOEs) for both conformers. We focused on the NOEs corresponding to the correlation between the arylamide NH and the quinoline H5 proton (**Figure 7A**) demonstrating the expected *cis* conformation. One NOE signal (**Figure 7A** red circle) is observed for the symmetrical conformer and three different NOEs were observed for the unsymmetrical conformer (**Figure 7A** green, blue and violet circles). The three NOE signals corresponding to the unsymmetrical conformer (**Figure 7A**, blue, green and violet circles) with two NOEs of similar intensity (**Figure 7A**; NOE at 7.9 ppm; 10.0 ppm and 7.7 ppm; 10 ppm) and a third NOE signal (**Figure 7A**; NOE at 7.3 ppm; 10.0 ppm). As known, the cross-peaks intensity is proportional to the cross signal relaxation, and thus the latter proportional to internuclei distances.<sup>(43)</sup> These results support our assignment of the unsymmetrical conformer, where one N-H needs to show a larger distance to H5 quinoline and two of three amide protons and H5

quinoline C-Hs show equal internuclei distances. Molecular modelling suggests several reasonable unsymmetrical conformers (one displayed in **Figure 7C**). The symmetrical triangular shaped conformation is based on identical distances between H5 and NH (**Figure 7A**, red circles, **Figure 1A**).

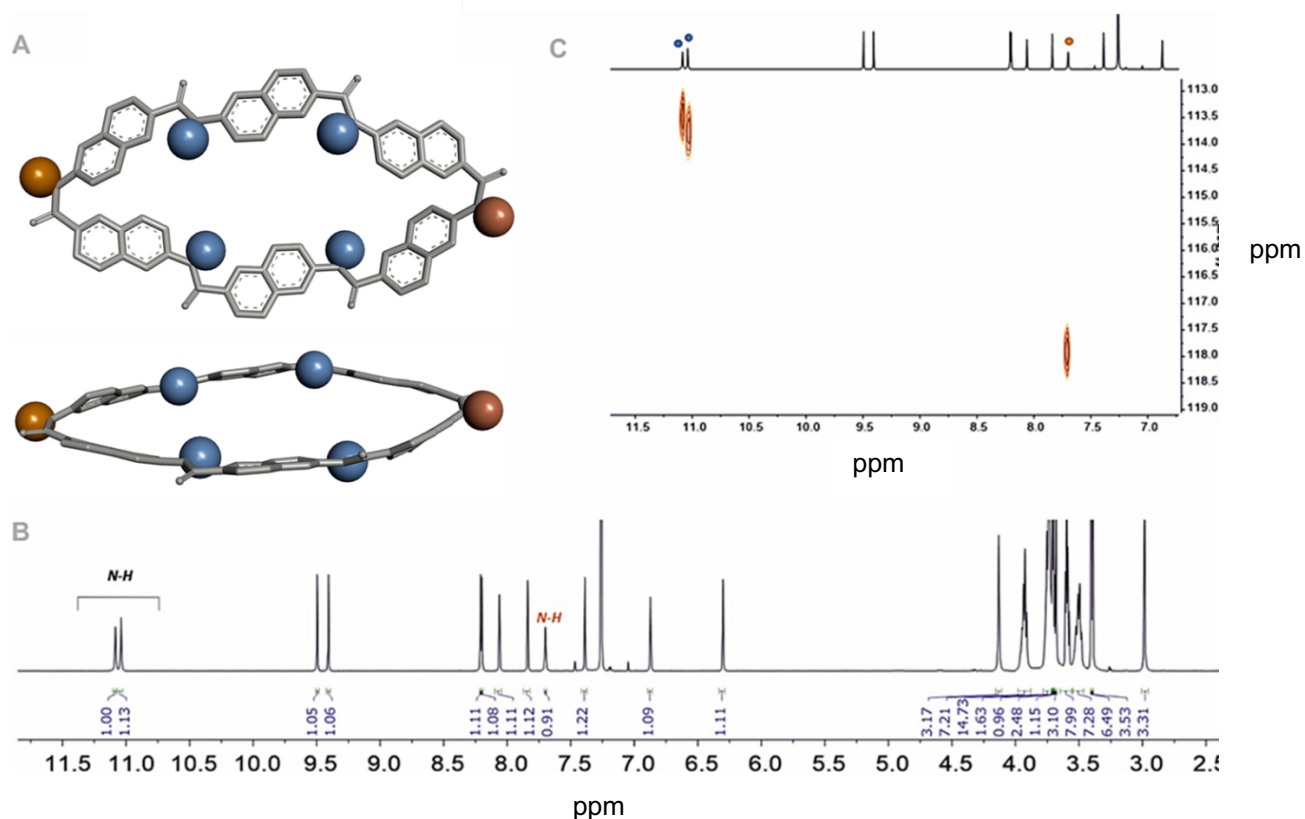


**Figure 8. Ellipse shaped  $c(QP)_6$**  (A) Model of ellipse shaped  $c(QP)_6$ ; hydrogen and sidechain atoms are omitted for clarity. (B)  $^1H$  NMR spectrum (500 MHz) of  $c(QP)_6$  in  $d_7$ - $CHCl_3$  at 25°C, *cis* amide marked in red. (C)  $^1H$ - $^{15}N$  NMR of the amide region, showing three individual crosspeaks (blue circles = *trans* amides, orange = *cis* amide).

The  $^1H$ -NMR spectrum of  $c(QP)_6$  in  $CDCl_3$  at 25°C shows one conformer with three individual signals for amide N-Hs and nine aromatic C-H signals, all in an 1:1 ratio suggesting a  $C_2$  or centro symmetrical conformation (**Figure 8A, B**). The third N-H signal shows a drastical change in its chemical shift, with a chemical shift value below 8 ppm, suggesting to be in *cis* conformation. The latter was proved by  $^{15}N$ - $^1H$ -HSQC-NMR spectroscopy, showing three individual crosspeaks for the amide protons (**Figure 8C**).

Variable temperature  $^1H$ -NMR measurements of  $c(QP)_3$  and of  $c(QP)_6$  macrocycle were performed revealing global shifts of proton signals, measured in  $d_7$ -DMF between -30°C and 70°C and in  $CDCl_3$  between -60°C and 50°C. No coalescence was observed for both macrocycles, suggesting the conformations are in a slow exchange regime

where *cis/trans* isomerism is presumably slower than NMR timescale. Upon cooling, hydrogen bonding interactions with the solvent is taking place explaining the downfield shift of the amide N-*H* signals. Due to low solubility, conformational behavior in polar protic solvents could not be studied (i.e. methanol or acetonitrile). Interestingly, the integration of the proton signals for **c(Q<sup>p</sup>)<sub>3</sub>** in DMF and CHCl<sub>3</sub> at each temperature during the temperature dependent NMR studies vary, leading to the conclusion, that interconversion of the conformers present in solution may take place.

Upon protonation of **c(Q<sup>p</sup>)<sub>6</sub>** with TFA, we see a change in the number of total resonances in the NMR spectrum, referring to a change in symmetry and thus, in conformation. The data suggests that upon protonation of the quinoline nitrogen, a new hydrogen bonding interaction with quinoline N-*H*<sup>+</sup> takes place and the quinoline units flip around the amide bond. To prove protonation and conformational switching of Q<sup>p</sup>, a dimeric model (cpd. **1**) was designed and synthesized according to the scheme in **Figure 9**. The synthesis for the precursor **12** has been already described in the literature.<sup>(14)</sup> Compound **1** is a dimeric acetylated methyl carboxylate based on Q<sup>p</sup> (Ac-(Q<sup>p</sup>)<sub>2</sub>-OMe).

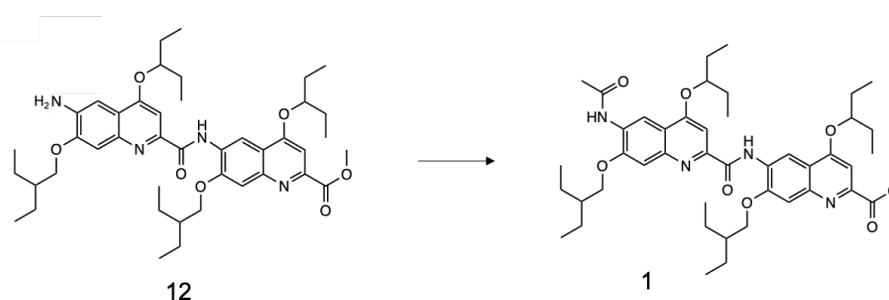


**Figure 9. Synthetic scheme of 1 (Ac-(Q<sup>p</sup>)<sub>2</sub>-OMe).**

The <sup>1</sup>H-NMR spectrum in 10% *d*-TFA in undeuterated TFA of **1** (**Figure 10A**) shows six aromatic C-*H*s and two N-*H*s and further, the presence of a quinolinium proton very upfield shifted due to presumably hydrogen bonding with its adjacent carbonyl oxygen (**Figure 10B**). Further, the <sup>15</sup>N-<sup>1</sup>H-HSQC spectrum proves the presence of a third N-*H* atom, with a higher chemical shift value presumably for the quinolinium N-*H*. ROESY <sup>1</sup>H-<sup>1</sup>H-NMR spectroscopy reveals one strong correlation between quinoline H<sub>3</sub> and the aryl amide N-*H*, proving the formation of a new hydrogen bonding pattern upon protonation of the quinoline nitrogen (**Figure 10A, H<sub>3</sub> and C**). Additionally, the missing correlation between H<sub>8</sub> on the 2<sup>nd</sup> quinoline ring with exchangeable protons (i.e. quinolinium N-*H* or amide N-*H*) in the ROESY agrees with the protonation pattern described in Figure 10A (**see Figure 10A, H<sub>8</sub>**).

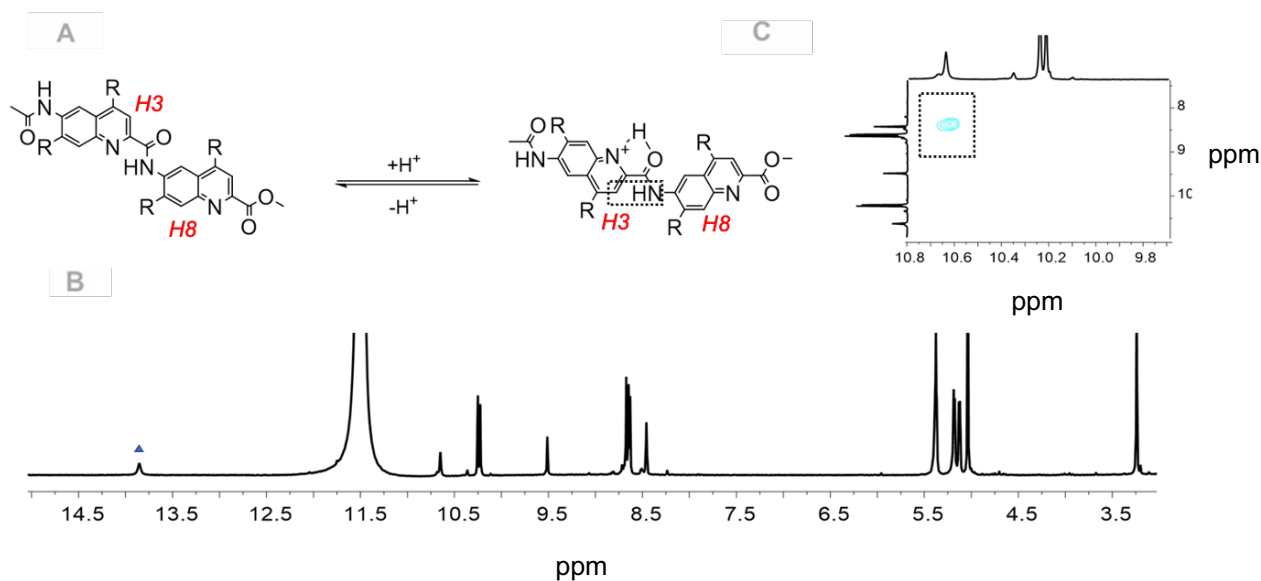


**Figure 10. Conformational switching upon protonation of 1.** (A) Protonation of **1** and formation of flipped hydrogen bonding pattern, correlation between H3 and NH marked in dotted square. H3 and H8 in red indicates the H3 and H8 proton of **1**. (B)  $^1\text{H}$ -NMR (500 MHz) spectrum of **1** in 10% d-TFA in TFA at 25°C, blue triangle marks quinolinium proton. (C) Zoom of the ROESY  $^1\text{H}$ - $^1\text{H}$  NMR spectrum of **1**, correlation between H3 and NH marked in dotted square.

#### 4.3.4 Host Guest complex formation

We further investigated the possibility to incorporate a guest molecule into the ellipse shaped macrocycle and to force the latter to undergo a conformational change towards the cone shaped architecture. The molecular model show that the circular cone shaped macrocycle cavity has a diameter of 1.7 nm, which is wide enough to incorporate a guest, for example a C60 fullerene with a 0.6 nm diameter size (**Figure 11 A,B**).

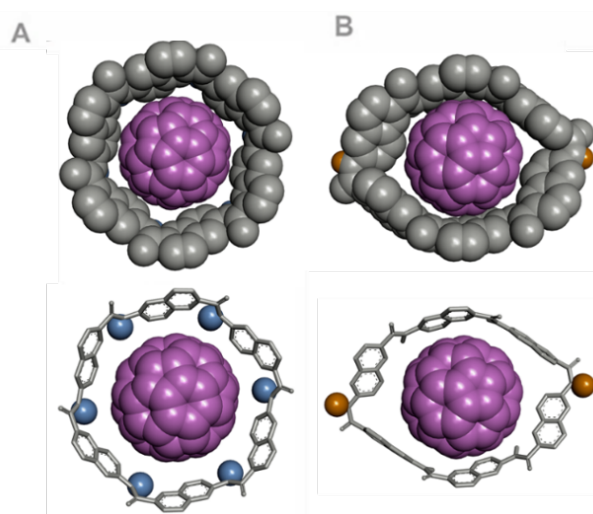


**Figure 11. Host guest complex of  $c(\text{QP})_6$  and Buckminsterfullerene C60** (A) Molecular model of the cone shaped host guest formation in space filling mode, C60 fullerene displayed in violet. (B) Molecular model of the saddle shaped host guest formation with two *cis* amides in stick and space filling mode, sidechain and hydrogen atoms are omitted for clarity.

The  $^1\text{H}$ -NMR titration of a 1 mM solution of  $\mathbf{c(Q^P)_6}$  in  $d$ -toluene with C60 Fullerene revealed chemical shift variations of the aromatic C-H proton signals and the *cis* N-H proton signal (**Figure 12**). The proton signal for the *cis* amide at 8.5 ppm shows drastic changes upon addition of the fullerene. Also, the aromatic C-H signals at 8.1 ppm shift and cross upon addition of the guest (**Figure 12, green box**). However, the expected change in conformation did not take place but presumably, binding of the fullerene to the ellipse shaped macrocycle occurred. The molecular modelling proposed a possible binding mode for a 1:1 binding of  $\mathbf{c(Q^P)_6}$  macrocycle in a saddle shape with the fullerene. The titration with larger guests, i.e. C70 fullerene and [6] cycloparaphenylene did not show any chemical shift variations. The calculated  $K_a$  for an 1:1 binding of the ellipse shaped macrocycle with the guest is  $460\text{ M}^{-1}$  with an error of 3 %.

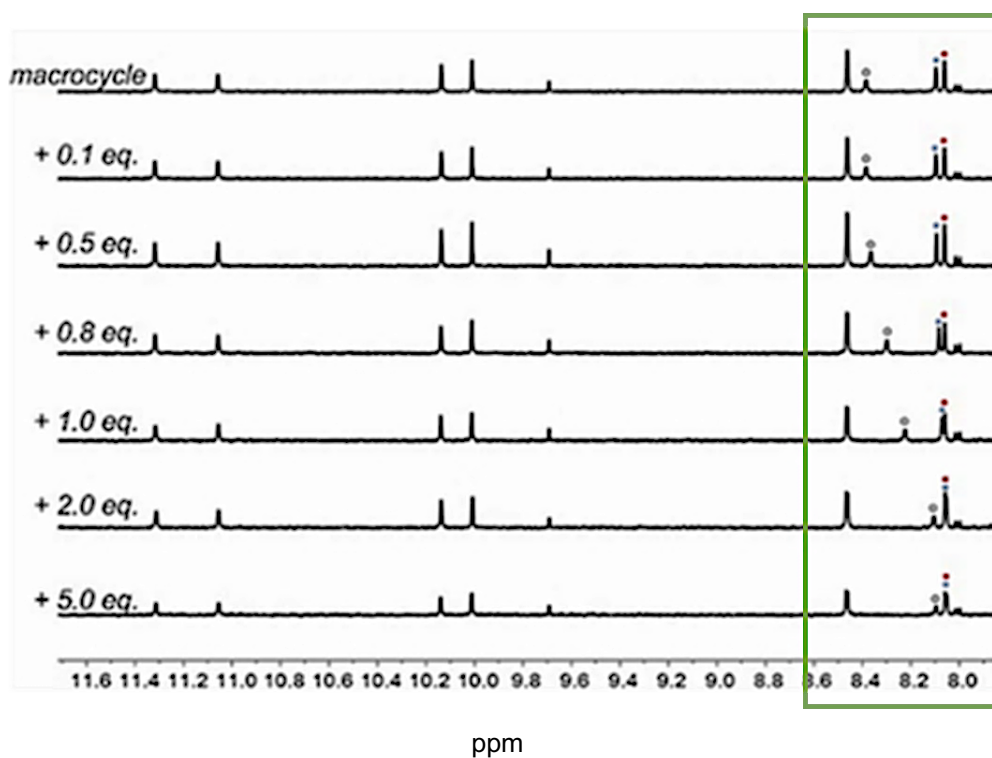


**Figure 12.** Host guest complex of  $\mathbf{c(Q^P)_6}$  and Buckminsterfullerene C60. The  $^1\text{H}$ -NMR (500 MHz) titration in  $d$ -toluene of  $\mathbf{c(Q^P)_6}$  with C60 Fullerene, circles display chemical shift variation of proton signals (grey = *cis* amide, blue and red = aromatic CHs).

## 4.4 Conclusion and Perspectives

The shortest possible Q<sup>p</sup> macrocycle **c(Q<sup>p</sup>)<sub>3</sub>** has shown to stay stable in an otherwise inaccessible conformation, with all secondary aryl amides locked in *cis* conformation due to the highly strained shape and lack of conformational freedom. The <sup>1</sup>H-NMR spectra showed more signals than for one conformation, referring to the existence of at least two conformers, presumably a C<sub>3</sub> symmetrical macrocycle, and an unsymmetrical conformation. The VT NMR spectra for **c(Q<sup>p</sup>)<sub>3</sub>** showed changes in chemical shift values and integration, leading to the conclusion that interconversion between the two species is a possibility.

The **c(Q<sup>p</sup>)<sub>6</sub>** shape persistent macrocycle shows a remarkable shape not referring to a preferable *all trans* conformation. The <sup>1</sup>H-NMR spectrum of **c(Q<sup>p</sup>)<sub>6</sub>** in deuterated DMSO, DMF and chloroform displayed an architecture, where two secondary arylamides are forced to stay in *cis* conformation, leading to the assumption of a C<sub>2</sub> symmetrical ellipse-like conformation that sharpens in chloroform and broadens in solvents with hydrogen bonding capacity, e.g., DMSO. The VT NMR spectra of **c(Q<sup>p</sup>)<sub>6</sub>** did not reveal coalescence of the proton signals. Interestingly, the conformation in *d*-TFA changes drastically, leading to the conclusion that protonation of the quinoline backbone affects the symmetry its conformation. Furthermore, the data presented for **c(Q<sup>p</sup>)<sub>6</sub>** clearly shows the potential of these macrocycles for further molecular recognition studies.

## 4.5 References

- (1) Bodine, K.; Gin, D.; Gin, MS. Synthesis of readily modifiable cyclodextrin analogues via cyclodimerization of an alkynylazido trisaccharide. *J. Am. Chem. Soc.* **2004**, *126* (6), 1638-9.
- (2) Ge, Y.; Gong, H.; Shang, J.; Jin, L.; Pan, T.; Zhang, Q. Supramolecular Gel Based on Crown-Ether-Appended Dynamic Covalent Macrocycles. *Macr. Commun.* **2019**, *40* (17), 1800731.
- (3) Moore, JS. Shape-persistent molecular architectures of nanoscale dimension. *Acc. Chem. Res.* **1997**, *30* (10), 402-13.
- (4) Xue, M.; Yang, Y.; Chi, X.; Zhang, Z.; Huang, F. Pillararenes, a new class of macrocycles for supramolecular chemistry. *Acc. Chem. Res.* **2012**, *45* (8), 1294-308.
- (5) Böhmer, V. Calixarenes, macrocycles with (almost) unlimited possibilities. *Angew. Chem.* **1995**, *34* (7), 713-45.
- (6) Yuan, L.; Feng, W.; Yamato, K.; Sanford, A.; Xu, D.; Guo, H. Highly efficient, one-step macrocyclizations assisted by the folding and preorganization of precursor oligomers. *J. Am. Chem. Soc.* **2004**, *126* (36), 11120-1.
- (7) Moore, JS.; Zhang, J. Efficient synthesis of nanoscale macrocyclic hydrocarbons. *Angew. Chem.* **1992**, *31* (7), 922-4.
- (8) Yamato, K.; Kline, M.; Gong, B. Cavity-containing, backbone-rigidified foldamers and macrocycles. *Chem. Commun.* **2012**, *48* (100), 12142-58.
- (9) Jiang, H.; Léger, J-M.; Guionneau, P.; Huc I. Strained aromatic oligoamide macrocycles as new molecular clips. *Org. Lett.* **2004**, *6* (17), 2985-8.
- (10) Urushibara, K.; Ferrand, Y.; Liu, Z.; Katagiri, K.; Kawahata, M.; Morvan, E.; Huc, I. Accessing Improbable Foldamer Shapes with Strained Macrocycles. *Chem. Eur. J.* **2021**, *27* (43), 11205.
- (11) Urushibara, K.; Ferrand, Y.; Liu, Z.; Masu, H.; Pophristic, V.; Tanatani, A.; Huc, I. Frustrated helicity: joining the diverging ends of a stable aromatic amide helix to form a fluxional macrocycle. *Angew. Chem.* **2018**, *57* (26), 7888-92.
- (12) Vágó, I.; Greiner, I. A useful acylation method using trichloroacetonitrile and triphenylphosphine for solid phase organic synthesis. *Tetrahedron Lett.* **2002**, *43* (34), 6039-41.
- (13) Aftahy, K; Arrasate, P; Bashkirov, P.; Kuzmin, P; Maurizot, V; Huc, I; Frolov, V. Molecular Sensing and Manipulation of Protein Oligomerization in Membrane Nanotubes with Bolaamphiphilic Foldamers. *JACS.* **2023**.
- (14) Jones, C.; Butts, C.; Harvey, J. Accuracy in determining interproton distances using Nuclear Overhauser Effect data from a flexible molecule. *BJOC.* **2011**, *7* (1), 145-50.
- (15) Snow, A.; Foos, E. Conversion of alcohols to thiols via tosylate intermediates. *Synth.* **2003**, *2003* (04), 0509-12.
- (16) Sebaoun, L; Kauffmann, B; Delclos, T; Maurizot, V; Huc, I. Assessing Stabilization through  $\pi$ - $\pi$  Interactions in Aromatic Oligoamide  $\beta$ -Sheet Foldamers. *Organic letters.* **2014**; *16* (9):2326-9.

## 4.6 Experimental Part

### 4.6.1. General remarks

**Nuclear Magnetic Resonance Spectroscopy (NMR)** An Avance III HD 400 MHz Bruker BioSpin (400 MHz) or an Avance III HD 500 MHz Bruker BioSpin (500 MHz) with a CryoProbe™ were used for recording <sup>1</sup>H NMR and <sup>13</sup>C NMR spectras. The chemical shifts ( $\delta$ ) were reported in ppm and the solvent resonance was used as internal standard. To interpret all NMR spectra the MestReNova x64 software was used, which was developed by the Mestrelab Research S.L. company. From the <sup>1</sup>H NMR spectra the chemical shift, the multiplicity (s = singlet, d = doublet, t = triplet, q = quartet, m = multiplet), the coupling constant (Hz) and the integration of the signals could be derived. Signals of <sup>13</sup>C NMR are stated with chemical shift.

**Mass Spectrometry (MS)** The used spectrometers to record high resolution MS spectra was Bruker micrOTOF II (ESI).

**Solid phase synthesis (SPS)** A CEM Discover Bio device was used for SPS.

**High-performance liquid chromatography (HPLC)** Thermo Scientific Dionex UltiMate 3000 with a MACHERY-NAGEL EC 100/4 Nucleodur® 100-3 C18 column was used to record analytical HPLC. Mixtures of CH<sub>3</sub>CN + 0.1% TFA and H<sub>2</sub>O + 0.1% TFA were used as mobile phase.

**PuriFlash system Interchim PuriFlash XS520 Plus** with PF-15SHIP-FO012 column was used for complicate column chromatographic purifications. Mixtures of methanol and DCM were used as mobile phase.

**Molecular modeling calculations** were performed using the Schrödinger 2017-1 suite. The starting structure was sketched in Maestro 11.5.011 (MMshare Version 4.1.011) and subsequently minimized with MacroModel. The minimizations were carried out with the GB/SA model for none solvent, using the TNCG method and the Merck Molecular Force Field statics (MMFFs) as introduced in the software. To find other possible minima dynamic simulations at different temperatures of the minimized structures were run with MacroModel. The dynamic simulations were carried out with the GB/SA model for none solvent, using the TNCG method and monitoring hundred structures in MMFFs. The simulations were carried out at 300 K and 400 K for a time of 1000 ps.

**Solution phase synthesis:** If not stated otherwise all reactions were carried out in ambient atmosphere and magnetically stirred. Glassware was evacuated and dried by heating in a drying cabinet (120 °C) before it was used when working under N<sub>2</sub> atmosphere was necessary. Drying over Na<sub>2</sub>SO<sub>4</sub> implies stirring of the organic solution with an appropriate amount of anhydrous salt for at least 10 min as well as filtration through a filter funnel with cotton wool and rinsing of the filter cake with additional solvent. Oil baths and electric heating plates were used for reaction at elevated temperatures up to 150°C. For reactions at higher temperatures than 150 °C a lab-heating mantle was used. Reactions at 0°C were cooled by an ice bath containing ice and H<sub>2</sub>O. For the transfer of liquids reagents and dry solvents syringes and cannulas were used. Prior to their use they were flooded with N<sub>2</sub>. For flash column chromatography purification silica gel (0.035 – 0.070 mm, 60 Å) by Acros Organics were used.

For monitoring reactions and analyzing fractions of column chromatography thin layer chromatography (TLC) on TLC silica gel 60 F254 from Sigma-Aldrich were used. The analytes on TLC plates were visualized by irradiation with UV-light (254 nm or 365 nm). All chemicals were purchased either from SIGMA Aldrich, Fisher Scientific, TCI Europe, VWR International, Honeywell, Acros Organics, or Alfa Aesar. Solvents were purchased in analytical grade quality and used without further purification. Anhydrous THF, Toluene and DCM for solution and solid phase synthesis were dispensed from a MBRAUN SPS-800 solvent purification system. DIPEA and Et<sub>3</sub>N were distilled over CaH<sub>2</sub>. All other reagents were used as purchased from commercial sources without further purification. Synthesis of the triethyleneglycol (TEG) sidechain is described in the literature (see Figure S1, R).<sup>(15)</sup>

#### 4.6.2 Monomer synthesis

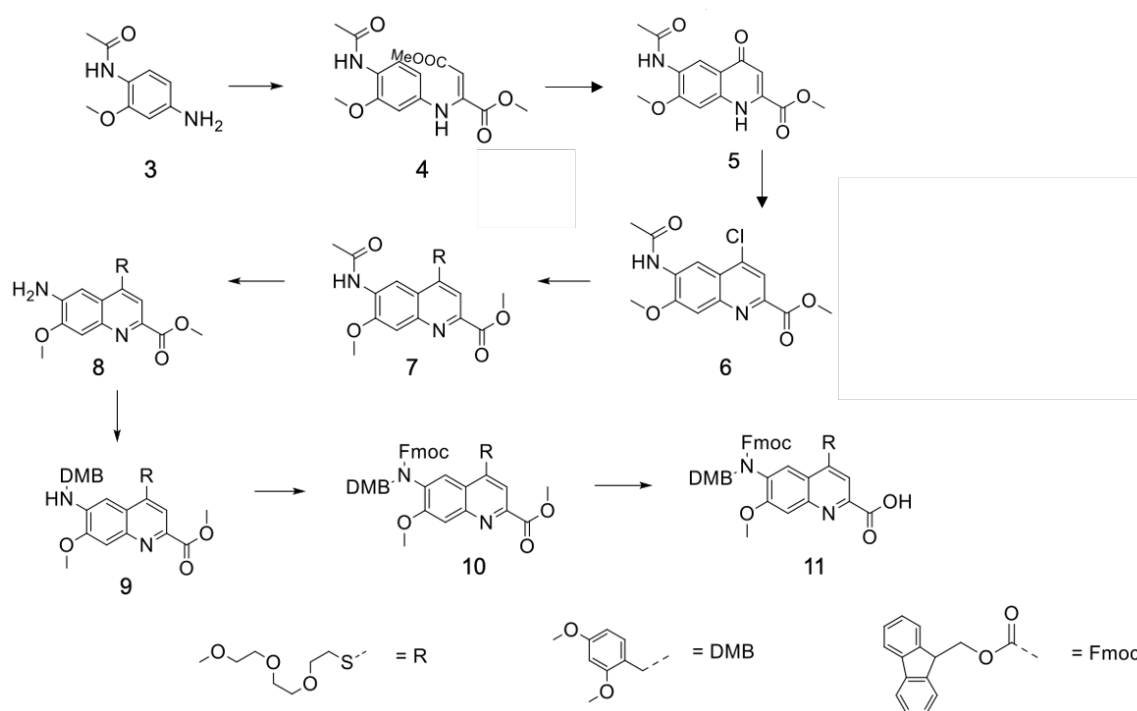


**Figure S1** Synthetic pathway for QP with TEG and methoxy sidechains starting from the commercially available 2-methoxynitroanilin.

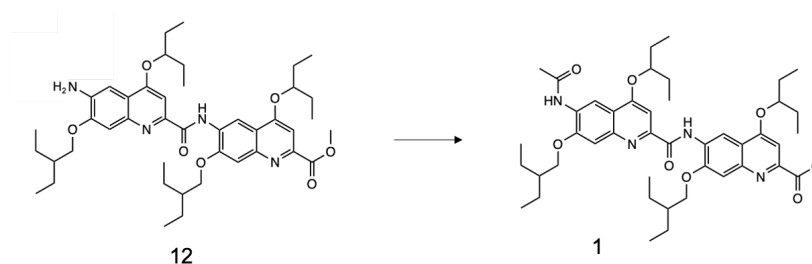
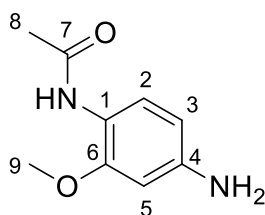


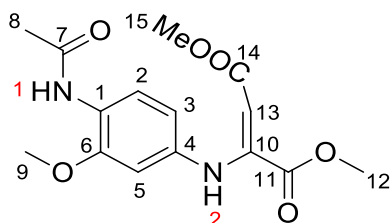
**Figure S2** Synthetic pathway for **1** via acetylation of **12** with 2-ethyl-1-butoxy sidechains. Compound **12** was synthesized according to Aftahy et al.<sup>(14)</sup>

### Compound 3



Compound **3** (1 eq. 0.3 mol, 69.8 g) was synthesized according to the procedure described in the art.<sup>(16)</sup> After purification, 62.5 g (yield: 99%) of pure **compound 3** were obtained. The analytical data for **3** is in accordance as described in the literature.

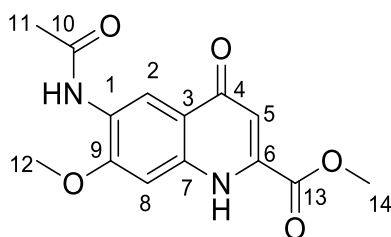
### Compound 4



Compound **4** (1 eq. 0.3 mol, 62.5 g) was synthesized according to the procedure described in the art.<sup>(16)</sup> After purification, 58.3 g (isolated yield 57 %) of pure **compound 4** were obtained. The analytical data for **4** is in accordance as described in the literature.

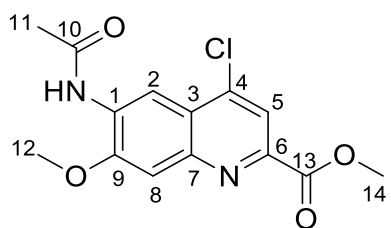
## Synthesis of new compounds:

### Compound 5



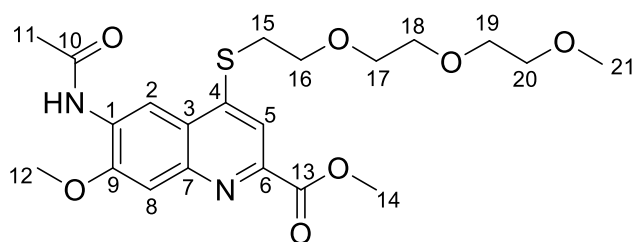
Compound **5** was synthesized according to the procedure described in the art.<sup>(16)</sup> After purification, 25.2 g (quant. yield) of **compound 5** was obtained. The analytical data for **5** is in accordance as described in the literature.

### Compound 6



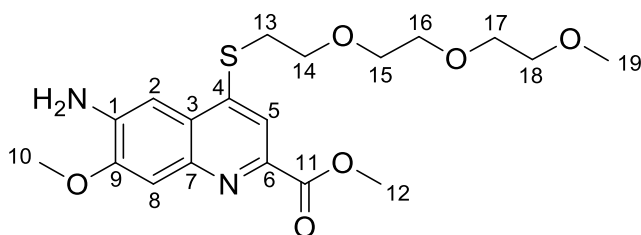
Compound **5** (7 g) was dissolved 70 mL of dry DMF and heated to 80°C using an oil bath. POCl<sub>3</sub> (2.24 mL) was added to the solution slowly and left stirring for 3.5 h. The reaction mixture was then cooled to rt and diluted with 200 mL of DCM and extracted with sat. NH<sub>4</sub>Cl solution (3x30 mL). The organic layer was collected, amount reduced using rotary evaporator and extracted with EtOAc and sat. NaCl solution (3 x 200 mL). EtOAc were combined, dried over MgSO<sub>4</sub>, filtered and evaporated to give 5.1 g (yield: 54 %) of **compound 6**. <sup>1</sup>H NMR (600 MHz, Chloroform-*d*, ppm): δ = 9.27 (s, 1H, H-2), 8.18 (s, 1H H-5), 8.13 (s, 1H, NH), 7.67 (s, 1H, H-8), 4.07 (s, 6H, H-12, H-14), 2.31 (s, 3H, H-11). <sup>13</sup>C NMR (150 MHz, Chloroform-*d*, ppm): δ = 168.76 (C-10), 165.30 (C-13), 151.66 (C-9), 146.31 (C-1), 146.05 (C-7), 143.21 (C-3), 131.35 (C-4), 123.68 (C-6), 120.47 (C-5), 111.53 (C2), 108.22 (C-8), 56.70 (C-14), 53.47 (C-12), 25.30 (C-11). ESI-MS (C<sub>14</sub>H<sub>12</sub>N<sub>2</sub>O<sub>4</sub>Cl): calc.: [M+1H]<sup>+</sup>: 307.7092, found: [M+1H]<sup>+</sup>: 307.0490.

## Compound 7



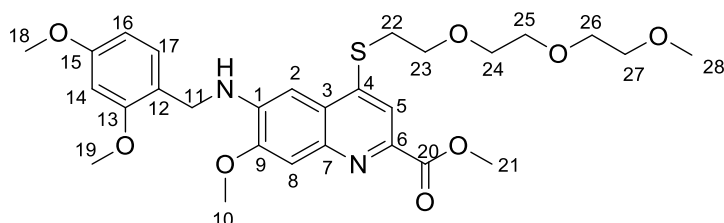
Intermediate **6** (1 eq. 7.4 mmol, 3.06 g) were dissolved in 40 mL of 1,4-dioxane.  $\text{NaHCO}_3$  (2 eq 14.8 mmol, 1.25 g) was dissolved in 25 mL  $\text{H}_2\text{O}$  and added to the solution. The reaction mixture was equipped with a dropping funnel and cooled to  $0^\circ\text{C}$  using an ice bath. Fmoc-Cl (1.5 eq. 11.1 mmol, 3.03 g) was dissolved in 20 mL dry DMF and poured into the dropping funnel. The addition was done during 30 min at  $0^\circ\text{C}$  and the reaction mixture was left stirring and warming up to rt for 8 h. After no more starting material was detected, the mixture was extracted with EtOAc and sat.  $\text{NH}_4\text{Cl}$  solution (3x100 mL) and the organic layers were combined, dried over  $\text{MgSO}_4$ , filtered and solvents evaporated. The obtained brownish oil was dissolved in 10 mL of DCM and 100 mL of  $\text{Et}_2\text{O}$  were added and left at  $8^\circ\text{C}$  to complete precipitation. The white solid was filtered of and dried well to give 3.2 g (isolated yield: 68 %) of pure **compound 7**.  $^1\text{H}$  NMR (500 MHz,  $\text{DMSO}-d_6$ , ppm):  $\delta$  = 9.59 (s, 1H, N-H), 9.00 (s, 1H, H-2), 7.84 (s, 1H, H-5), 7.58 (s, 1H, H-8), 4.05 (s, 3H, H-12), 3.93 (s, 3H, H-14), 3.78 (t,  $J$  = 6.2 Hz, 2H, H-16), 3.60 – 3.57 (m, 2H), 3.54 – 3.48 (m, 4H), 3.43 (t,  $J$  = 6.2 Hz, 2H, H-15), 3.41 – 3.38 (m, 2H), 3.21 (s, 3H, H-21), 2.22 (s, 3H, H-11).  $^{13}\text{C}$  NMR (126 MHz,  $\text{DMSO}-d_6$ , ppm):  $\delta$  = 170.06 (C-10), 166.02 (C-13), 152.50 (C-9), 147.25 (C-4), 145.80 (C-3), 144.42 (C-7), 130.97 (C-1), 122.40 (C-6), 114.44 (C-5), 111.80 (C-2), 108.68 (C-8), 71.71, 70.25, 70.23, 70.08, 68.69 (C-16), 58.48 (C-21), 56.83 (C-12), 52.97 (C-14), 30.75 (C-15), 24.82 (C-11). ESI-MS ( $\text{C}_{21}\text{H}_{28}\text{N}_2\text{O}_7\text{S}$ ): calc.:  $[\text{M}-1\text{H}]^-$ : 452.5232, found:  $[\text{M}-1\text{H}]^-$ : 452.4323.

## Compound 8



Intermediate 7 (1.0 eq, 5.5 g) was dissolved in 200 mL of MeOH and sulfuric acid (1 eq.) was added slowly to the bright yellow solution and left stirring refluxing for 24h. The solution turned bright orange and after no more starting material was detected on TLC, solid  $\text{NaHCO}_3$  was added and mixed until no more bubbling appeared, the solution filtered and evaporated to dryness. g (yield: quant.) of pure final **compound 8**.  $^1\text{H}$  NMR (500 MHz,  $\text{DMSO-}d_6$ , ppm):  $\delta$  = 7.93 (s, 1H, H-5), 7.70 (s, 1H, H-2), 7.17 (s, 1H, H-8), 4.03 (s, 3H, H-10), 4.03 (s, 3H, H-11), 3.82 (t,  $J$  = 5.9 Hz, 2H), 3.60 – 3.57(m, 4H), 3.53 – 3.51 (m, 2H), 3.49 – 3.47 (m, 2H), 3.39 – 3.38 (m, 2H), 3.20 (s, 3H, H-20).  $^{13}\text{C}$  NMR (126 MHz,  $\text{DMSO-}d_6$ , ppm):  $\delta$  = 161.74 (C-11), 154.22 (C-9), 142.95 (C-1), 133.61 (C-7), 124.70 (C-3), 113.59 (C-5), 101.42 (C-2), 99.52 (C-8), 71.24 (C-6), 69.84, 69.77, 69.59, 68.21, 58.03 (C-12), 56.46 (C-10), 53.61 (C-19), 52.78, 48.60, 30.87. ESI-MS ( $\text{C}_{19}\text{H}_{26}\text{N}_2\text{O}_6\text{S}$ ): calc.:  $[\text{M}+1\text{H}]^+$ : 411.1591, found:  $[\text{M}+1\text{H}]^+$  : 411.1283.

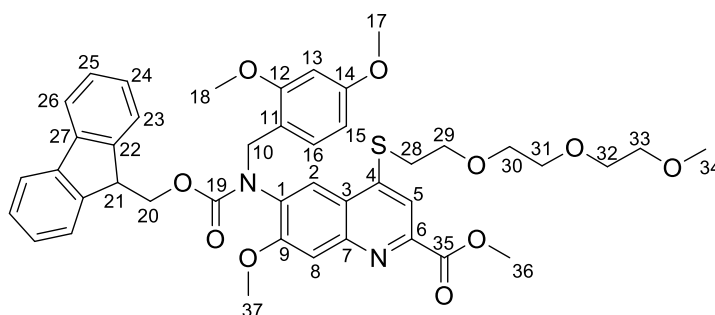
## Compound 9



Compound 8 (1.0 eq., 1.6 g) was dissolved in 150 mL 1,2- dichloroethane. Sodium triacetoxyborohydride (1.65 g) was added, followed by the addition of 0.71 g of dimethoxybenzaldehyde. The reaction mixture was stirring at room temperature for 24h. after no starting material was detected by TLC, 30 mL of sat.  $\text{NaHCO}_3$  solution was added and the organic layer collected. The aqueous layer was reextracted with EtOAc (3 x 30 mL) and the organic layers were combined, dried over  $\text{MgSO}_4$  and concentrated under reduced pressure. The crude material was purified on silica gel

using EtOAc and cyclohexane (9/1 vol/vol) as eluent to give 1.7 g of pure **compound 9** (yield: 78%). <sup>1</sup>H NMR (400 MHz, DMSO- *d*<sub>6</sub>, ppm): δ = 7.73 (s, 1H, H-5), 7.33 (s, 1H, H-2), 7.16 (d, J = 8.4 Hz, 1H, H-13), 6.69 (s, 2H, H-8), 6.57 (d, J = 2.4 Hz, 1H, H-16), 6.44 (dd, J = 8.4, 2.4 Hz, 1H, H-14), 4.36 (d, J = 6.1 Hz, 2H, H-11), 4.01 (s, 3H, H-10), 3.90 (s, 3H, H-18), 3.88 (s, 3H, H-21), 3.71 (s, 5H, H-19 and H-22), 3.57 – 3.56 (m, 2H), 3.54 – 3.48 (m, 4H), 3.42 – 3.38 (m, 2H), 3.30 – 3.29 (m, 2H) 3.21 (s, 3H, H-28). <sup>13</sup>C NMR (126 MHz, DMSO-*d*<sub>6</sub>, ppm) δ 166.26 (C-20), 160.09 (C-17), 158.37 (C-15), 151.76 (C-9), 142.31 (C-6), 141.67 (C-7), 141.44 (C-3), 140.75 (C-1), 129.33 (C-13), 124.64 (C-4), 118.45 (C-12), 114.94 (C-5), 107.53 (C-2), 105.10 (C-14), 98.47 (C-16), 96.73 (C-8), 71.72, 70.25, 70.19, 70.08, 68.82 (C-22), 58.49 (C-28), 56.52 (C-10), 56.14 (C-18), 55.58 (C-19), 52.61 (C-21), 30.77. ESI-MS (C<sub>28</sub>H<sub>36</sub>N<sub>2</sub>O<sub>8</sub>S): calc.: [M+1H]<sup>+</sup>: 561.2271, found: [M+1H]<sup>+</sup>: 561.1911.

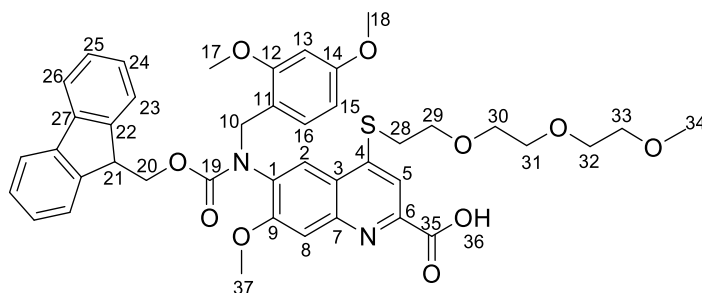
## Compound 10



Intermediate **9** (1 eq. 7.4 mmol, 3.06 g) was dissolved in 40 mL of 1,4-dioxane. NaHCO<sub>3</sub> (2 eq 14.8 mmol, 1.25 g) was dissolved in 25 mL H<sub>2</sub>O and added to the solution. The reaction mixture was equipped with a dropping funnel and cooled to 0°C using an ice bath. 3.03 g (1.5 eq. 11.1 mmol) of Fmoc-Cl were dissolved in 20 mL dry DMF and poured into the dropping funnel. The addition was done during 30 min at 0°C and the reaction mixture was left stirring and warming up to rt for 8 h. After no more starting material was detected, the mixture was extracted with EtOAc and sat. NH<sub>4</sub>Cl solution (3x100 mL) and the organic layers were combined, dried over MgSO<sub>4</sub>, filtered and solvents evaporated. The obtained brownish oil was dissolved in 10 mL of DCM and 100 mL of Et<sub>2</sub>O were added and left at 8°C to complete precipitation. The white solid was filtered off and dried well to give 3.2 g (isolated yield: 68 %) of pure **compound 10**. <sup>1</sup>H NMR (400 MHz, DMSO-*d*<sub>6</sub>, ppm): δ = 7.86 (s, 1H), 7.67 (s, 1H), 7.56 (s, 2H), 7.26 (s, 2H), 7.09 (s, 4H), 6.40 (s, 2H), 4.92 (s, 1H), 4.39 – 4.27 (m, 2H), 3.95 (s, 2H), 3.87 (s, 3H), 3.76 (t, J = 6.1 Hz, 2H), 3.69 (s, 3H), 3.59 – 3.55 (m, 2H), 3.52 (s, 1H),

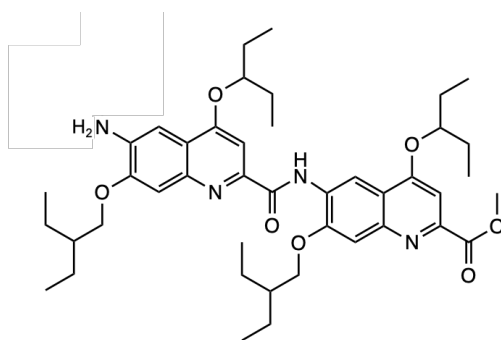
3.50 (s, 3H), 3.49 – 3.46 (m, 3H), 3.43 (t,  $J = 6.2$  Hz, 2H), 3.38 – 3.36 (m, 2H), 3.18 (s, 3H). The spectra is too broad to assign. ESI-MS ( $C_{43}H_{46}N_2O_{10}S$ ): calc.:  $[M+1H]^+$ : 783.2952, found:  $[M+1H]^+$ : 783.2933.

## Compound 11



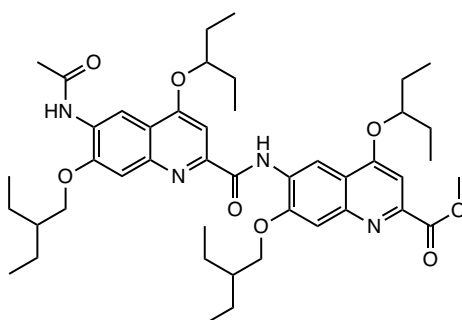
Compound **10** (5.5 g) was dissolved in 150 mL of degassed EtOAc and heated to reflux. 3.49 g of well dried LiI were added slowly to the light protected mixture and left stirring refluxing for 16h. After no more starting material was detected on TLC, the reaction mixture was cooled to rt and extracted with 5 %  $Na_2S_2O_3$  solution (3x 10 mL) and the organic layer was collected and extracted afterwards with 1M HCl solution (3x 10 mL) and the organic layers combined, dried over  $MgSO_4$ , filtered and evaporated to give 2.12 g (isolated yield: 42 %) of pure final **compound 11**.  $^1H$  NMR (500 MHz,  $DMSO-d_6$ , ppm):  $\delta = 13.39$  (s, 1H, H-36), 7.86 (s, 1H, H-8) 7.68 – 7.61 (m, 2H), 7.57 (s, 1H, H-5), 7.53 (s, 1H, H-2), 7.27 (s, 3H), 7.15 – 7.02 (m, 6H), 6.41 (s, 2H), 4.93 (s, 1H, H-21), 4.39 (s, 2H, H-10), 4.23 (d,  $J = 38.2$  Hz, 2H, H-20), 3.87 (s, 3H, H-37), 3.76 (t,  $J = 6.3$  Hz, 2H, H-29), 3.69 (s, 3H), 3.59 – 3.56 (m, 2H), 3.52 (s, 3H), 3.51 – 3.50 (m, 2H), 3.47 (t,  $J = 4.8$  Hz, 2H), 3.43 (t,  $J = 6.2$  Hz, 2H, H-28), 3.37 (t,  $J = 4.7$  Hz, 2H), 3.18 (s, 3H, H34).  $^{13}C$  NMR (126 MHz,  $DMSO$ , ppm):  $\delta = 166.31$  (C-19), 160.64 (C-35), 160.26, 158.23 (C-6), 157.40 (C-9), 154.76, 148.09 (C-4), 146.79, 143.62, 140.60, 131.11 (C-3), 127.49, 126.78, 124.83 (C-5), 123.62, 120.88 (C-1), 119.94, 116.67, 113.88 (C-8), 109.07 (C-2), 104.38, 98.05, 71.22, 69.78 (C-29), 69.78, 69.60, 68.24, 67.12 (C-20), 57.99 8 (C-34), 56.20 (C-37), 55.14, 51.58, 47.53 (C-21), 46.26 (C-10), 30.46 (C-28). ESI-MS ( $C_{42}H_{44}N_2O_{10}S$ ): calc.:  $[M+1H]^+$ : 769.2796, found:  $[M+1H]^+$ : 769.2352.

## Compound 12



Compound **12** was synthesized according to previously described methods in the art.<sup>(14)</sup> The analytical data was in accordance with the data as described in the literature.

## Compound 1



Compound **12** (0.1 g, 1 eq.) was dissolved in in 20 ml acetic acid acetic and anhydride (1 eq.) was added. The solution was left stirring for 4h at room temperature. A precipitate was formed. The precipitate was filtered and washed 3 times with 200 mL water to give 0.1 g of pure compound 1. <sup>1</sup>H NMR (500 MHz, Trifl-*d*<sub>1</sub>) δ 13.85 (s, 1N-H), 10.68 (s, 1H), 10.65 (d, *J* = 3.6 Hz, 1H), 10.25 (d, *J* = 3.6 Hz, 1H), 9.51 (s, 1H), 8.72 (s, 1H), 8.70 (d, *J* = 3.6 Hz, 1H), 8.46 (s, 1H), 5.38 (m, 6H), 5.18 (m, 3H), 5.13 (m, 3H), 5.04 (s, 3H), 3.24 (s, 3H), 2.81 (m, 6H), 2.47 (m, 12H), 2.39 (m, 3H), 1.87 (m, 3H). <sup>13</sup>C NMR (126 MHz, Trifl-*d*<sub>1</sub>) δ 175.00, 171.51, 170.53, 162.82, 162.53, 162.00, 161.61, 161.52, 158.95, 157.24, 157.11, 142.28, 141.12, 139.70, 139.07, 131.66, 130.02, 117.84, 117.76, 114.67, 113.03, 102.35, 100.41, 99.76, 98.68, 75.91, 75.82, 75.76, 75.47, 74.50, 73.99, 55.64, 41.64, 41.34, 41.04, 40.94, 23.64, 23.56, 23.51, 23.30, 23.16, 10.13, 9.91, 9.89, 9.85, 9.81, 9.78. HRMS (ESI+) calcd. for C<sub>47</sub>H<sub>67</sub>N<sub>4</sub>O<sub>8</sub> [M+H]<sup>+</sup> (m/z): 816.0588, found: 816.0973.

### 4.6.3 solid phase assisted synthesis of oligomers

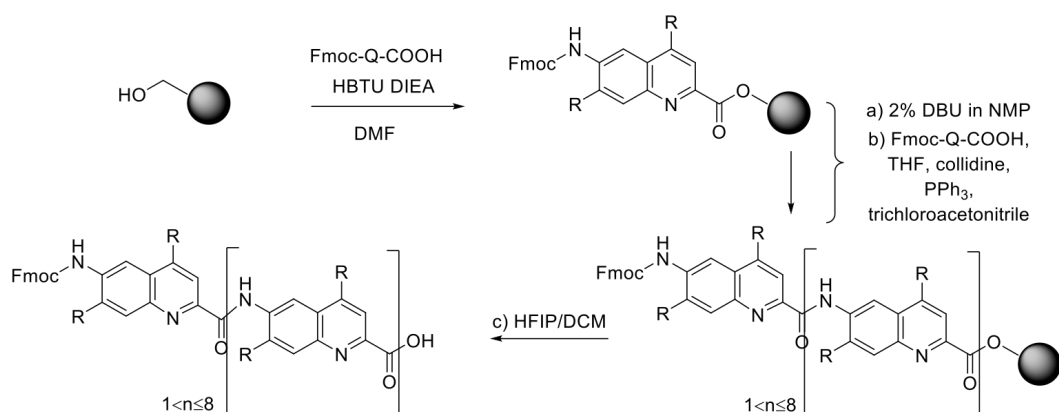


**Figure S3** Solid Phase synthesis of Q<sup>p</sup> oligomer

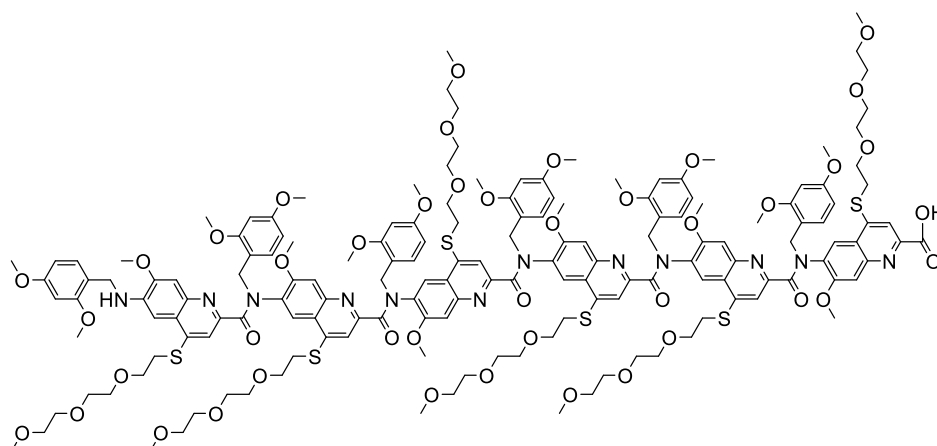
**Loading:** SASRIN resin (100 mg, 1 - 0.8 mmol g<sup>-1</sup>) was swollen in anhydrous DMF (2 mL) for 1 h under N<sub>2</sub>. Quinoline monomer Q (3.0 eq.), HBTU (3 eq.) and DIEA (10 eq.) were then added and left for 24 h at room temperature. The resin was washed with anhydrous DMF (3 x 3 mL) and the process was repeated once. The resin was then washed thoroughly with DMF (6 x 3 mL). The loading has been calculated by using UV-Vis absorption and resulted to be 0.44 mmol/g. The calculations for the subsequent coupling steps were adapted to this loading.

**Fmoc deprotection:** To Fmoc-Q-SASRIN resin was added a 2% vol/vol solution of DBU in NMP (3 mL) and the resin was stirred for 10 min at room temperature. The resin was washed with NMP (3 x 3 mL) and the deprotection was repeated once for another 10 min. The resin was then washed thoroughly with DMF (6 x 3 mL) and anhydrous THF (3 x 3 mL) prior to coupling reaction.

**In situ Coupling<sup>(12)</sup>:** NH<sub>2</sub>-Q-SASRIN resin (100 mg, 0.44 mmol g<sup>-1</sup>, 44 μmol) was suspended in anhydrous THF (1.25 mL) to which was added 2,4,6-Collidine (9 eq). Fmoc acid monomer and PPh<sub>3</sub> (8 eq.) were dissolved in THF (1.25 mL) and TCAN (8eq.) was added to this mixture. The preactivated monomer was then quickly added to the solution of resin containing collidine and placed under microwave irradiation at 50°C for 10 min. The resin was filtered off and washed with THF (2x 3ml) and the step was repeated once again. After the second coupling the resin was filtered off, washed with fresh THF and deprotection conditions were applied. The same deprotection and coupling cycles were performed until target length has been arrived. At last, final Fmoc deprotection was performed. Resin cleavage: The completed resin-bound foldamer

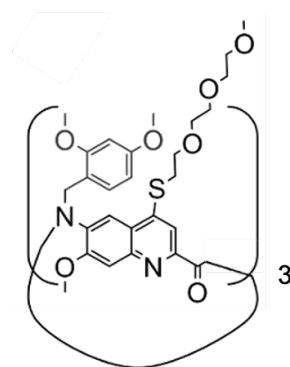


## Oligomer 15



Oligomer **15** was obtained using solid phase synthesis conditions described earlier on SASRIN resin (0.04 mmol) releasing 120mg of crude yellow oil. The oligomer 2a was obtained by purification on semi preparative reversed phase HPLC using C<sub>18</sub> phase column and 30-100% water and acetonitrile with 0.1 % TFA as additive. The collected fraction was lyophilized to give 52 mg of **pure oligomer 15**. HRMS (ESI) m/z: calcd. for C<sub>162</sub>H<sub>194</sub>N<sub>12</sub>O<sub>43</sub>S<sub>6</sub> [M+H]<sup>+</sup> 3190.7315; found 3190.3689. RP-HPLC retention time (*t<sub>ret</sub>*) on C<sub>18</sub> stationary phase using acetonitrile/water +0.1% TFA in 12 min: 7.4 min.

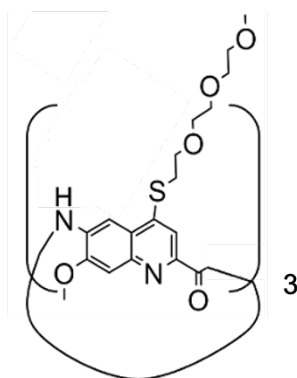
## Oligomer 16



Compound **14** (1 eq. 40 μmole) was dissolved in CHCl<sub>3</sub> (2 ml) under argon atmosphere, and PPh<sub>3</sub> (2 eq.) were added, following by the addition of TCAN (2.25 eq.). After 1 min, collidine (2.25 eq.) was then added to the reaction mixture and left stirring at room temperature for 2 h. The reaction was monitored using Liquid chromatography on C<sub>18</sub> phase column and acetonitrile and water as eluent and coupled mass spectrometry with Electro Spray Ionization in positive mode. After no more starting material was detected, the reaction mixture was quenched with sat. aqueous NaHCO<sub>3</sub> solution and the organic layer was collected, and further washed with sat. aqueous NHCl<sub>4</sub> solution.

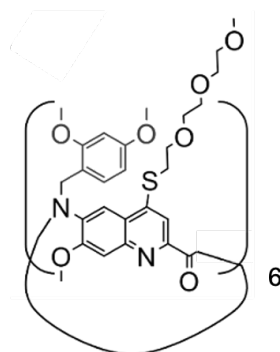
The macrocycle **16** was extracted with more  $\text{CHCl}_3$  (2x5 ml), the organic layers combined and dried over  $\text{NaSO}_4$ , filtered and concentrated under high pressure. The resulting yellow oil was purified on semi-preparative reversed phase chromatography with 50-100% water / acetonitrile with 0.1% TFA as additive. The collected fractions were lyophilized to give 25 mg of pure **oligomer 16**. HRMS (ESI)  $m/z$ : calcd for  $\text{C}_{81}\text{H}_{96}\text{N}_6\text{O}_{21}\text{S}_3$   $[\text{M}+\text{H}]^+$ : 1585.8581; found 1585.6399. RP-HPLC retention time ( $t_{ret}$ ) on  $\text{C}_{18}$  stationary phase using acetonitrile/water +0.1% TFA in 12 min: 7.9 min.

### Oligomer 17



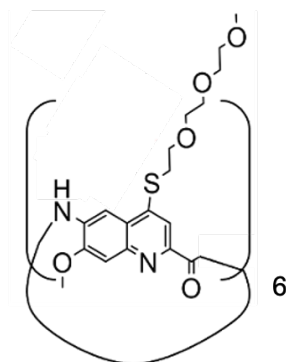
Macrocycle **16** (1 eq. 40  $\mu\text{mole}$ , 45 mg) was dissolved in pure TFA (4 ml) under argon atmosphere and left stirring at  $60^\circ\text{C}$  for 4 h. The reaction was monitored using Liquid chromatography on  $\text{C}_{18}$  phase column and acetonitrile and water as eluent and coupled mass spectrometry with Electro Spray Ionization in positive mode. After no more starting material was detected, the reaction mixture was quenched with sat. aqueous  $\text{NaHCO}_3$  solution and  $\text{CHCl}_3$  was added and the organic layer was collected, and further washed with more sat. aqueous  $\text{NaHCO}_3$  solution. The macrocycle **17** was extracted with more  $\text{CHCl}_3$  (2x5 ml), the organic layers combined and dried over  $\text{NaSO}_4$ , filtered and concentrated under high pressure. The resulting yellow oil was purified on semi-preparative reversed phase chromatography with 90-100% water / acetonitrile with 0.1% TFA as additive. The collected fractions were lyophilized to give 25 mg of pure **oligomer 17**.  $^1\text{H}$  NMR (400 MHz,  $\text{DMSO-d}_6$ , ppm):  $\delta$  = 7.86 (s, 1H), 7.67 (s, 1H), 7.56 (s, 2H), 7.26 (s, 2H), 7.09 (s, 4H), 6.40 (s, 2H), 4.92 (s, 1H), 4.39 – 4.27 (m, 2H), 3.95 (s, 2H), 3.87 (s, 3H), 3.76 (t,  $J$  = 6.1 Hz, 2H), 3.69 (s, 3H), 3.59 – 3.55 (m, 2H), 3.52 (s, 1H), 3.50 (s, 3H), 3.49 – 3.46 (m, 3H), 3.43 (t,  $J$  = 6.2 Hz, 2H), 3.38 – 3.36 (m, 2H), 3.18 (s, 3H). HRMS (ESI)  $m/z$ : calcd. for  $\text{C}_{54}\text{H}_{66}\text{N}_6\text{O}_{15}\text{S}_3$   $[\text{M}+\text{H}]^+$ : 1135.3336, found 1135.4601. RP-HPLC retention time ( $t_{ret}$ ) on  $\text{C}_{18}$  stationary phase using acetonitrile/water +0.1% TFA in 12 min: 4.5 min.

## Oligomer 18



Compound **15** (1 eq. 40  $\mu$ mole) was dissolved in  $\text{CHCl}_3$  (2 ml) under argon atmosphere, and  $\text{PPh}_3$  (2 eq.) were added, following by the addition of TCAN (2.25 eq.). After 1 min collidine (2.25 eq.) was then added to the reaction mixture and left stirring at room temperature for 2 h. The reaction was monitored using Liquid chromatography on  $\text{C}_{18}$  phase column and acetonitrile and water as eluent and coupled mass spectrometry with Electro Spray Ionization in positive mode. After no more starting material was detected, the reaction mixture was quenched with sat. aqueous  $\text{NaHCO}_3$  solution and the organic layer was collected, and further washed with sat. aqueous  $\text{NHCl}_4$  solution. The macrocycle **2b** was extracted with more  $\text{CHCl}_3$  (2x5 ml), the organic layers combined and dried over  $\text{NaSO}_4$ , filtered and concentrated under high pressure. The resulting yellow oil was purified on semi-preparative reversed phase chromatography with 50-100% water / acetonitrile with 0.1% TFA as additive. The collected fractions were lyophilized to give 25 mg of pure **oligomer 18**. HRMS (ESI)  $m/z$ : calcd for  $\text{C}_{162}\text{H}_{192}\text{N}_{12}\text{O}_{42}\text{S}_6$   $[\text{M}+2\text{H}]^+$ : 1585.8581; found 1585.8621. RP-HPLC retention time ( $t_{\text{ret}}$ ) on  $\text{C}_{18}$  stationary phase using acetonitrile/water +0.1% TFA in 12 min: 10.9 min.

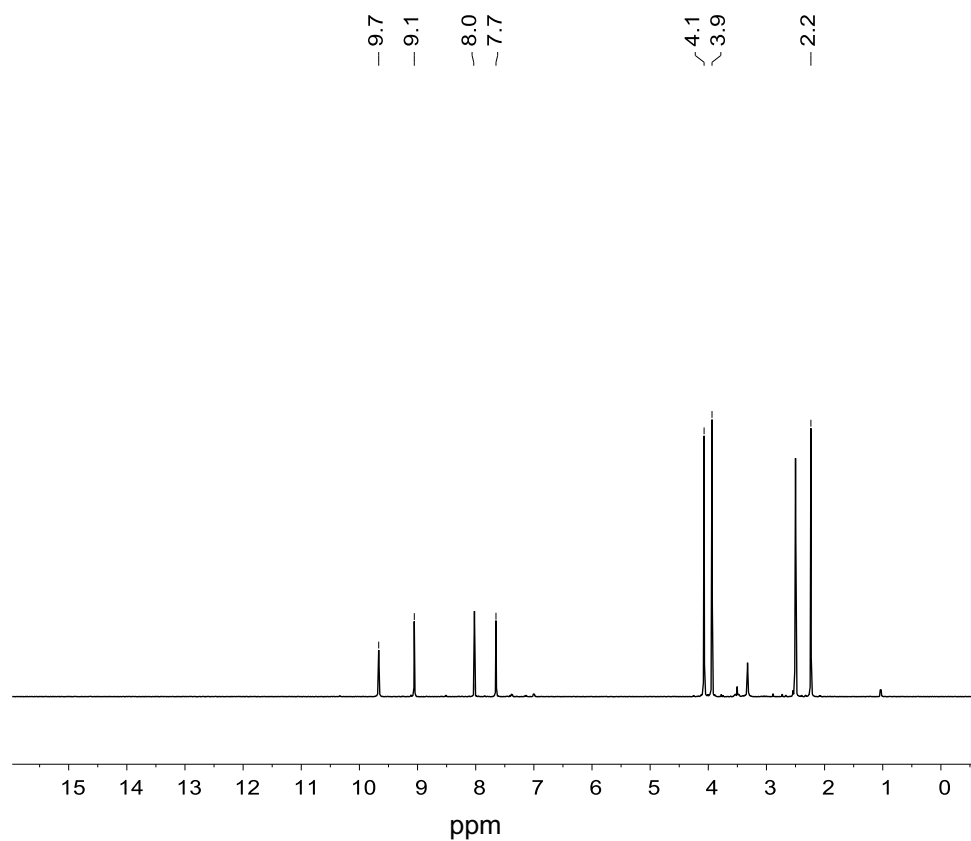
## Oligomer 19



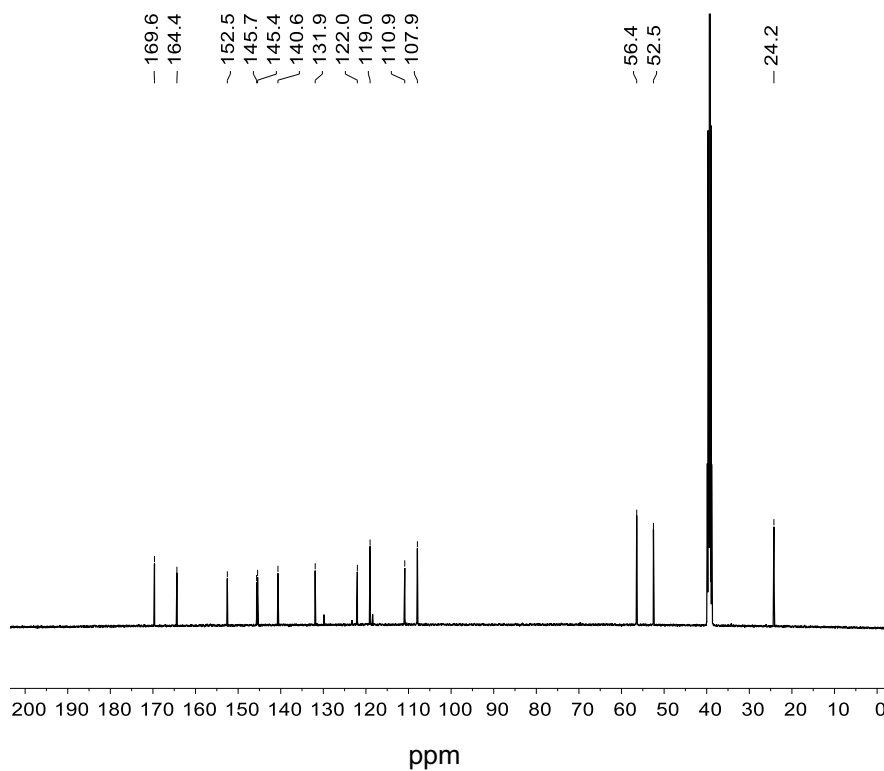
Macrocyclic **18** (1 eq. 40  $\mu\text{mole}$ ) was dissolved in pure TFA (2 ml) under argon atmosphere and left stirring at 60°C for 4 h. The reaction was monitored using RP HP Liquid chromatography on C<sub>18</sub> phase column and acetonitrile and water as eluent and coupled mass spectrometry with Electro Spray Ionization in positive mode. After no more starting material was detected, the reaction mixture was quenched with sat. aqueous NaHCO<sub>3</sub> solution and the organic layer was collected, and further washed with more sat. aqueous NaHCO<sub>3</sub> solution. The macrocycle was extracted with more CHCl<sub>3</sub> (2x5 ml), the organic layers combined and dried over NaSO<sub>4</sub>, filtered and concentrated under high pressure. The resulting yellow oil was purified on semi-preparative reversed phase chromatography with 90-100% water / acetonitrile with 0.1% TFA as additive. The collected fractions were lyophilized to give 25 mg of pure **oligomer 19**. <sup>1</sup>H NMR (400 MHz, DMSO-d<sub>6</sub>, ppm):  $\delta$  = 7.86 (s, 1H), 7.67 (s, 1H), 7.56 (s, 2H), 7.26 (s, 2H), 7.09 (s, 4H), 6.40 (s, 2H), 4.92 (s, 1H), 4.39 – 4.27 (m, 2H), 3.95 (s, 2H), 3.87 (s, 3H), 3.76 (t, J = 6.1 Hz, 2H), 3.69 (s, 3H), 3.59 – 3.55 (m, 2H), 3.52 (s, 1H), 3.50 (s, 3H), 3.49 – 3.46 (m, 3H), 3.43 (t, J = 6.2 Hz, 2H), 3.38 – 3.36 (m, 2H), 3.18 (s, 3H). HRMS (ESI) m/z: calcd for C<sub>108</sub>H<sub>132</sub>N<sub>12</sub>O<sub>30</sub>S<sub>6</sub> [M+H]<sup>+</sup> 2270.6672; found 2270.8899. RP-HPLC retention time ( $t_{ret}$ ) on C<sub>18</sub> stationary phase using acetonitrile/water +0.1% TFA in 12 min: 5.3 min.

#### 4.6.4 NMR and HPLC data of new compounds

### Compound 6 Methyl 6-acetamido-4-chloro-7-methoxyquinoline-2-carboxylate

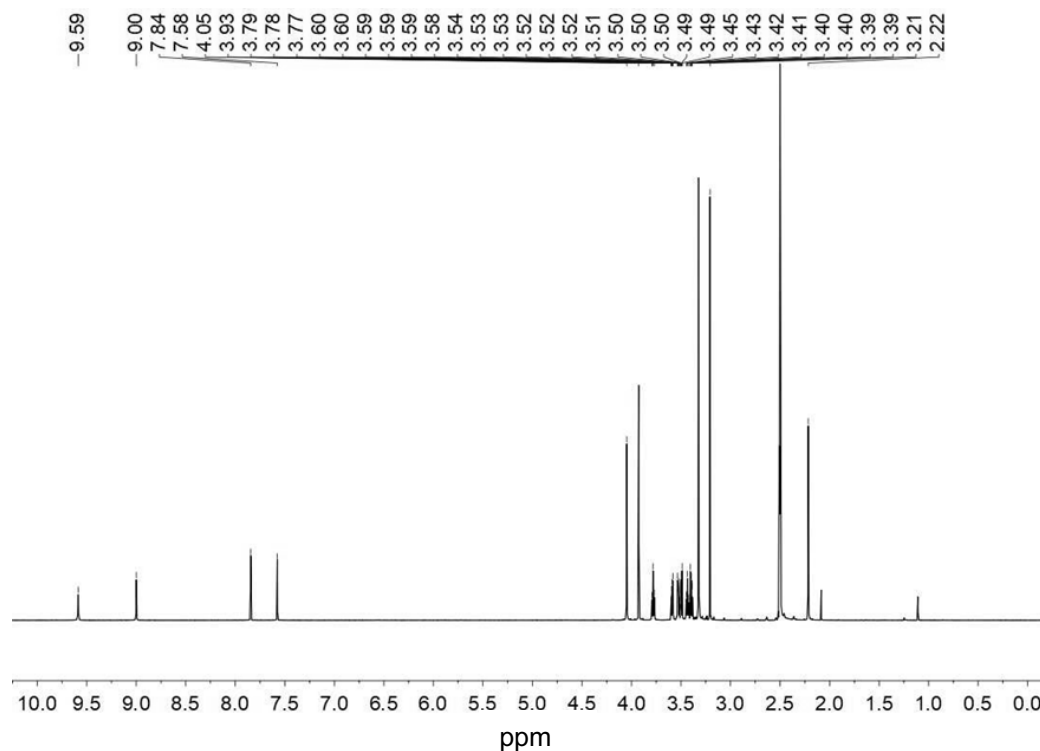


<sup>1</sup>H NMR spectrum of **6** in *d*-DMSO at 500 MHz and 128 scans

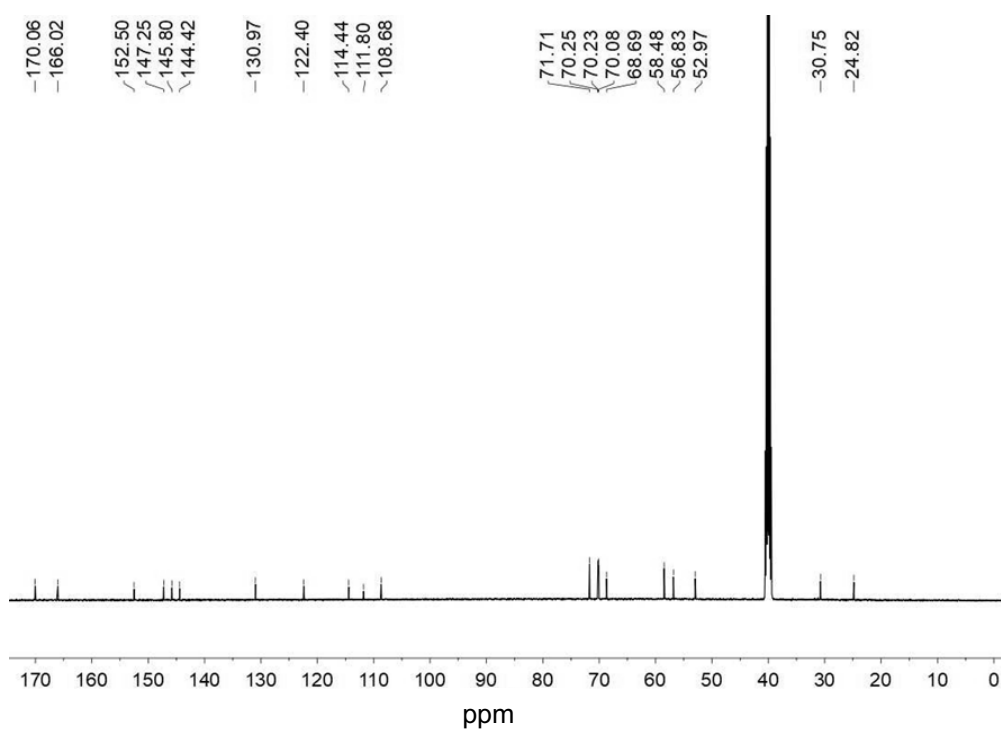


<sup>13</sup>C NMR spectrum of **6** in *d*-DMSO at 126 MHz

**Compound 7 Methyl 6-acetamido-7-methoxy-4-((2-(2-(2-methoxyethoxy)ethoxy)ethyl)thio)quinoline-2-carboxylate**

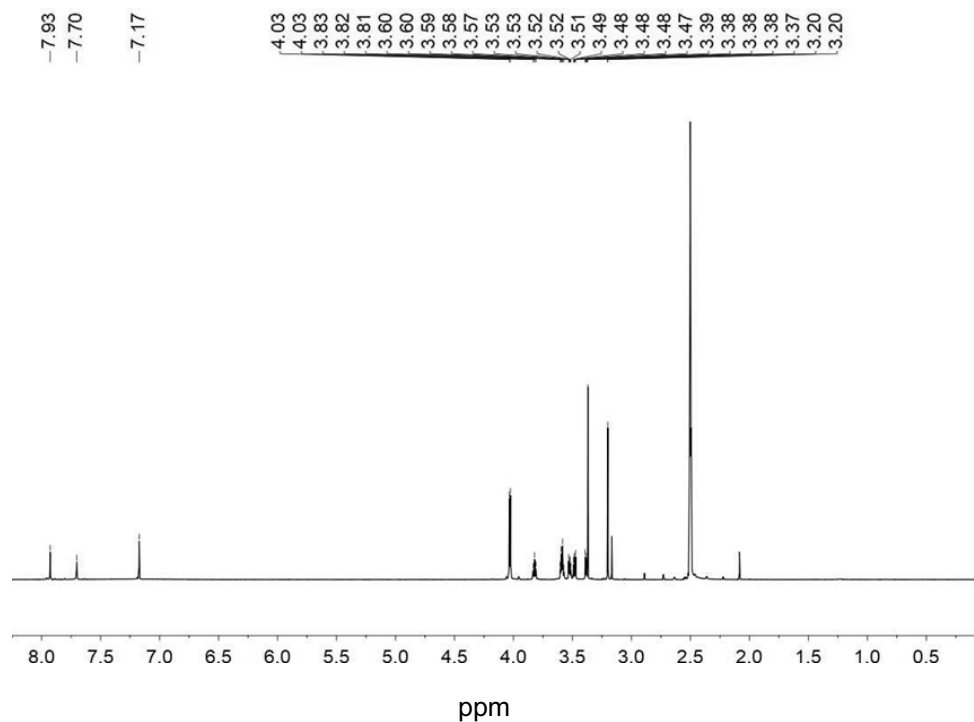


<sup>1</sup>H NMR spectrum of **7** in *d*-DMSO at 500MHz and 128 scans

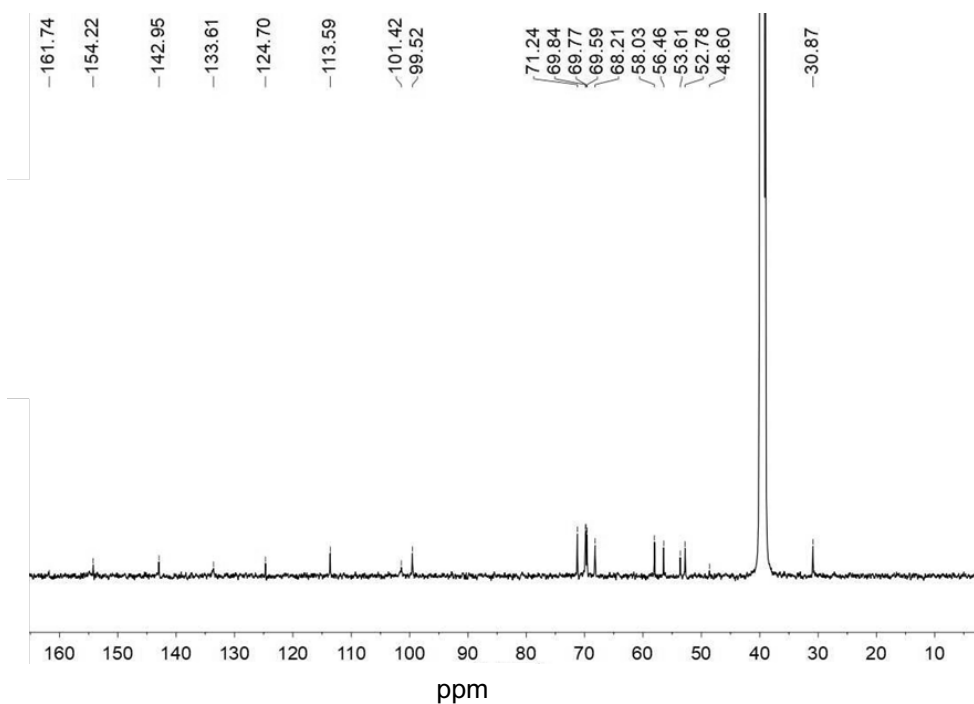


<sup>13</sup>C NMR spectrum of **7** in *d*-DMSO at 126MHz

**Compound 8 Methyl 6-amino-7-methoxy-4-((2-(2-(2-methoxyethoxy)ethoxy)ethyl)thio)quinoline-2-carboxylate)**

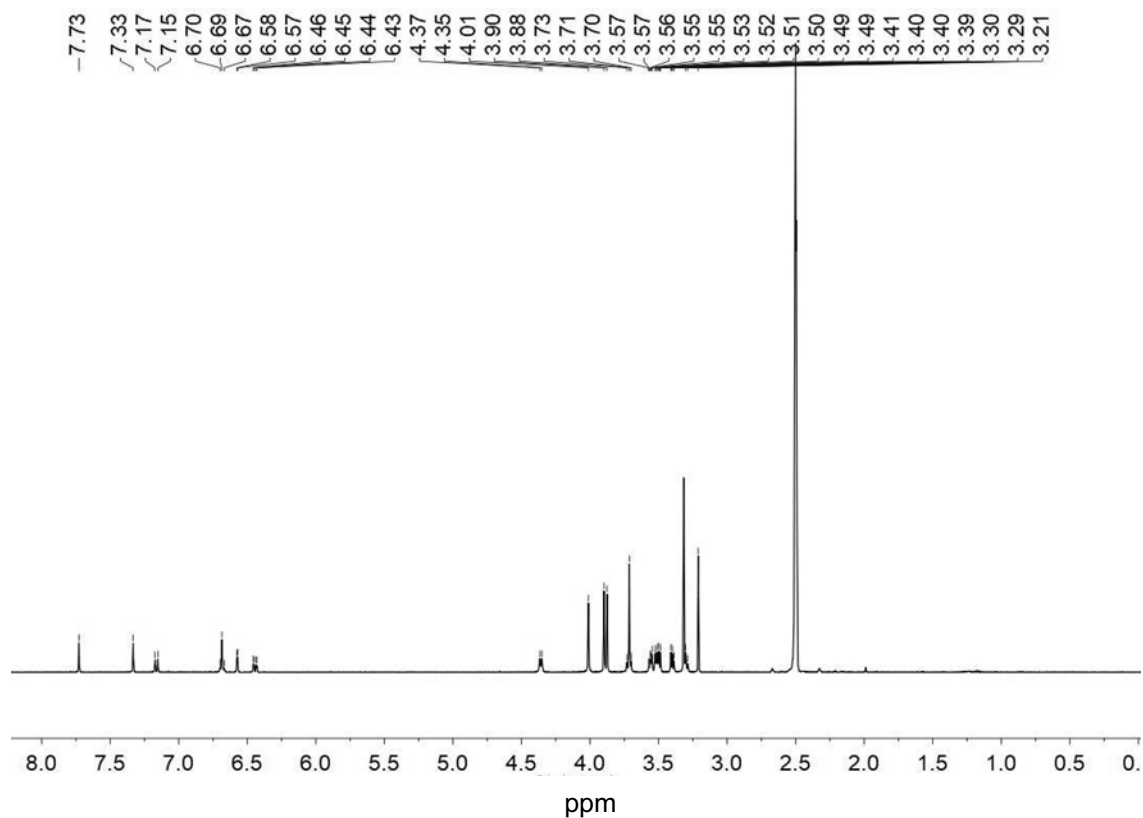


<sup>1</sup>H NMR spectrum of **8** in *d*-DMSO at 500MHz and 128 scans

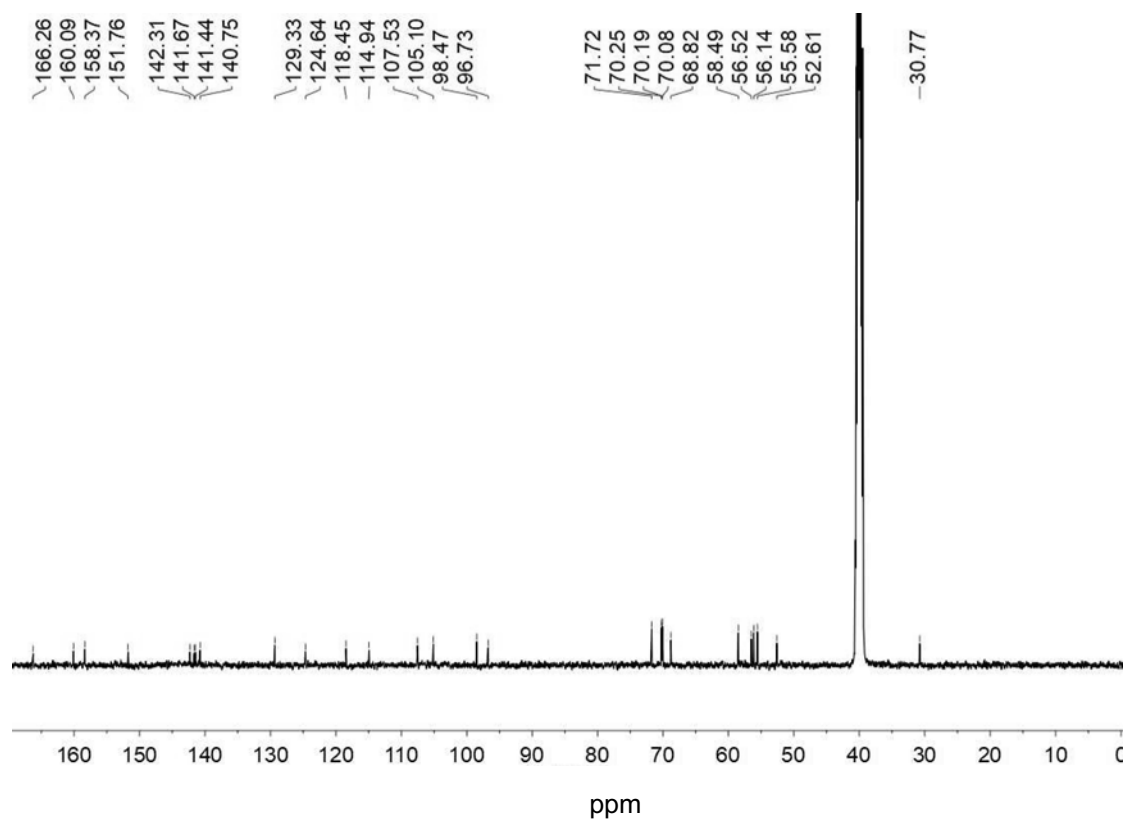


<sup>13</sup>C NMR spectrum of **8** in *d*-DMSO at 126MHz

**Compound 9 Methyl 6-((2,4-dimethoxybenzyl)amino)-7-methoxy-4-((2-(2-methoxyethoxy)ethoxy)ethyl)thio)quinoline-2-carboxylate )**



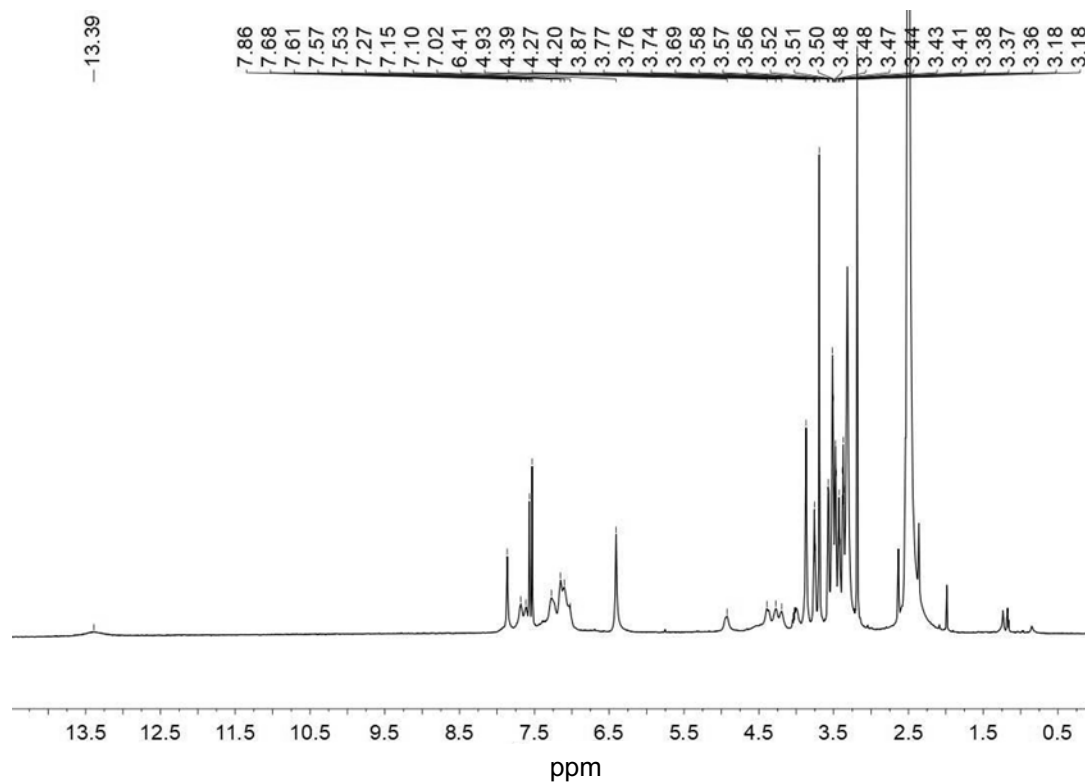
<sup>1</sup>H NMR spectrum of **9** in *d*-DMSO at 500MHz and 128 scans



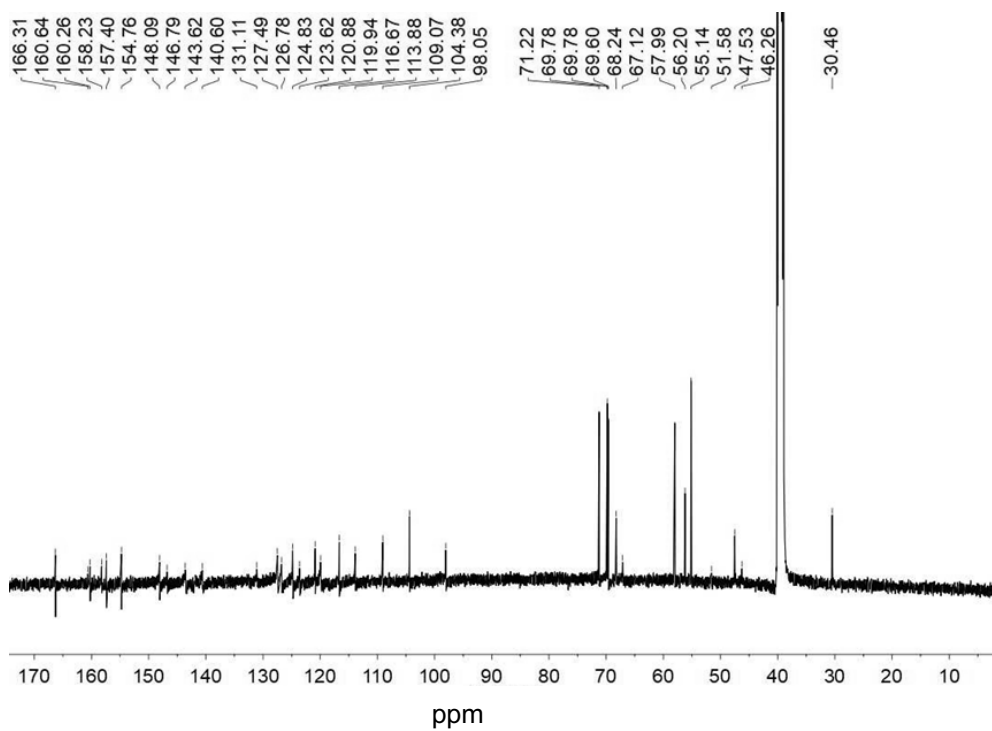
<sup>13</sup>C NMR spectrum of **9** in *d*-DMSO at 126MHz



**Compound 11 6-(((9H-fluoren-9-yl)methoxy)carbonyl)(2,4-dimethoxybenzyl)amino)-7-methoxy-4-((2-(2-(2-methoxyethoxy)ethoxy)ethyl)thio)quinoline-2-carboxylic acid**

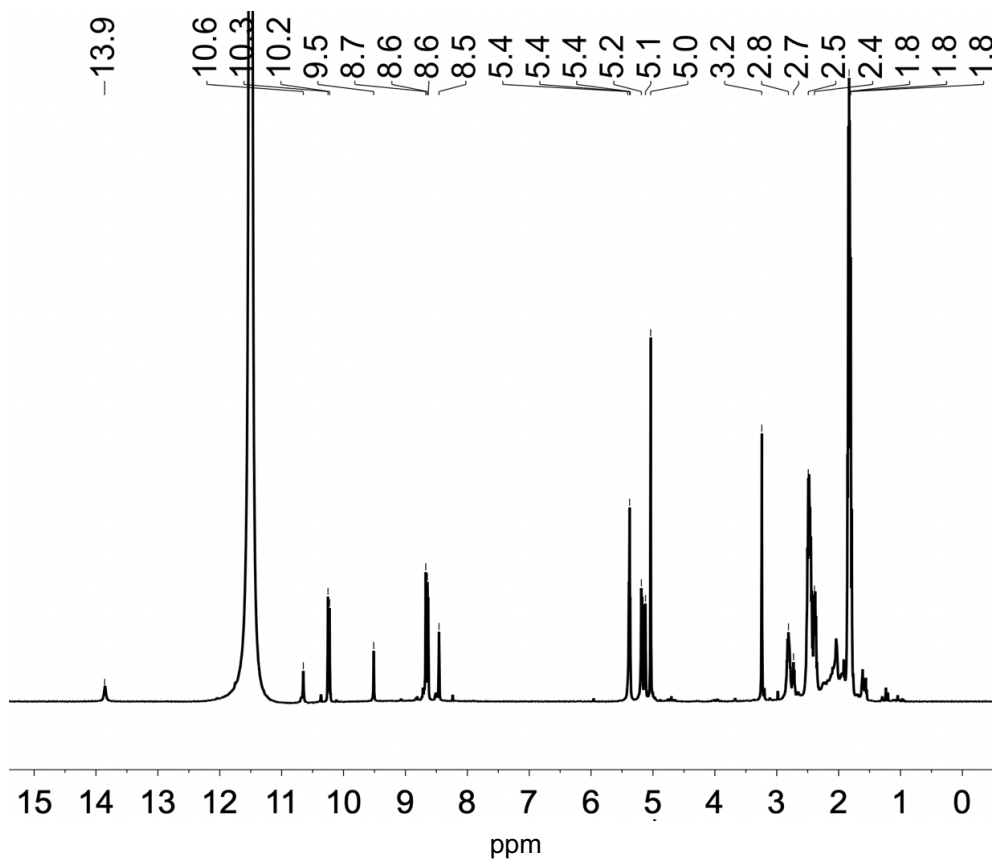


<sup>1</sup>H NMR spectrum of **11** in *d*-DMSO at 500MHz and 128 scans

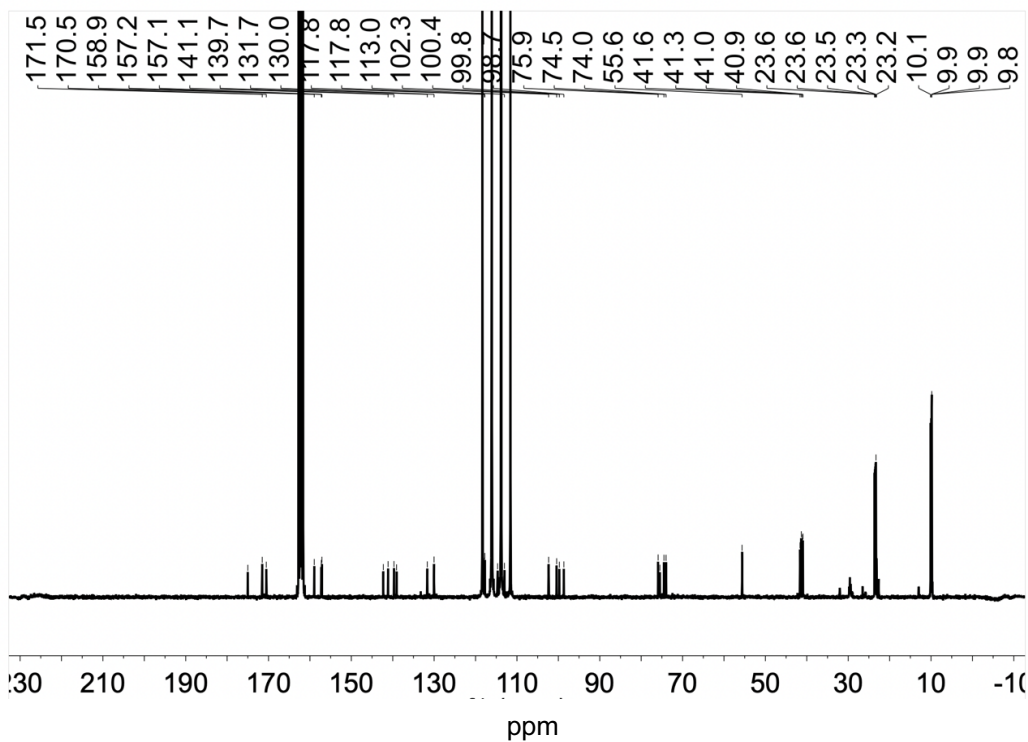


<sup>13</sup>C NMR spectrum of **11** in *d*-DMSO at 126MHz

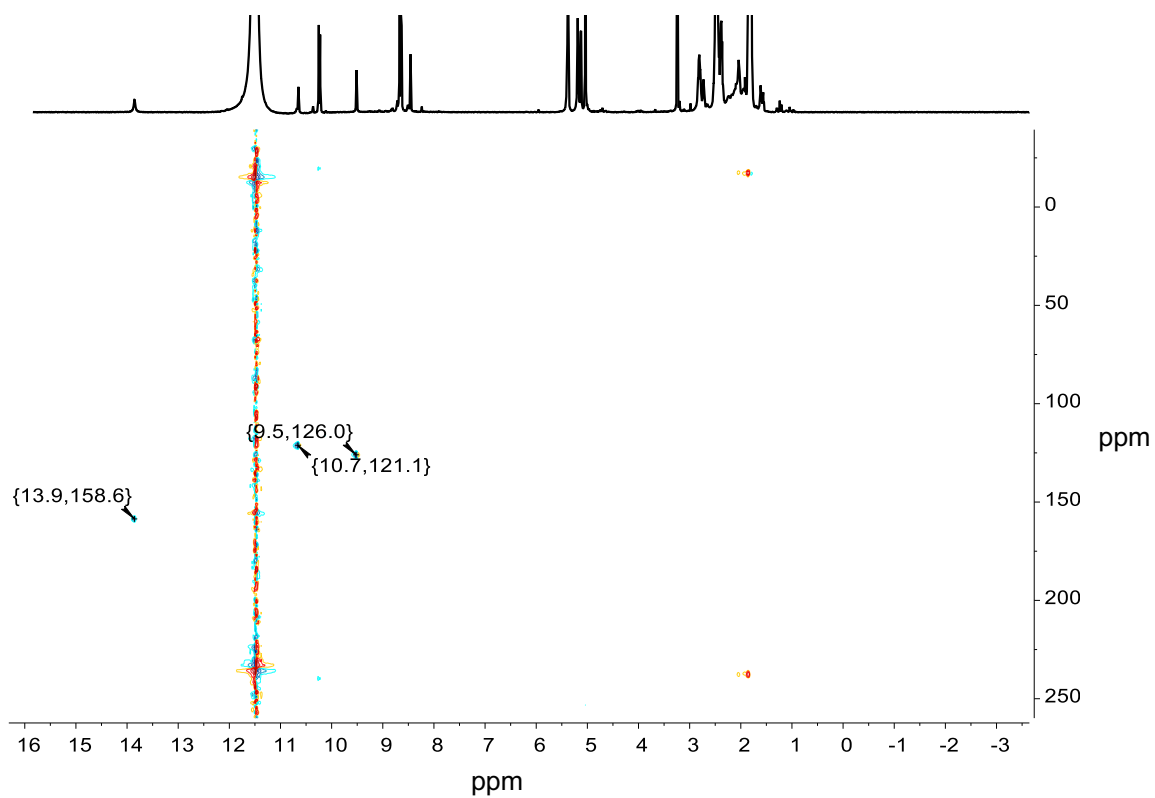
### Compound 1



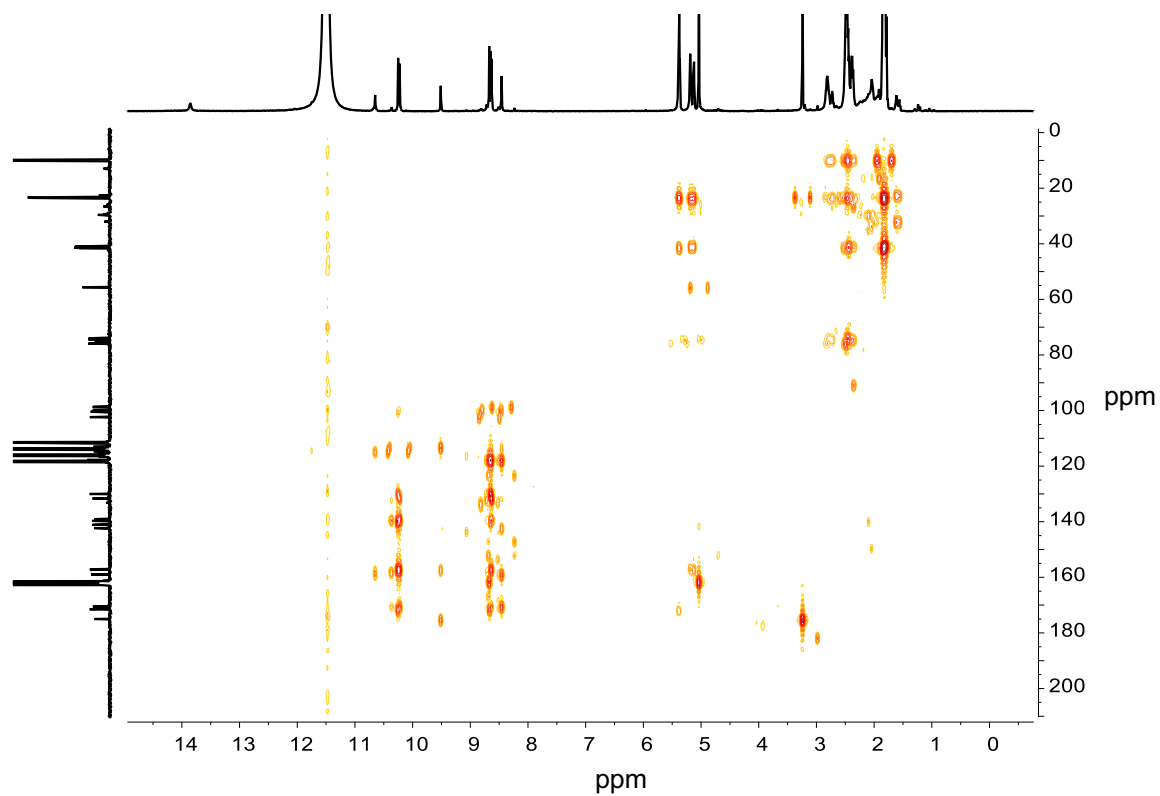
<sup>1</sup>H NMR spectrum of **1** in *d*-TFA with 10 vol.-% TFA at 500MHz



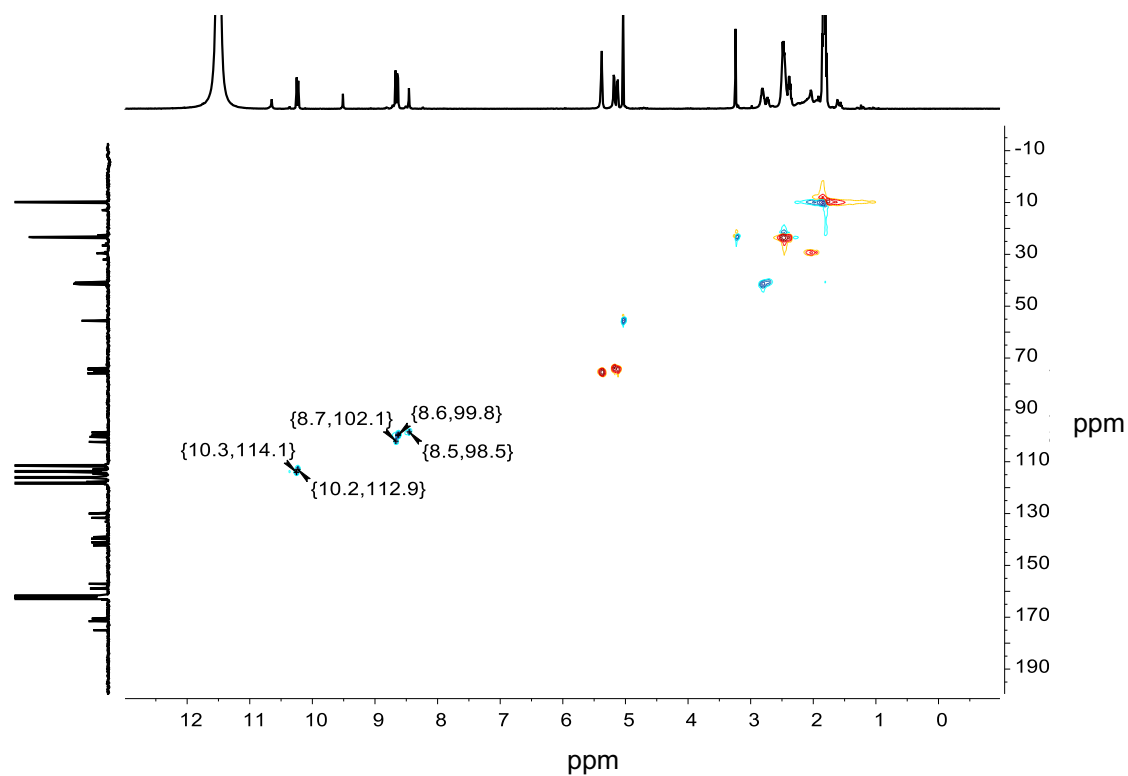
<sup>13</sup>C NMR spectrum of **1** in *d*-TFA with 10 vol.-% TFA at 500MHz



$^1\text{H}$ - $^{15}\text{N}$ -HSQC NMR spectrum of **1** in *d*-TFA with 10 vol.-% TFA at 500MHz

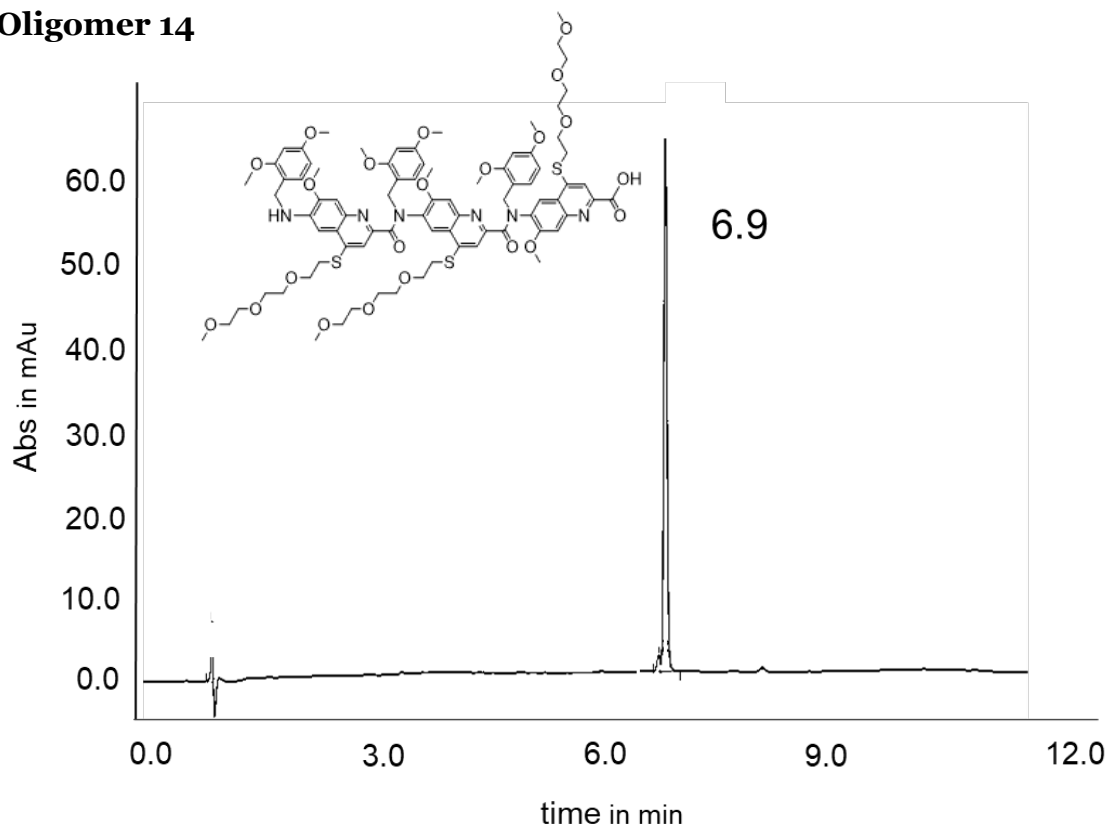


$^1\text{H}$ - $^{13}\text{C}$ -HSQC NMR spectrum of **11** in *d*-TFA with 10 vol.-% TFA at 500MHz

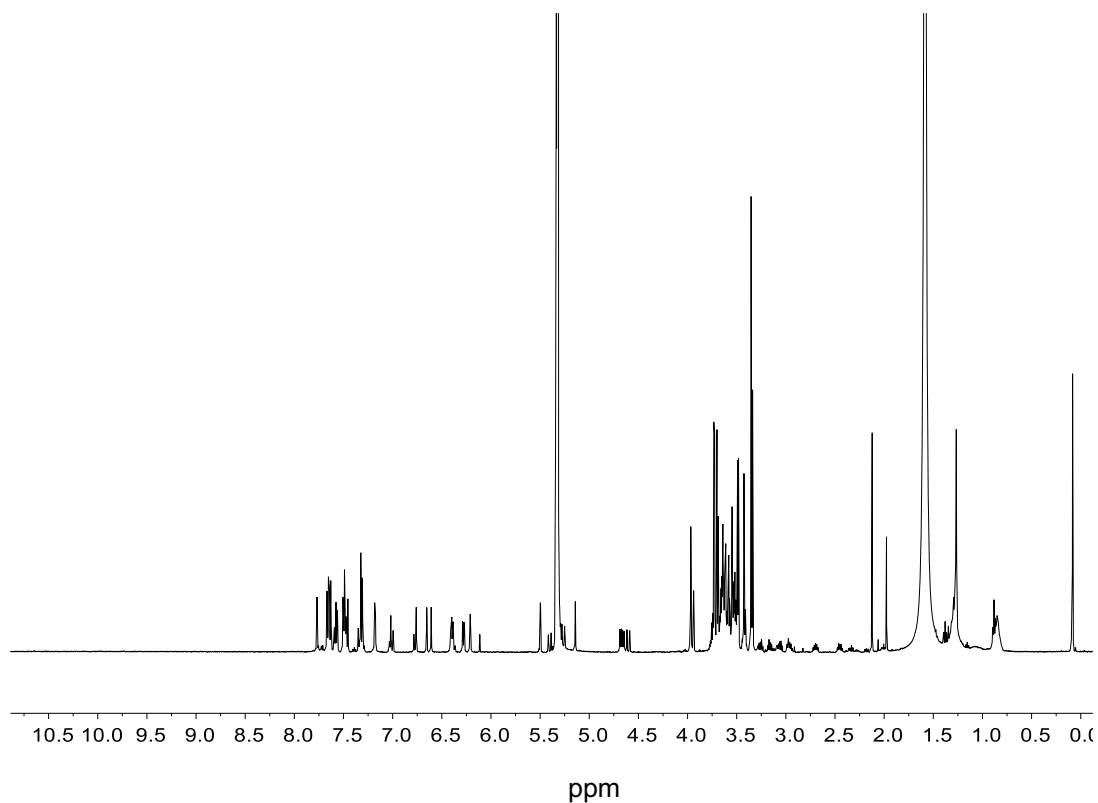


$^1\text{H}$ - $^{13}\text{C}$ -HMBC (up) and  $^1\text{H}$ - $^{13}\text{C}$ -HSQC (down) NMR spectrum of **11** in *d*-TFA with 10% TFA at 500MHz

### Oligomer 14

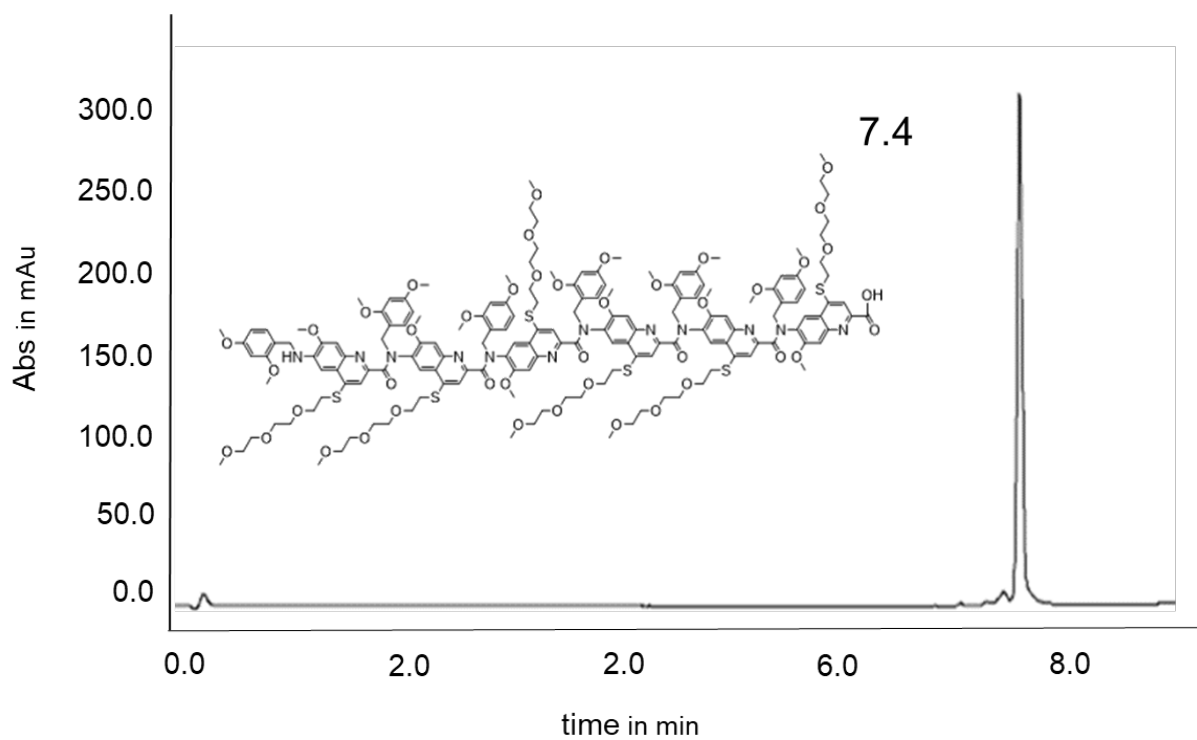


RP HPLC chromatogram of **14** on  $\text{C}_{18}$  and 10-100% A/B (water/acetonitrile) +0.1% TFA in 12 min at 300nm

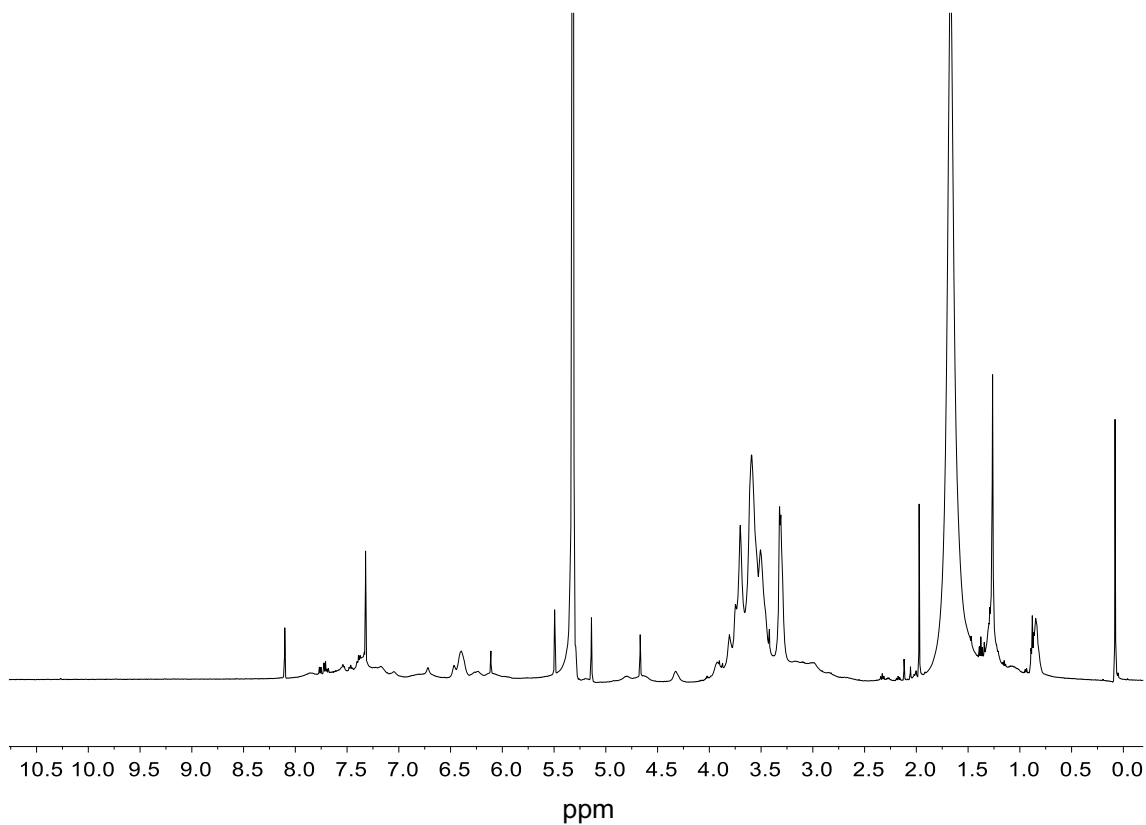


<sup>1</sup>H NMR spectrum of **14** in *d*-CH<sub>2</sub>Cl<sub>2</sub> at 500MHz and 128 scans

### Oligomer 15

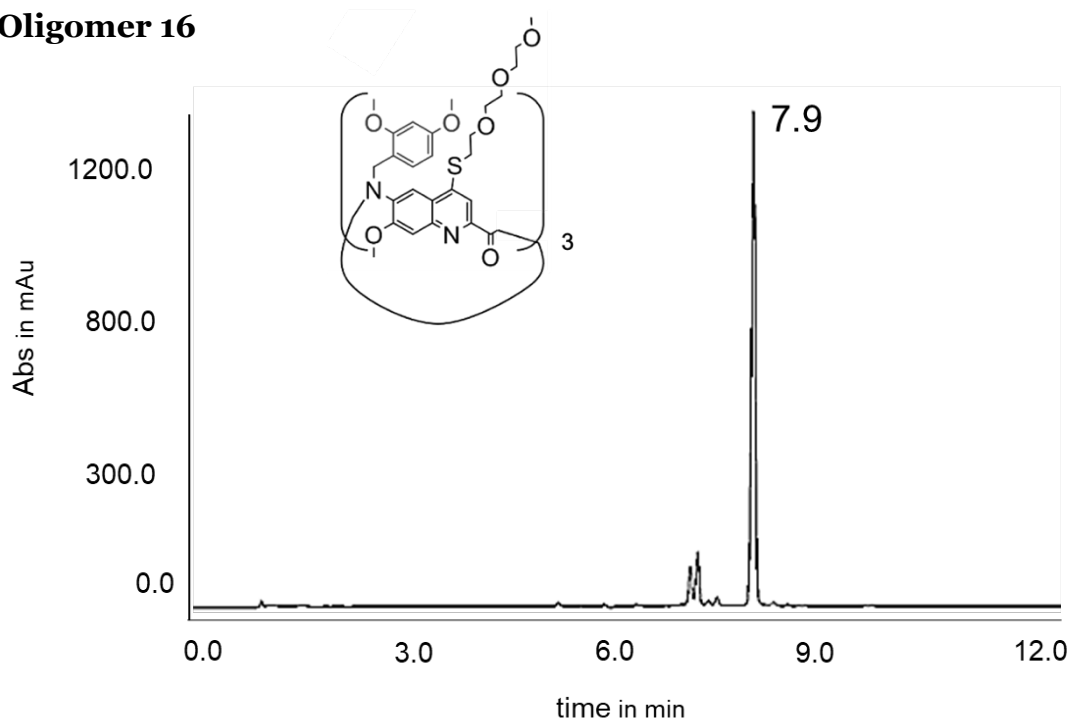


RP HPLC chromatogram of **15** on C<sub>18</sub> and 10-100% A/B (water/acetonitrile) +0.1% TFA in 9 min at 300nm

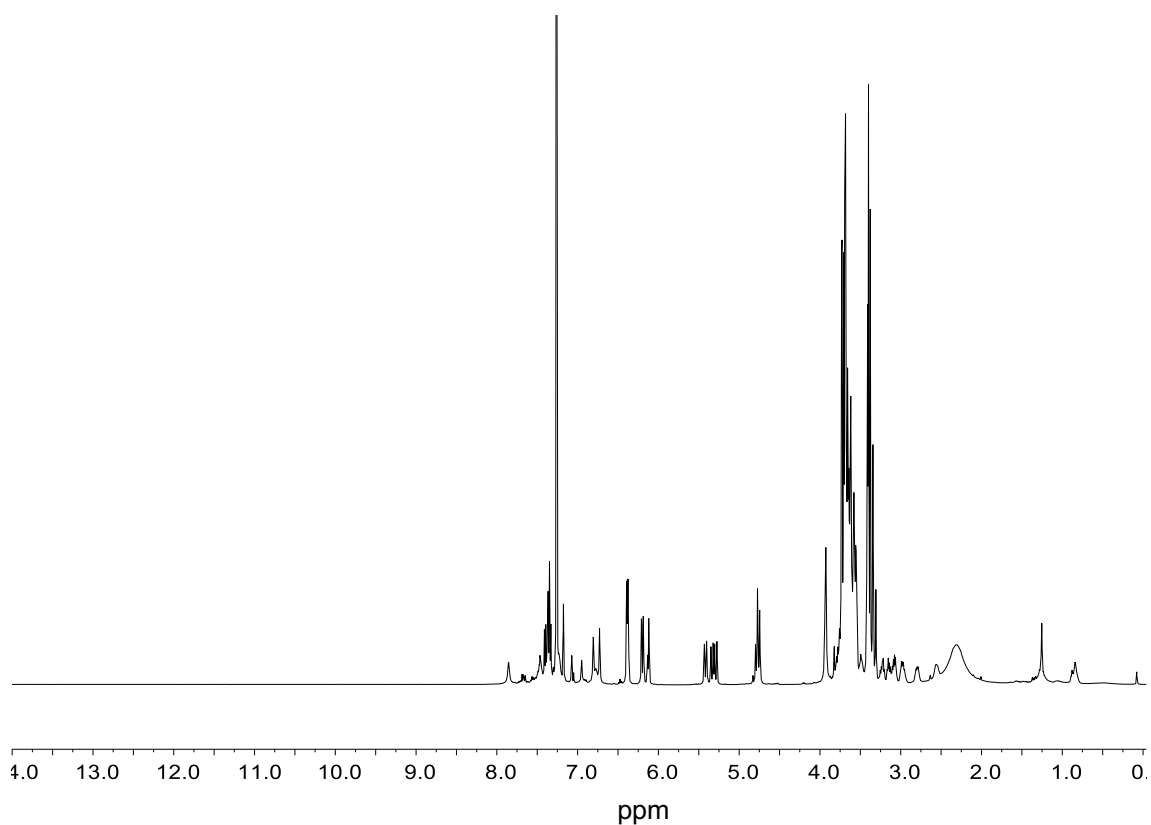


$^1\text{H}$  NMR spectrum of **15** in  $d\text{-CH}_2\text{Cl}_2$  at 500MHz and 128 scans

### Oligomer 16

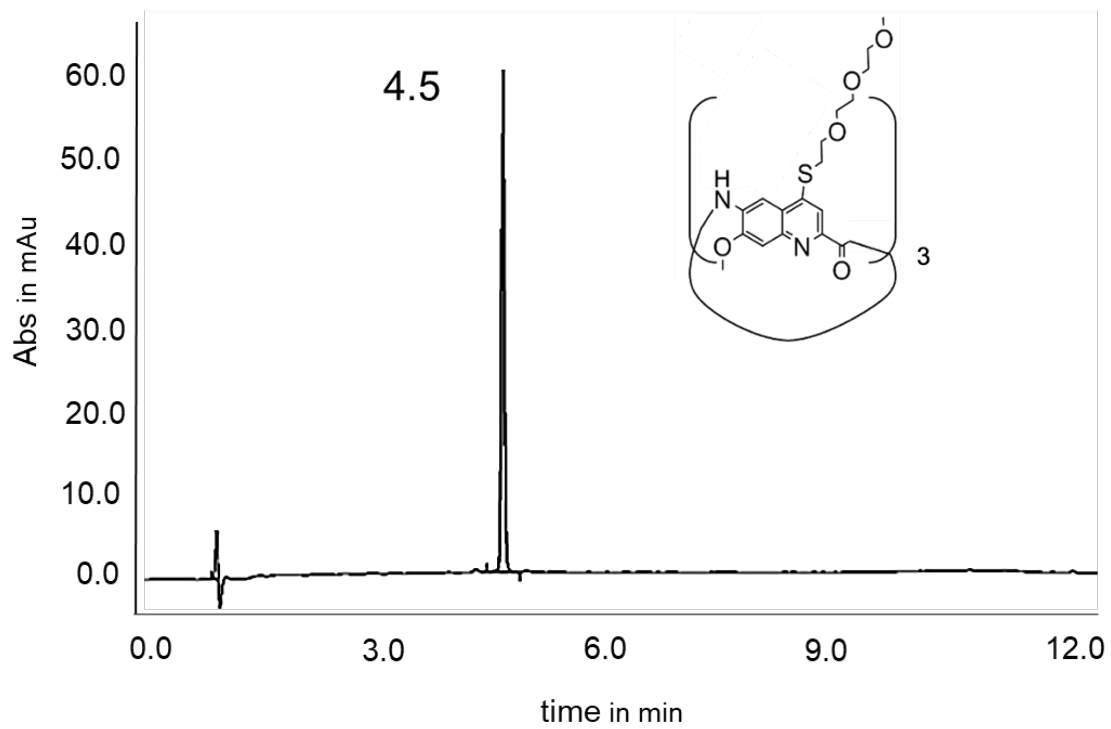


RP HPLC chromatogram of **16** on  $\text{C}_{18}$  and 10-100% A/B (water/acetonitrile) +0.1% TFA in 12 min at 300nm

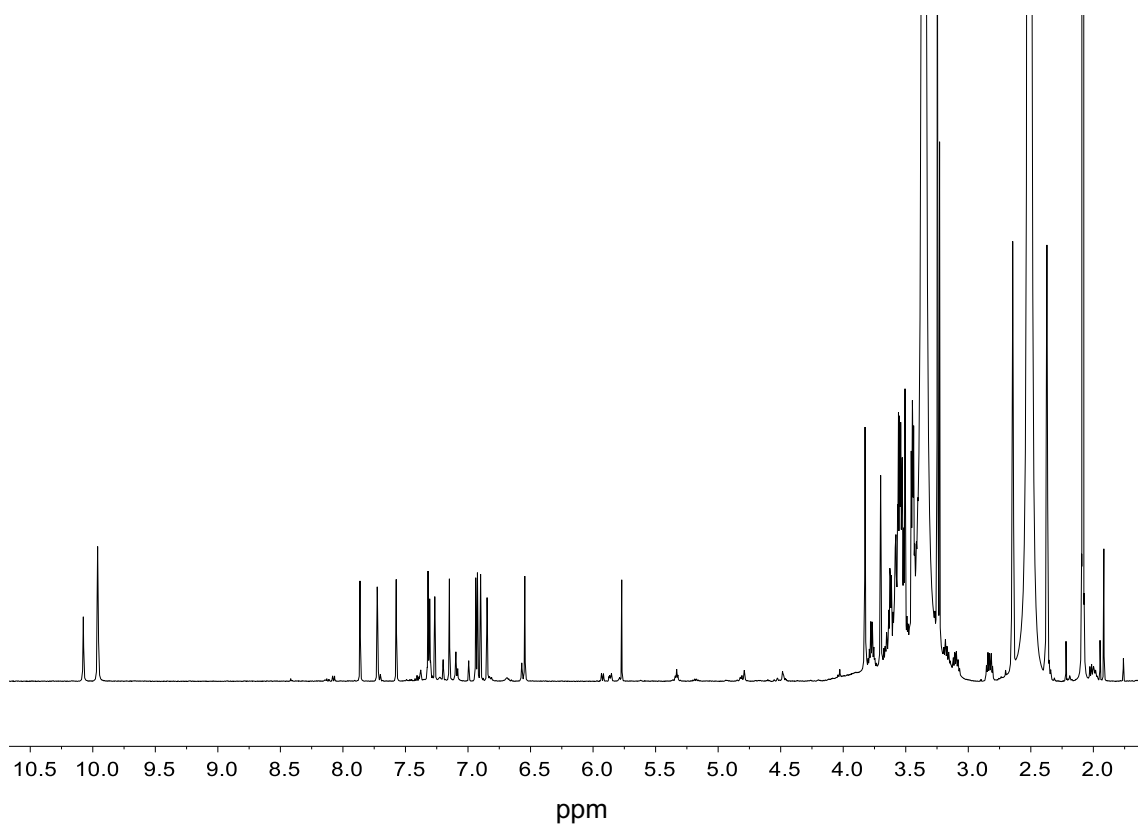


<sup>1</sup>H NMR spectrum of **16** in *d*-DMSO at 500MHz and 128 scans

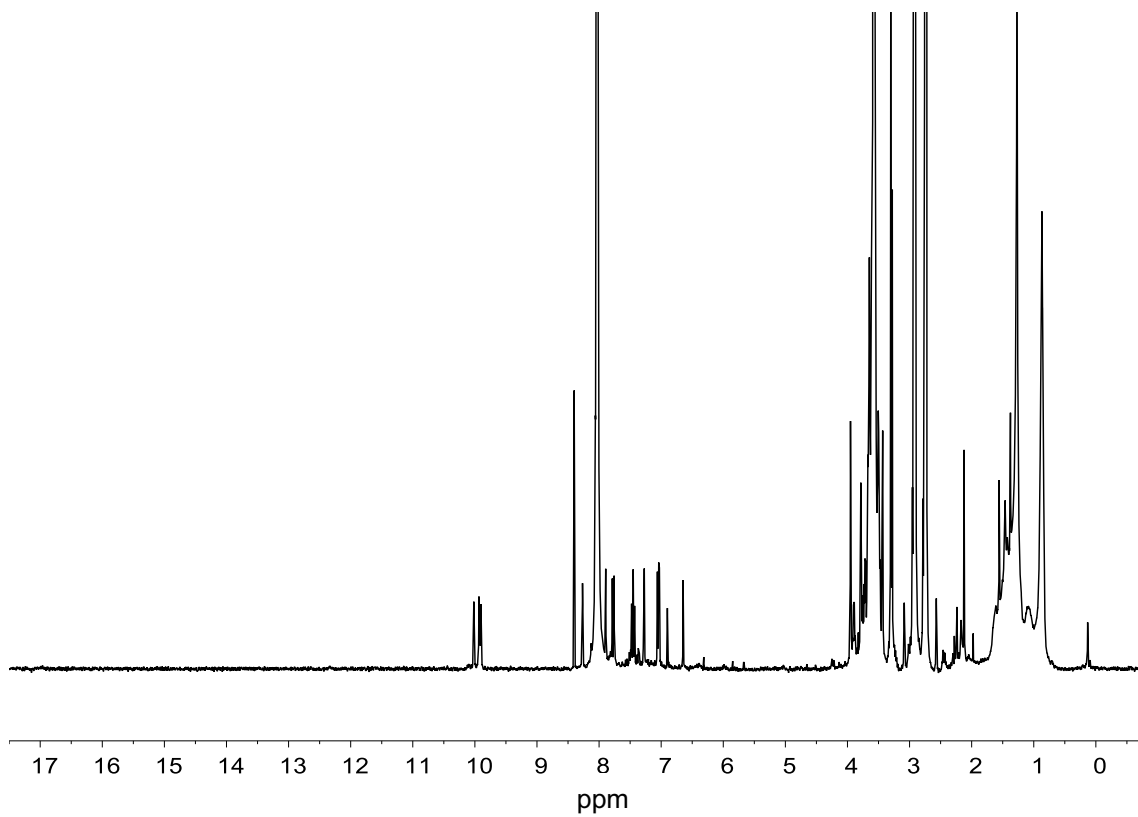
### Oligomer 17



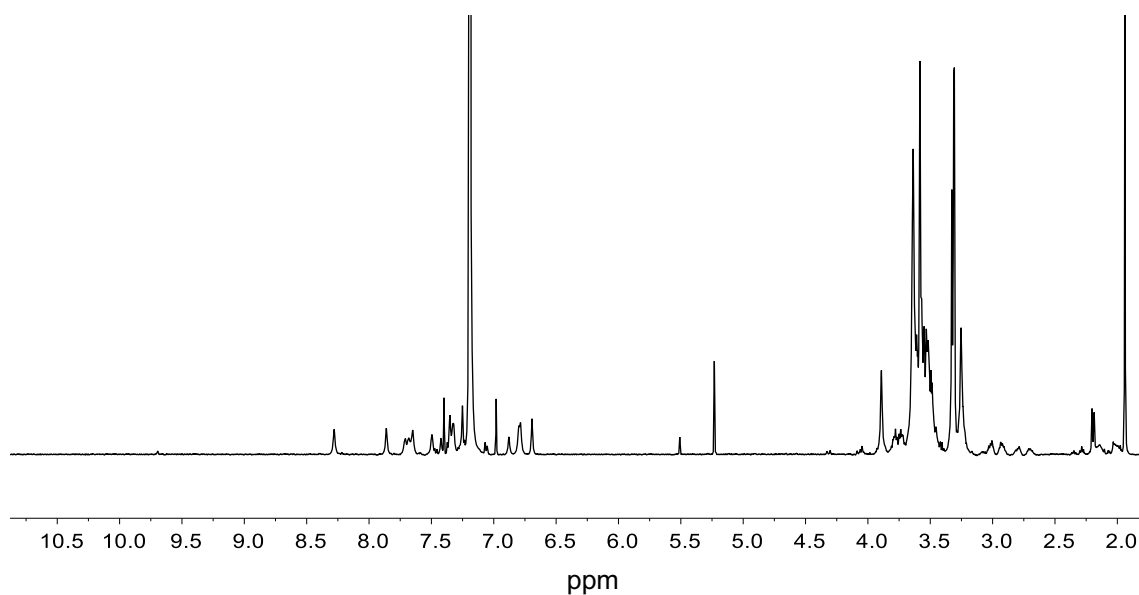
RP HPLC chromatogram of **17** on C<sub>18</sub> and 10-100% A/B (water/acetonitrile) +0.1% TFA in 12 min at 300nm



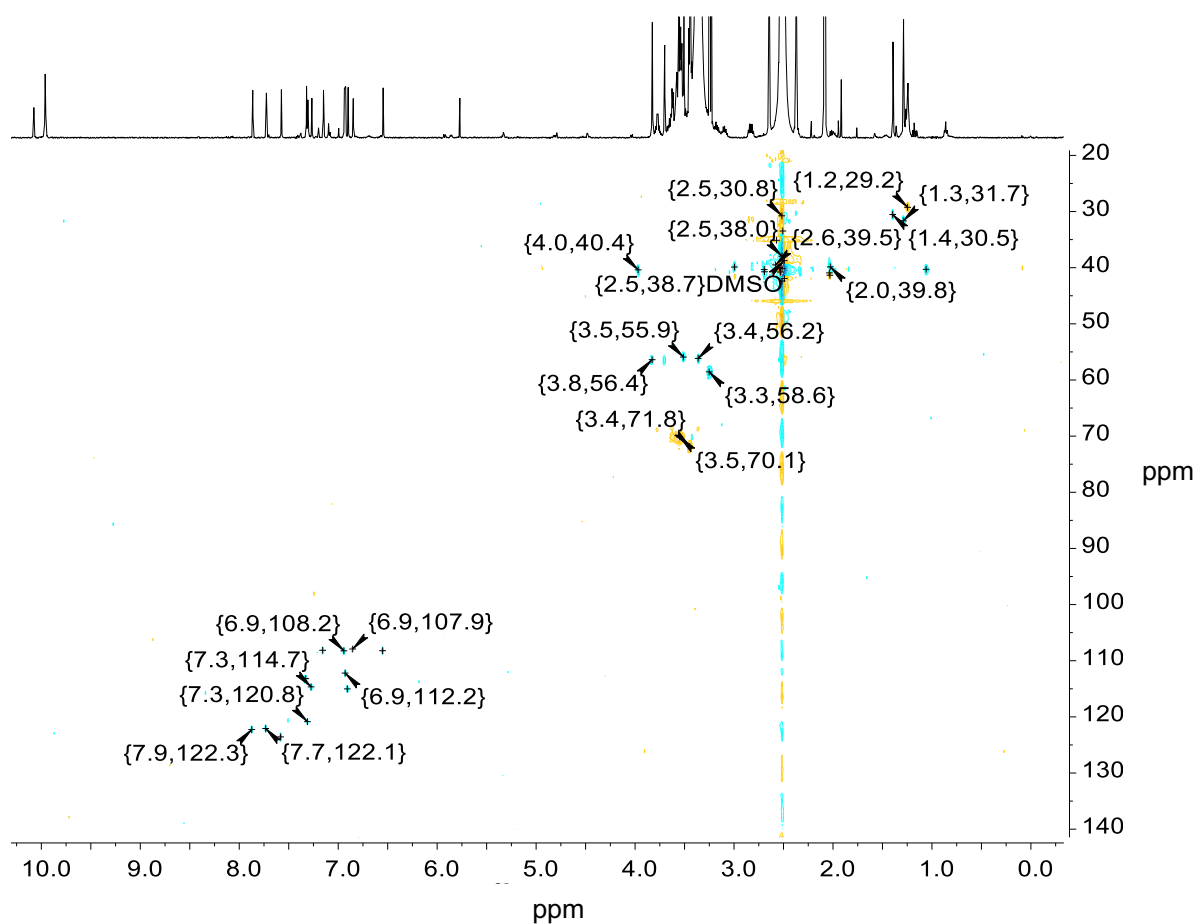
$^1\text{H}$  NMR spectrum of **17** in *d*-DMSO at 500MHz and 128 scans



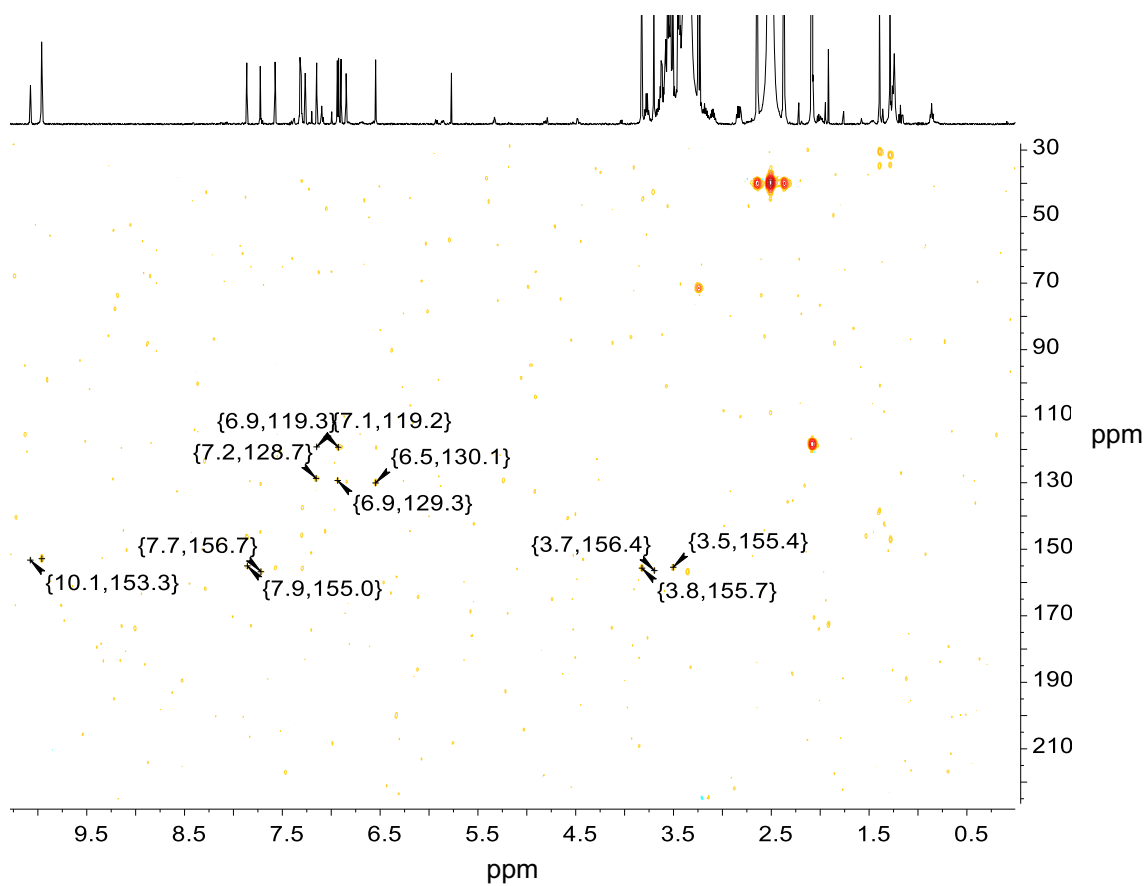
$^1\text{H}$  NMR spectrum of **17** in *d*-DMF at 500MHz and 128 scans



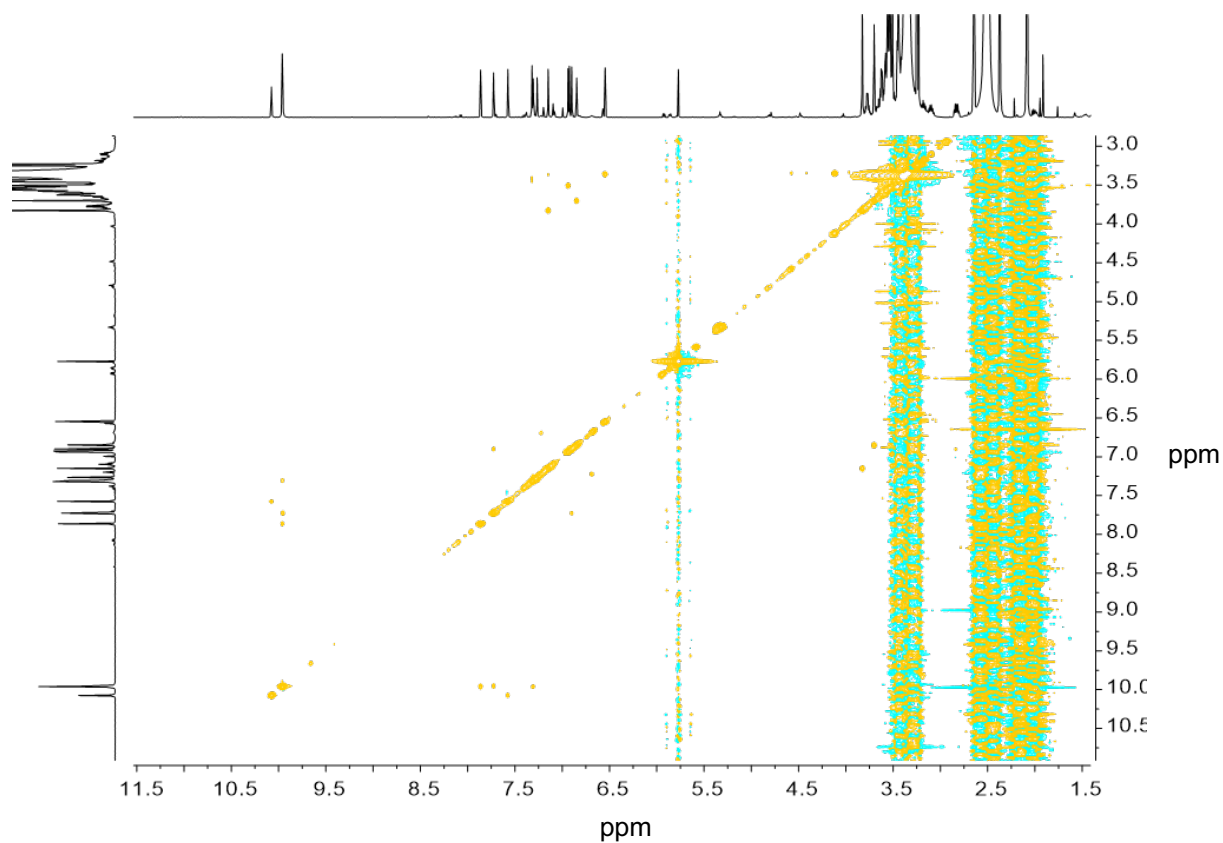
$^1\text{H}$  NMR spectrum of **17** in *d*- $\text{CHCl}_3$  at 500MHz and 128 scans



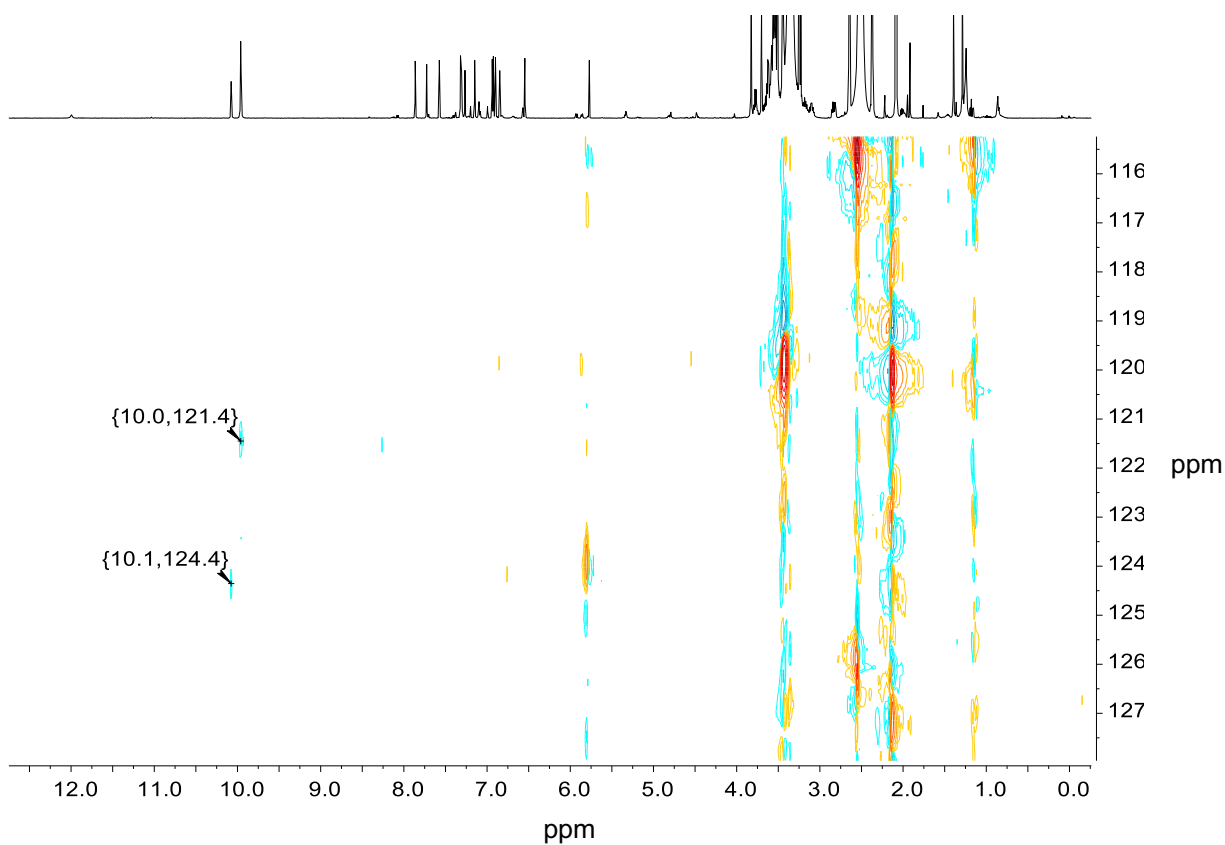
$^1\text{H}$ - $^{13}\text{C}$ -HSQC NMR spectrum of **17** in *d*-DMSO at 500MHz and 128 scans



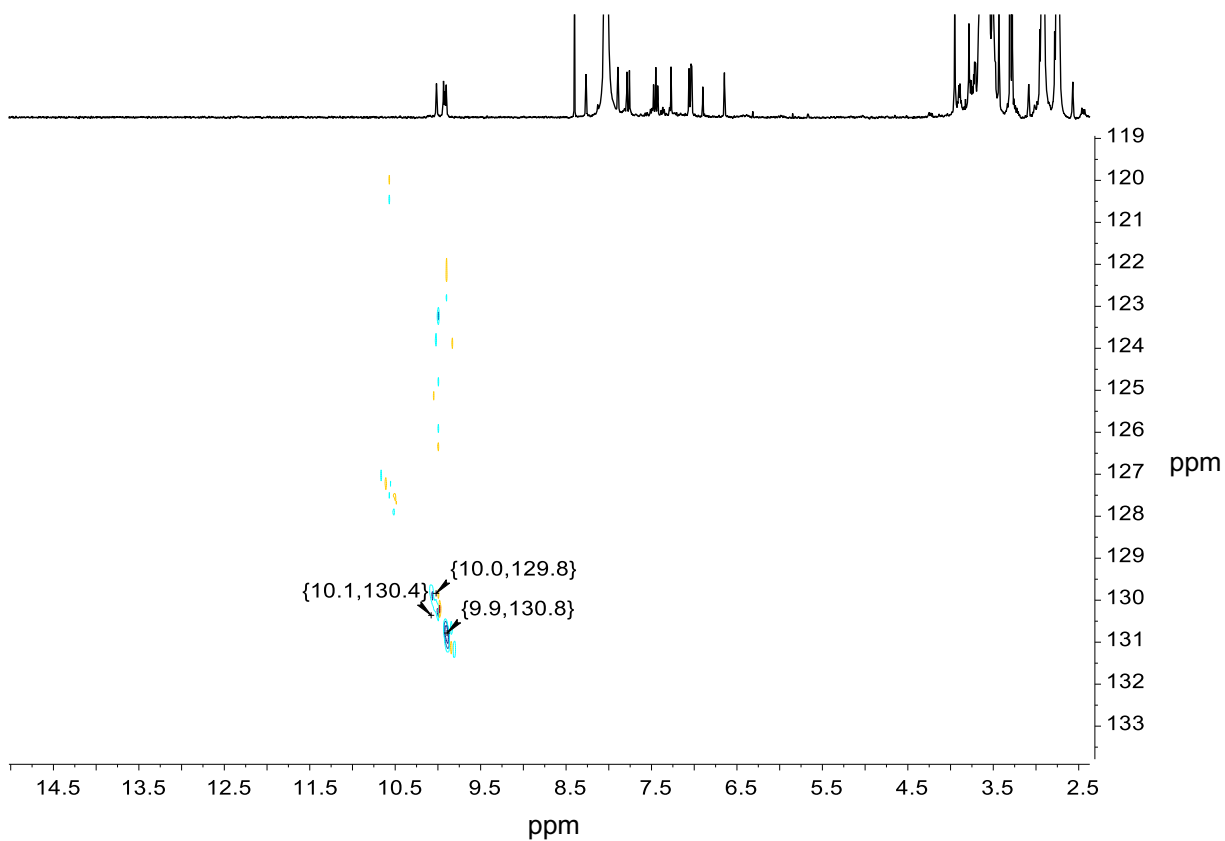
$^1\text{H}$ - $^{13}\text{C}$ -HMBC NMR spectrum of **17** in *d*-DMSO at 500MHz and 128 scans



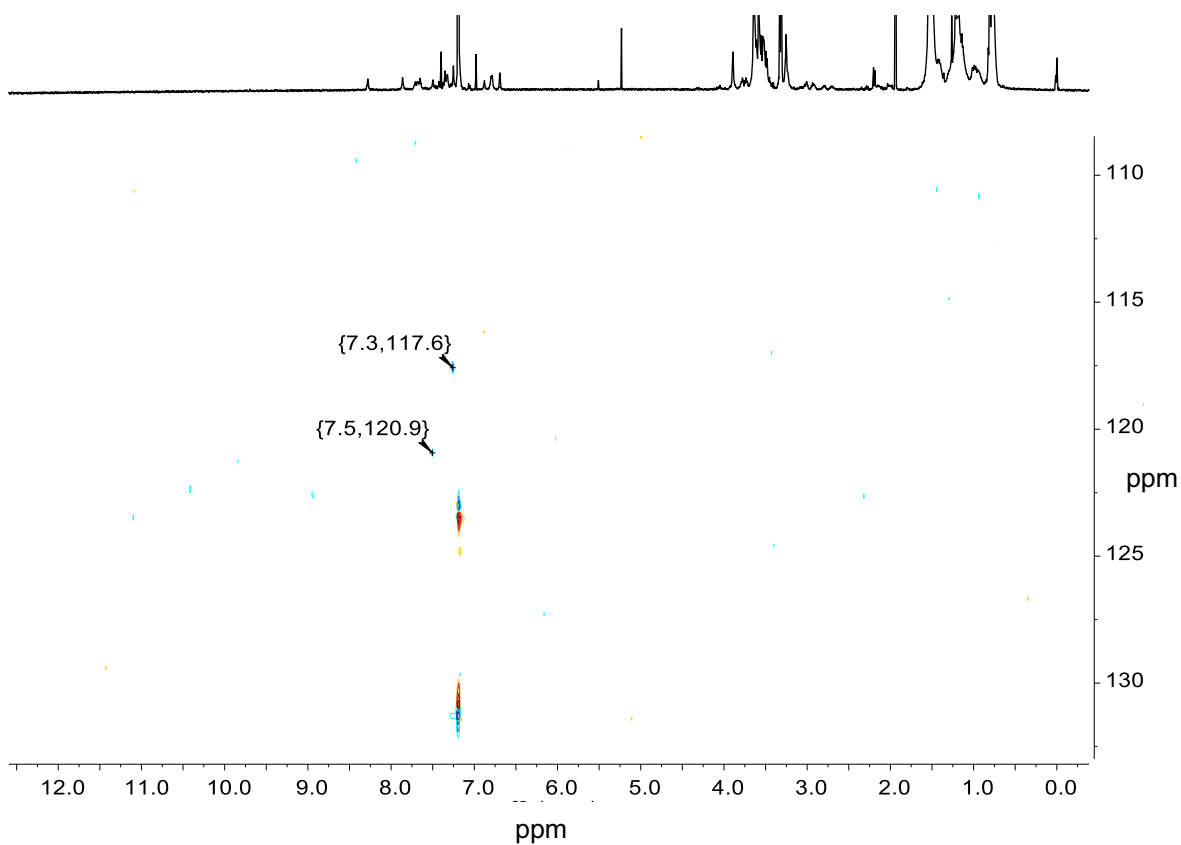
$^1\text{H}$ - $^1\text{H}$ -NOESY NMR spectrum of **17** in *d*- $\text{CHCl}_3$  at 500MHz and 128 scans



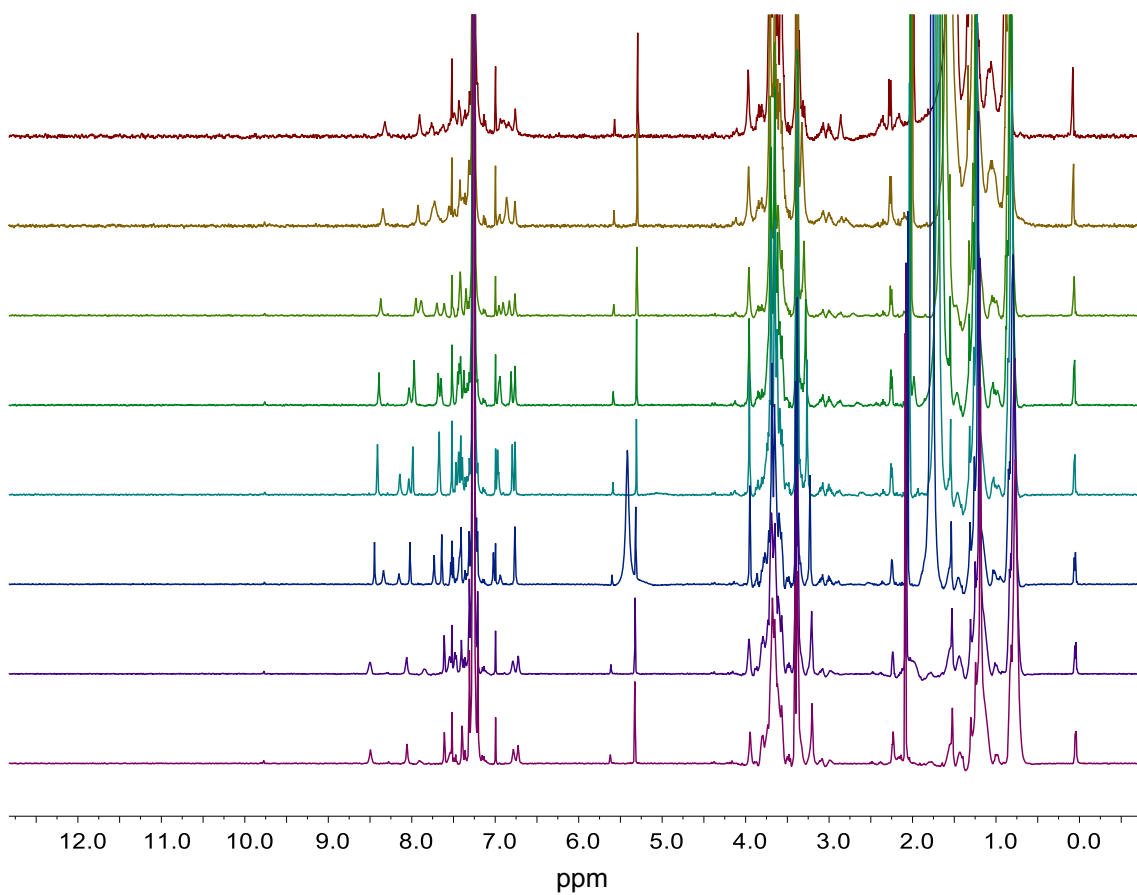
$^1\text{H}$ - $^{15}\text{N}$ -HSQC NMR spectrum of **17** in *d*-DMSO at 500MHz and 128 scans



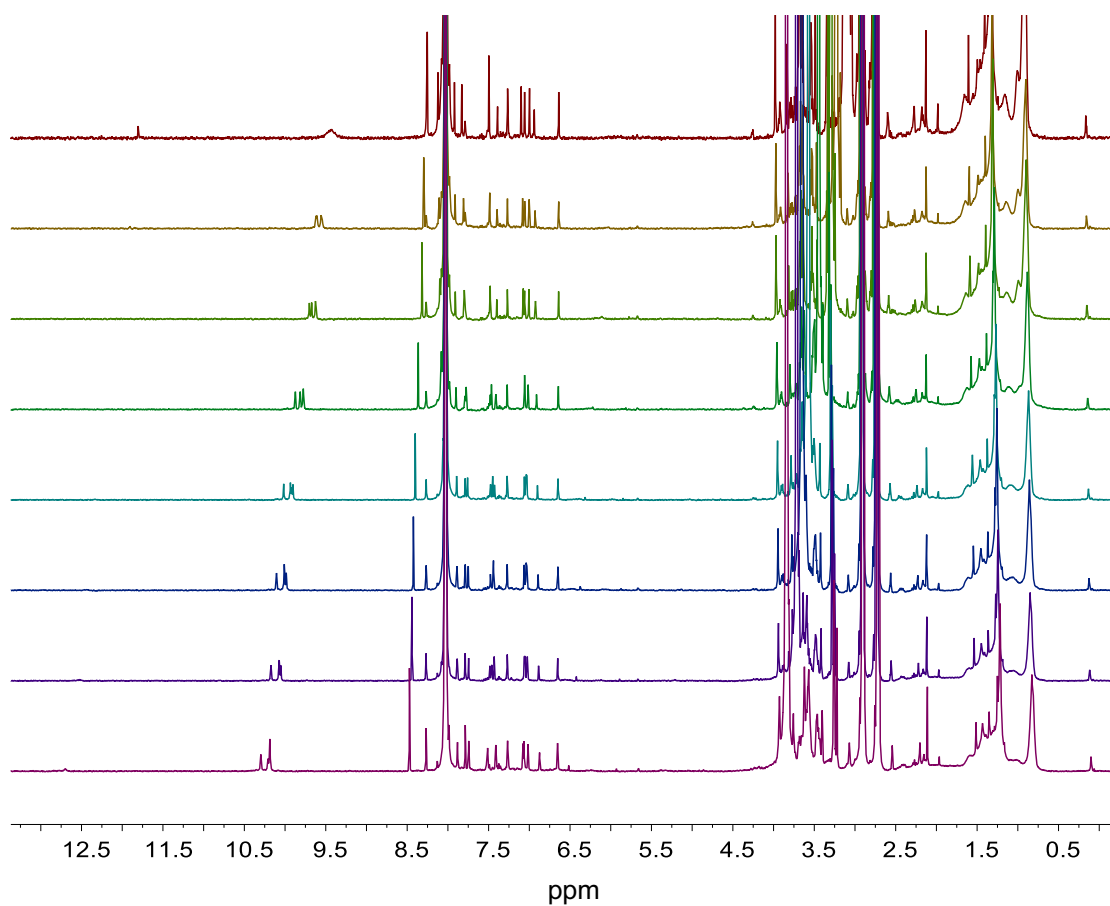
$^1\text{H}$ - $^{15}\text{N}$ -HSQC NMR spectrum of **17** in *d*-DMF at 500MHz and 128 scans



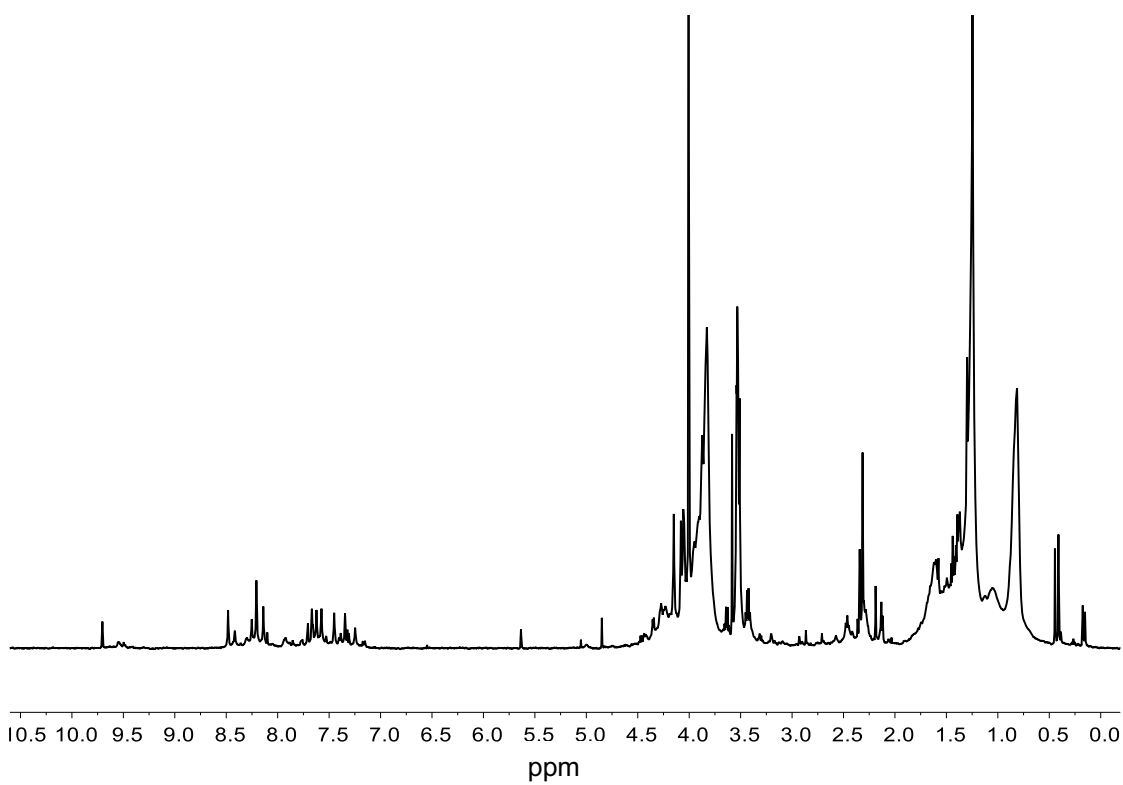
$^1\text{H}$ - $^{15}\text{N}$ -HSQC NMR spectrum of **17** in  $d\text{-CHCl}_3$  at 500MHz and 128 scans



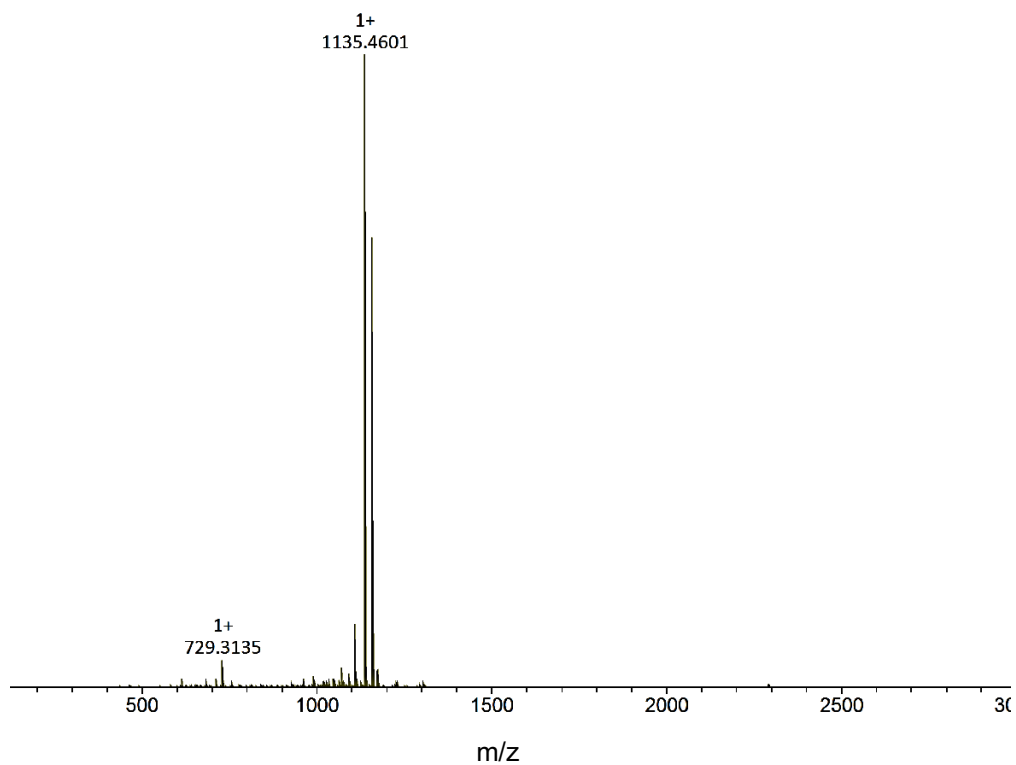
$^1\text{H}$  NMR spectrum of **15** in  $d\text{-CHCl}_3$  at 500MHz and 128 scans at (from up to down) 323K, 303K, 283K, 273K, 263K, 243K, 223K, and 213K



<sup>1</sup>H NMR spectrum of **17** in *d*-DMF at 500MHz and 128 scans at (from up to down) 353K, 333K, 323K, 303K, 283K, 273K, 263K, and 243K

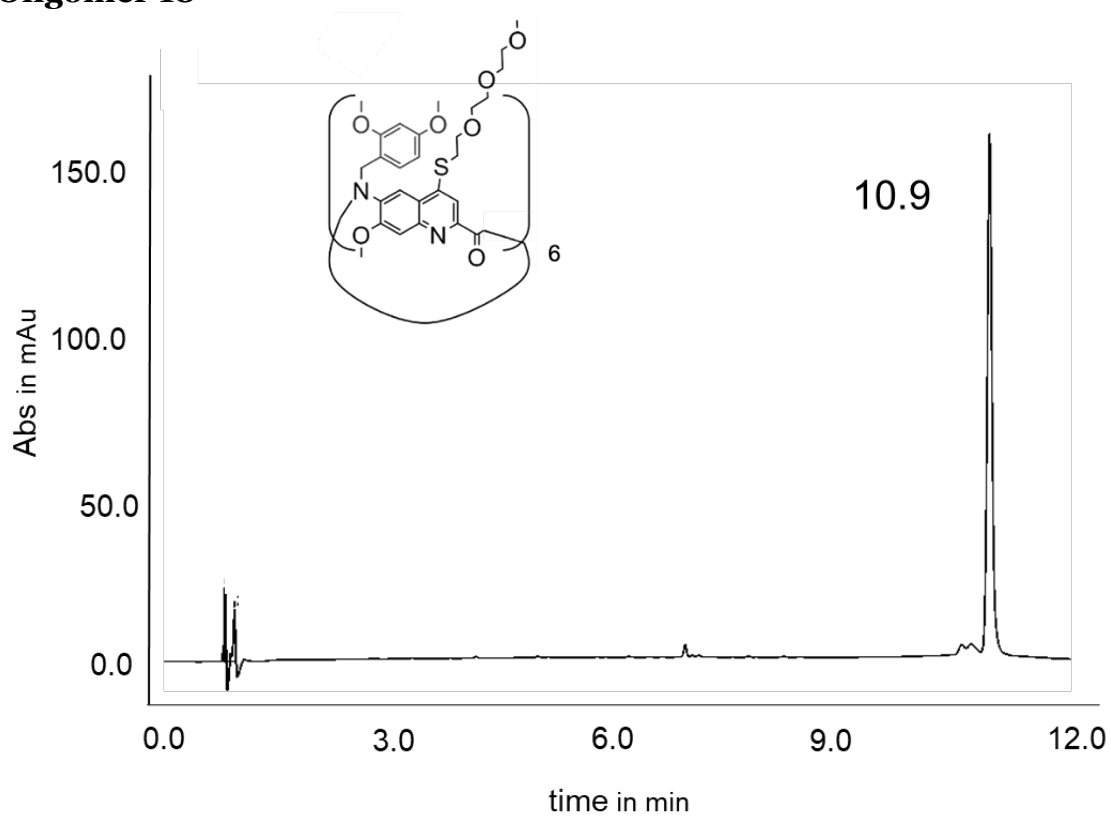


<sup>1</sup>H NMR spectrum of **17** in *d*-TFA at 500MHz and 128 scans

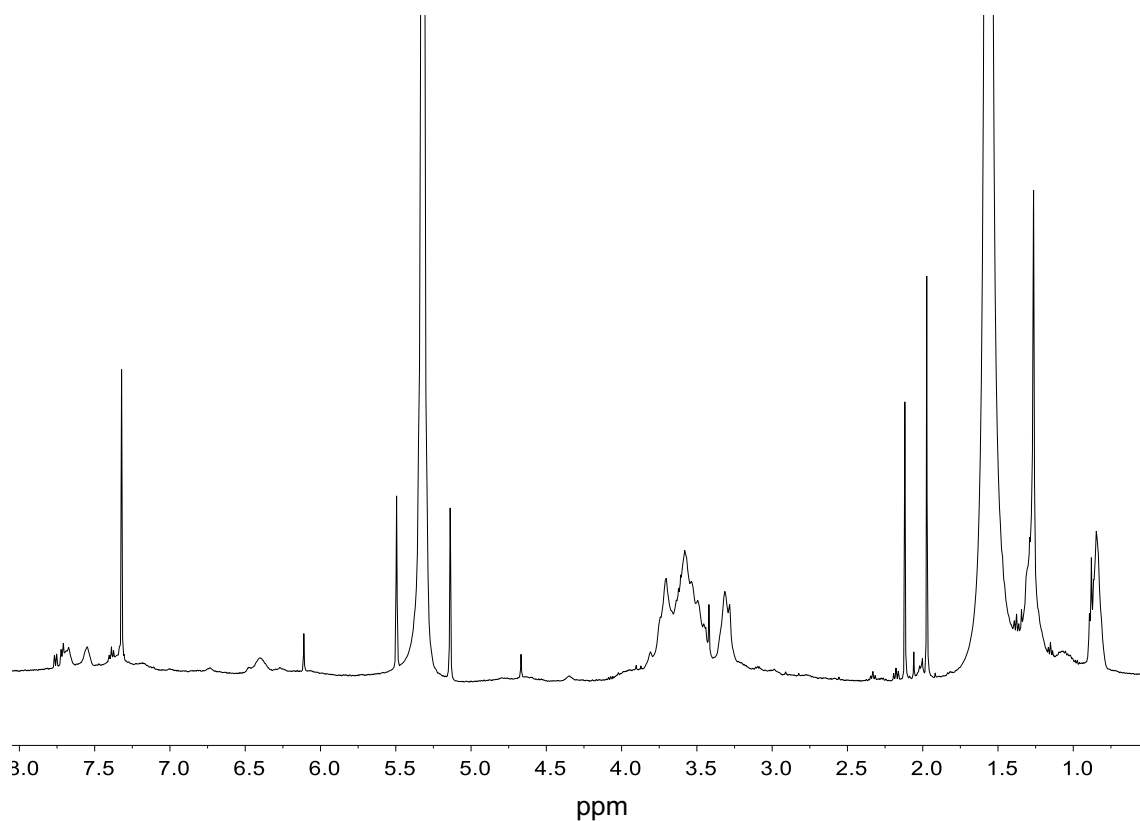


ESI-MS spectrum of **17** in positive mode

### Oligomer **18**

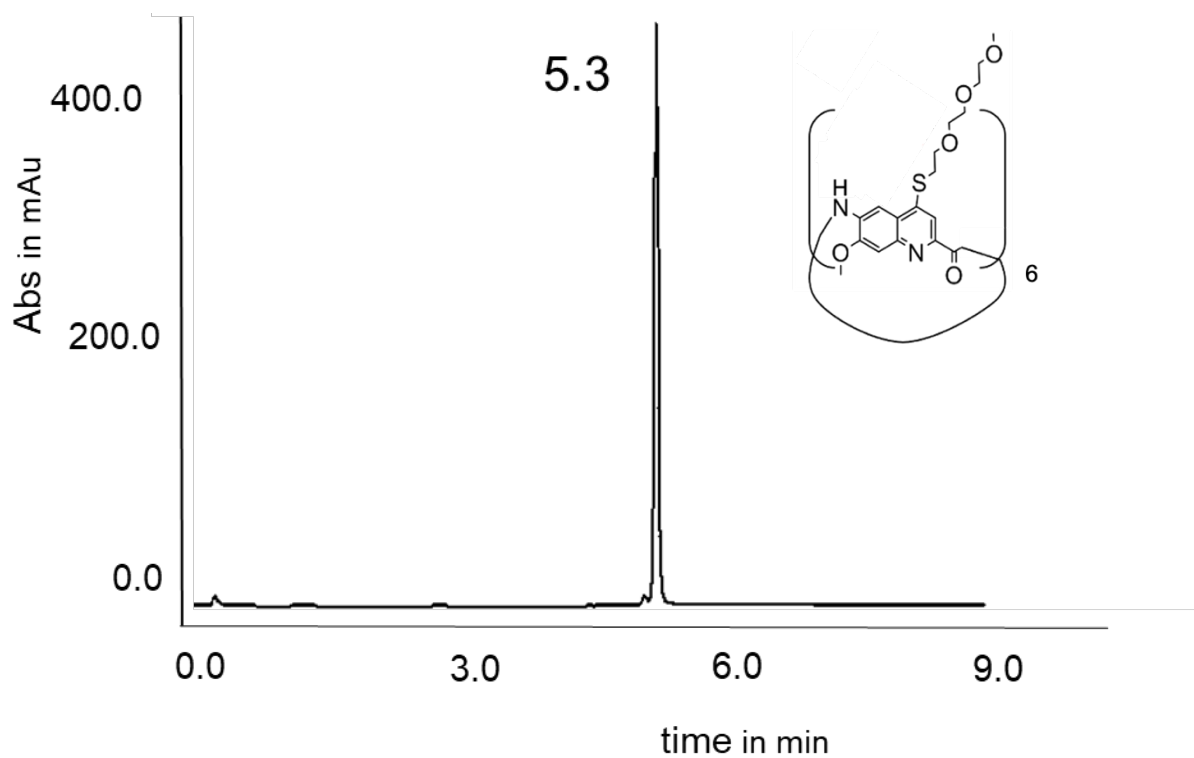


RP HPLC chromatogram of **18** on C<sub>18</sub> and 10-100% A/B (water/acetonitrile) +0.1% TFA in 12 min at 300nm

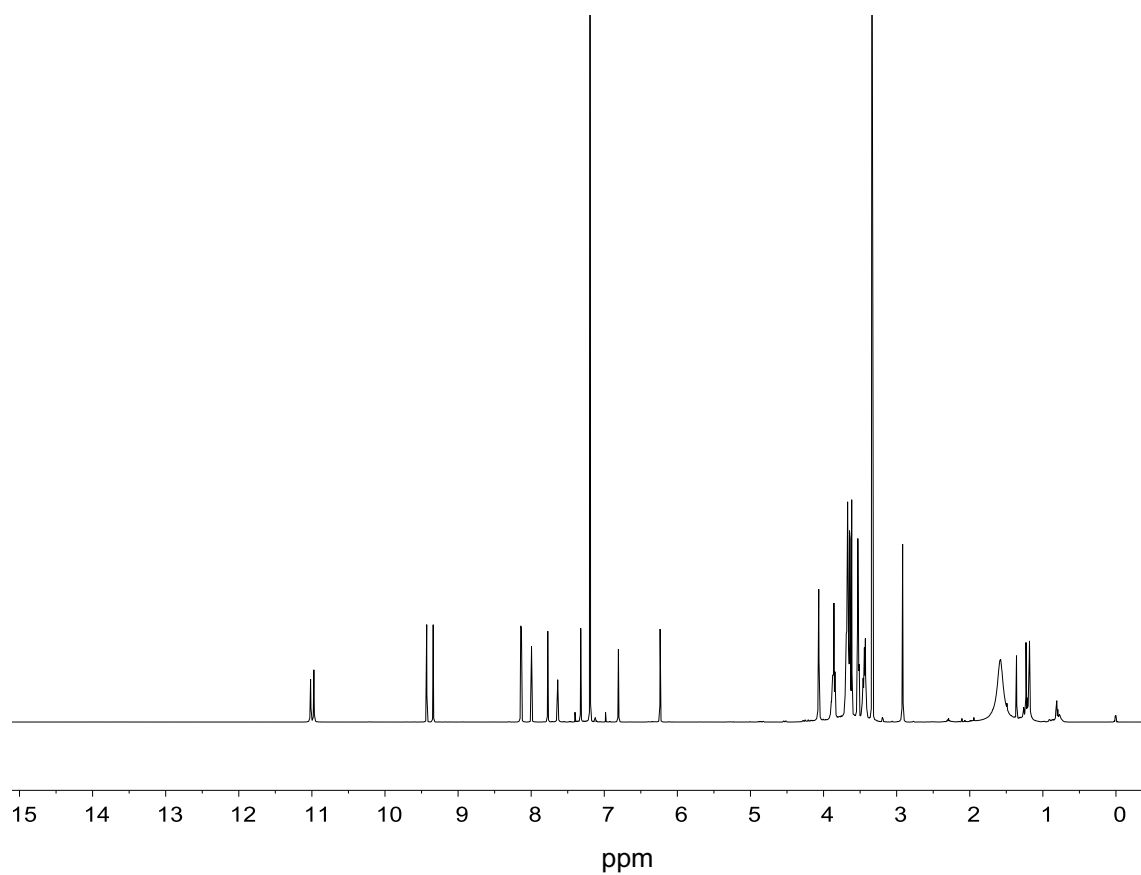


$^1\text{H}$  NMR spectrum of **18** in  $d\text{-CH}_2\text{Cl}_2$  at 500MHz and 128 scans

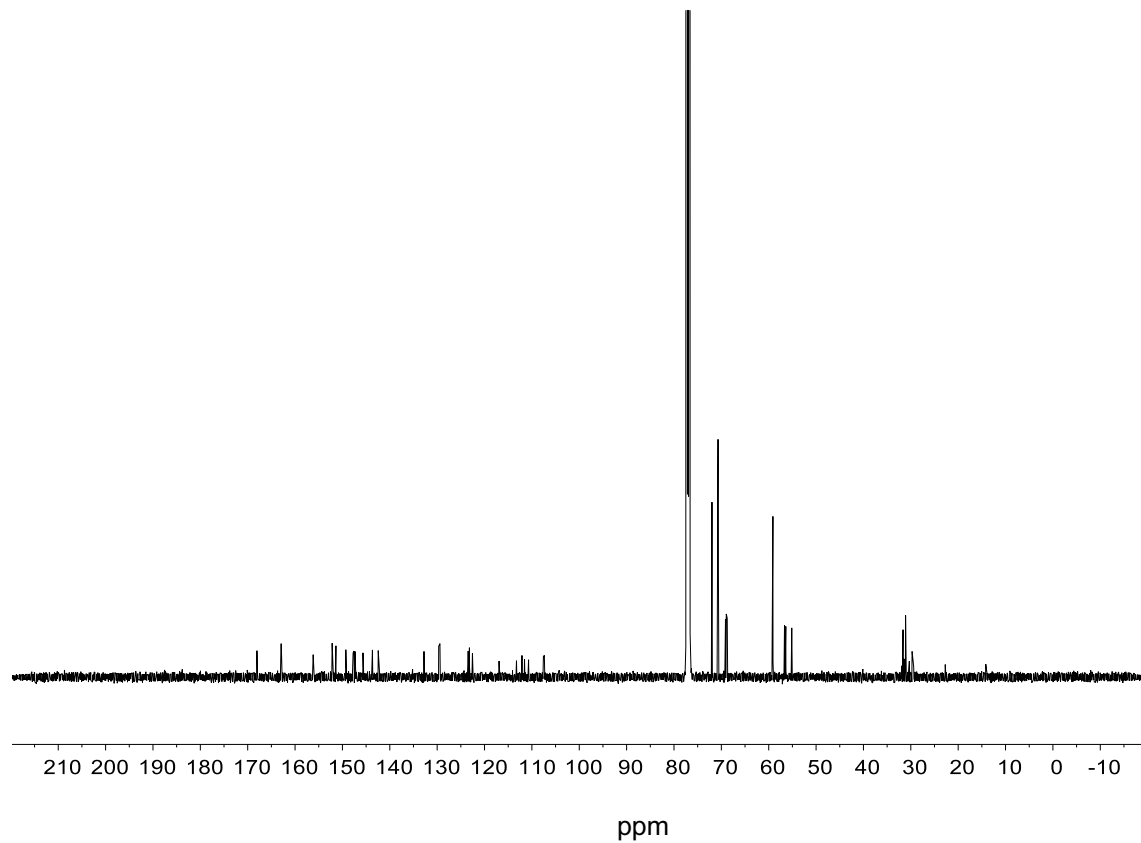
### Oligomer **19**



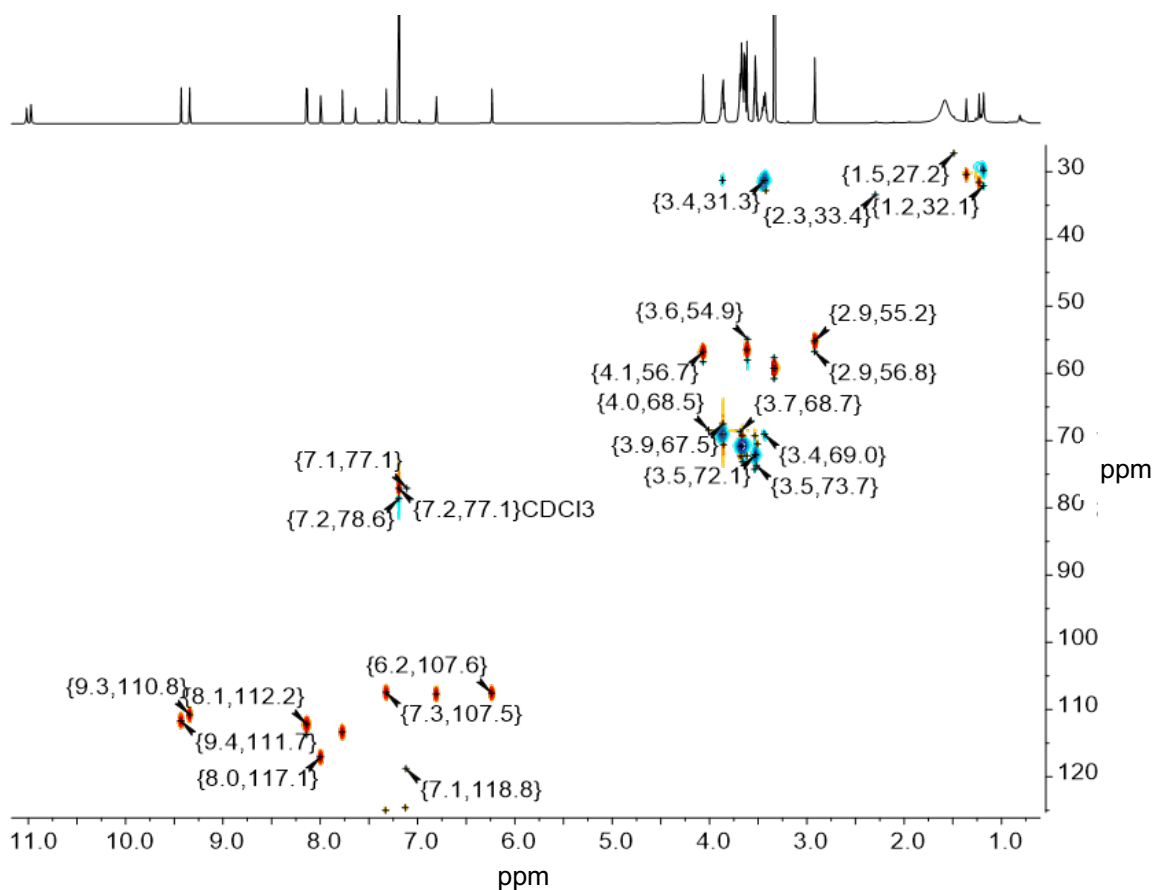
RP HPLC chromatogram of **19** on  $\text{C}_{18}$  and 50-100% A/B (water/acetonitrile) +0.1% TFA in 9 min at 300nm



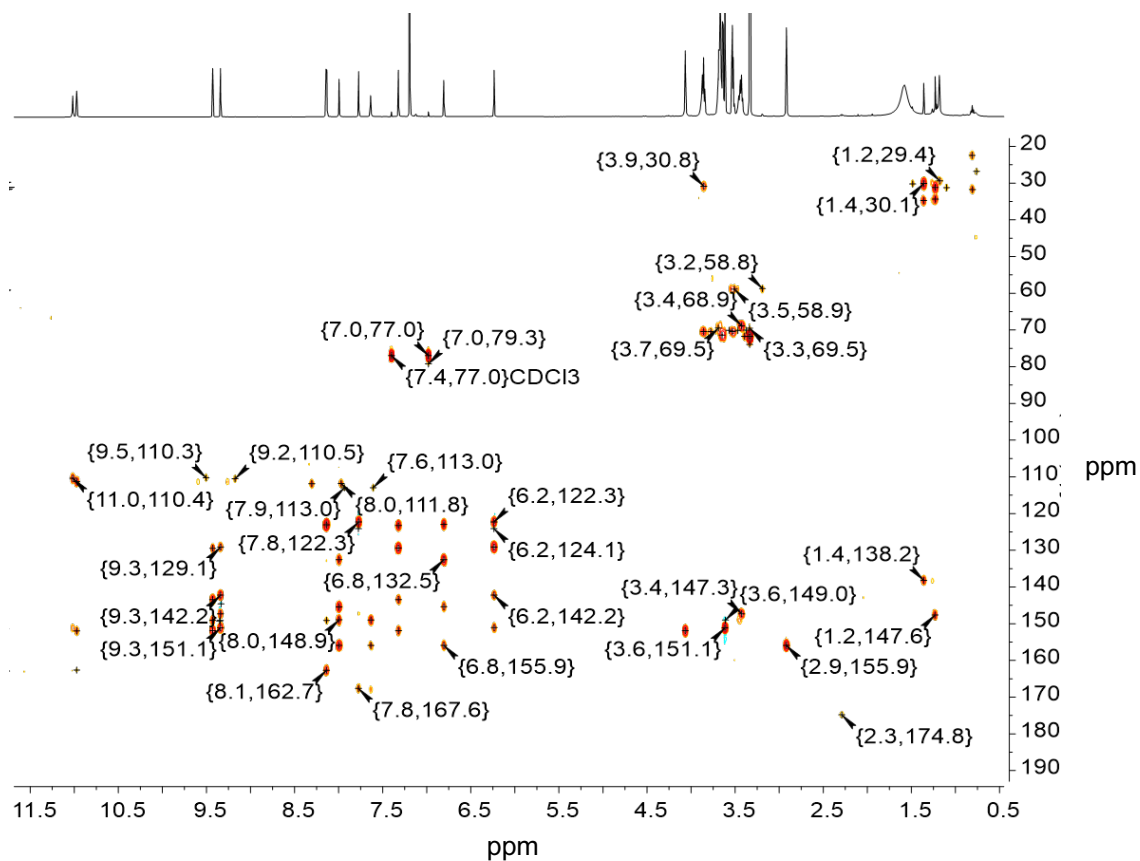
$^1\text{H}$  NMR spectrum of **19** in  $d\text{-CHCl}_3$  at 500MHz and 512 scans



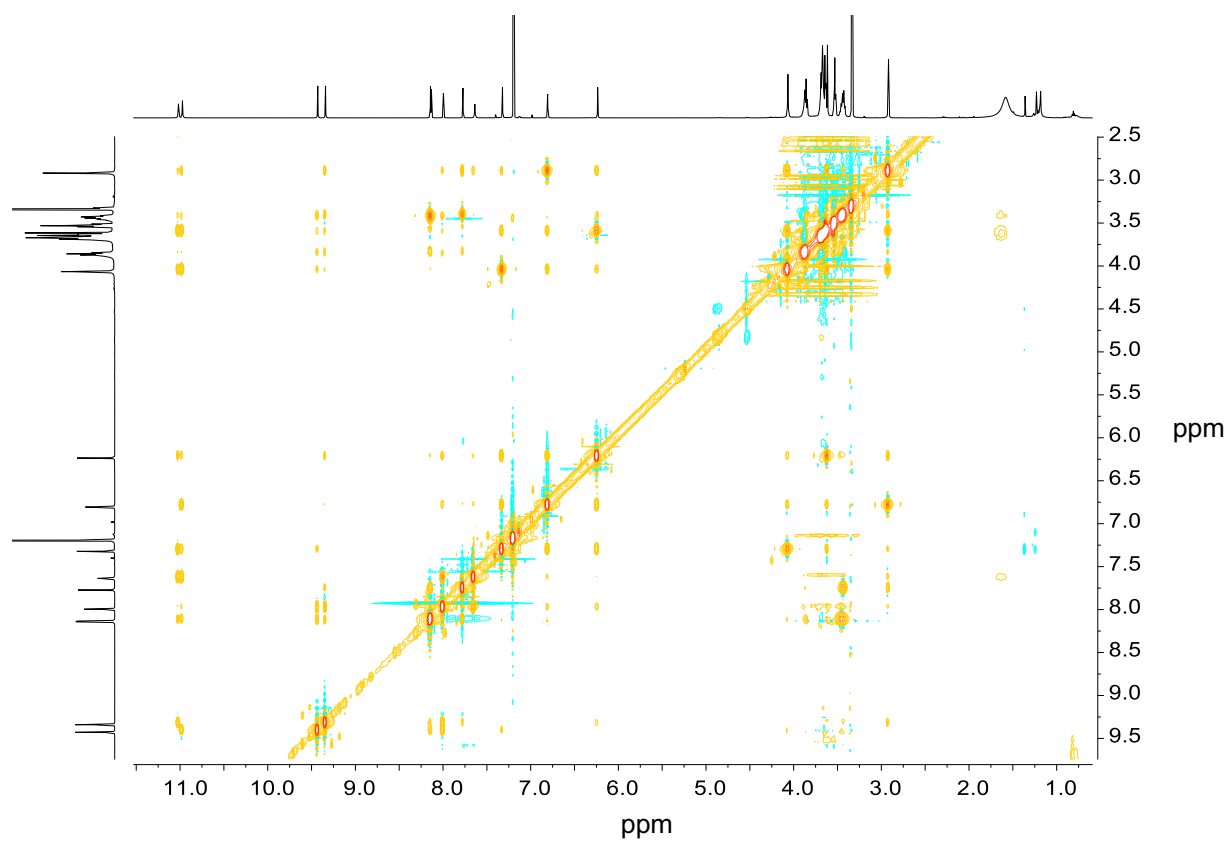
$^{13}\text{C}$  NMR spectrum of **19** in  $d\text{-CHCl}_3$  at 128 MHz and 128 scans



<sup>1</sup>H-<sup>13</sup>C-HSQC NMR spectrum of **19** in *d*-CHCl<sub>3</sub> at 500MHz and 128 scans



<sup>1</sup>H-<sup>13</sup>C-HMBC NMR spectrum of **19** in *d*-CHCl<sub>3</sub> at 500MHz and 128 scans



$^1\text{H}$ - $^1\text{H}$ -NOESY NMR spectrum of **19** in *d*- $\text{CHCl}_3$  at 500MHz

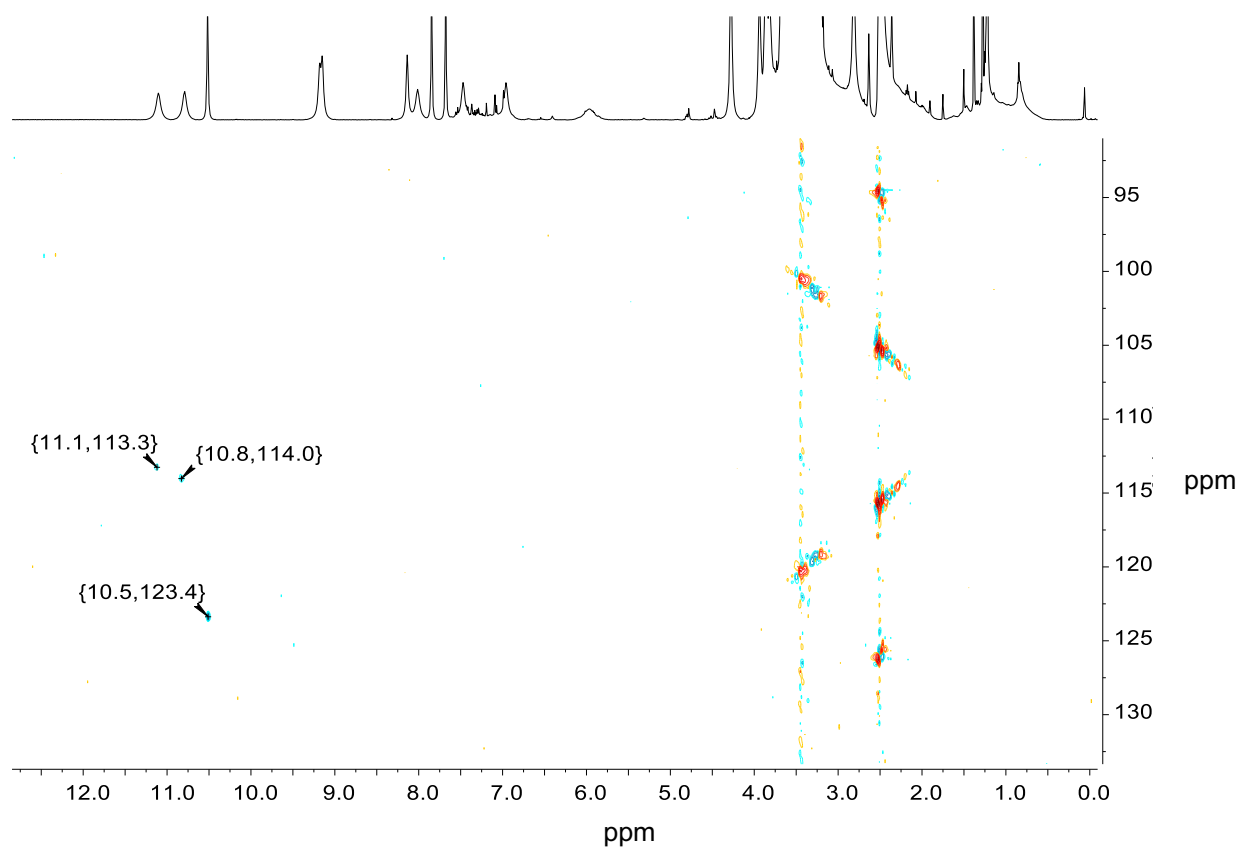
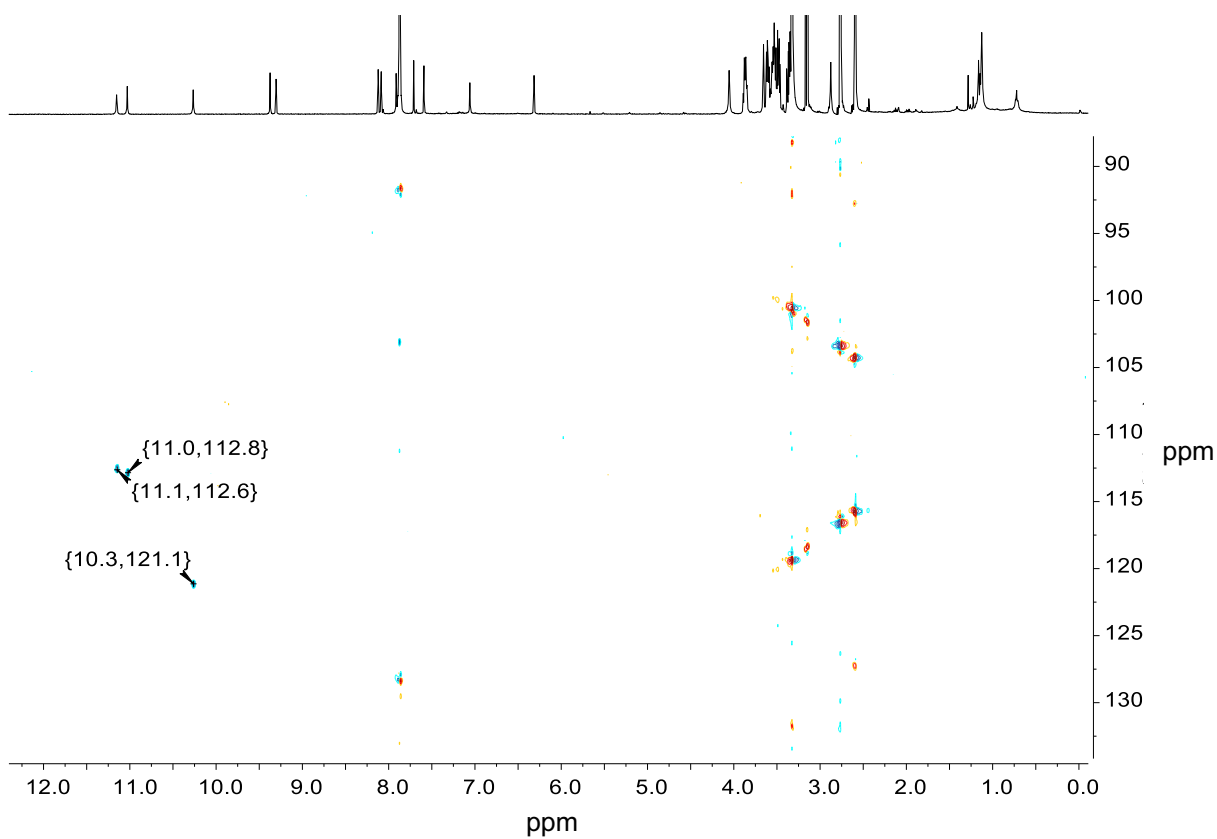
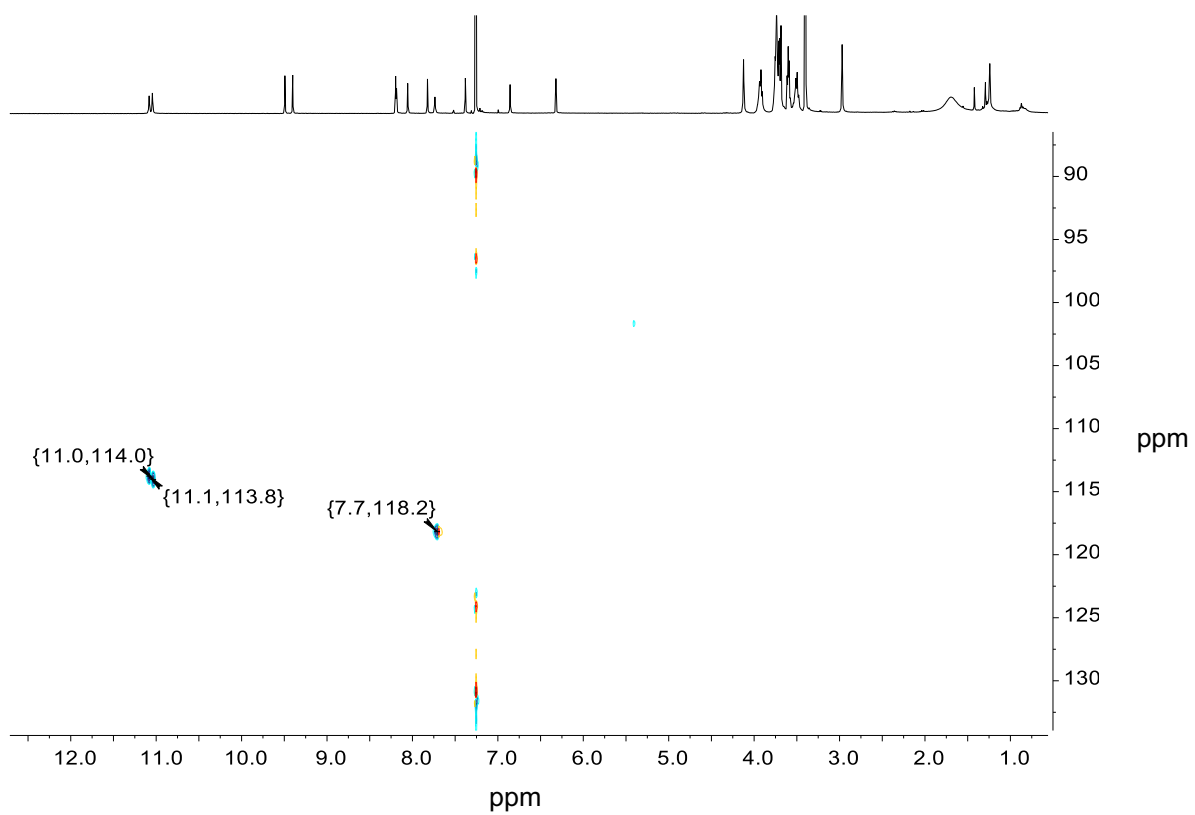


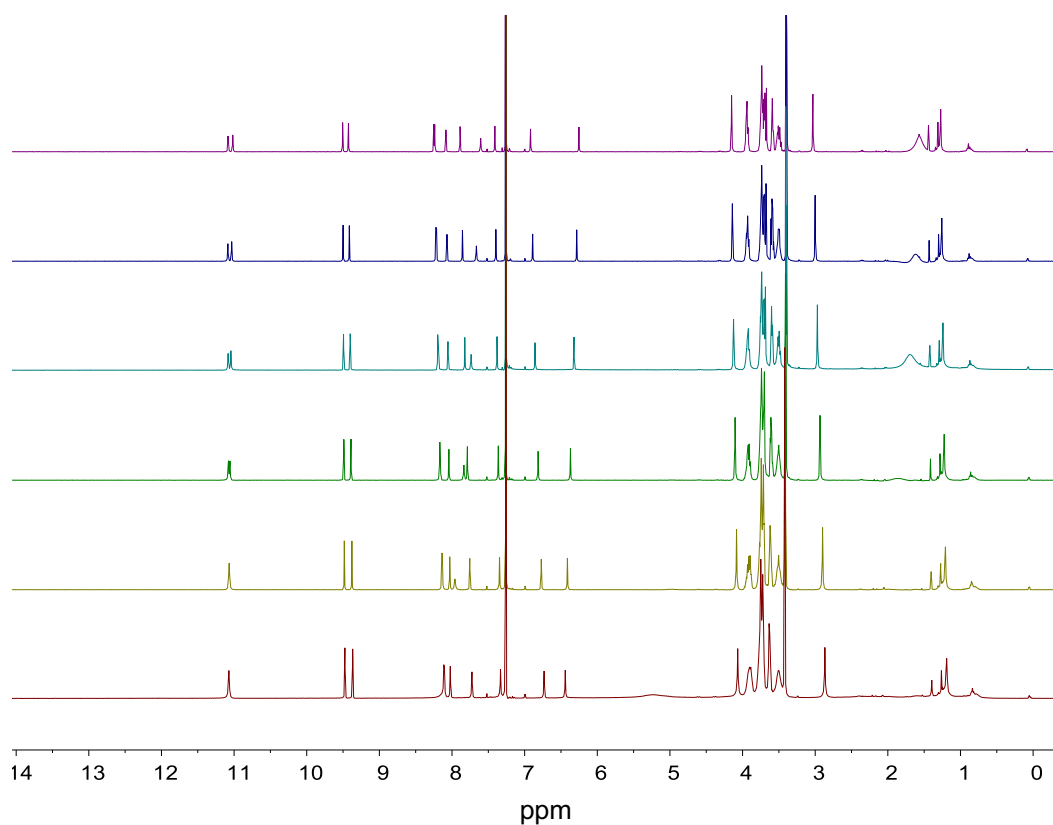
Figure S55  $^1\text{H}$ - $^{15}\text{N}$ -HSQC NMR spectrum of **19** in *d*-DMSO at 500MHz



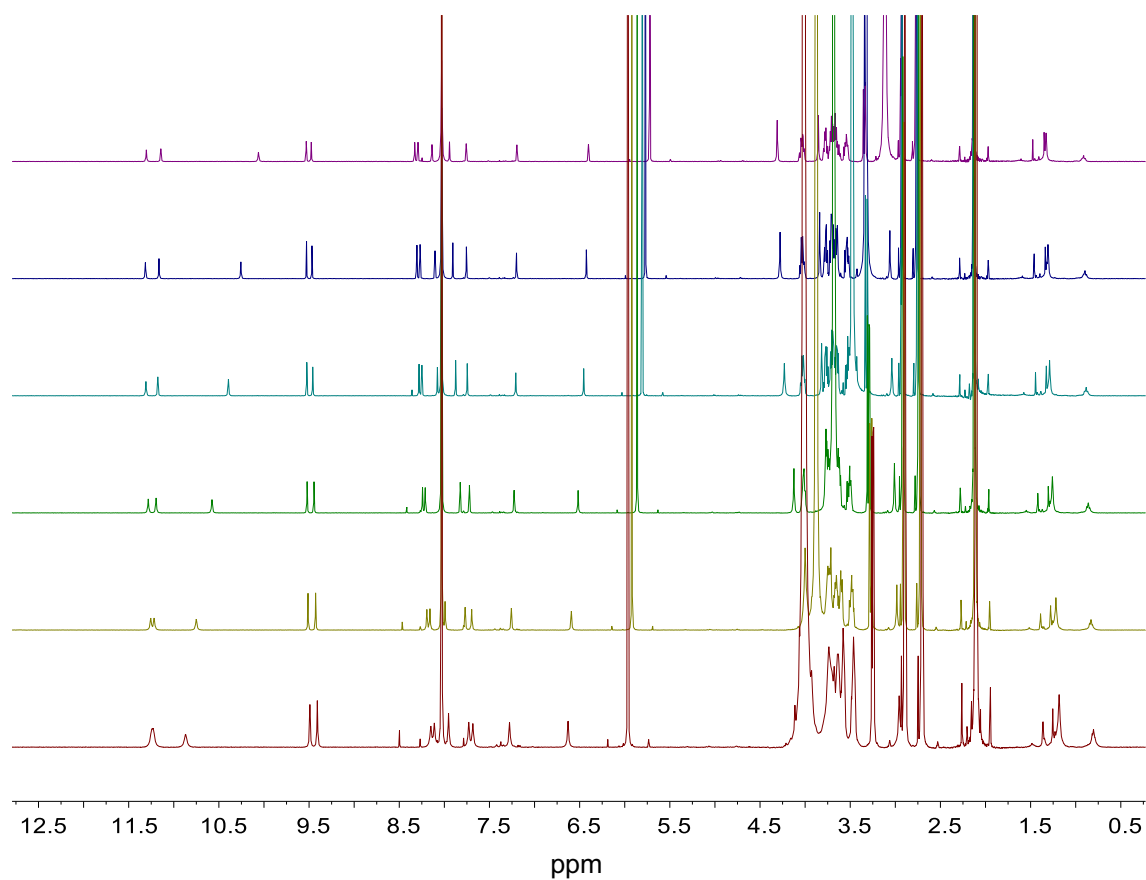
$^1\text{H}$ - $^{15}\text{N}$ -HSQC NMR spectrum of **19** in *d*-DMF at 500MHz



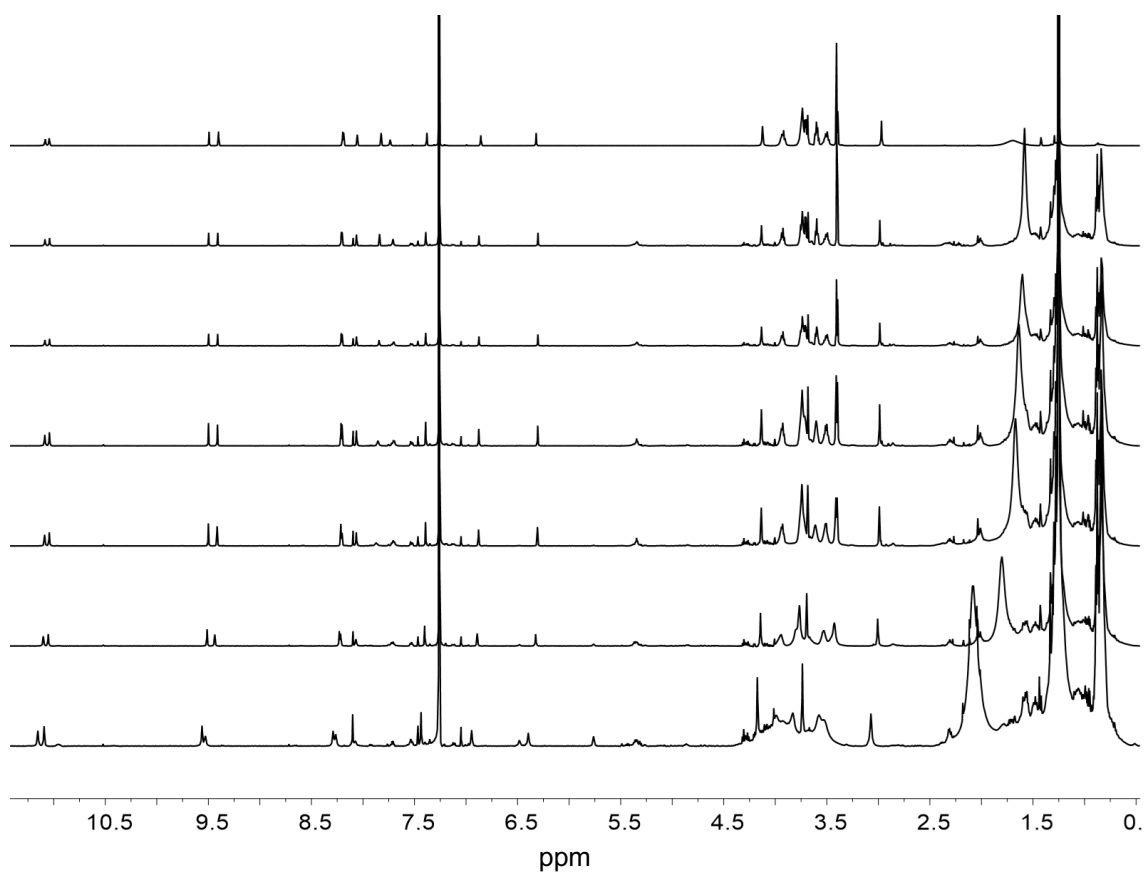
$^1\text{H}$ - $^{15}\text{N}$ -HSQC NMR spectrum of **19** in *d*- $\text{CHCl}_3$  at 500MHz



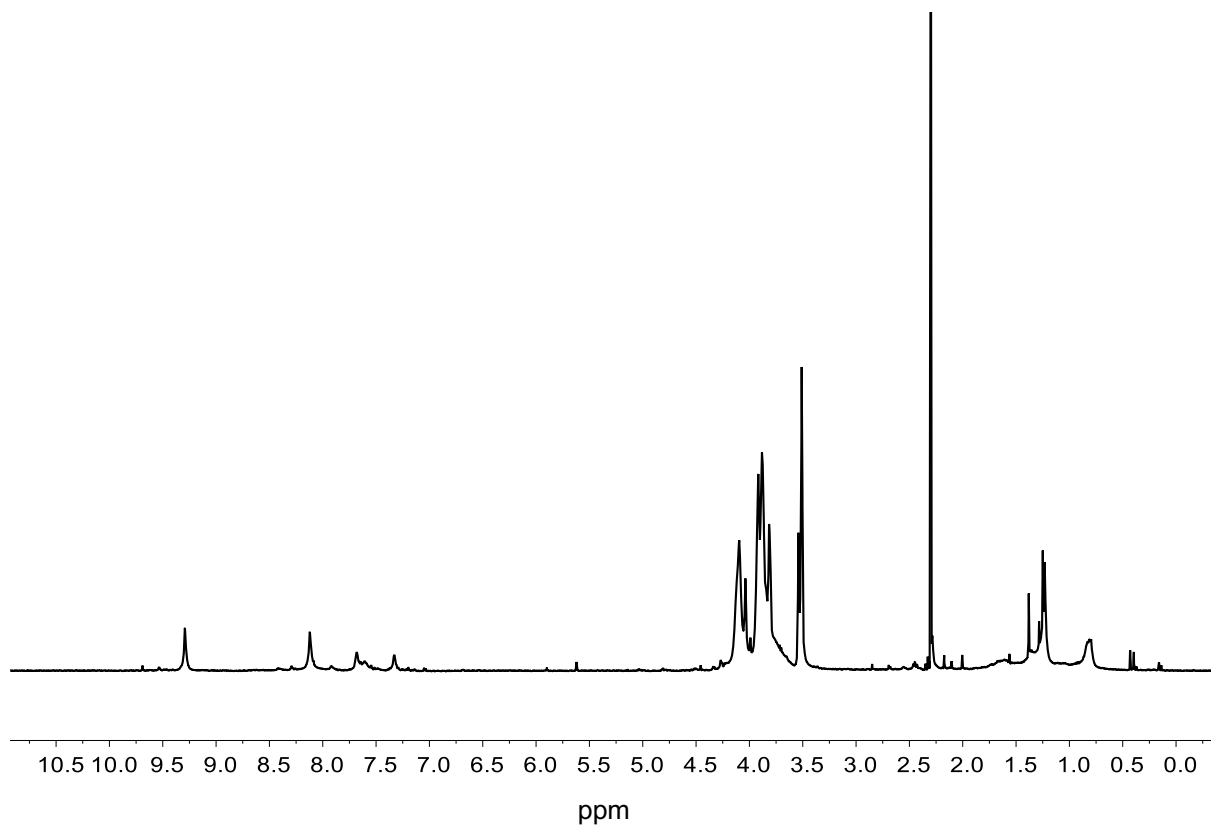
<sup>1</sup>H-NMR spectrum of **19** in *d*-CHCl<sub>3</sub> at 500MHz and 128 scans at (from up to down) 323K, 303K, 283K, 273K, 263K, 243K, 223K, and 213K



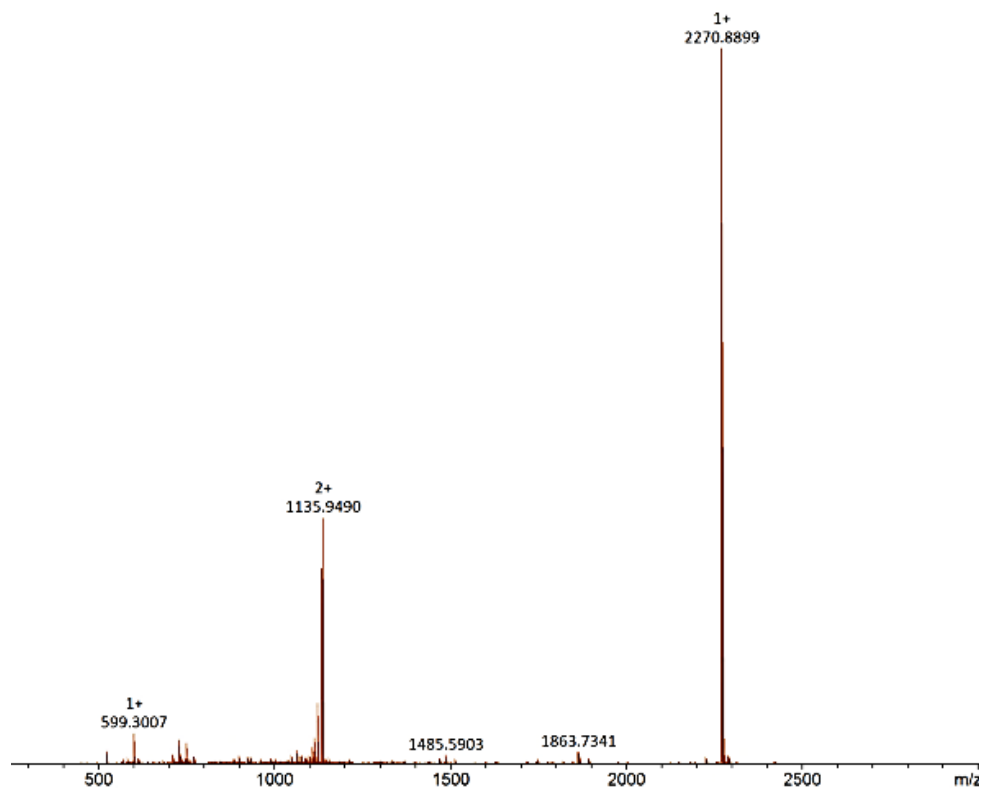
<sup>1</sup>H-NMR spectrum of **19** in *d*-DMF at 500MHz and 128 scans at (from up to down) 353K, 333K, 323K, 303K, 283K, 273K, 263K, and 243K



$^1\text{H-NMR}$  spectrum of **19** in  $d\text{-CHCl}_3$  at 500MHz and 200 scans with  $\text{Eu}(\text{hf})_3$ : (from up to down) **2c** alone, 1:20, 1:10, 1:5, 1:2; 1:1.5 and 1:1



$^1\text{H-}^{15}\text{N-HSQC}$  NMR spectrum of **19** in  $d\text{-TFA}$  at 500MHz



ESI-MS spectrum of **19** in positive mode

## **5. Peptide-Foldamer Macrocyclic Hybrid**

**(to be submitted)**

### **Contributions:**

The project and the designs of the peptide foldamer hybrid was planned in collaboration with Prof. I. Huc. The synthetic routes and conditions for the synthesis of the Q<sup>p</sup> monomer with triethyleneglycol sidechains have been developed and established by me. The synthetic routes and conditions for the synthesis of the peptide as well as the chloroacetyl installation has been developed and established by Dr. Sebastian Dengler. The oligomer synthesis and subsequent analysis was performed by me. 2D-NMR experiments were performed with the help of Dr. Lars Allmendinger.

## 5.1 Introduction

Peptides play essential roles in almost every physiological process. A lot has been done in the field of peptide therapeutics, as they can mimic, replace and interfere with the function of biological peptides.<sup>(1)</sup> To better understand their mechanism of action, it is crucial to study and investigate their dynamical conformational behavior. Due to their short time of plasma half-life and their proneness to enzymatic cleavages, new techniques have been used to enhance their pharmaceutical potential, i.e. cyclization,<sup>(2)</sup> PEGylation<sup>(3)</sup> or usage of peptide hybrids.<sup>(4)</sup> The latter has been described by Huc *et al.* using 8-aminoquinoline 2-carboxylic acid and pyridine-based monomers, showing successfully post translational modification. Moreover, it has been successfully shown that ribosomal translation *in vitro* is compatible with short foldamer segments.<sup>(5,6)</sup> These foldamers have a strong propensity to fold in a specific manner. It has been shown that the foldamer, when covalently bound to the peptide, prevails and directs the conformation of the whole peptide-foldamer hybrid. Specifically, the peptide is getting stretched due to helical folding of the foldamer. In the following, a novel class of peptide-foldamer hybrid macrocycles will be described using 6-aminoquinoline 2-carboxylic acid (see **Figure 1A**, “Q<sup>p</sup>”) to build linear oligomeric foldamers, connected to a sarcosine and glycine rich peptide strand (**Figure 1A, B**). These hybrids are characterized by the fact that the hybrid sequence is in principle too short to enable macrocyclization when the foldamer is in its extended conformation.

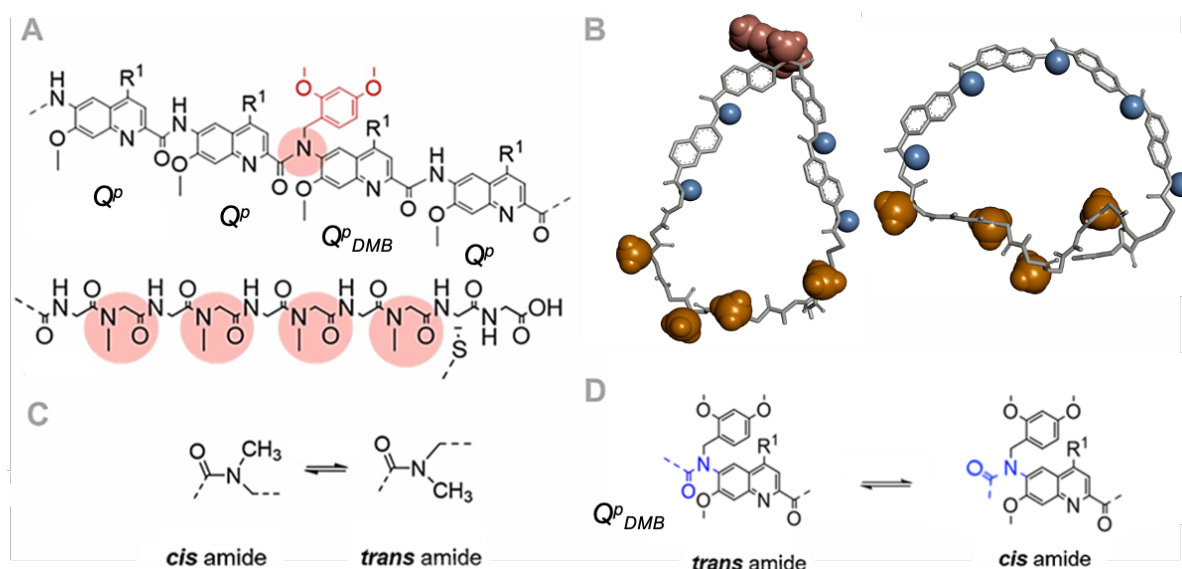


**Figure 1. Peptide foldamer hybrid macrocycles studied in this work and their conformational preferences. (A)** Chemical structure of the DMB-functionalized foldamer based on Q<sup>p</sup> and Q<sup>p</sup><sub>DMB</sub> monomers and the peptide sequence. Pink circles indicate tertiary amides. **(B)** Molecular

model of the DMB protected (left) and the unprotected peptide foldamer hybrid macrocycle (right). DMB (red), Sar-CH<sub>3</sub> (orange) and amide NH (blue; involved in hydrogen bonding) displayed in space filling mode. Hydrogen and sidechain atoms are omitted for clarity. **(C)** *Cis-trans* isomerism of sarcosine amino acid. **(D)** *Cis-trans* isomerism of Q<sup>P</sup><sub>DMB</sub> monomer.

## 5.2. Concept and experimental Design

For the purpose of macrocyclization, a Q<sup>P</sup> tetramer is “kinked” by introducing a DMB functionality so that the distance between the terminal amino function and the carboxylic acid group is reduced. To enable macrocyclization, we used one central 2,4-dimethoxybenzyl (DMB) group to create kinking on the foldamer backbone. To do so, we introduced one DMB-functionalized Q<sup>P</sup> unit into the sequence (**Figure 1A**, “Q<sup>P</sup><sub>DMB</sub>”). After macrocyclization, the tertiary arylamide is deprotected and reversed to the secondary arylamide which largely prefers *trans* conformation (**Figure 1B**, left and right). In this manner, the foldamer segment is reverted to a more linear and rod-like shaped foldamer which may constrain the conformational behavior of the connected peptide (**Figure 1B right**), and thus, the whole hybrid. In this way, we demonstrated a new concept of straightening the oligopeptide through *cis/trans* isomerism (**Figure 1B**, **D**) of the foldamer sequence. The choice of the peptide sequence design was driven *inter alia* by the fact to enable simple spectroscopical analysis thereof as will be explained in the following. In detail, N-methylated amino acids are widely used because of their increased resistance to biodegradation, enhanced hydrophobicity and reduced hydrogen bonding capacity.<sup>(7)</sup> In the present case, we choose sarcosine residues that are N-methylated and show *cis/trans* isomerism in solution (**Figure 1A bottom**, **C**). This isomerism can be analyzed and monitored using <sup>1</sup>H-NMR spectroscopy, and in particular in the range of 1-4.5 ppm, where the sarcosine CH<sub>3</sub> singlet is expected.

Finally, the glycine residues were introduced to create some level of floppiness that allows for the individual conformational dynamic of the two segments (**Figure 1A bottom**). In other words, the glycine residues were introduced for mitigating the conformational influence of the foldamer onto the peptide sequence, in particular in the direct contact zone (i.e. the neighboring residues of the foldamer sequence). Another reason for the choice of glycine residues in the sequence design was to reduce the numbers of sarcosine residues needed to a minimal extent. The conformational



**Figure 2. Macrocycle 1 and 2 based on the Q<sup>p</sup> building block. (A)** Q<sup>p</sup> building block with triethylene glycol sidechains in position 4 and methoxy group on position 7 (hereafter referred to as Q<sup>p</sup> (TREG) building block). The curvature angle is 180°. **(B)** Chemical structure of the protected kinked macrocycle **1**, thioether group of the cysteine residue covalently bound to the arylamide in red. Green circle indicates the *cis* amide. **(C)** Chemical structure of the unprotected macrocycle **2**, N-methylated sarcosine residues in red. Green circle indicates the *trans* amide.

The peptide foldamer hybrid macrocycle precursor based on the Q<sup>p</sup> building block is bearing one DMB group in the center of the foldamer segment – working as a linearity disruptor – forming a tertiary aryl alkyl amide, known to be stable in *cis* conformation which creates a torsion angle of 60° (**Figure 3, top**). The macrocycle precursor comprises one chloroacetamide functionality and the N-terminus of the foldamer segment and one thiol group in close proximity to the C-terminus (**Figure 3, top**).

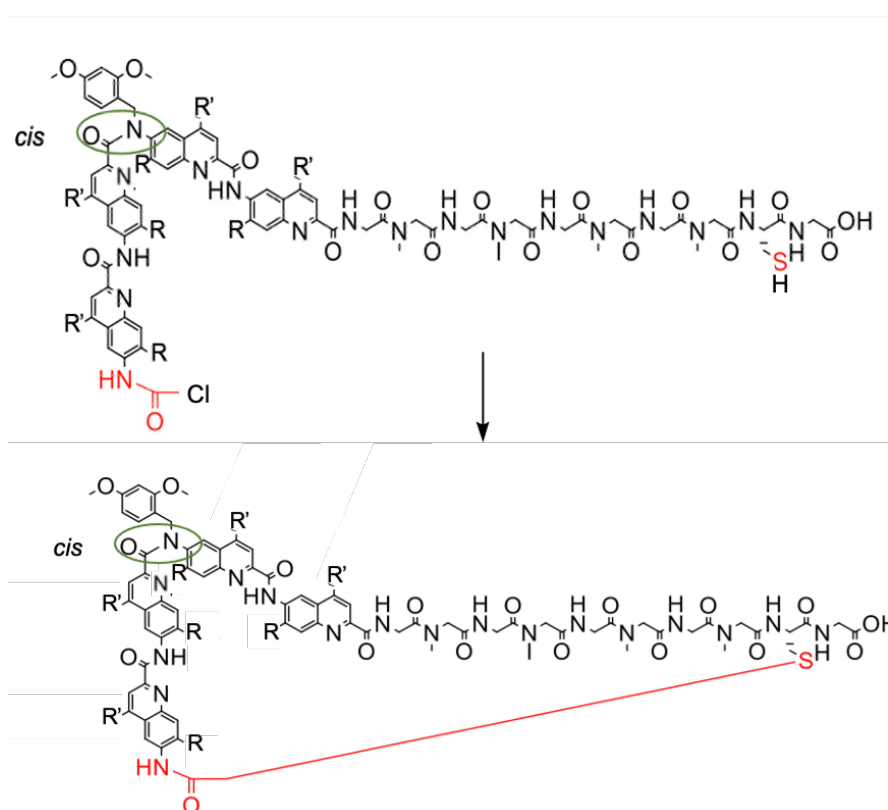


**Figure 3. Precursor of Macrocycle 1.**

After macrocyclization of the latter through spontaneous substitution of the chlorine of the chloroacetamide on the N-terminus through the thiol function on the mandatory cysteine (**Figure 3**), the DMB-functionalized macrocycle is obtained (**Figure 3, bottom and Figure 2B cpd. 1**). Afterwards the DMB group is removed leading to the final stretched macrocycle (**Figure 2C cpd. 2, 1B**).

Through DMB removal in acid media, the secondary aryl amide is produced leading to an all *trans* conformation of the foldamer backbone and lengthening the foldamer

sequence and thus, stretching the connected peptide (**Figure 2C, B**). The N-methylated amino acid sarcosine (Sar) has been chosen due to its aliphatic tertiary amide functionality. Oligo sarcosine peptides are known to undergo *cis trans* isomerism on the NMR timescale, leading to more than one signal for its  $CH_3$  protons. By elongating the oligo sarcosine peptide sequence, assigning the NMR spectra has been shown to be complex and sometimes difficult and thus, characterizing favored isomers is not always easy.<sup>(8)</sup> We used these characteristics to reflect the effect of conformationally switching of the foldamer backbone to study its influence on the sarcosine rich peptide sequence via  $^1H$  NMR spectroscopy. To support solution state data, we also computed 32 molecular models of possible isomers within the peptide sequence, and determined via molecular dynamic simulations favorable conformations of the sarcosine residues in the final macrocycles.

## 5.3 Results and Discussion

### 5.3.1 compound synthesis

The Fmoc- $Q_{DMB}$  with triethylene glycol sidechains in position 4 and methoxy group on position 7 (hereafter referred to as  $Q^P$  (TREG) building block) was synthesized to previously described methods (for more details see experimental part of chapter 4).

The Fmoc-protected  $Q^P$  unit was synthesized according to **Figure 4**. The foldamer as well as the peptide were prepared via solid phase. The former was synthesized on SPFS leading to the Fmoc-NH-terminated foldamer and the latter as a resin bound peptide using commercially available Fmoc-protected amino acids and coupling reagents (**Figure 5**).

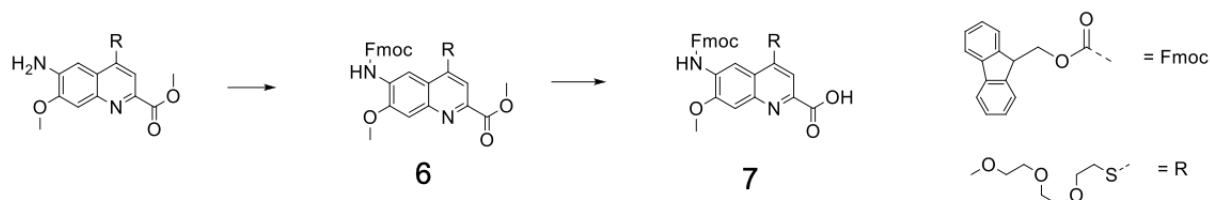


**Figure 4. Synthesis of the  $Q^P$  monomer with methoxy and triethylene groups.**

SASRIN resin was used for peptide synthesis with one mandatory glycine residue on the C-terminus. The fragment condensation reaction of the resin-bound  $NH_2$ -terminated peptide and Fmoc-NH foldamer acid was performed via phosphonium based coupling reagents. After successful condensation of the fragments, Fmoc was

removed. This was followed by N- terminal chloroacetylation and full resin cleavage and cysteine deprotection.<sup>(9)</sup>

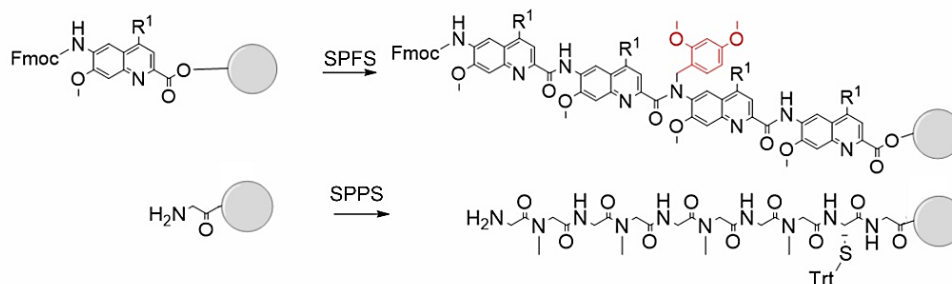


**Figure 5. Solid phase synthesis of the Q<sup>p</sup> tetramer and the oligopeptide.** SPPS indicates solid phase peptide synthesis. SPFS indicates solid phase foldamer synthesis.

The macrocyclization reaction in presence of triethyl amine leads to spontaneous substitution of the chlorine *via* thioether formation of the cysteine thiol with 61% yield (**Figure 3**). The final DMB deprotection in pure TFA at 60°C releases the stretched and strained peptide-foldamer hybrid macrocycle in quantitative yield (**Figure S10**). The kinked (**cpd. 1**) as well as the stretched (**cpd. 2**) hybrid macrocycles were studied further in solution and in computational studies (**Figure 2B, C**).

### 5.3.2 solution state studies of macrocycle **1** and **2**

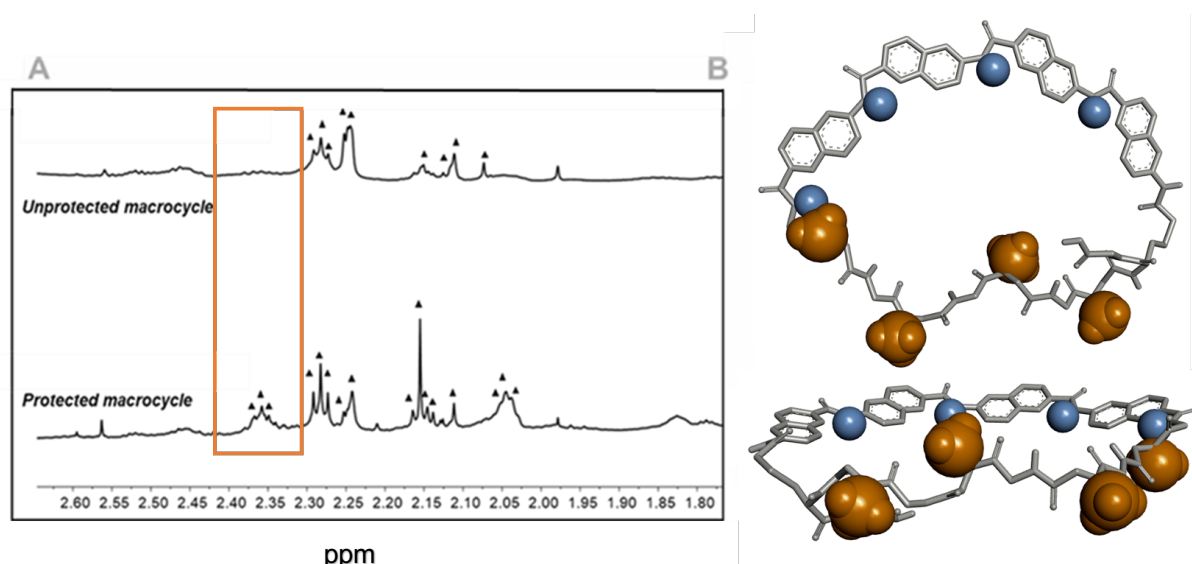


**Figure 6. Macrocycle protected macrocycle 1 and unprotected macrocycle 2 in d<sub>7</sub>-DMF.** (A) Zoom in the sarcosine CH<sub>3</sub> region in d<sub>7</sub>-DMF of the protected **1** and unprotected **2** macrocycle. Orange box indicates Sar-CH<sub>3</sub> region in *cis* conformation with change in signal quantity and (B) MD Model of an unprotected macrocycle **2**, Sar-CH<sub>3</sub> (orange) and amide NH (blue; involved in hydrogen bonding) displayed in space filling mode, hydrogen and sidechain atoms are omitted for clarity.

$^1\text{H}$  NMR measurements of **1** and **2** (**Figure 6B**) in a variety of deuterated solvents (e.g.,  $\text{CDCl}_3$ ,  $d_6$ -DMSO,  $d_5$ -pyridine and  $\text{CD}_2\text{Cl}_2$ ) showed multiple sets of signals in the amide region as well as in the more up field region, where sarcosine  $\text{CH}_3$  signals are expected. The integration of the proton signals in the aromatic region always suggested more than one conformer. In all cases, not all theoretically possible conformations of sarcosine  $\text{CH}_3$  protons are reflected, but an exact assignment was not possible. Interestingly, the  $^1\text{H}$  NMR in  $d_7$ -DMF for **2** was showing a reduced number of resonances in the Sar- $\text{CH}_3$  region compared to the spectrum of **1** (**Figure 6A**). The spectra show that in the unprotected macrocycle **2**, less proton signals are visible whereas more signals are present in comparison to its precursor (**Figure 6A, orange box**). As the  $\text{CH}_3$  signals with *cis* conformation of the sarcosine residue are known to be distinct from the  $\text{CH}_3$  signals in *trans* conformation,<sup>(10, 11)</sup> the change in the spectra for **1** and **2** indicates that less Sar- $\text{CH}_3$  in *cis* conformation are present.

To obtain further structural information about the final macrocycle hybrids, we performed molecular dynamic modulations to better interpret the solution state data.

### 5.3.3 Computational simulation of macrocycle **1** and **2**

Molecular modelling of the protected macrocycle **1** and the final unprotected macrocycle **2** foldamer peptide hybrid macrocycle (**Figure 7A**) was performed using Schrödinger Maestro MacroModel in order to distinguish possible isomers within the protected and unprotected macrocycle and to gain information about the macrocycle conformation in solution. As four sarcosine residues are present in the peptide sequence, which can exist in two different conformations,  $4^2$  isomers of the peptide sequence are possible. Therefore,  $4^2$ , i.e. sixteen models were built for **1** and **2** in which only the conformation for the respective sarcosine residue was changed (**Figure 7C**). In sum, 32 models with different conformations of the peptide sequence were obtained.

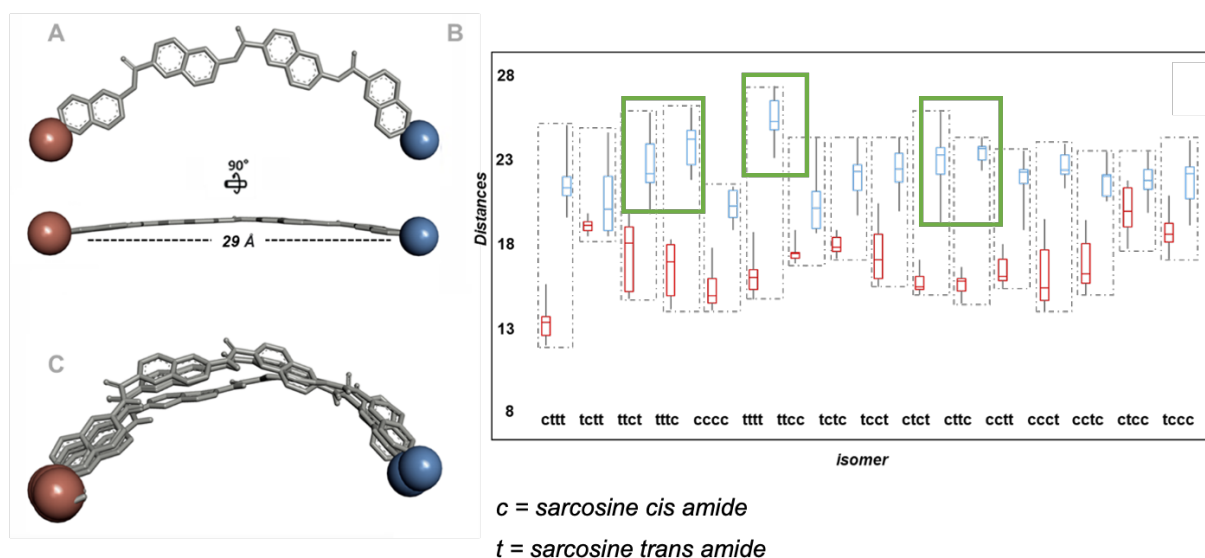


**Figure 7. MD simulation boxplot** (A) Front view of and side view of a tetramer model; dotted line represents distance between N- and C-terminus (29 Å); C-terminus (red) and N-terminus (blue) displayed in space filling mode, hydrogen and sidechain atoms are omitted for clarity. (B) The boxplot for the distance measurements during MD of **1** (red) and **2** (blue). In the isomers, **c** indicates cis conformation of the sarcosine amide, **t** indicates trans conformation of the sarcosine amide, from their N- to C-terminus. Green boxes indicate the most preferred conformational states for **2**. (C) The overlay of four snapshots; carbonyl C (red) and amide NH (blue) displayed in space filling mode. The peptide strand, hydrogen and sidechain atoms are omitted for clarity.

The following models for each **1** and **2** were built from the N-to the C-terminus of the peptide: **cttt** = cis-trans-trans-trans, **tctt** = trans-cis-trans-trans, **ttct** = trans-trans-cis-trans, **ttcc** = trans-trans-trans-cis, **cccc** = cis-cis-cis-cis, **tttt** = trans-trans-trans-trans, **ttcc** = trans-trans-cis-cis, **tctc** = trans-cis-trans-cis, **tcct** = trans-cis-cis-trans, **ctct** = cis-trans-cis-trans, **cttc** = cis-trans-trans-cis, **cctt** = cis-cis-trans-trans, **ccct** = cis-cis-cis-cis, **cctc** = cis-cis-trans-cis, **ctcc** = cis-trans-cis-cis, **tccc** = trans-cis-cis-cis (Figure 7B in the boxplot, horizontal scale).

The models were energy minimized using MMFFs Force field. Molecular dynamic simulation experiments at 300 K were then carried out. During the MD simulations, minimized molecular models (snapshots) were saved. The time steps during the molecular dynamic studies were 1.5 fs with an equilibration time of 1.5 fs. The Molecular models of the macrocycle and its isomers regarding the bending of the foldamer backbone were studied. During the MD simulations, we observed that the isomers comprising the least amount of *cis* configured sarcosine is favored. We further observed, that the *all trans* isomer is the most “floppiest” conformation and, therefore, the possibly most unstrained. In order to measure the strain in the different conformations, the distance between the foldamer N- and C-terminus was measured for each model during the 32 MD simulations (Figure 7A, C red and blue balls).

As a reference value, we choose the distance between the N- and C-terminus in a simple tetramer foldamer sequence, which is not bound to any peptide sequence (**Figure 7A red and blue balls**, 29 Å) and thus is unstrained. We assumed that this distance is the most unstrained and thus, favored distance for the foldamer sequence.

Ten structures were created for each isomer model during these MD simulations (100 ps) and box plotted (**Figure 7B**; red values for **1**, blue for **2**). In a next step, we compared the box plotted distances to 29 Å which is the favored distance in an unstrained Q<sup>p</sup> tetramer foldamer. Consequently, one to five possible isomers for **2** as a favorable conformational state. Beside the *all trans* isomer “**tttt**”, the other populated isomers in solution should be preferably the “**ttct**”, “**tttc**” “**ctct**” and “**cttc**” isomers (**Figure 7B, green boxes**).

## 5.4 Conclusion and Perspectives

It has been shown, that peptide-foldamer hybrid macrocycles can consist of Q<sup>p</sup> derivatives and successfully macrocyclized to peptide foldamer hybrid macrocycles. Further, it has been shown that the foldamer conformation affects the connected peptide conformational state, meaning that the transition of the former- from a tertiary amide (DMB protected) to a secondary amide - influences the conformation of the latter. Although we only get qualitative information, the <sup>1</sup>H NMR spectra suggests that the amount of sarcosine CH<sub>3</sub> resonances between **1** and **2** is reduced in *d*<sub>7</sub>-DMF, presumably in *cis* conformation. Additionally, it has been shown, that MD simulations support the solution state data. The preferred isomers according to our simulation study show that the *all trans* conformation is the most preferred, followed by isomers that have a reduced number of *cis* conformation. Accordingly, the computational studies are a useful tool to determine and rule out unfavorable conformational states and to shrink the number of theoretical possibilities.

In conclusion, the data shows a reduction of sarcosine resonances. The reduction of the signals indicates a diminished amount of presumably *cis* sarcosine CH<sub>3</sub> signals present in the peptide sequence. Moreover, the reduction of the *cis* sarcosine CH<sub>3</sub> signals has been shown in the MD models to correlate with a unstrained foldamer segment. Consequently, this indicates that the foldamer segment interplays with the conformation of the peptide sequence. Accordingly, it can be concluded that the

foldamer segment achieves to overturn the conformation of the whole peptide-foldamer sequence.

These hybrid macrocycles could be further tested to mimic as biological peptides, and interfere in biological processes. As they show higher resistance towards enzymatic degradation, they can be used as a possible design for further therapeutic application.

## 5.5 References

- (1) Fosgerau, K.; Hoffmann T. Peptide therapeutics: current status and future directions. *Drug Disc. Today*. **2015**, *20* (1), 122-8.
- (2) Sim, S.; Kim, Y.; Kim, T.; Lim, S.; Lee, M. Directional assembly of  $\alpha$ -helical peptides induced by cyclization. *J. Am. Chem. Soc.* **2012**, *134* (50), 20270-2.
- (3) Agency EM.; CHMP Safety Working Party's response to the PDCO regarding the use of PEGylated drug products in the paediatric population. *EMA*, UK; 2012.
- (4) Fremaux, J.; Venin, C.; Mauran, L.; Zimmer, R.; Guichard, G.; Goudreau, S. Peptide-oligourea hybrids analogue of GLP-1 with improved action in vivo. *Nat. Comm.* **2019**, *10* (1), 1-9.
- (5) Rogers, J.; Kwon, S.; Dawson, S.; Mandal, P.; Suga, H.; Huc, I. Ribosomal synthesis and folding of peptide-helical aromatic foldamer hybrids. *Nat. Chem.* **2018**, *10* (4), 405-12.
- (6) Tsiamantas, C.; Kwon, S.; Rogers, J.; Douat, C.; Huc, I.; Suga, H. Ribosomal incorporation of aromatic oligoamides as peptide sidechain appendages. *Angew. Chem.* **2020**, *132* (12), 4890-4.
- (7) Sýkora, D.; Záková, L.; Buděšínský, M. High-performance liquid chromatography and nuclear magnetic resonance study of linear tetrapeptides and octapeptides containing N-methylated amino acid residues. *J. Chromatogr. A*. **2007**, *1160* (1-2), 128-36.
- (8) Toniolo, C.; Bonora, G.; Schilling, F.; Bovey, F. Proton magnetic resonance study of linear sarcosine oligomers. *Macromolecules*. **1980**, *13* (6), 1381-5.
- (9) Dengler, S.; Mandal, P.; Allmendinger, L.; Douat, C.; Huc, I. Conformational interplay in hybrid peptide-helical aromatic foldamer macrocycles. *Chem. Sci.* **2021**, *12* (33), 11004-12.
- (10) Matsoukas, J.; Moore, G. Proton magnetic resonance studies of angiotensin II conformation: cis-trans isomerism in sarcosine7-containing analogs. *Arch. Biochem. Biophys.* **1986**, *248* (1), 419-23.
- (11) Kowalewski, V.; de Kowalewski, DG. Proton NMR Spectra of the N, N-Dimethylformamide, N-Methylformamide, and N, N-Dimethylacetamide. *J. Chem. Phys.* **1960**, *32* (4), 1272-3.

## 5.6 Experimental Part

### 5.6.1. General remarks

**Molecular modeling calculations** were performed using the Schrödinger 2017-1 suite. The starting structure was sketched in Maestro 11.5.011 (MMshare Version 4.1.011) and subsequently minimized with MacroModel. The minimizations were carried out with the GB/SA model for none solvent, using the TNCG method and the Merck Molecular Force Field statics (MMFFs) as introduced in the software. To find other possible minima dynamic simulations at different temperatures of the minimized structures were run with MacroModel. The dynamic simulations were carried out with the GB/SA model for none solvent, using the TNCG method and monitoring 10 structures in MMFFs.

The simulations were carried out at 300 K and 400 K for a time of 100 ps. If not stated otherwise all reactions were carried out in ambient atmosphere and magnetically stirred. Glassware was evacuated and dried by heating in a drying cabinet (120 °C) before it was used when working under N<sub>2</sub> atmosphere was necessary. Drying over Na<sub>2</sub>SO<sub>4</sub> implies stirring of the organic solution with an appropriate amount of anhydrous salt for at least 10 min as well as filtration through a filter funnel with cotton wool and rinsing of the filter cake with additional solvent. Oil baths and electric heating plates were used for reaction at elevated temperatures up to 150 °C. For reactions at higher temperatures than 150 °C a lab-heating mantle was used.

Reactions at 0 °C were cooled by an ice bath containing ice and H<sub>2</sub>O. For the transfer of liquids reagents and dry solvents syringes and cannulas were used. Prior to their use they were flooded with N<sub>2</sub>. For flash column chromatography purification silica gel (0.035 – 0.070 mm, 60 Å) by Acros Organics were used. For monitoring reactions and analyzing fractions of column chromatography thin layer chromatography (TLC) on TLC silica gel 60 F254 from Sigma-Aldrich were used. The analytes on TLC plates were visualized by irradiation with UV-light (254 nm or 365 nm). All chemicals were purchased either from SIGMA Aldrich, Fisher Scientific, TCI Europe, VWR International, Honywell, CARLO ERBA Reagents, Grüssing, Acros Organics, Bernd Kraft or Alfa Aesar. Solvents were purchased in analytical grade quality and used without further purification. Anhydrous THF, Toluene and DCM for solution and solid phase synthesis were dispensed from a MBRAUN SPS-800 solvent purification

system. DIPEA and Et<sub>3</sub>N were distilled over CaH<sub>2</sub>. All other reagents were used as purchased from commercial sources without further purification.

### 5.6.2. Peptide synthesis, fragment condensation and chloroacteylation

Peptide synthesis on solid phases and following fragment condensation conditions were described earlier by Dengler *et al.* <sup>(9)</sup>

### 5.6.3. computational data

#### MD measurement data for macrocycle **1**

tffc	24.360	24.870	24.190	25.920	22.510	22.740	24.100	21.760	23.930	22.040	25.120
ttct	25.620	21.510	24.270	21.450	22.070	23.350	24.910	21.680	22.110	19.810	22.400
tctt	24.480	22.680	22.440	19.270	21.470	18.950	18.740	18.520	20.080	18.610	20.190
cttt	24.660	20.780	24.910	20.910	19.960	21.540	22.060	19.590	21.290	20.950	21.830
ttcc	24.160	18.820	21.200	18.690	20.960	20.550	18.700	19.310	20.120	21.960	19.110
tctc	24.180	19.710	22.840	22.570	21.030	22.220	20.230	21.280	22.350	21.390	22.680
tcct	24.220	20.990	23.480	19.940	22.560	21.930	23.730	22.270	22.370	23.100	21.340
cttc	23.900	22.900	23.550	24.200	22.630	23.690	23.650	23.570	22.290	23.200	22.910
ctct	25.680	19.270	22.780	21.610	21.990	22.160	23.730	24.050	23.480	23.180	23.180
cctt	23.430	22.210	18.880	21.790	23.010	22.430	21.270	22.260	21.530	22.270	21.570
tttt	27.160	26.540	24.870	24.250	26.060	25.120	24.810	26.620	25.550	23.000	24.460
cccc	21.060	19.290	21.240	18.860	21.320	20.320	19.690	19.500	21.350	19.980	20.260
tccc	24.020	23.430	22.100	21.290	22.130	22.290	19.150	20.030	22.730	21.770	19.310
ctcc	23.380	21.270	21.170	21.580	22.560	21.820	20.600	21.720	22.120	19.860	22.780
cctc	23.380	20.620	21.020	21.970	22.910	20.570	22.040	22.070	21.100	22.040	20.530
ccct	23.170	22.120	22.130	22.800	23.410	21.280	22.060	21.260	23.820	22.310	23.220

Figure S1 Measured distances of different conformers of **1**

	Q1	Min		Median	Q1		Q3	Median		max	Q3	
tffc	21.76	22.625	0.865	24.1	22.625	1.475	24.615	24.1	0.515	25.92	24.615	1.305
ttct	19.81	21.595	1.785	22.11	21.595	0.515	23.81	22.11	1.7	25.62	23.81	1.81
tctt	18.52	18.845	0.325	20.08	18.845	1.235	21.955	20.08	1.875	24.48	21.955	2.525
cttt	19.59	20.845	1.255	21.29	20.845	0.445	21.945	21.29	0.655	24.91	21.945	2.965
ttcc	18.69	18.965	0.275	20.12	18.965	1.155	21.08	20.12	0.96	24.16	21.08	3.08
tctc	19.71	21.155	1.445	22.22	21.155	1.065	22.625	22.22	0.405	24.18	22.625	1.555
tcct	19.94	21.635	1.695	22.37	21.635	0.735	23.29	22.37	0.92	24.22	23.29	0.93
cttc	22.29	22.905	0.615	23.55	22.905	0.645	23.67	23.55	0.12	24.2	23.67	0.53
ctct	19.27	22.075	2.805	23.18	22.075	1.105	23.605	23.18	0.425	25.68	23.605	2.075
cctt	18.88	21.55	2.67	22.21	21.55	0.66	22.35	22.21	0.14	23.43	22.35	1.08
tttt	23	24.635	1.635	25.12	24.635	0.485	26.3	25.12	1.18	27.16	26.3	0.86
cccc	18.86	19.595	0.735	20.26	19.595	0.665	21.15	20.26	0.89	21.35	21.15	0.2
tccc	19.15	20.66	1.51	22.1	20.66	1.44	22.51	22.1	0.41	24.02	22.51	1.51
ctcc	19.86	21.22	1.36	21.72	21.22	0.5	22.34	21.72	0.62	23.38	22.34	1.04
cctc	20.53	20.82	0.29	21.97	20.82	1.15	22.055	21.97	0.085	23.38	22.055	1.325
ccct	21.26	22.09	0.83	22.31	22.09	0.22	23.195	22.31	0.885	23.82	23.195	0.625

Figure S2 Calculated Q1, Minimum, Maximum Q3 and median for different conformers of **1**

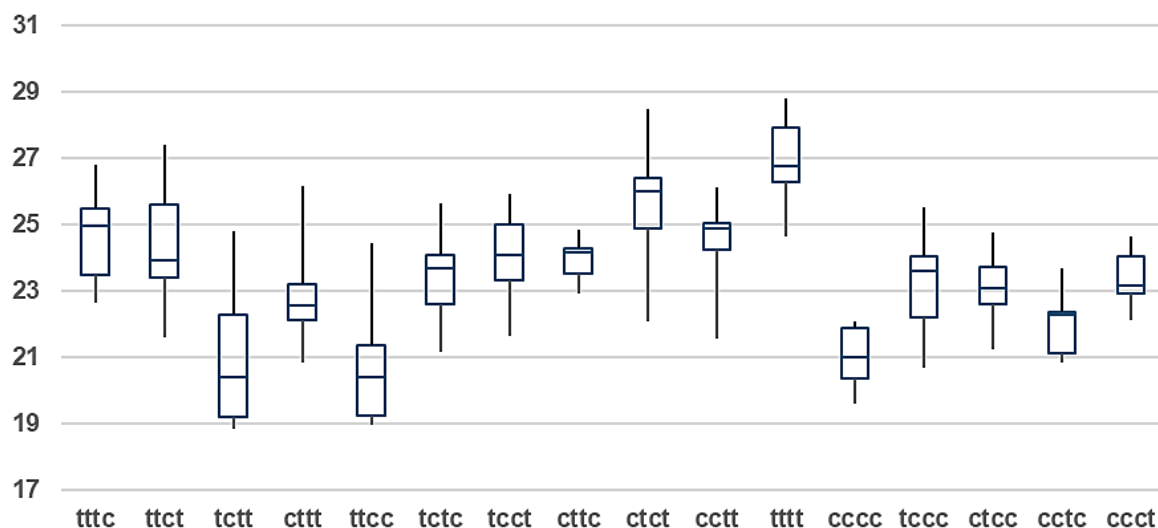


Figure S3 Boxplot for different conformers of **1**

### MD measurement data for macrocycle **2**

cttt	15.19	12.96	13.21	13.14	13.56	13.44	13.01	12.29	11.98	11.67	12.18
tctt	18.17	18.3	18.83	19.13	18.65	18.75	18.8	18.37	19.06	18.96	19.5
ttct	19.46	19.29	18.68	18.57	18.47	17.67	14.52	15.61	15.06	14.46	14.74
tttc	14.65	13.77	13.54	14.29	14.33	16.26	16.74	17.56	17.26	17.25	17.25
cccc	17.43	15.77	15.68	15.67	15.16	14.52	14.18	13.83	14.01	14.67	14.32
tttt	18.2	16.46	15.87	14.75	14.36	14.31	15	15.4	15.58	15.76	16.2
ttcc	18.56	17.89	16.78	16.69	17.1	17.2	17.27	17.25	17.18	17.24	16.63
tctc	18.04	17.4	16.82	17.05	16.94	17.41	18.46	18.13	18.06	17.48	17.48
tcct	16.67	16.43	15.15	15.12	15.1	16.04	16.73	18.05	18.22	19.64	19.91
ctct	15.92	16.86	15.89	15.18	14.86	15.12	14.95	15.19	15.31	16.03	15.84
cttc	14.71	13.94	14.46	15.22	15.14	15.35	14.58	15.33	15.39	15.64	16.05
cctt	16.76	15.04	15.06	15.59	15.76	15.45	15.54	16.74	16.39	16.73	17.62
ccct	18.87	17.77	17.37	16.86	15.29	14.92	14.51	14.24	14.03	14.12	13.55
cctc	18.76	17.52	17.57	17.3	16.82	15.67	15.44	14.94	15.31	14.58	14.43
ctcc	17.81	16.54	16.99	17.78	18.5	18.7	19.87	19.96	20.48	20.37	20.11
tccc	19.86	18.74	18.39	18.17	17.65	17.65	17.75	17.51	16.85	16.37	16.19

Figure S4 Measured distances of different conformers of **2**

	Q1	Min	diff	Median	Q1	diff	Median	Q3	diff	Max	Q3	diff
cttt	12.235	11.67	0.565	13.01	12.235	0.775	13.01	13.325	0.315	15.19	13.325	1.865
tctt	18.51	18.17	0.34	18.8	18.51	0.29	18.8	19.01	0.21	19.5	19.01	0.49
ttct	14.9	14.46	0.44	17.67	14.9	2.77	17.67	18.625	0.955	19.46	18.625	0.835
tttc	14.31	13.54	0.77	16.26	14.31	1.95	16.26	17.25	0.99	17.56	17.25	0.31
cccc	14.25	13.83	0.42	14.67	14.25	0.42	14.67	15.675	1.005	17.43	15.675	1.755
tttt	14.875	14.31	0.565	15.58	14.875	0.705	15.58	16.035	0.455	18.2	16.035	2.165
ttcc	16.94	16.63	0.31	17.2	16.94	0.26	17.2	17.26	0.06	18.56	17.26	1.3
tctc	17.225	16.82	0.405	17.48	17.225	0.255	17.48	18.05	0.57	18.46	18.05	0.41
tcct	15.595	15.1	0.495	16.67	15.595	1.075	16.67	18.135	1.465	19.91	18.135	1.775
ctct	15.15	14.86	0.29	15.31	15.15	0.16	15.31	15.905	0.595	16.86	15.905	0.955
cttc	14.645	13.94	0.705	15.22	14.645	0.575	15.22	15.37	0.15	16.05	15.37	0.68
cctt	15.495	15.04	0.455	15.76	15.495	0.265	15.76	16.735	0.975	17.62	16.735	0.885
ccct	14.18	13.55	0.63	14.92	14.18	0.74	14.92	17.115	2.195	18.87	17.115	1.755
cctc	15.125	14.43	0.695	15.67	15.125	0.545	15.67	17.41	1.74	18.76	17.41	1.35
ctcc	17.795	16.54	1.255	18.7	17.795	0.905	18.7	20.035	1.335	20.48	20.035	0.445
tccc	17.18	16.19	0.99	17.65	17.18	0.47	17.65	18.28	0.63	19.86	18.28	1.58

Figure S5 Calculated Q1, Minimum, Maximum Q3 and median for different conformers of **2**

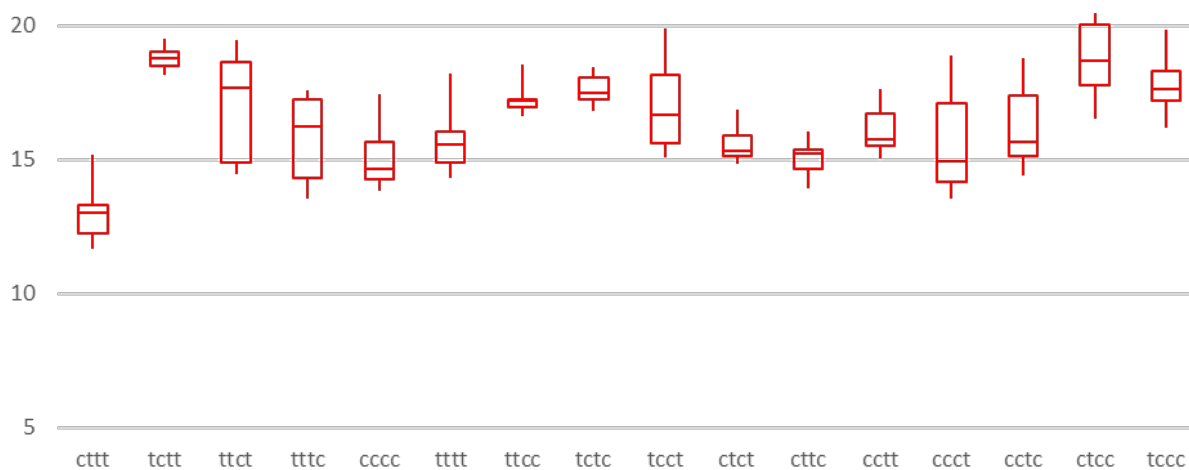


Figure S6 Boxplot for different conformers of **2**

### 5.6.4. Monomer and Oligomer synthesis

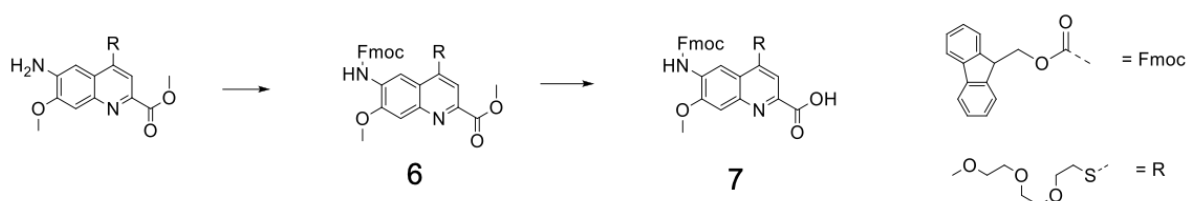


Figure S7 synthetic route of  $Q^p$  (<sup>TREG</sup>) (bottom) building block. For more details on the synthesis of  $Q^{pDMB}$  see experimental of chapter 4.

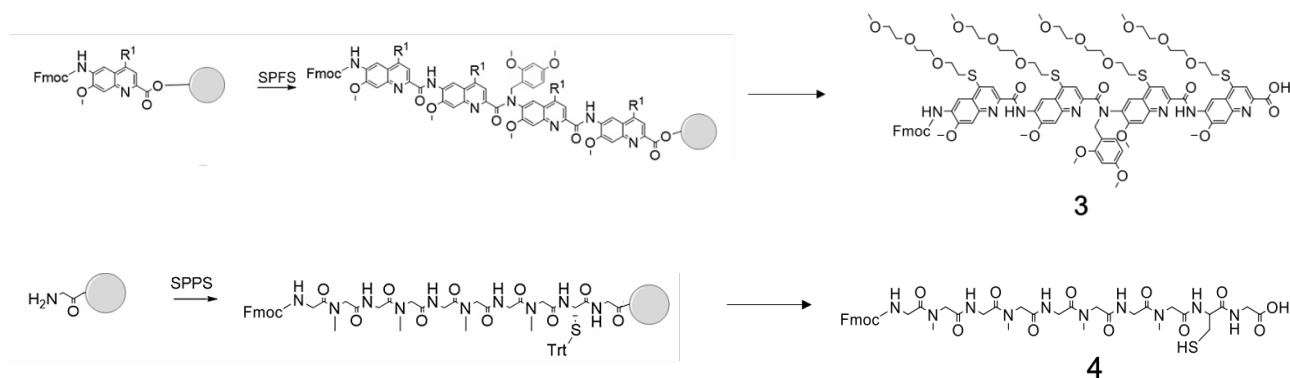


Figure S8 Synthesis of **3** and **4**

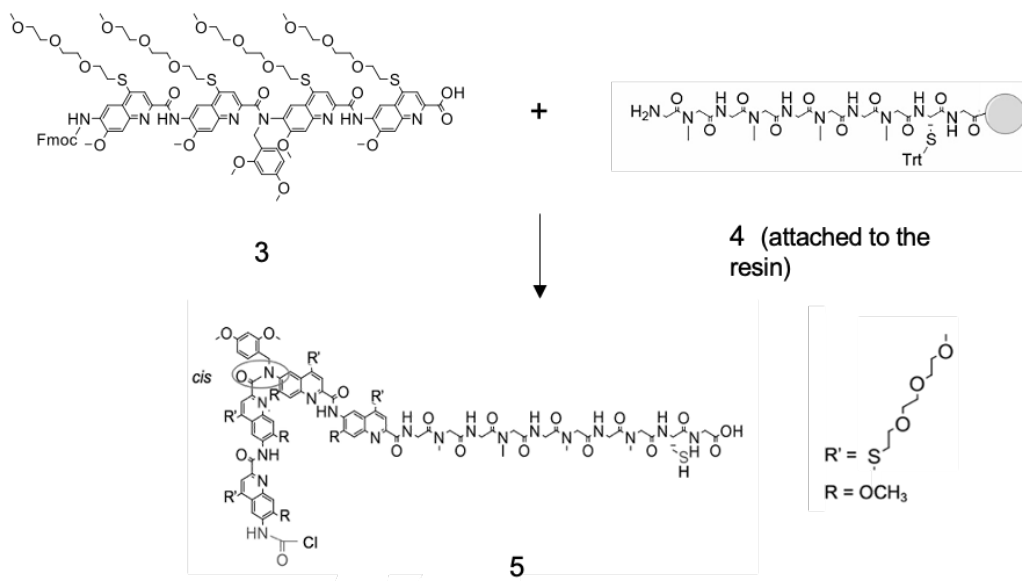


Figure S9 Synthesis of **5** via fragment condensation reaction and chloroacetamide installation.

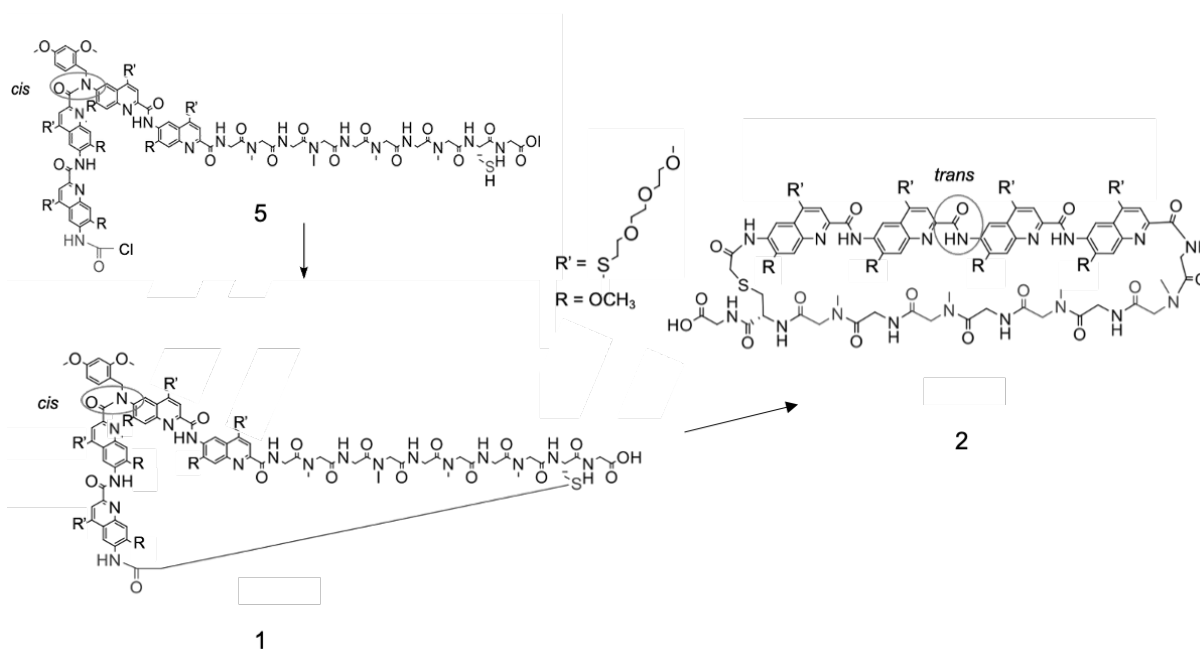
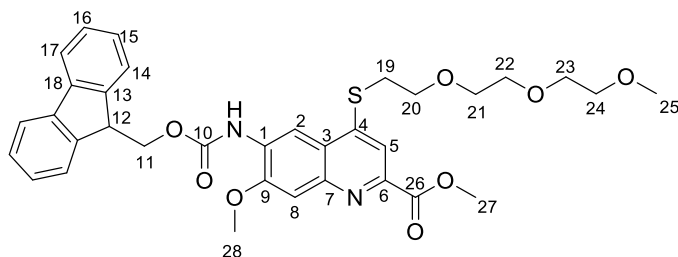


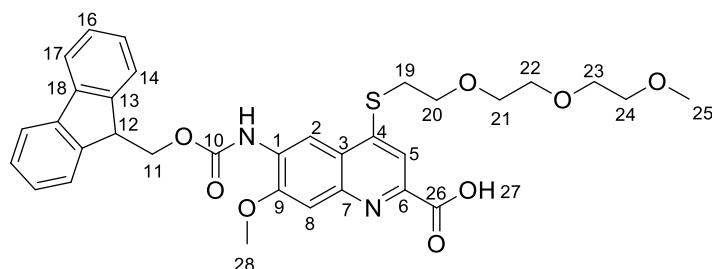
Figure S10 Synthesis of **1** and **2**. Nucleophilic substitution in basic media gives **1** followed by DMB removal in acid media to produce **2**.

## Compound 6



Methyl 6-amino-7-methoxy-4-((2-(2-(2-methoxyethoxy)ethoxy)ethyl)thio)quinoline-2-carboxylate (2.90 g, 7.07 mmol, 1.00 eq) was solved in dioxane (100 mL). NaHCO<sub>3</sub> (2.36 g, 28.2 mmol, 4.00 eq) in water (20.0 mL) was added. FmocCl (5.40 g, 21.2 mmol, 3.00 eq) in dioxane (50.0 mL) was added dropwise. The mixture was stirred for 2 d. Water (150 mL) was added and the mixture was extracted with DCM (3×100 mL) and the organic layer was dried over Na<sub>2</sub>SO<sub>4</sub>. The solvent was removed. The residue was purified by column chromatography to remove remaining FmocCl (SiO<sub>2</sub>, DCM to DCM/methanol 3%). The obtained solid was solved in DCM and was crystalized with methanol. A light red solid was obtained (2.6 g, 59%). <sup>1</sup>H NMR (500 MHz, DMSO-*d*<sub>6</sub>, ppm):  $\delta$  = 7.88 (dt,  $J$  = 7.5, 1.0 Hz, 2H, H-14 or H-17), 7.84 (dt,  $J$  = 7.5, 1.0 Hz, 2H, H-14 or H-17), 7.75 (s, 1H, H-5), 7.41 (td,  $J$  = 7.4, 1.2 Hz, 2H, H-15 or H-16), 7.36 – 7.33 (m, 3H, H-8 and H-15 or H-16), 7.07 (s, 1H, H-2), 5.99 (s, 1H, N-H), 3.97 (s, 3H, H-28), 3.89 (s, 3H, H-27), 3.75 (t,  $J$  = 6.3 Hz, 2H, H-24), 3.59 – 3.56 (m, 2H), 3.54 – 3.49 (m, 5H), 3.41 – 3.39 (m, 2H), 3.37 (t,  $J$  = 6.3 Hz, 3H, H-23), 3.21 (s, 3H, H-25). <sup>13</sup>C NMR (126 MHz, DMSO, ppm):  $\delta$  = 165.83 (C-26), 151.33 (C-10), 142.56, 141.59, 141.52, 141.25, 141.03, 139.41, 137.42, 128.92, 127.29, 124.14 (C-1), 121.39, 120.03, 114.19 (C-5), 109.78, 107.63 (C-8), 99.98 (C-2), 71.24 (C-23), 69.78, 69.74, 69.60, 68.37 (C-24), 58.02 (C-25), 55.85 (C-28), 52.14 (C-27), 30.23. ESI-MS (C<sub>42</sub>H<sub>44</sub>N<sub>2</sub>O<sub>10</sub>S): calc.: 632.2192, found: [M+1H]<sup>+</sup>: 633.1878.

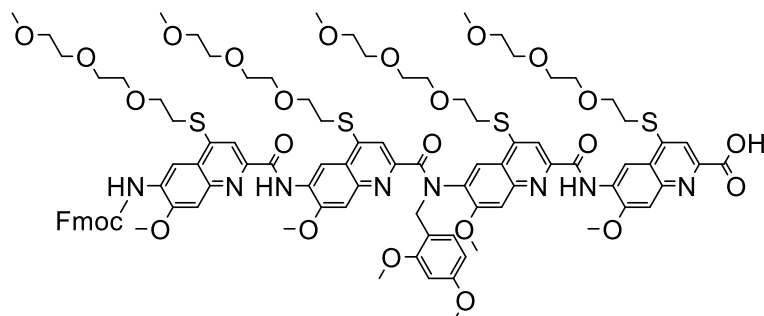
## Compound 7



Methyl-6-(((9H-fluoren-9-yl)methoxy)carbonyl)amino)-7-methoxy-4-((2-(2-(2-methoxy ethoxy)ethoxy)ethyl)thio)quinoline-2-carboxylate (1.00 g, 1,58 mmol, 1.00 eq) was solved in degassed ethyl acetate (50 mL). LiI (630 mg, 4.71 mmol, 3.00 eq) was added and the mixture was refluxed for 2 d by exclusion of light. The reaction mixture was quenched with Na<sub>2</sub>S<sub>2</sub>O<sub>3</sub> (50 mL, 5%) solution. Then it was extracted with DCM (3× 50 mL) and washed with citric acid (3× 50 mL). The organic layer was dried over Na<sub>2</sub>SO<sub>4</sub> and the solvent was removed. A yellow solid was obtained (977 mg, 100%). <sup>1</sup>H NMR (500 MHz, DMSO-*d*<sub>6</sub>, ppm): δ=9.28 (s, 1H, N-H), 8.66 (s, 1H, H-2), 7.92 (d, *J*=7.5 Hz, 2H, H-14), 7.85 (s, 1H, H-5), 7.83 (d, *J*=7.5 Hz, 2H, H-16), 7.57 (s, 1H, H-8), 7.44 (t, *J*=7.4 Hz, 2H, H-16), 7.36 (td, *J*=7.5, 1.2 Hz, 2H, H-15), 4.48 (d, *J*=7.2 Hz, 2H, H-11), 4.35 (t, *J*=7.1 Hz, 1H, H-12), 4.05 (s, 3H, H-28), 3.77 (t, *J*=6.2 Hz, 2H, H-20), 3.57 (dd, *J*=6.0, 3.5 Hz, 2H), 3.51 (dd, *J*=5.9, 3.5 Hz, 2H), 3.48 (dd, *J*=5.8, 3.7 Hz, 2H), 3.43 (t, *J*=6.2 Hz, 2H, H-19), 3.38 (dd, *J*=5.8, 3.7 Hz, 2H), 3.18 (s, 3H, H-25). <sup>13</sup>C NMR (126 MHz, DMSO, ppm): δ = 166.35 (C-26), 153.63 (C-10), 152.25 (C-9), 146.80 (C-4), 146.36 (C-7), 143.71 (C-13), 140.75 (C-18), 130.32 (C-1), 127.78 (C-15), 127.18 (C-6), 125.44 (C-17), 121.77 (C-6), 120.18 (C-14), 113.98 (C-5), 110.95 (C-2), 108.18 (C-8), 103.07 (C-3), 71.22, 69.77, 69.73, 69.59, 68.16 (C-20), 66.61 (C-12), 57.98 (C-25), 56.32 (C-28), 46.49 (C-12), 30.35 (C-19). ESI-MS (C<sub>42</sub>H<sub>44</sub>N<sub>2</sub>O<sub>10</sub>S): calc.: 618.2036, found: [M+1H]<sup>+</sup>: 619.2109.

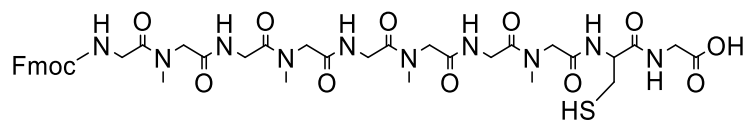
### 5.5.5. Oligomer synthesis

#### Oligomer 3



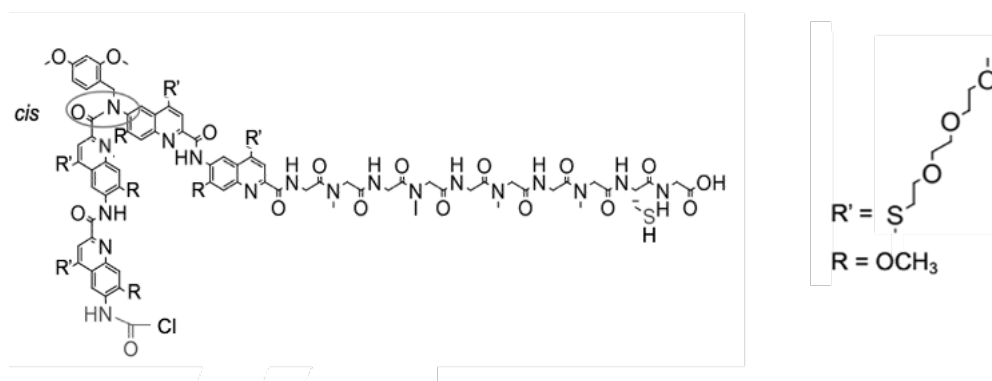
Oligomer **3** was obtained using solid phase synthesis conditions described earlier on SASRIN resin (0.04 mmole) releasing 120mg of crude yellow oil. The oligomer 1a was obtained by purification on semi preparative reversed phase HPLC using C<sub>18</sub> phase column and 10-100% water and acetonitrile with 0.1 % TFA as additive. The collected fraction was lyophilized to give 52 mg of pure oligomer **3**. HRMS (ESI) m/z: calcd. for C<sub>96</sub>H<sub>110</sub>N<sub>8</sub>O<sub>25</sub>S<sub>4</sub> [M+H]<sup>+</sup>: 1904.646; found 1904.213. <sup>1</sup>H NMR (500 MHz, *d*-CDCl<sub>3</sub>): δ 10.97(s, 1H, N-H), 9.45 (s, 1H), 9.24 (s, 1H), 8.72 (s, 1H), 8.70 (s, 1H), 8.04 (s, 1H), 7.96(s, 1H, N-H), 7.80(s, 1H, N-H), 7.78 (s, 1H), 7.68 (s, 1H), 7.65 (s, 1H), 7.63 (s, 1H), 7.55 (s, 1H), 7.53, 7.50, 7.42, 7.41, 7.35, 7.34, 7.17, 7.03, 6.47, 6.46, 6.26, 5.47, 5.44, 5.30, 5.02, 4.99, 4.61, 4.58, 4.57, 4.34, 4.22, 4.19, 4.15, 4.09, 3.94, 3.88, 3.82, 3.76, 3.69, 3.68, 3.68, 3.67, 3.65, 3.58, 3.57, 3.56, 3.55, 3.54, 3.49, 3.46, 3.38, 3.36, 3.35, 3.33, 3.27. <sup>13</sup>C NMR (126 MHz, *d*-CDCl<sub>3</sub>): δ 143.58, 141.32, 137.59, 128.62, 128.37, 127.87, 127.19, 126.82, 125.01, 120.33, 120.09, 115.44, 112.34, 71.83, 70.67, 70.43, 58.93, 54.92, 47.02, 43.00, 30.06, 29.71, 29.37, 18.57, 17.28, 12.26.

#### Oligomer 4



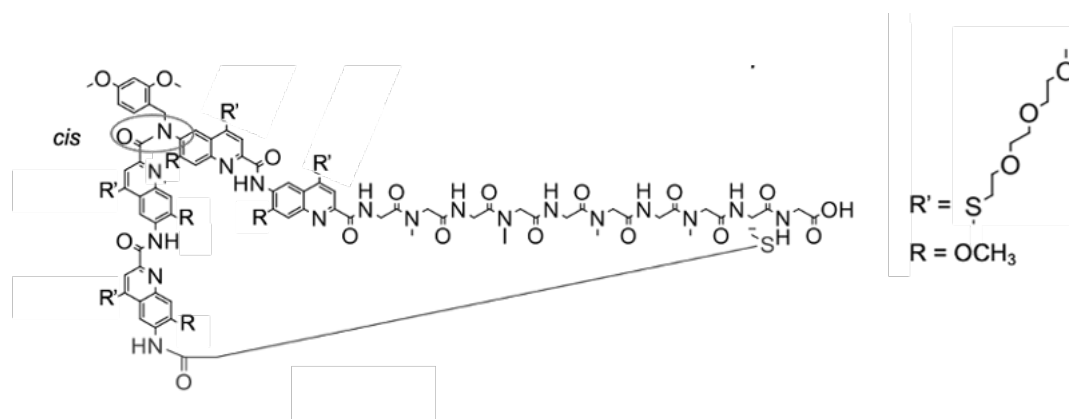
Peptide **4** was built by relying on the CEM Liberty Blue microwave automated peptide synthesizer for the peptide segment and on the Liberty Bio for the stepwise assembly of the foldamer part on a 50 μmol scale. The peptide bound on the resin was directly used for the fragment condensation reaction. HRMS (ESI<sup>+</sup>) m/z calcd. for C<sub>40</sub>H<sub>52</sub>N<sub>10</sub>O<sub>13</sub>S [M+H]<sup>+</sup>: 913.9760; found 913.4328.

## Oligomer 5



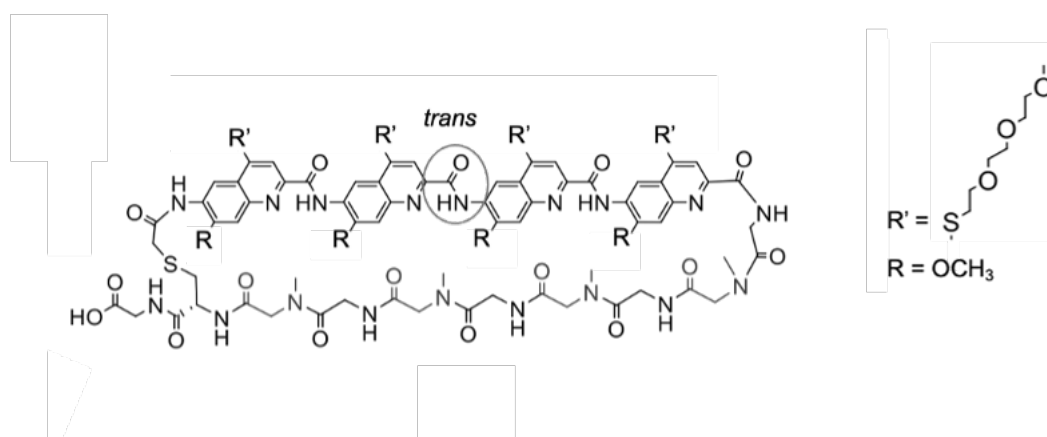
Peptide 4 (trityl protected, i.e. Fmoc -Gly-Sar-Gly- Sar-Gly- Sar- Gly- Sar-Gly - Cys(Trt)-Gly) loaded on a SASRIN resin (0.32 mmol/g) using CEM Liberty Blue microwave automated peptide synthesizer on a 50  $\mu\text{mol}$  scale, was Fmoc deprotected and 3 was coupled by fragment condensation on an 20  $\mu\text{mol}$  scale.<sup>(9)</sup> After final chloroacetylation and HFIP cleavage, crude 2a (8 mg, 61%) was purified on reversed phase semi-preparative HPLC to obtain pure peptide-foldamer hybrid **5** (20 mg 43%). HRMS (ESI<sup>+</sup>)  $m/z$  calcd. for  $\text{C}_{108}\text{H}_{138}\text{ClN}_{18}\text{O}_{34}\text{S}_5$   $[\text{M}+\text{H}]^+$ : 2428.1394; found 2428.3422.

## Oligomer 1



Oligomer **5** (1 eq. 50  $\mu\text{mol}$ ) was dissolved in 10 mL of a water/ $\text{CH}_3\text{CN}$  50:50 (v/v) solvent mixture and TEA (352  $\mu\text{L}$ ) was added. After 10 min at r.t. without agitation, the solvents were evaporated by freeze drying and the crude macrocycle was purified by using semi-preparative RP-HPLC with a gradient 10% to 100% solvent A/B over 25 minutes at 50  $^\circ\text{C}$  to give **1** as a light-yellow solid (35.0 mg, 61%). HRMS (ESI<sup>+</sup>)  $m/z$  calcd. for  $\text{C}_{108}\text{H}_{138}\text{N}_{18}\text{O}_{34}\text{S}_5$   $[\text{M}+\text{H}]^+$ : 2392.6868; found 2392.4235.

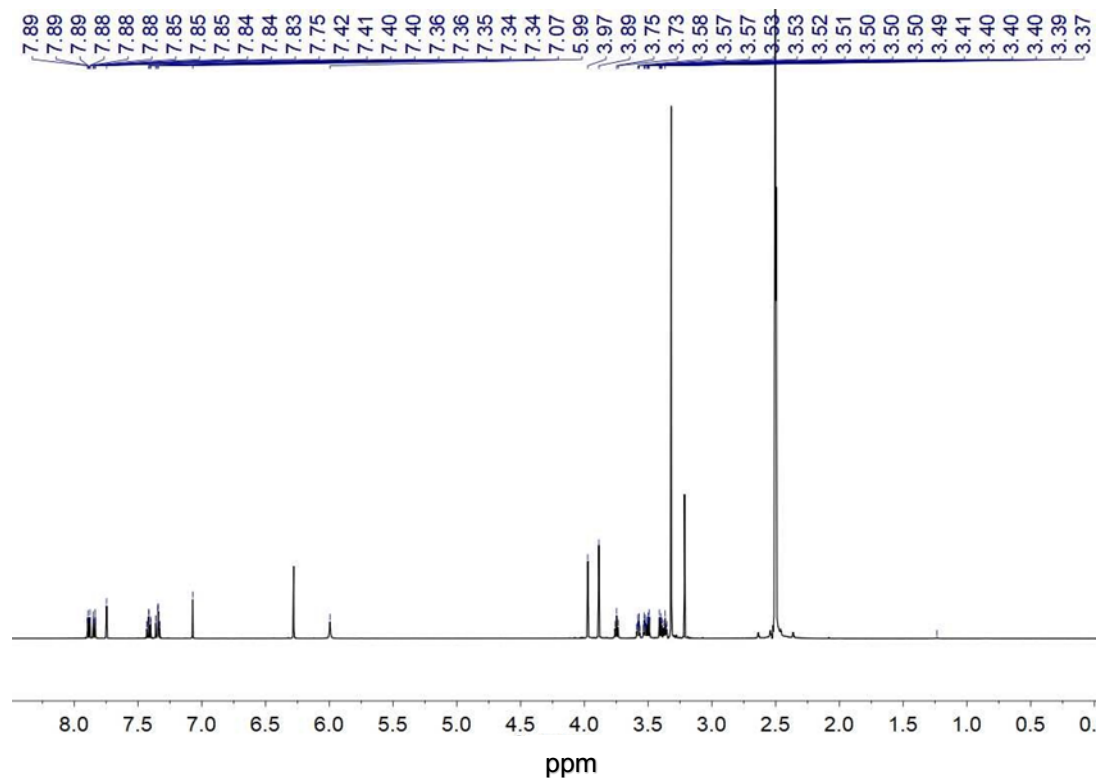
## Oligomer 2



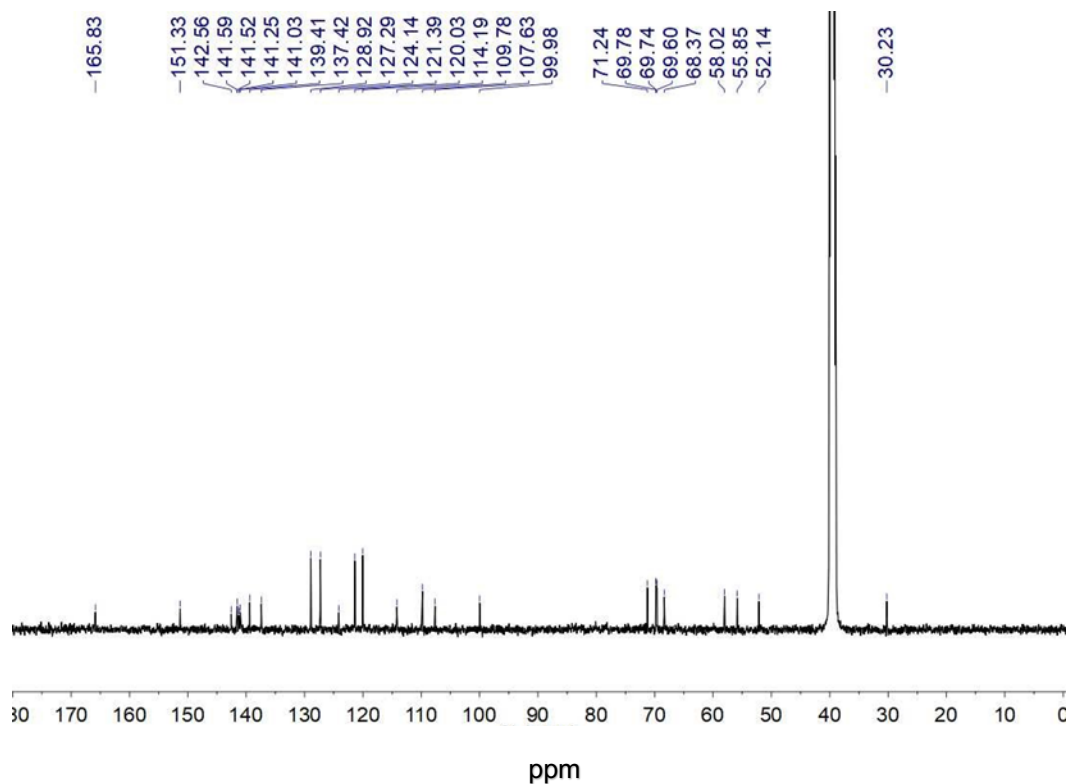
Macrocycle **1** (1 eq. 40  $\mu$ mole) was dissolved in pure TFA (2ml) under argon atmosphere and left stirring at 60 °C for 32 h. The reaction was monitored using Liquid chromatography on C<sub>18</sub> phase column and acetonitrile and water as eluent and coupled mass spectrometry with Electro Spray Ionization in positive mode. After no more starting material was detected, the reaction mixture was quenched with sat. aqueous NaHCO<sub>3</sub> solution and the organic layer was collected, and further washed with more sat. aqueous NaHCO<sub>3</sub> solution. The macrocycle 3 was extracted with more CHCl<sub>3</sub> (2x5 ml), the organic layers combined and dried over NaSO<sub>4</sub>, filtered and concentrated under high pressure. The resulting yellow oil was purified on semi-preparative reversed phase chromatography with 10-100% water/acetonitrile with 0.1% TFA as additive. The collected fractions were lyophilized to give 25 mg of pure oligomer **2**. HRMS (ESI<sup>+</sup>) m/z calcd. for C<sub>99</sub>H<sub>128</sub>N<sub>18</sub>O<sub>33</sub>S<sub>5</sub> [2M+H]<sup>+</sup>: 1123.2503; found 1123,4215.

### 5.5.6. NMR and HPLC data of new compounds

#### Compound 1 Methyl 6-(((9H-fluoren-9-yl)methoxy)carbonyl)amino)-7-methoxy-4-((2-(2-(2-methoxyethoxy)ethoxy)ethyl)thio)quinoline-2-carboxylate)

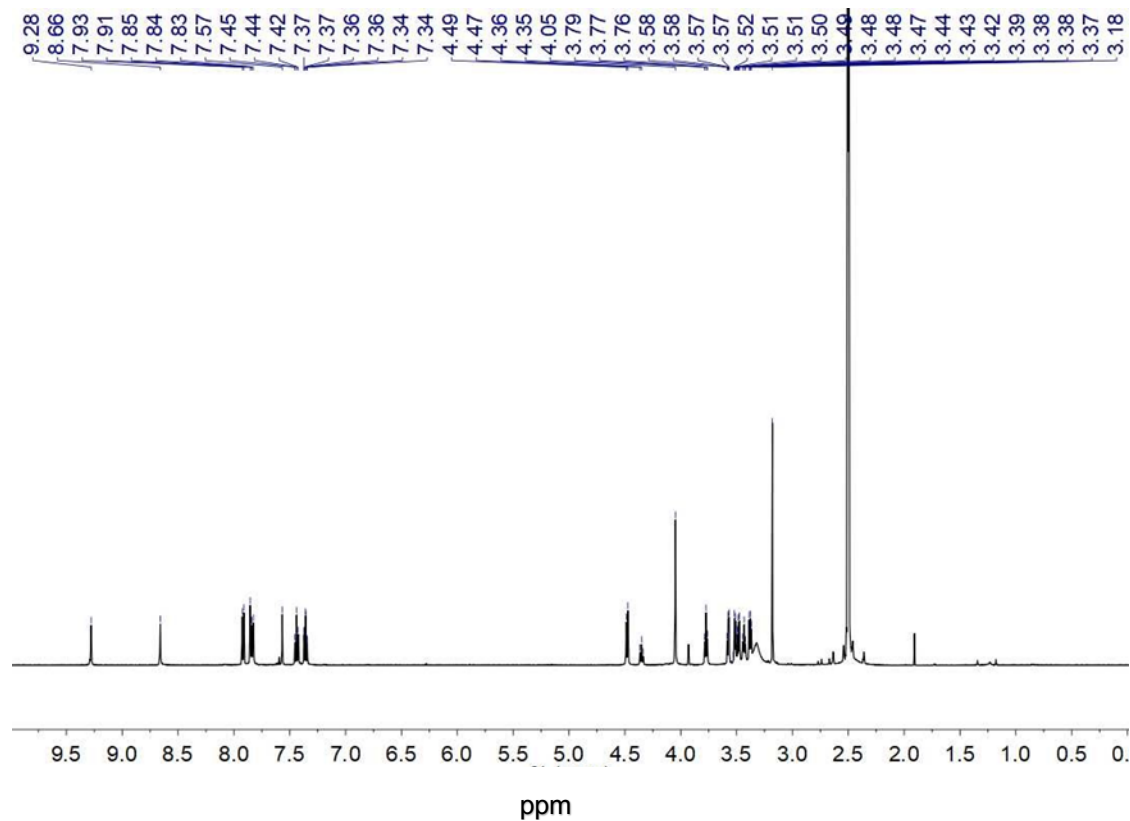


<sup>1</sup>H NMR spectrum of **6** in *d*-DMSO at 500 MHz and 128 scans

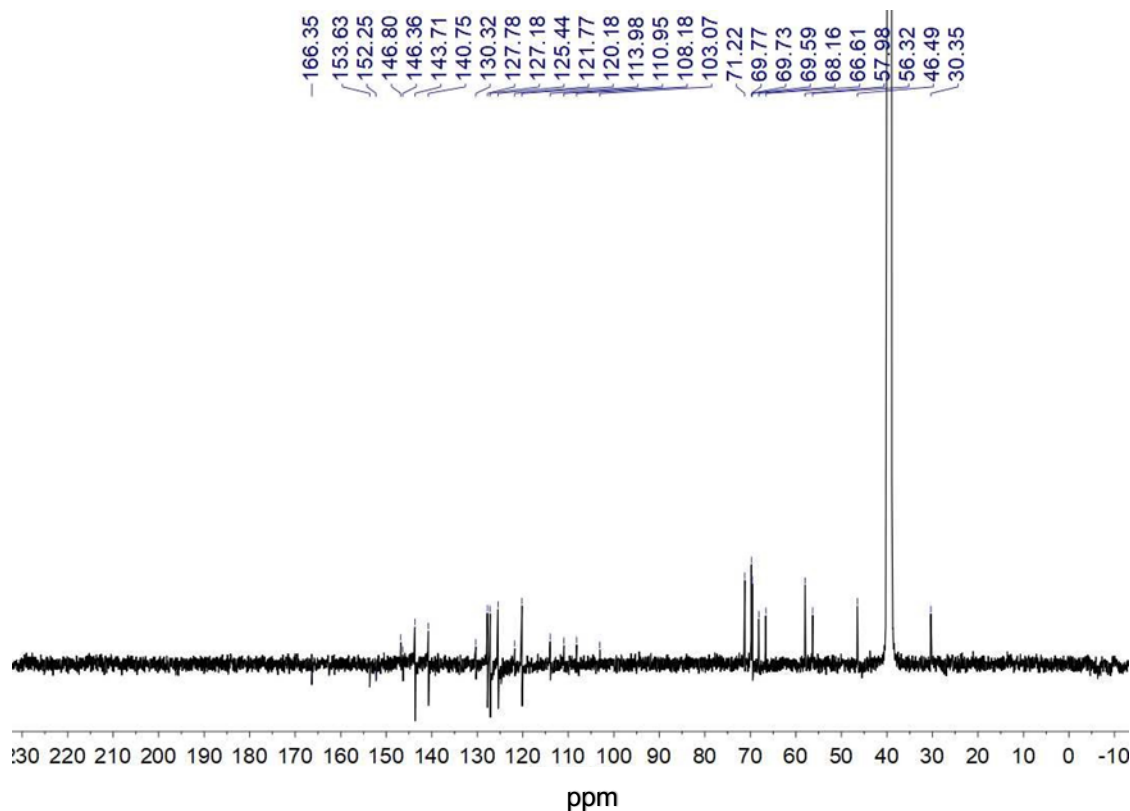


<sup>13</sup>C NMR spectrum of **6** in *d*-DMSO at 126 MHz

**Compound 2 6-(((9H-fluoren-9-yl)methoxy)carbonyl)amino)-7-methoxy-4-((2-(2-(2-methoxyethoxy)ethoxy)ethyl)thio)quinoline-2-carboxylic acid**

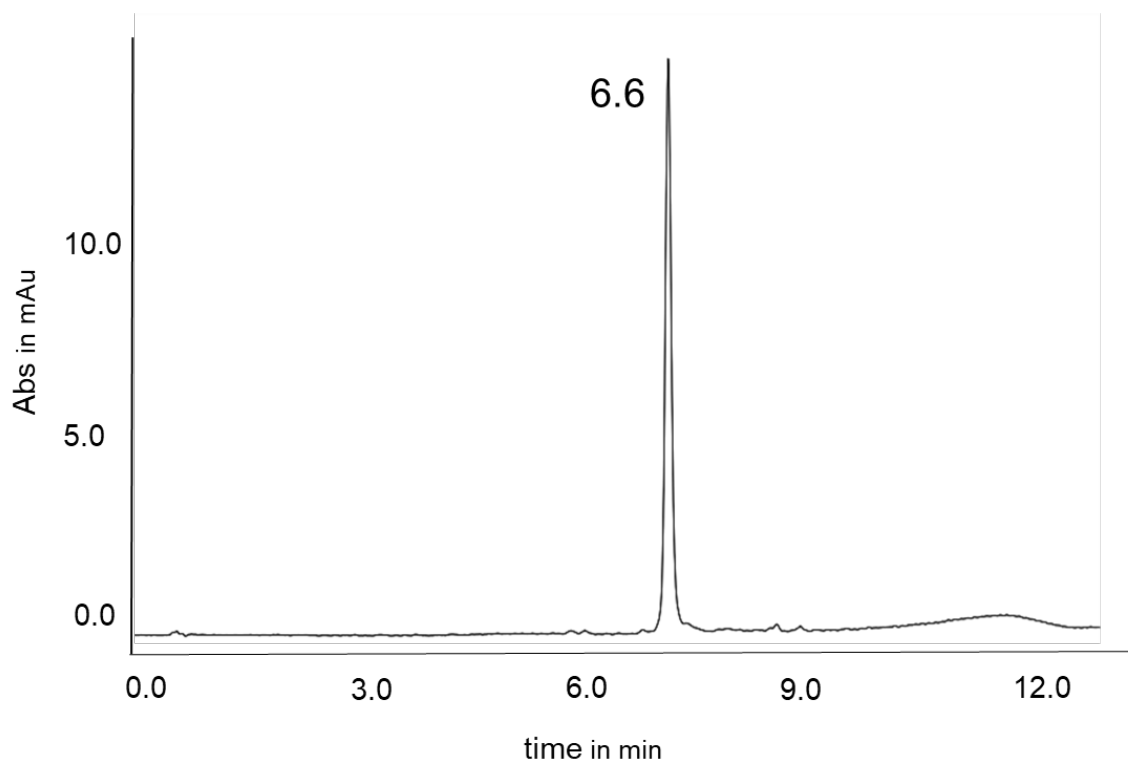


$^1\text{H}$  NMR spectrum of **7** in *d*-DMSO at 500MHz and 128 scans



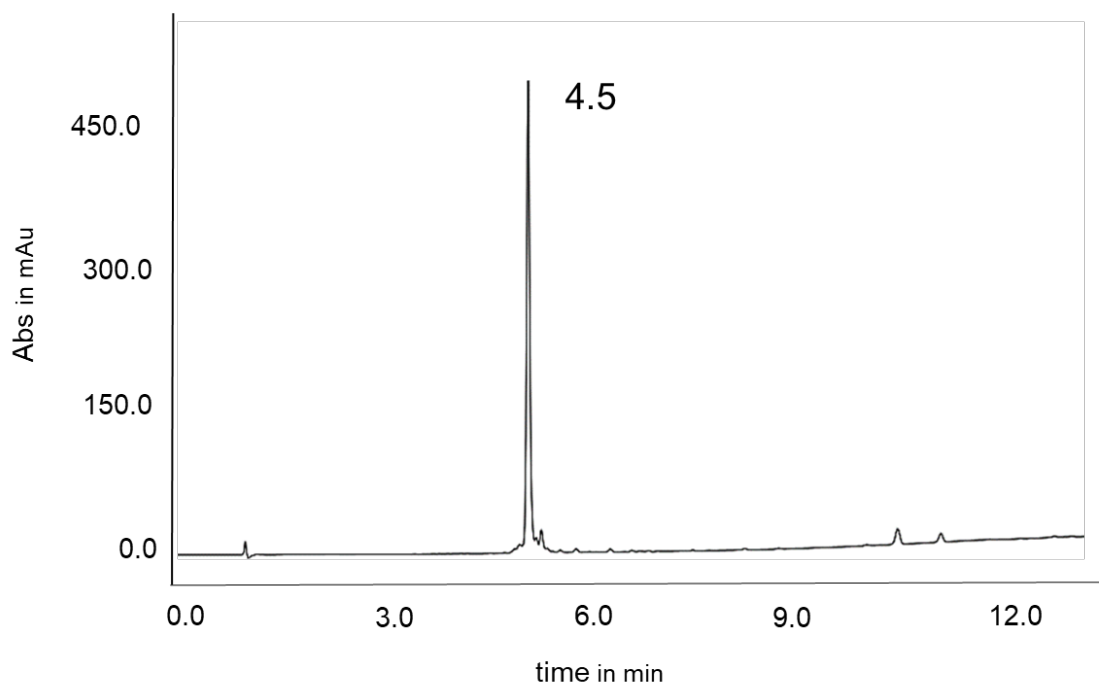
$^{13}\text{C}$  NMR spectrum of **7** in *d*-DMSO at 126MHz



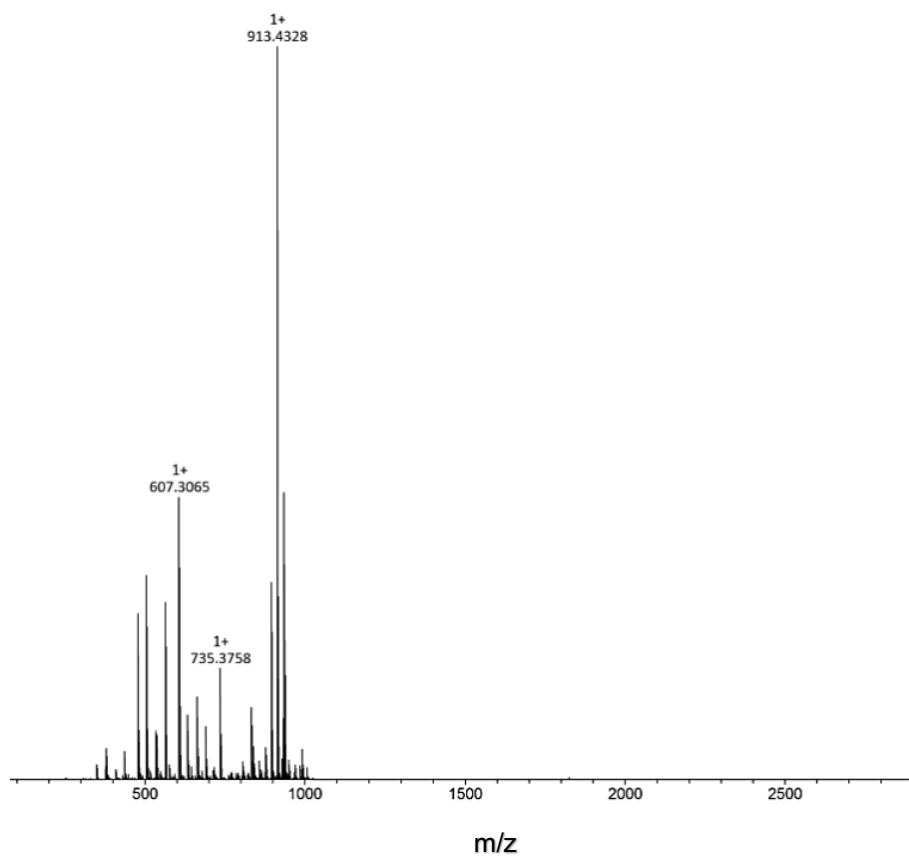


RP HPLC chromatogram of **3** on C<sub>18</sub> and 10-100% A/B (water/acetonitrile) +0.1% TFA in 12 min at 300nm

#### **Oligomer 4**

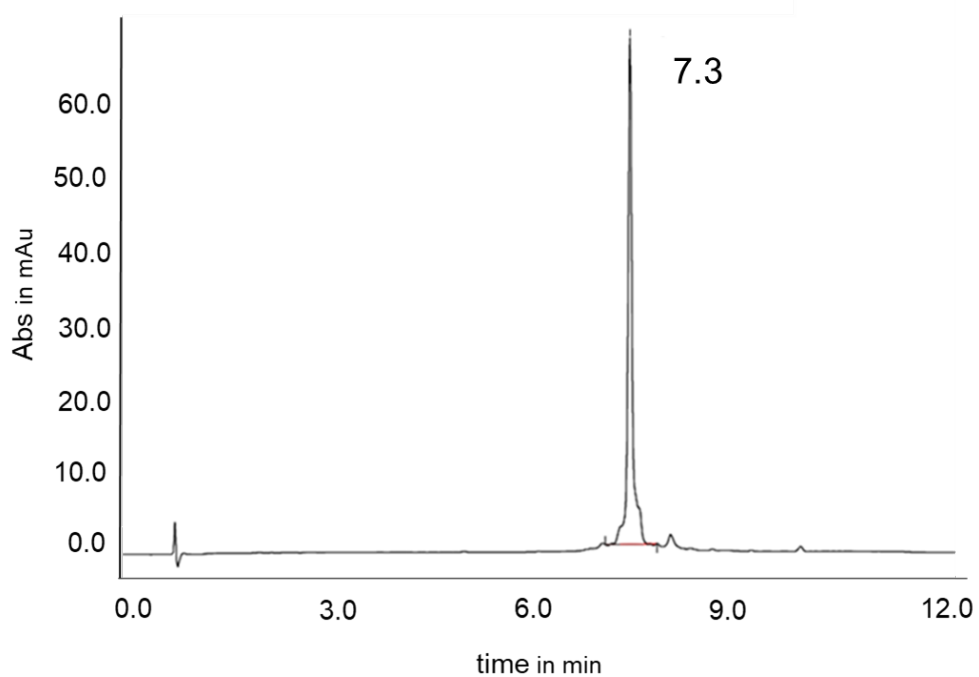


RP HPLC chromatogram of **4** on C<sub>18</sub> and 10-100% A/B (water/acetonitrile) +0.1% TFA in 12 min at 300nm

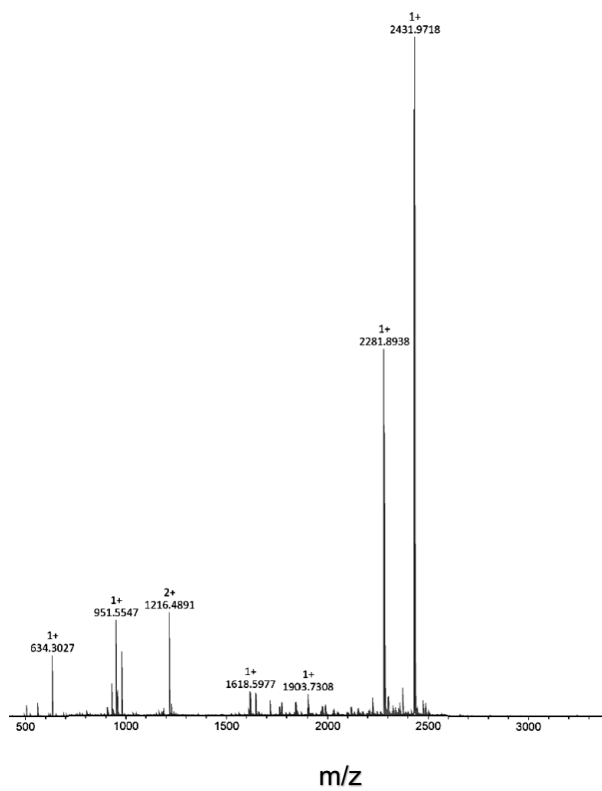


ESI-MS spectrum of **4** in positive mode

### Oligomer **5**

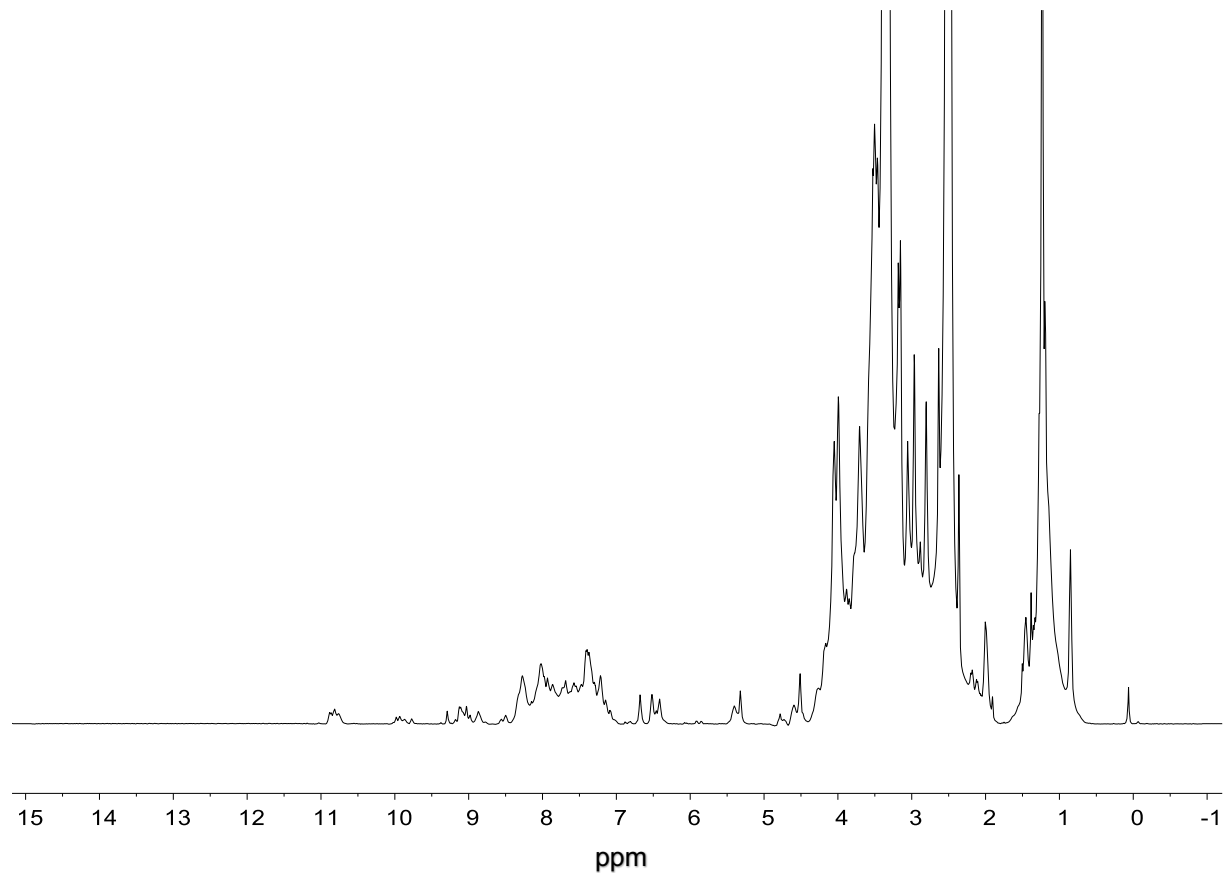


RP HPLC chromatogram of **5** on  $C_{18}$  and 10-100% A/B (water/acetonitrile) + 0.1% TFA in 12 min at 300nm

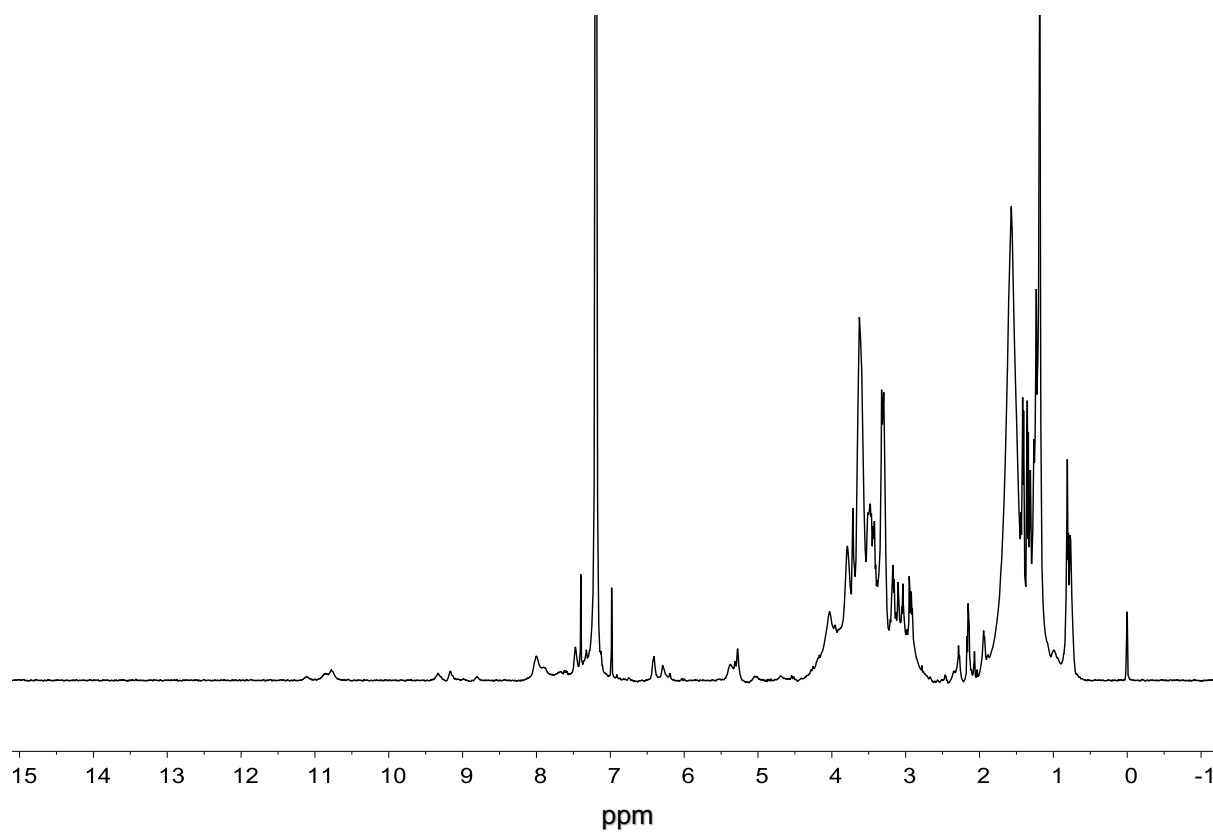


ESI-MS spectrum of **5** in positive mode

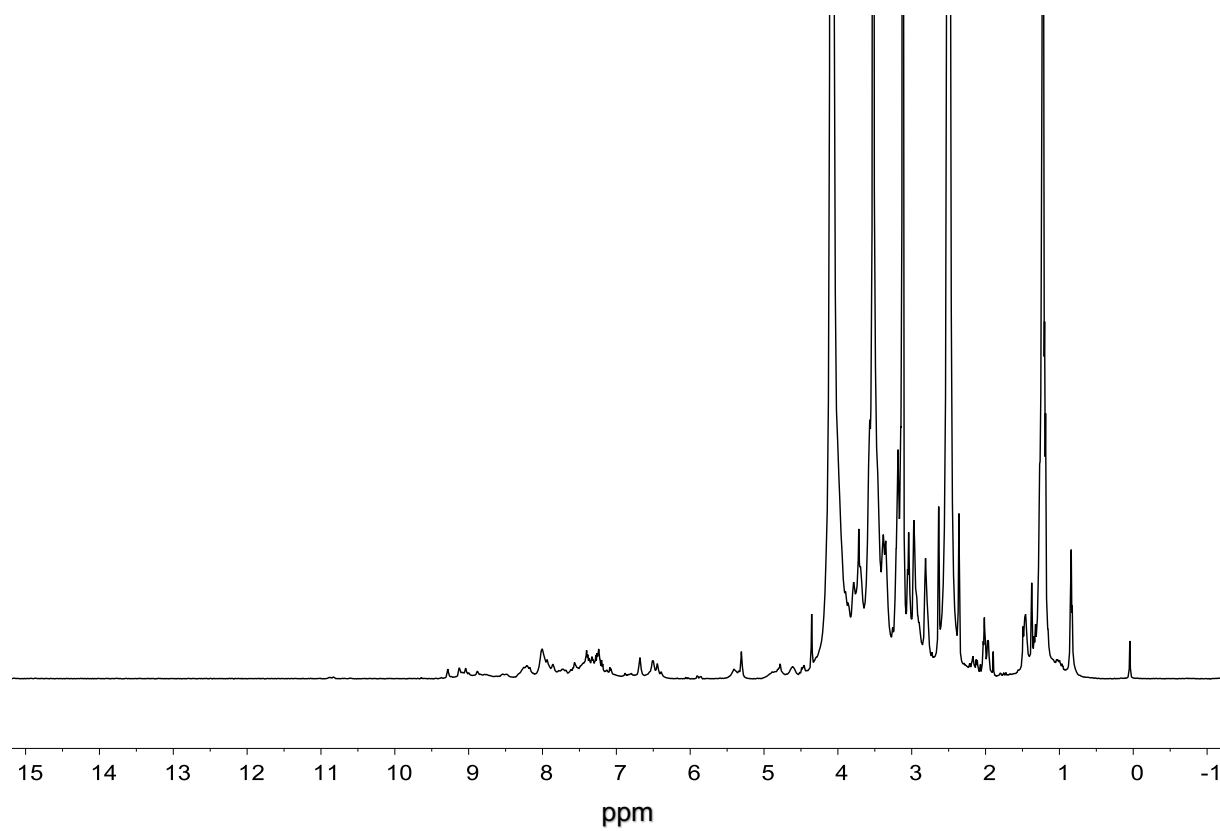
### Macrocycle **1**



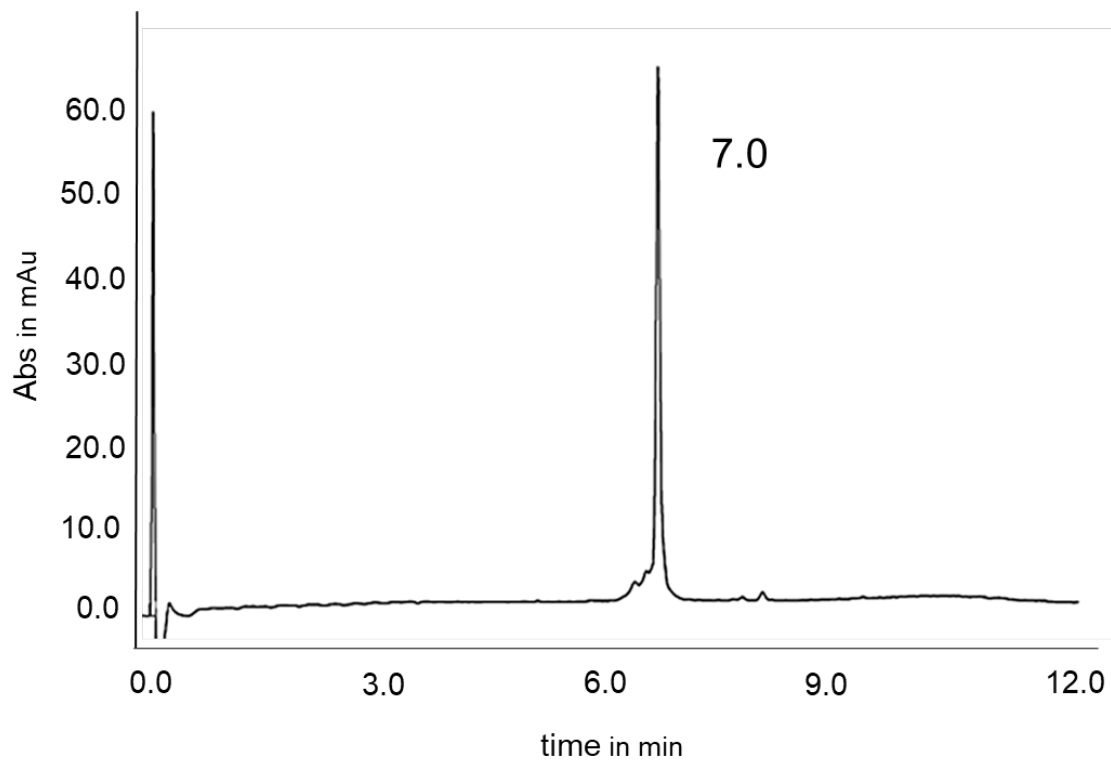
<sup>1</sup>H NMR spectrum of **1** in *d*-DMSO at 500MHz and 512 scans



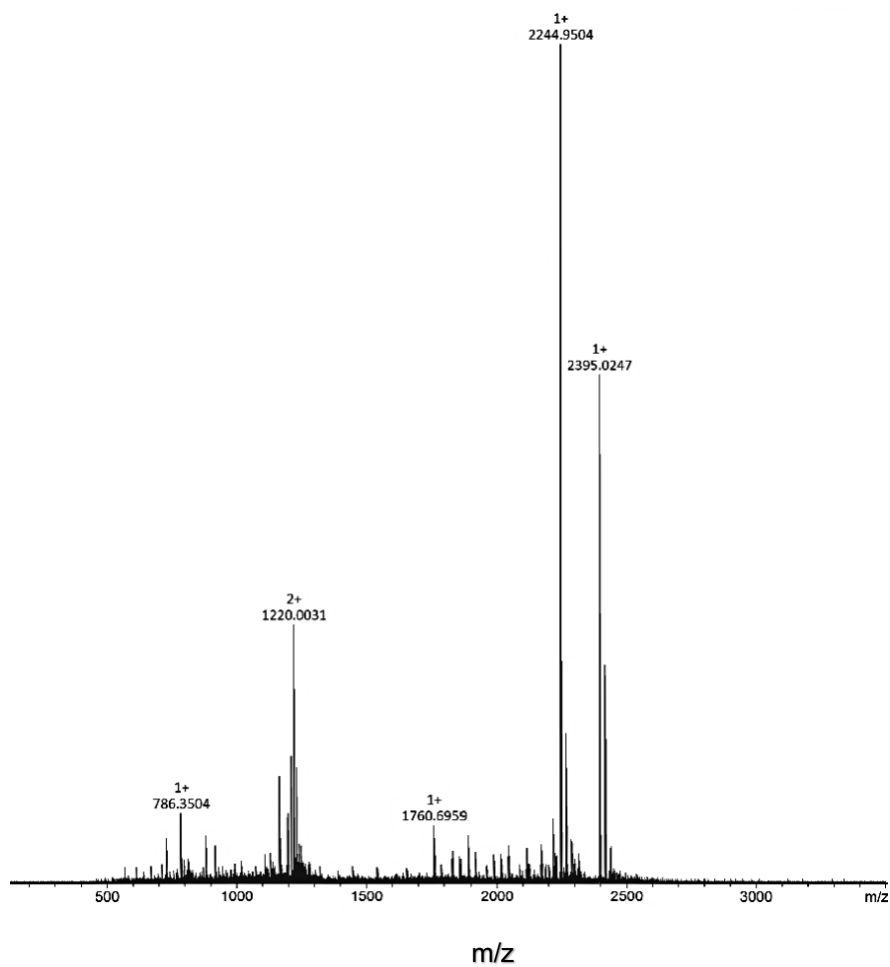
$^1\text{H}$  NMR spectrum of **1** in  $d\text{-CHCl}_3$  at 500MHz and 512 scans



$^1\text{H}$  NMR spectrum of **1** in  $d\text{-DMF}$  at 500MHz and 512 scans

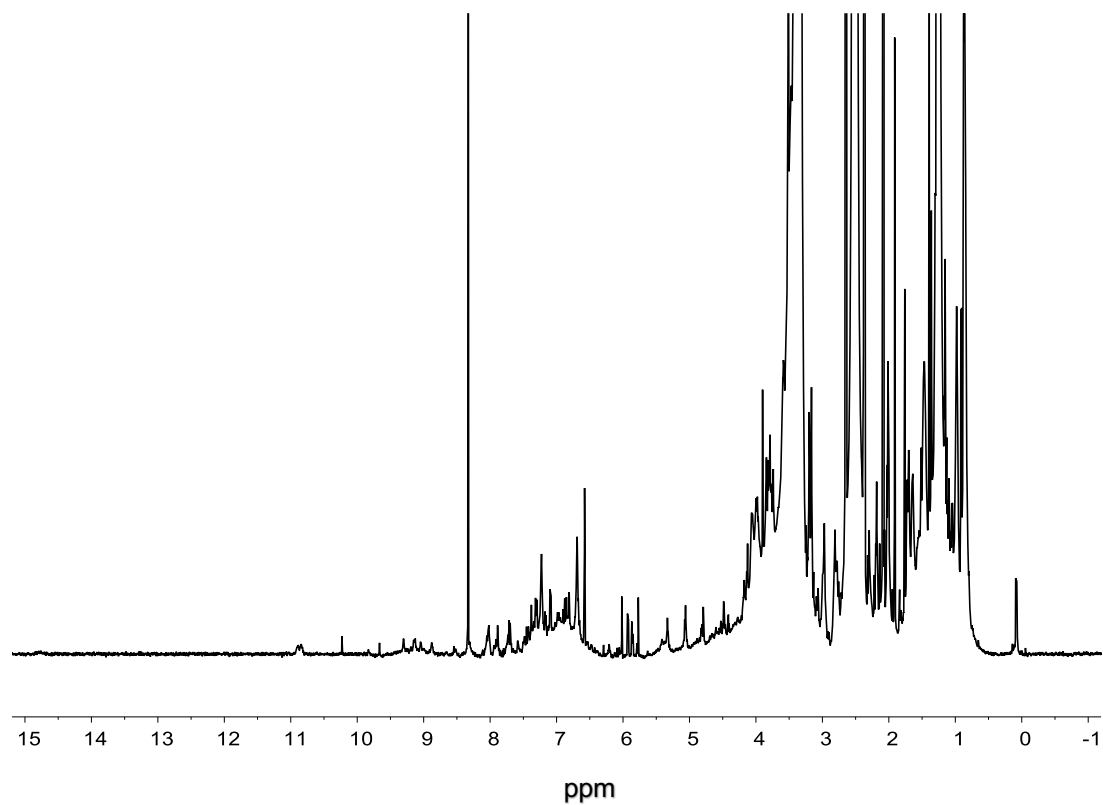


RP HPLC chromatogram of **1** on C<sub>18</sub> and 10-100% A/B (water/acetonitrile) +0.1% TFA in 12 min at 300nm

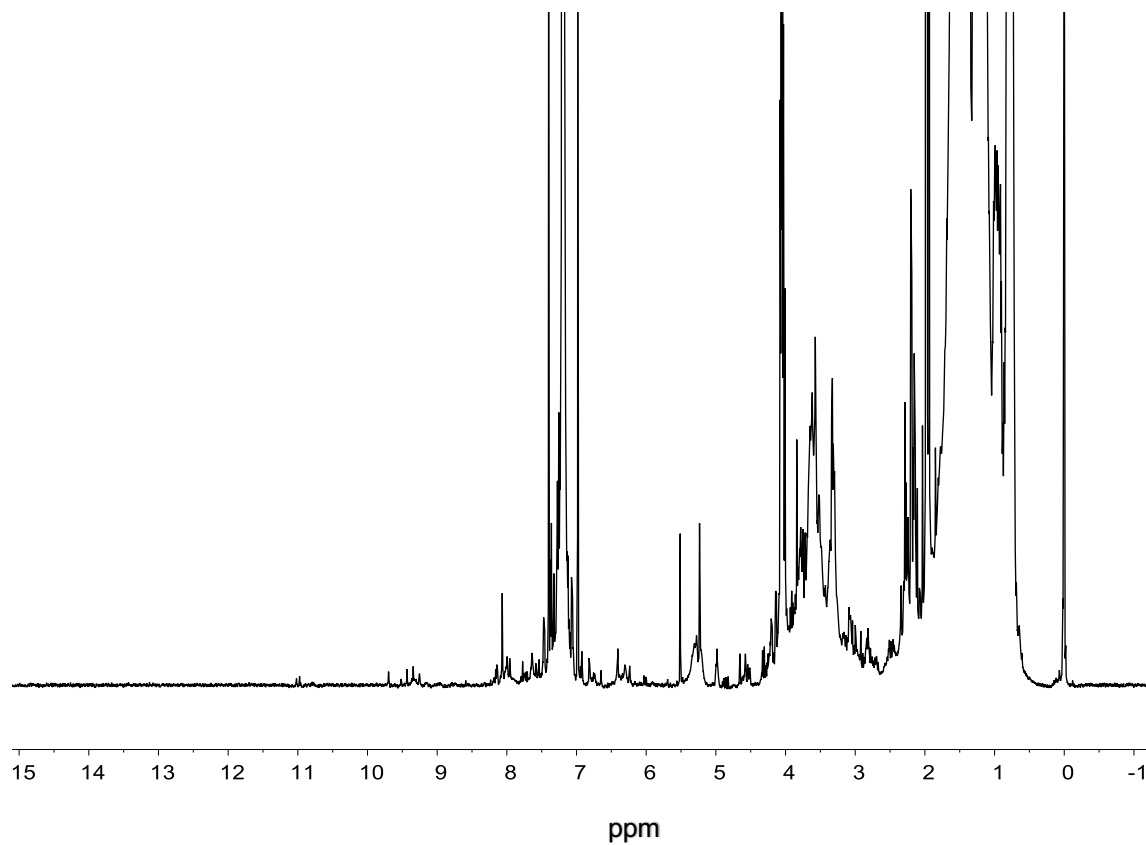


ESI-MS spectrum of **1** in positive mode

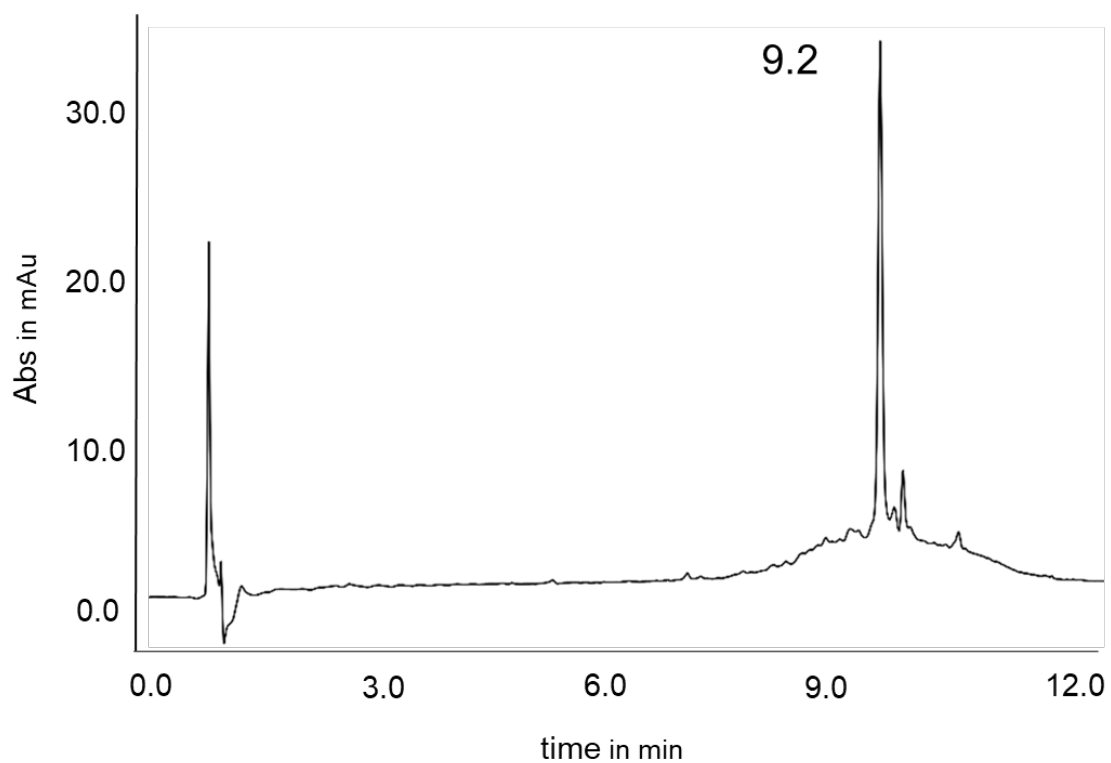
## Macrocycle **2**



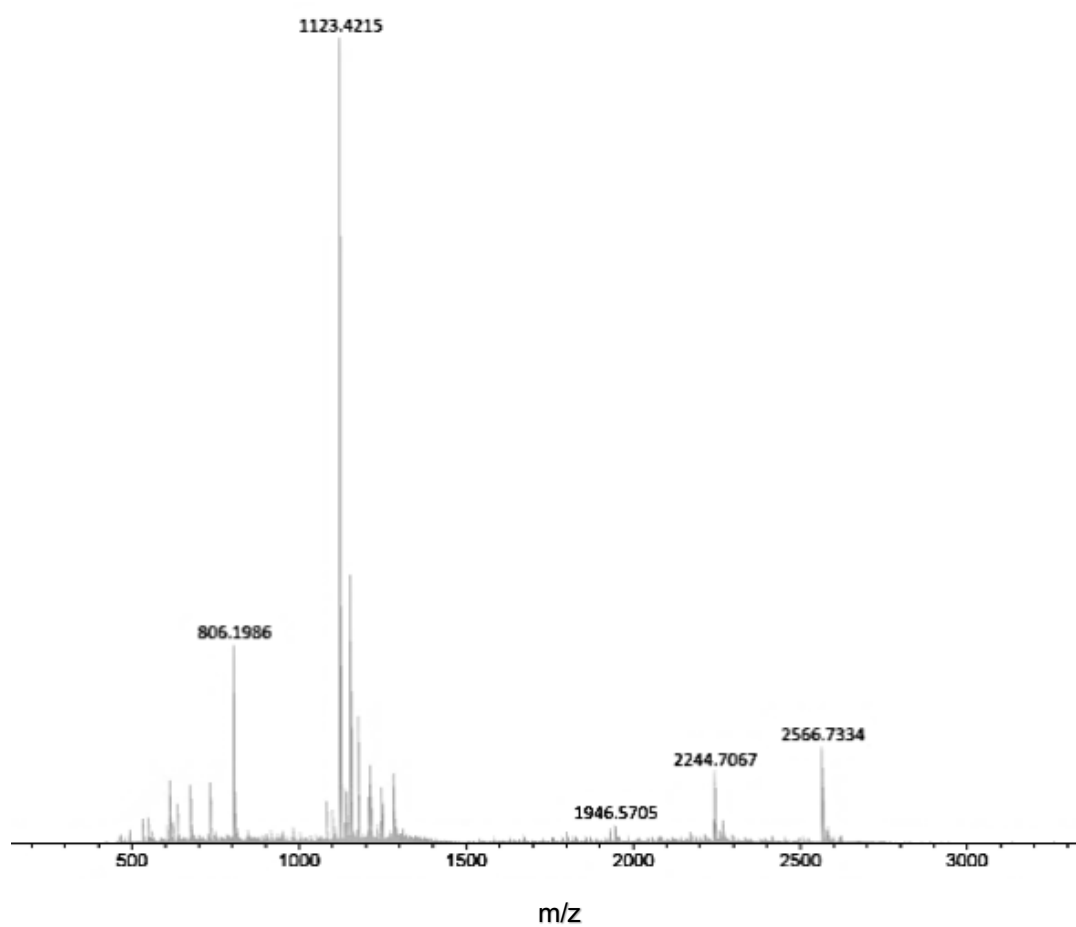
<sup>1</sup>H NMR spectrum of **2** in *d*-DMF at 500MHz and 512 scans



<sup>1</sup>H NMR spectrum of **2** in *d*-CHCl<sub>3</sub> at 500MHz and 512 scans



RP HPLC chromatogram of **2** on C<sub>18</sub> and 10-100% A/B (water/acetonitrile) +0.1% TFA in 12 min at 300nm



ESI-MS spectrum of **2** in positive mode

## 6. Summary and Outlook

### 6.1 Conclusions through this work

In this work, a new family of rod-like molecules has been presented. These rod-like molecules are based on 6-aminoquinoline 2-carboxylic acid units ( $Q^P$ ; see chapter 1 for more details on this monomer) which are covalently bound to a central terephthalic acid unit. The terephthalic acid unit has been shown to work as a center of inversion of the foldamer's directionality. The interconversion was established by using the terephthalic acid unit which created linearity in the foldamer sequence. Further, it has been shown and proved that rod-like molecules based on  $Q^P$  can be incorporated in lipid bilayer membranes. Furthermore, they propose a new tool to control geometry, bending rigidity and molecular composition of membranes by using ultra-short nanotubes (usNT). Moreover, they can be traced by single-molecule measurements *via* distinct current response and show binding affinity towards membrane proteins e.g., Annexin V and ENTH (see chapter 3 for more details).

Another concept that has been demonstrated in this work is the use of linearity disruptor groups i.e. DMB groups on this monomer family. They enabled kinking of the foldamer backbone and changing the overall geometry through *cis/trans* isomerism. In this way, the final sequence length of the  $Q^P$  foldamer has been dramatically reduced for enabling intramolecular cyclization. Moreover, the successful macrocyclization of the  $Q^P$  sequences has been demonstrated. Specifically, the shortest possible foldamer sequence based on  $Q^P$  was synthesized and studied. Moreover, larger macrocycles were found to comprise potential for molecular recognition, that prompts for further investigations. Their solvent and temperature dependency as well as their dependency to external stimuli was studied and shown (see chapter 4 for more details).

Macrocyclic architectures consisting of  $Q^P$  unit either – homomeric sequences or in hybrid models – has been shown to be successfully synthesized on solid phase and effectively macrocyclized in the last step. Furthermore,  $Q^P$  foldamers were hybridized with oligopeptides, opening up their application for future peptidomimetic designs. Finally, it has been shown in the peptide-foldamer hybrids that the  $Q^P$  foldamer conformation affect the oligopeptide conformation and overturn the whole conformation of these hybrids (see chapter 5 for more details).

## 6.2 Challenges and possible problems

Aromatic oligoamide foldamer synthesis – either solid phase assisted or in solution – relies on efficient amide couplings and solubility of the intermediate sequences throughout the whole synthesis. The reactivity of the arylamine is the critical driving force during the repetitive couplings to the activated acid chloride. Beside the latter, steric hindrance of the aminogroup during sequence prolongation contributes to a to deletions in the sequence which consequently lead poor coupling yield. Within the different monomer families, e.g., 1,8-naphthyridines, quinolines, anthracenes, pyridines or benzenes, and their substitutions, the reactivity of each building block varies depending on their chemical backbone. Additionally, monomers cannot be simply purchased commercially and need to be synthesized beforehand. That being so, the choice of the monomer for the foldamer design plays a key role in the whole synthesis, where sidechain and backbone characteristic need to be taken into account in an early stage.

Rod-like foldamers are prone to unspecific aggregation and thus, purification *post* synthesis is challenging. Moreover, rod-like molecules with prolonged sequence length may lead to analytical drawbacks. Specifically, we experienced analytical bottlenecks when targeting longer Q<sup>p</sup> sequences. Their wide aromatic surface, which is increased with each coupling step enhances non-covalent interactions, such as aromatic interactions and thus promotes aggregation. Consequently, we changed the design and choose solubilizing sidechains. The use of ethyleneglycol derivatives as sidechains enabled solubility in most organic solvents and thus, common analytical detection and purification of short Q<sup>p</sup> foldamer rods became possible.

Finally, the use of DMB groups during the synthesis can further help in this respect. Specifically, by creating tertiary arylamide functionalities, and thus kinking of the sequence, unspecific aggregation in solution or on resin could be avoided. Nevertheless, when removing the latter, final purification can be demanding when targeting larger designs.

### 6.3 Perspectives

$\beta$ -barrel proteins represent a wide family of  $\alpha$ -helical and  $\beta$ -sheet conformed molecules with distinct conformation and overall pore-like structures. Their biological functions are manifold. For the purpose to mimic these  $\beta$ -barrel proteins macrocyclic  $\beta$ -barrel-like molecules can be designed based on  $Q^p$  building blocks. These macrocycles need to be composed of building blocks that provide both rigidity and stability through wide aromatic surfaces providing  $\pi$  -  $\pi$  stacking, as well as comprising a low curvature to create a wide cavity.

As an extend to this work, two  $\beta$ -barrel architectures based on  $Q^p$  monomers were designed and visualized using MacroModel Software from Schrödinger. For the  $\beta$ -barrel backbone, we decided to use  $Q^p$  monomers as main building block for the synthesis. As the turn unit, the  $N,N'$ -dimethyl- $N,N'$ -diphenyl-squaramide turn unit (hereafter referred to as "S") was chosen to mimic the naturally occurring  $\beta$ -hairpin motif.

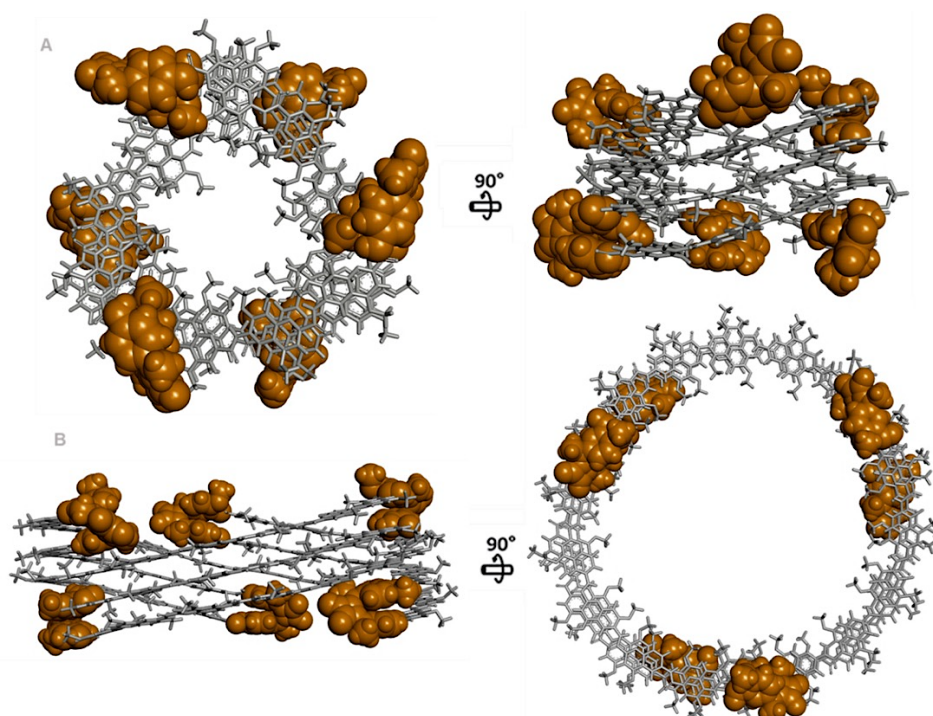


**Fig. 1 Molecular models of  $\beta$ -barrel mimics.** (A) 39<sup>mer</sup> and (B) 60<sup>mer</sup> barrel, turn units S shown in space filling mode and colored in orange.

After rationalizing the design i.e. that the foldamer barrel mimic has the general formula of  $((SX_nSX_m)_p)$  (wherein X is the monomer; n and m are numbers of monomer used and p is the number of sheets within the barrel) we concluded that the shear

number ( $s$ ) of the barrel needs to be close to the natural curvature of the monomer. The shear number  $s$  can be calculated according to

$$\text{Eq. (1)} \quad s = p|n - m|$$

According to Eq. 1, the total number of  $Q^p$  units needed for a  $\beta$ -barrel design is 60 (**Figure 1B**). As can be seen in the model shown in **Fig. 1B**, the 60<sup>mer</sup> comprises a wide cavity with three strands being stacked on top of each other. In order to reduce the number of units needed in total, we further investigated how to combine the  $Q^p$  unit with other monomers to target a possible shorter sequence length.

In further computational studies, we designed a heteromeric backbone composed of the  $Q^p$  monomer together with 7-aminoquinoline 2-carboxylic acid building block ( $Q^m$ ; see chapter 1 for more details for the monomers). As the  $Q^m$  building block has a smaller folding angle, the length of the  $\beta$ -strands could be minimized in terms of number of units (**Figure 1A**). By doing so, we obtained a  $\beta$ -barrel model based on  $Q^p$  and  $Q^m$  with the total number of 39 units.

As for now, no artificial peptidomimetic  $\beta$ -barrel have been described successfully. To endeavor these large barrel architectures it is necessary to prevent aggregation of the intermediate molecules and establish straightforward analytical methods. By forming macrocyclic molecules, the cavity and interior of the  $\beta$ -barrels can be functionalized and used for molecular recognition, i.e. as transport or transmembrane pore-like molecules. It remains to be seen to what extent these findings will help in this respect and what the design of artificial  $\beta$ -barrel mimics will look like.